

## **General Disclaimer**

### **One or more of the Following Statements may affect this Document**

- This document has been reproduced from the best copy furnished by the organizational source. It is being released in the interest of making available as much information as possible.
- This document may contain data, which exceeds the sheet parameters. It was furnished in this condition by the organizational source and is the best copy available.
- This document may contain tone-on-tone or color graphs, charts and/or pictures, which have been reproduced in black and white.
- This document is paginated as submitted by the original source.
- Portions of this document are not fully legible due to the historical nature of some of the material. However, it is the best reproduction available from the original submission.

X93-36235

**FINAL REPORT OF WORK  
COMPLETED UNDER NAS8-36479**

**SUBMITTED TO:**

**NATIONAL AERONAUTICS AND SPACE ADMINISTRATION  
MARSHALL SPACE FLIGHT CENTER, ALABAMA**

**SUBMITTED BY:**

**DR. RICHARD T. MCNIDER**

**EARTH SYSTEM SCIENCE LABORATORY  
UNIVERSITY OF ALABAMA IN HUNTSVILLE  
HUNTSVILLE, ALABAMA 35899**

**JUNE 18, 1992**

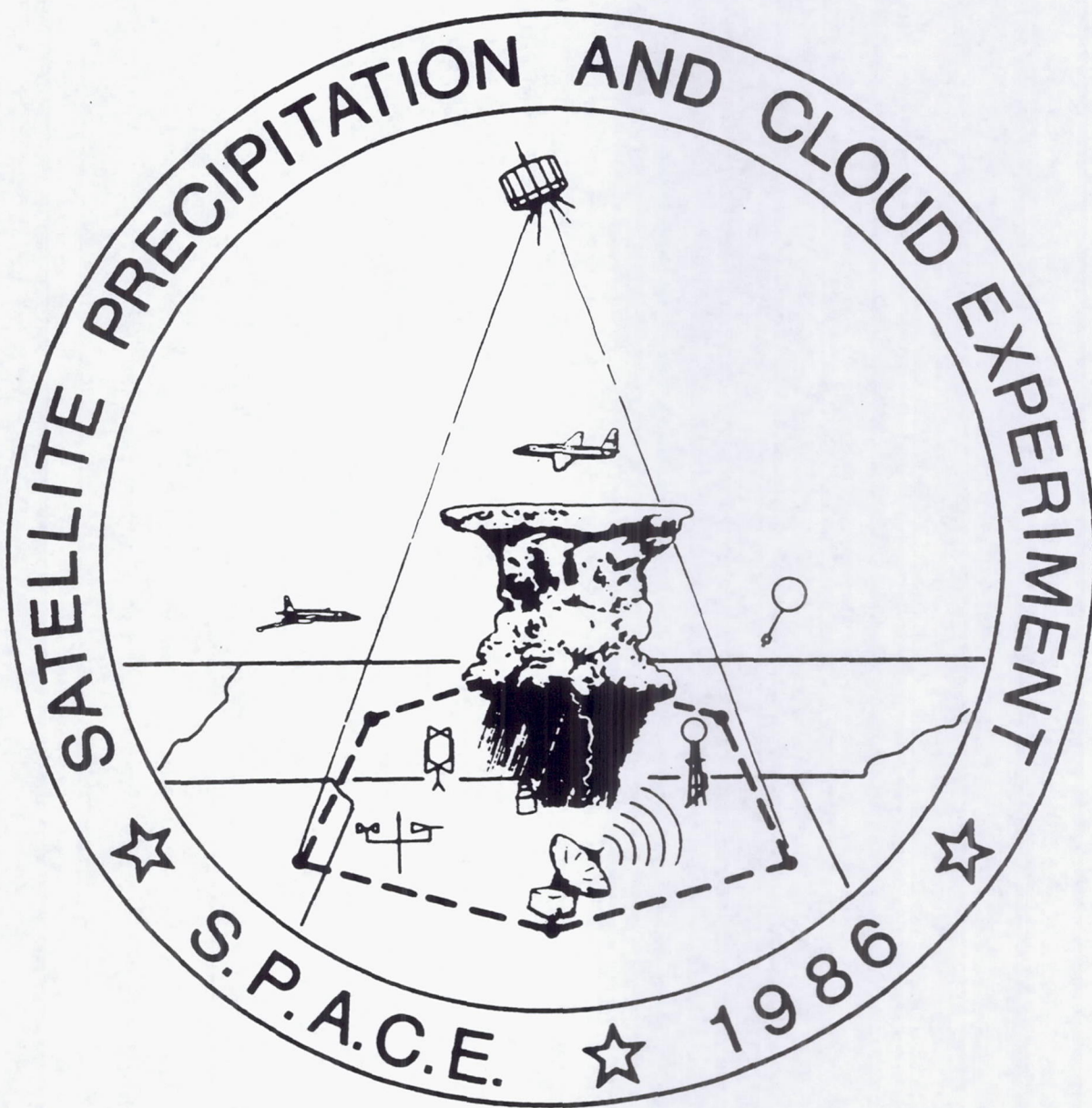
The work performed on this contract was related to understanding the initiation, organization and structure of moist convection in the Southeast environment. The work can be categorized into four basic areas which are:

- 1. Planning and coordination of a major interagency atmospheric field program (SPACE-COHMEX).** This work first involved studying the climatology and characteristics of moist convection in the South in order to develop time schedules and observational strategies for carrying out field program observations. The second aspect of this component involved developing the type of observational platforms needed to carry out the program. Thirdly, interagency agreements and schedules were negotiated in developing the operation plans for the SPACE-COHMEX field program. This involved interaction with the FAA, NASA-Goddard, NASA Marshall, NCAR, University of Chicago, UCLA, Penn State, and other universities. The attached document describes the planning process for the SPACE component of COHMEX. This document was the formal planning and operational document for SPACE.
- 2. Field Program Observations under SPACE-COHMEX.** This part of program involved making field program observations during the SPACE-COHMEX field program during June-July, 1986. The major observational activity was the operation of an upper air rawinsonde network to provide ground truth for aircraft and spacecraft operations. During the course of the program approximately 1,000 rawinsonde launches were made and the data processed. This data was contributed to the SPACE-COHMEX archive at MFSC. The second major activity under this program was the siting and operation of a surface mesonet program. Five UAH/MSFC mesonet sites were established and operated in addition to the siting of the NCAR PAM system. A solar observational component was also carried out at each of the mesonet sites. The attached figures show the rawinsonde and mesonet-pyranometer networks.
- 3. Mesoscale Numerical Modeling of Boundary Layer Initiation of Convection.** This program involved using boundary layer mesoscale models to study and simulate the initiation and organization of moist convection due to mesoscale thermal and mechanical circulations. The first series of experiments involved the simulation of a mesoscale squall line initiated during the AVE-VAS field experiment during 1982. The attached papers (McNider, Jedlovec and Wilson and McNider, Kopp and Kalb and McNider and Kopp) describe the results of these experiments. A second set of experiments began to simulate the organization of convection under the SPACE -COHMEX. The attached figures show preliminary results from these experiments.

- 4. Collection, archival and distribution of COHMEX -SPACE data sets.**  
During and after the COHMEX field program a concerted effort was made to collect and archive all pertinent supporting data set and information. The attached portion of a document shows the typical summary of each COHMEX field program day and the available data. In addition to the data summary, supporting information such as weather analyses, TVA raingauge data, radar catalogs were archived. Immediately after the field program UAH began to handle the request and distribution of the data. This continued through the remainder of the contract with only minimal charges incurred for this activity toward the end of the contract period.

**Planning and coordination of a major interagency atmospheric  
field program (SPACE-COHMEX).**

# Satellite Precipitation and Cloud Experiment



Experiment Design Document  
March 1986

## FORWARD

The initiation, structure and organization of convection is an active area of research within NASA's Mesoscale Atmospheric Processes Research Program because of its importance in developing new remote sensors and in interpreting remotely sensed data. In the spring and summer of 1986, NASA/Marshall Space Flight Center (MSFC) will sponsor the Satellite Precipitation And Cloud Experiment (SPACE) to be conducted in the Central Tennessee, Northern Alabama, and Northeastern Mississippi area. The field program will incorporate high altitude flight experiments associated with meteorological remote sensor development for future space flight, and an investigation of precipitation processes associated with mesoscale and small convective systems. In addition to SPACE, the Microburst and Severe Thunderstorm (MIST) program, sponsored by the National Science Foundation (NSF), and the FAA-Lincoln Laboratory Operational Weather Study (FLOWS), sponsored by the Federal Aviation Administration (FAA), will take place concurrently within the SPACE experiment area.

This document is meant to provide an overview of the NASA SPACE program to participants in SPACE as well as to participants in the companion MIST and FLOWS programs. We feel that a broad understanding of the goals and designs of the many individual experiments which make up a field program will lead to more efficient scientific collaboration and interaction.

This document is made up of contributions from a number of different investigators. We gratefully acknowledge these contributions made under a short time schedule. These contributions were prefaced, edited and reorganized in an attempt to make a coherent document. We take full responsibility for any errors that may have arisen from this process.

Finally, we would like to acknowledge Dr. William Vaughan, Chief of the Atmospheric Science Division at Marshall Space Flight Center, and Dr. James Dodge, Manager of the Mesoscale Atmospheric Processes Research Program at NASA Headquarters, for their support and assistance in this program.

James Arnold  
Gregory Wilson

Atmospheric Physics Branch  
Atmospheric Science Division  
NASA/MSFC  
Huntsville, AL 35812

Steven Williams  
Richard McNider

Atmospheric Science Laboratory  
K.E. Johnson Research Center  
University of Alabama at Huntsville  
Huntsville, AL 35899

## **ACKNOWLEDGEMENTS**

The following are acknowledged for their timely contributions to this document: R. Adler, R. Blakeslee, H. Christian, J. Arnold, G. Jedlovec, R. Spencer, S. Goodman, J. Simspson, W.-K. Tao, R. McNider, P. Robertson, M. Kalb, K. Knupp, S. Williams, P. Smith, H. Fuelberg, J. Spinhirne, G. Heymsfield, T. Wilheit, G. Szejwach, and A. Negri.

Lori McCain and Dawn Ryan are commended for their diligent preparation of the manuscript. This work was sponsored under NASA Contract NAS8-36479.

Published by: Atmospheric Sciences Laboratory  
K.E. Johnson Research Center  
University of Alabama at Huntsville  
Huntsville, AL 35899

**NASA/SPACE Field Program  
Experiment Design**

<b>1. INTRODUCTION</b>	1
1.1 Objectives and Facilities of SPACE/COHMEX	1
1.1.1 SPACE	1
1.1.2 MIST	3
1.1.3 FLOWS	3
1.2 Location and Period of Field Studies	3
1.3 SPACE Project Management	5
<b>2. REMOTE SENSING OBJECTIVES</b>	9
2.1 Fine Resolution Atmospheric Scanning and Sounding	9
2.1.1 Multispectral Atmospheric Mapping Sensor (MAMS)	9
2.1.2 High Resolution Interferometer Sounder (HIS)	14
2.2 Lightning Observations (LIP, LRP)	14
2.2.1 Lightning Instrumentation Package	14
2.2.2 Lightning Research Package	16
2.3 Investigating the Multifrequency Microwave Signature of Clouds and Precipitation (MPR)	16
2.3.1 Justification	16
2.3.2 MPR Data Analysis	17
2.3.3 Impact	17
2.4 Precipitation, Sounding and Cloud Structure (AMMS, MCR, CLS, MTS, HIS, MPR)	17
2.4.1 Precipitation	17
2.4.2 Temperature and Moisture Sounding	18
2.4.3 Storm Structure	19
2.4.4 Moisture Sounding	19
<b>3. SCIENTIFIC OBJECTIVES</b>	20
3.1 Pre-storm Environment	21
3.1.1 Moisture Variability	21
3.1.2 Mesoscale Convergence	21

3.2 Relationships Between Bulk Convection and Its Environment	22
3.2.1 Diabatic Processes and Vertical Transports in MCS's	22
3.2.2 Dynamics of MCS Environments	27
3.3 Precipitation Processes and Electrical Activity	28
3.3.1 Convective Cloud and Precipitation Relations and the Development of Visible/IR Rain Estimation Techniques	28
3.3.2 Precipitation Processes and Electrical Activity	28
3.4 Numerical Modeling	33
3.4.1 Regional Scale Models (Meso-alpha)	33
3.4.2 Mesoscale Boundary Layer Models (Meso-beta, Meso-gamma)	33
3.4.3 Cloud Scale Models	36
3.4.4 Multi-scale Models	36
3.5 Convective Structure and Evolution	36
3.5.1 Internal Convective Structure	37
3.5.2 Cumulus Population and Mergers	37
<b>4. EXPERIMENT DESIGN</b>	<b>42</b>
4.1 Regional Climatology and Expected Synoptic Conditions	42
4.1.1 Climatology	42
4.1.2 Strong Synoptic-scale Forcing (6/7/85)	42
4.1.3 Synoptic-scale or Meso-scale Forcing at Low Levels (7/4/85)	45
4.1.4 Negligible Synoptic-scale Forcing (7/18/85, 7/19/85)	45
4.2 Upper Air Network	59
4.2.1 Ground Truth for Remote Sensors	59
4.2.2 Mass, Momentum, and Moisture Budgets	60
4.2.3 Initialization and Verification of Numerical Models	60
4.2.4 Background Environmental Conditions	60
4.3 Associated Radar Network	60
4.4 Surface Network	61
<b>5. SPECIAL OBSERVING PROGRAM AND FACILITIES</b>	<b>66</b>
5.1 Aircraft Systems	66
5.1.1 NASA/ARC ER-2	66
5.1.2 NASA/ARC U-2C	74

5.1.3 T-28	74
5.2 Radar Systems	76
5.2.1 RADAP II/ICRAD	76
5.2.2 Kavouras	76
5.2.3 CP-2	77
5.2.4 Other Doppler Radars	77
5.3 Sounding Systems	80
5.3.1 Meso-alpha Rawinsonde	80
5.3.2 Meso-beta Rawinsonde	80
5.3.3 Meso-gamma Rawinsonde	80
5.4 Surface Mesonet Systems	87
5.4.1 Portable Automated Mesonet System (PAM II)	87
5.4.2 NASA Mesonet System (NAMS)	87
5.4.3 FAA Mesonet Station Network	88
5.5 Lightning Detection System	98
5.5.1 Real-time Displays	98
5.5.2 Data Archive	98
5.6 Raingage Systems	100
5.6.1 TVA Automated Raingages	100
5.6.2 Supplemental Raingages	100
5.7 Meteorological Satellite Systems	100
5.7.1 Geostationary Platforms	105
5.7.2 Polar Orbiting Platforms	105
<b>6. OPERATIONS CONTROL</b>	<b>109</b>
6.1 Facility Description	109
6.2 Operations Forecast Center	111
6.2.1 Operational Data Flow	111
6.2.2 Nowcasting	111
6.2.3 Operational Briefings	112
6.2.4 Long Range Outlooks	112
6.3 Coordination and Communication	112
6.3.1 Coordination with COHMEC Operational Centers	113
6.3.2 Air Traffic Coordination	113
6.3.3 Radar Coordination	116
6.3.4 Communications and Real-time Data Transfer	117

<b>7. DATA MANAGEMENT</b>	119
<b>7.1 Data Types</b>	119
7.1.1 Conventional Data	119
7.1.2 Special Experimental Data	119
<b>7.2 Data Sets</b>	123
7.2.1 Documentation of Daily Operations	123
7.2.2 Preliminary Data Sets	124
7.2.3 Final Data Sets	124
7.2.4 Documents	124
<b>7.3 Data Processing</b>	125
7.3.1 Facilities	125
7.3.2 Data Quality Assurance and Validation	126
<b>7.4 Data Archiving and Distribution</b>	127
<b>References</b>	129
<b>Appendix A</b>	133
SPACE Mailing List	
<b>Appendix B</b>	144
Acronyms	

## 1.0 INTRODUCTION

In the spring and summer of 1986, NASA/Marshall Space Flight Center (MSFC) will sponsor the Satellite Precipitation And Cloud Experiment (SPACE) to be conducted in the Central Tennessee, Northern Alabama, and Northeastern Mississippi area. The field program will incorporate high altitude flight experiments associated with meteorological remote sensor development for future space flight, and an investigation of precipitation processes associated with mesoscale and small convective systems. In addition to SPACE, the Microburst and Severe Thunderstorm (MIST) program, sponsored by the National Science Foundation (NSF), and the FAA-Lincoln Laboratory Operational Weather Study (FLOWS), sponsored by the Federal Aviation Administration (FAA), will take place concurrently within the SPACE experiment area. All three programs (under the joint acronym COHMEX (COoperative Huntsville Meteorological EXperiment)) will provide a data base for detailed analysis of mesoscale convective systems while providing ground truth comparisons for remote sensor evaluation.

The purpose of this document is to outline the experiment design criteria for SPACE, and describe the special observing facilities and data sets that will be available under the COHMEX joint program. An Operations Plan and Data Management Plan for SPACE will be prepared under separate cover to describe the experiment execution in greater detail.

### 1.1 Objectives and Facilities of SPACE/COHMEX

Each component of the COHMEX program has unique and independent objectives and goals, but together provide an excellent opportunity to share resources and facilities in a cooperative manner. The program is structured such that coordination of mesoscale convection research activities and cooperative data exchange can address all objectives. The following sections overview the objectives and facilities of each component of COHMEX.

#### 1.1.1 SPACE

NASA's SPACE experiment effort has both a scientific and engineering purpose. An understanding of the physics, behavior, and distributions of the parameters which are to be measured from sensors on space-based platforms is necessary to both evaluate and improve existing measurement systems and develop new measurement systems. Thus, both objectives are closely related and can be defined as follows:

- o Contribute to the understanding of precipitation processes associated with mesoscale and small convective systems and use this understanding to help define space sensor requirements for remote sensing applications.
- o Provide a testing ground using diverse measurement systems to evaluate new remote sensors to be flown on high altitude aircraft.

During the pre-storm period, the experiment will focus on observations of the physical processes leading to the formation of small convective systems. Once convection develops, emphasis will be placed upon observations of precipitation and hydrometeor evolution and the influence of moisture sources in the storm environment for the develop-

ment and maintenance of the precipitation process. During the mature phases of the storms, studies will be conducted to relate electrical activity to precipitation and dynamical processes. Before, during and after the development of convection, detailed sets of atmospheric state variable data will be collected to enable numerical modeling of the boundary layer, tropospheric and cloud-scale thermodynamics, and environmental variability related to the life cycle of small convective systems.

Crucial observations for NASA's SPACE experiment will be obtained from numerous flights of two high-altitude aircraft (a NASA U-2C and ER-2) with a total complement of ten experimental remote sensing systems. These systems will measure visible, infrared, and microwave radiation for determination of various storm/environment characteristics such as cloud top structure, cloud microphysics, precipitation, cloud and environmental temperature and moisture soundings, lightning characteristics, and high-resolution cloud, water vapor and surface features.

The South Dakota School of Mines and Technology's T-28 storm penetrating aircraft will be employed for conventional observations of liquid water and hail size concentrations, hydrometeor size distributions, internal cloud temperature, and electric field structure. In addition, networks of raingages, upper air rawinsonde stations, surface stations, and lightning location and detection stations will operate at high time resolutions to define the pre-storm and storm environments. A meso-alpha scale rawinsonde network consisting of the National Weather Service (NWS) stations surrounding the COHMEX region will collect data to support a multi-scale analysis of convective events.

Digitized reflectivities from the Nashville, Tennessee, WSR-57 radar will be processed using a Radar Data Processor/Interactive Color Radar Display (RADAP II/ICRAD) system and recorded throughout the experiment. The National Center for Atmospheric Research (NCAR) CP-2 Doppler radar will be shared with the other experiments for high-resolution, calibrated estimates of mesoscale rainfall and multi-parameter cloud measurements.

The NOAA GOES satellite will be operated in dwell image, dwell sounding and rapid-scan modes to provide the maximum information consistent with operational and research requirements of both NOAA and experiment objectives. In addition to the GOES satellite data, information from polar orbiting satellites will be utilized. In particular, Tiros Operational Vertical Sounder (TOVS), High resolution Infrared Radiometer Sounder (HIRS), Microwave Sounding Unit (MSU), and Advanced Very High Resolution Radiometer (AVHRR) data as well as the Defense Meteorological Satellite Program (DMSP) Special Sensor Microwave Imager (SSM/I) data, should it be available, will all be archived to the data base.

The target area for the SPACE experiment will be within the drainage basin of the Tennessee River north of Huntsville, Alabama. This area is well instrumented with the Tennessee Valley Authority (TVA) raingage system as well as the National Weather Service (NWS) Cooperative observer raingage network. This region also provides an excellent area to study warm-based cumulus convection in a sub-tropical humid environment. The SPACE experiment will begin to collect data during the spring when frontal and squall-line convective activity produce heavy precipitation and severe thunderstorms. The most intense operational period will occur in the summer when surrounding moisture fields of smaller convective activity can be better defined by satellite, radar, and aircraft sensors. To understand the precipitation process and development/feedback mechanism fully, it is important to measure and define both the pre-storm and storm environment. In this respect, certain remote sensors are directly associated with the measurement of conditions in the pre-storm environment while others have direct application once the precipitation process has

begun. The goal of SPACE is to define these conditions on a scale consummate with storm development on a meso-beta and meso-gamma spatial scale.

### 1.1.2 MIST

The National Science Foundation (NSF) component of the COHME experiment is concerned with investigating the three-dimensional structure of microburst from thunderstorms and their environment in a humid region of the United States. Of particular interest in this investigation is understanding the time-dependent airflow of a microburst and the structure and development of vortex rolls associated with microbursts. The physical conditions of microbursts and their environment will be analyzed using three (3) Doppler radars, a surface mesonet station network, and penetration aircraft. Because the MIST facilities are enveloped by the SPACE network, microburst environmental forcing also can be studied.

### 1.1.3 FLOWS

The FAA sponsored component of COHME is concerned with the development and testing of automatic algorithms for wind shear (especially microburst and gust front) detection using pulse Doppler weather radars. The results from FLOWS will be used to develop algorithms for the Next Generation Weather Radar (NEXRAD) and for the FAA Terminal Doppler Radar (TDR). The principal sensor for FLOWS is an S-band Doppler Radar which is functionally equivalent to a NEXRAD system with certain additional features to provide improved clutter suppression such as may be utilized by the TDR.

Other facilities and sensors for FLOWS include a C-band Doppler Radar and Citation aircraft (both operated by the University of North Dakota), 30 FAA mesonet stations, and the Convair 580 aircraft operated by the FAA Technical Center.

Both FLOWS radars have clutter suppression filters which have been found to yield simplified post experiment (e.g. dual Doppler) analysis. Because FLOWS and MIST coverage regions and objectives are related, it is anticipated that multiple Doppler analysis will be accomplished on many microbursts which occur in this area. However, FLOWS radars will primarily utilize operationally oriented scan sequences as part of the automatic detection algorithm test program.

## 1.2 Location and Period of Field Studies

The SPACE experiment will be performed in the Central Tennessee, Northern Alabama, and Northeastern Mississippi area. This area is principally known as the Tennessee valley, and is bounded by the Tennessee and Cumberland rivers. The target area overlies the western section of TVA's raingage network, west of the Appalachian range foothills. Terrain in the area is generally small rolling hills with no major orographic features. Figure 1.2.1 shows the SPACE experiment area in greater detail. This area encompasses approximately 90,000 square km.

The MIST/FLOWS experiment area is located west of Huntsville, Alabama and lies within the SPACE target area. Therefore, experiments performed by MIST/FLOWS will

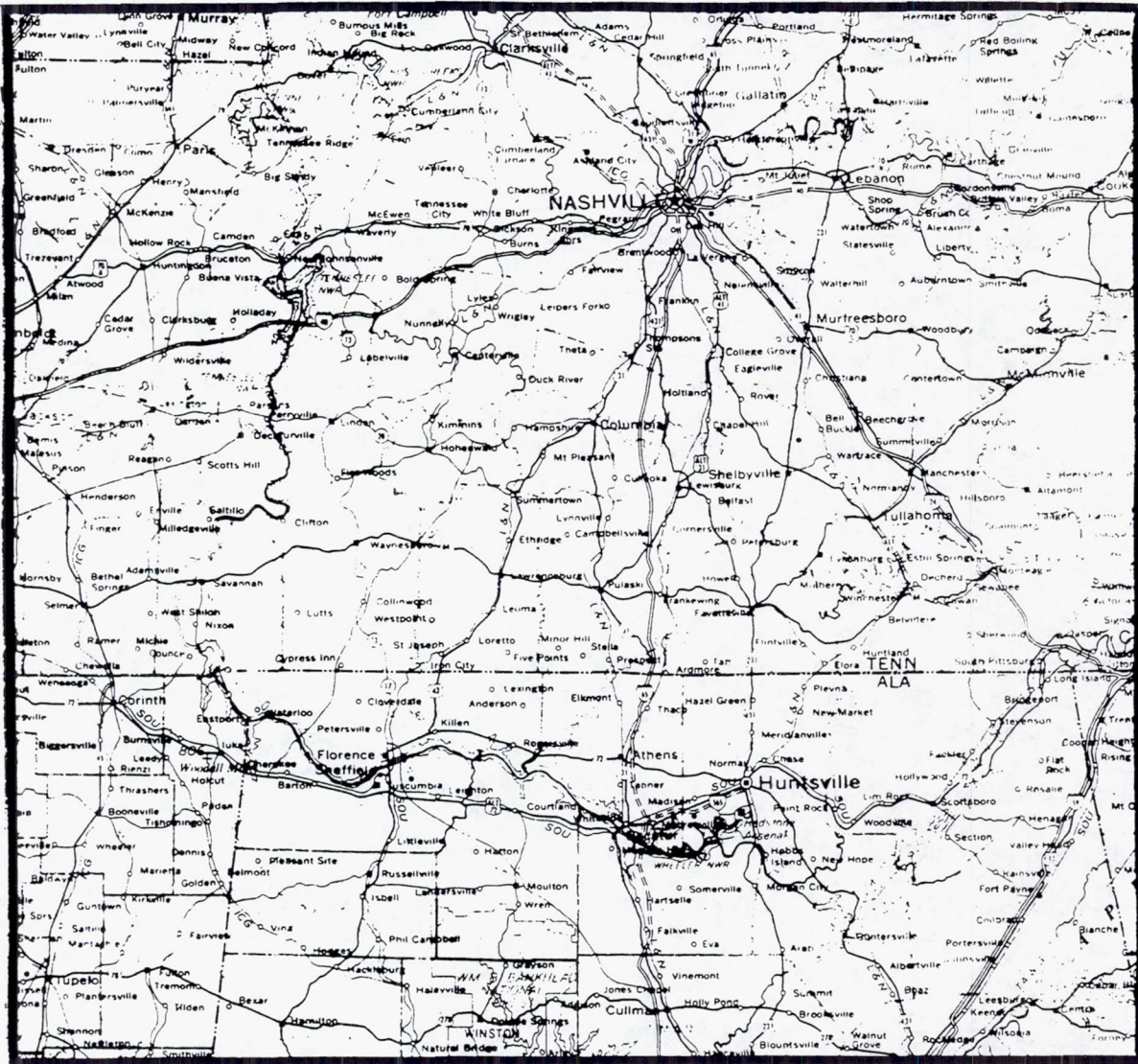


Fig. 1.2.1. Detailed SPACE experiment area.

also be of interest to SPACE objectives. The terrain in the MIST/FLOWS area is primarily cleared level farm and pastureland suitable for optimum radar and surface mesonet exposure. The area is bounded by the Tennessee river to the south, and a ridge of hills north of the Tennessee-Alabama border. This experiment area encompasses approximately 1300 square km.

The period of field studies varies with each component of COHMEX. The SPACE experiment will begin collecting data on April 15 and continue through July 31. There are two major periods of data collection during the experiment. Phase I will run April 15 through May 31, and will focus on frontal and squall line induced convection and larger mesoscale systems. Data collection will be limited to several case studies as various facilities are incorporated and calibrated. The major effort of SPACE will be performed under Phase II of the experiment during June and July when MIST program facilities become operational. Phase II data collection will focus on smaller mesoscale systems, and individual air mass convective activity.

The FLOWS experiment field study will begin approximately April 1 (as facilities become operational) and continue to autumn 1986. The experiment duration is conditional upon the amount of data collection and required time to relocate for future operational experiments. Joint resources of SPACE/FLOWS will provide excellent opportunities to study spring season convection and severe activity.

The MIST experiment field study will be performed during June and July 1986. This period will provide the greatest density of observing facilities from each component of COHMEX. Because of the cooperative data exchange, this period will be the most intensive study effort for each experiment. Figure 1.2.2 summarizes the period of field studies for each component of COHMEX.

### 1.3 SPACE Project Management

The SPACE field program is managed by the Atmospheric Physics Branch within the Atmospheric Science Division at NASA Marshall Space Flight Center in Huntsville, Alabama with Dr. Gregory Wilson, Branch Chief. Fiscal support for SPACE and related science is primarily derived through the Mesoscale Atmospheric Processes Research Program at NASA Headquarters in Washington, D.C. headed by Dr. James Dodge. Project scientist for the SPACE program is Dr. James Arnold of the Atmospheric Physics Branch at MSFC, who has been the lead organizer for SPACE and coordinator with the MIST and FLOWS programs.

In any large undertaking such as SPACE there must be a sub-division of management tasks. This submanagement has been delegated to civil service positions within the Atmospheric Physics Branch at MSFC, to inhouse contractor personnel (USRA) as well as off-site contractors such as university groups (UAH, FSU).

The following lists key members of the management team and their primary responsibilities. Figure (1.3.1) illustrates the management structure.

J. Arnold (MSFC) - Project Scientist - responsible for SPACE planning, implementation and coordination with MIST and FLOWS.

F. R. Robertson (MSFC) - Scientific Planning - responsible for science objectives and coordination with experiment design.

S. F. Williams (UAH) - Field Program Coordinator - responsible for SPACE rawinsonde and surface networks.

K. R. Knupp (UAH) - Data Management - responsible for developing plans for data ingest, archival and distribution.

O.H. Vaughan (MSFC) - Aircraft Operations - responsible for aircraft schedule, deployment and distribution.

M. Kalb (USRA) - Forecast Coordinator - responsible for developing forecast operations and dissemination.

H. Fuelberg (FSU) - Satellite Products - responsible for scheduling and receiving satellite products for operation and archival.

R. Blakeslee (MSFC) - Aircraft Coordination - responsible for developing plans for aircraft operations and communications, and coordinating remote sensing objectives of the high altitude aircraft.

D. Buechler (USRA) - Radar Products - responsible for RADAP/ICRAD, lightning network, and radar communications.

M. Goodman (UAH) - Precipitation Networks - responsible for precipitation data and data communication.

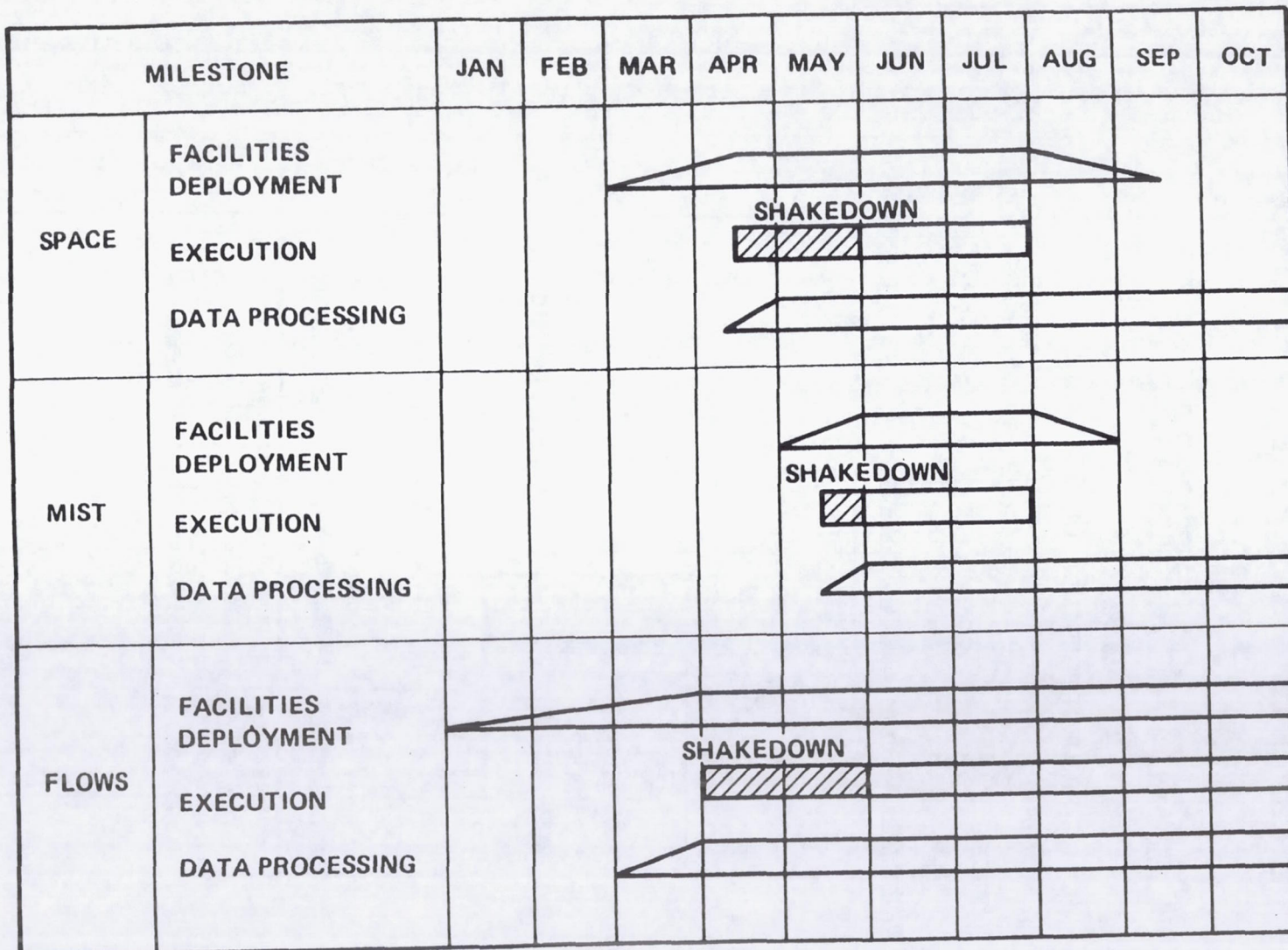


Fig. 1.2.2. COHMEX experiment scheduling and milestones.

# SATELLITE PRECIPITATION AND CLOUD EXPERIMENT

*SPACE*

PROJECT SCIENTIST: DR. J. ARNOLD

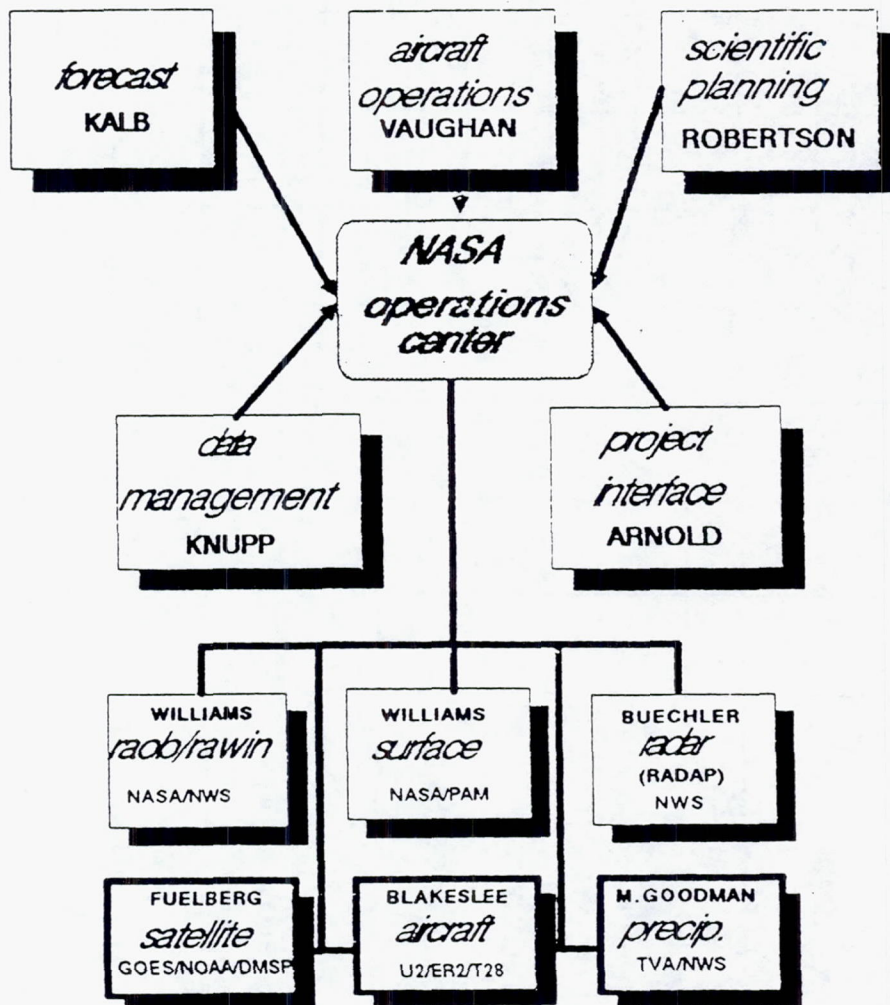


Fig. 1.3.1. Organizational and subtask management structure for SPACE.

## 2.0 REMOTE SENSING OBJECTIVES

The SPACE field program will provide a unique opportunity for testing and evaluating new atmospheric remote sensors flown on high altitude aircraft. Traditional measurements systems such as rawinsondes, radar and in situ aircraft measurements will provide ground truth for the remote sensors. At the same time the number of different remote sensors will allow comparisons among the sensors which here-to-fore have not been available.

The responsibilities for the remote sensors have generally been divided between MSFC and GSFC. Figure 2.0.1 gives an overview of the remote sensors and their acronyms. The following sections describe the type experiments to be conducted and a more detailed description of the sensor characteristics.

### 2.1 Fine Resolution Atmospheric Scanning and Sounding

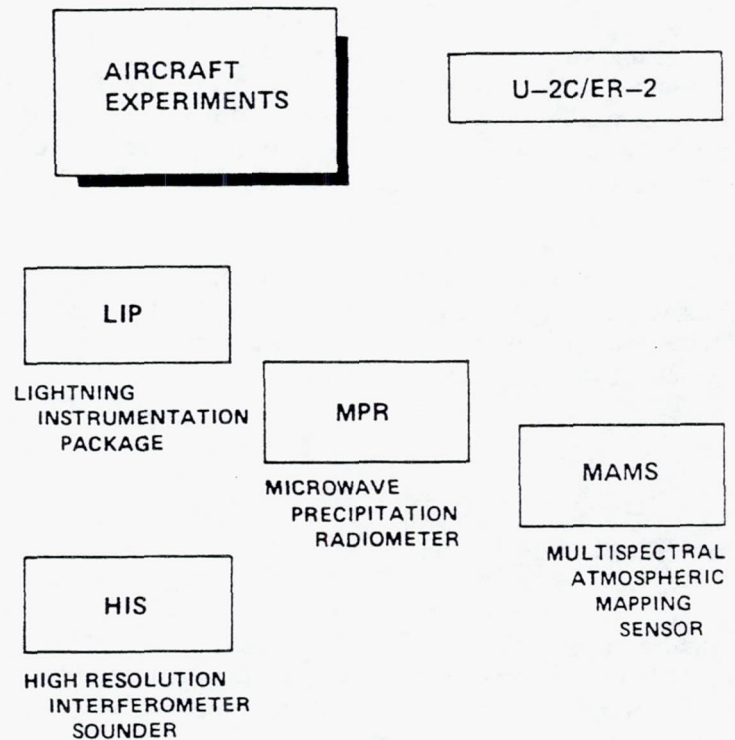
Remote sensing strategies in the past have been primarily limited to meso-alpha scale environmental features. While remote sensors (VAS) and supporting field experiments (Hill and Turner, 1983) have improved understanding of the sub-synoptic environment, evidence indicates that large variability exists in atmospheric variables at much finer scales. In particular moisture and precipitation may have most of their spectral energy at wavelengths below 200 km (Barnes and Lilly, 1975).

As an objective under the SPACE program, aircraft remote sensing will attempt to verify and quantify moisture structure at high vertical and horizontal resolutions. This will be accomplished using the Multispectral Atmospheric Mapping Sensor (MAMS) for high horizontal resolution (approximately 1 km) and the High resolution Interferometer Sounder (HIS). Such measurements have significant implications for defining the pre-storm boundary layer (see Section 2.1) and for possible differential infrared cooling which may be important to local convective events. The following describes in more detail the MAMS and HIS instruments and combined use under SPACE.

#### 2.1.1 *Multispectral Atmospheric Mapping Sensor (MAMS)*

MAMS is a new remote sensor designed to produce high resolution imagery in eight visible and three infrared spectral bands. Thermal emission from the earth's surface, clouds, and atmospheric water vapor is measured at 12.3, 11.2 and 6.5 microns. Figure 2.1.1 gives the spectral response curves for MAMS compared to VAS, while Table 2.1.1 gives a detailed description of the resolution and characteristics of MAMS. Under the SPACE program the MAMS will be flying on the U-2C/ER-2 aircraft at an altitude of 20 km. From this altitude the horizontal ground resolution of each individual field of view is 50 m. The width of the entire cross-path field of view scanned by the sensor will be roughly 40 km, providing detailed resolution over a relatively large area. Figure 2.1.2 gives a schematic of the scanning geometry.

## MARSHALL SPACE FLIGHT CENTER



## GODDARD SPACE FLIGHT CENTER

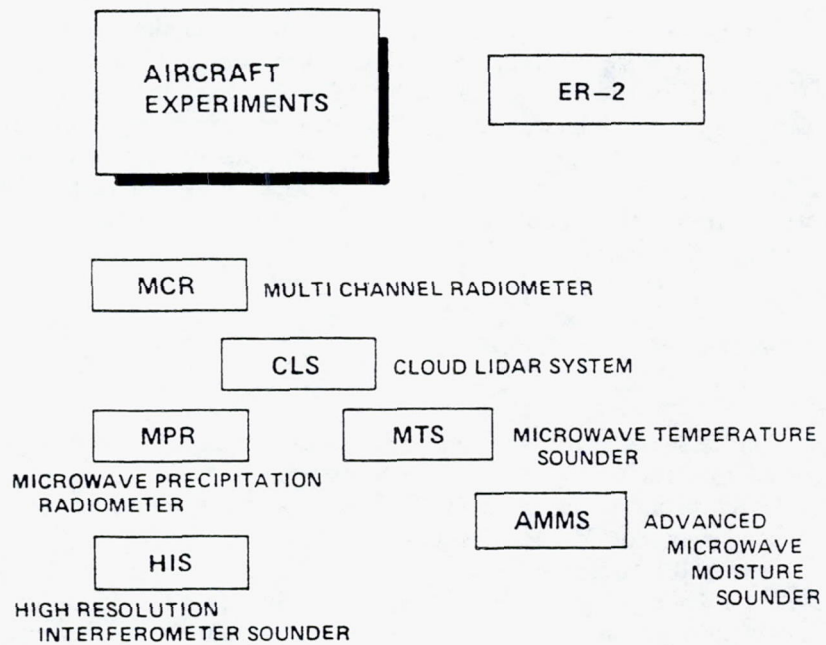


Fig. 2.0.1. Remote sensors (and acronyms) to be flown on high altitude aircraft in SPACE.

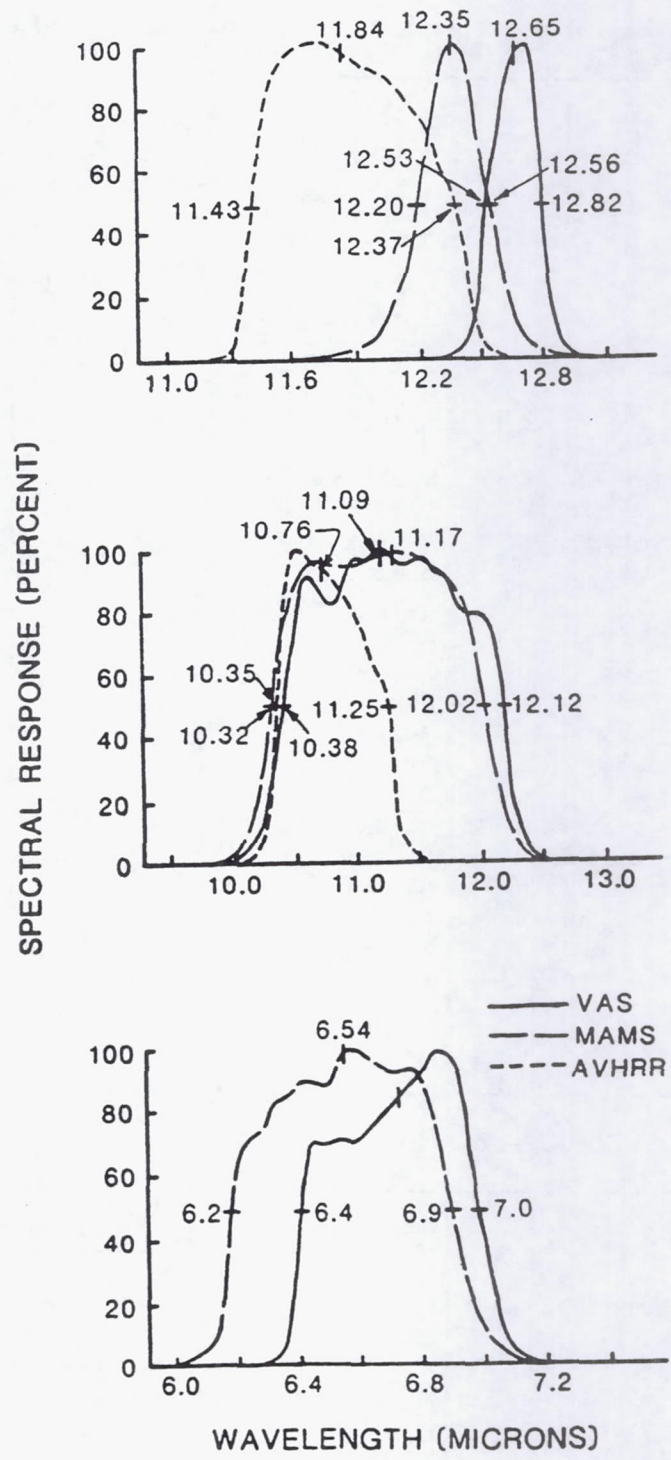


Fig. 2.1.1. Spectral response curves indicating the sensitivity of the MAMS, VAS, and AVHRR instruments in the 12 micron, 11 micron, and 6 micron regions.

Table 2.1.1 Details of MAMS scanning and spectral resolution

Scan rate	6.25 or 12.50 rps
Instantaneous field-of-view	2.5 or 5.0 mrad
Ground resolution (nadir, 19.8km)	50m or 100m
Total field-of-view	86°
Roll correction	+/-15°
Calibration sources	IR, 2 controllable bbs
Pixels per scan line	716

Spectral Bands

Channel	Wavelength (microns)	Spectral Region	Single Sample Noise (I) 2.5/5.0@6.25rps
1	.42 - .45	blue	.280
2	.45 - .52	blue/green	.052
3	.52 - .60	green	.018
4	.60 - .62	yellow/orange	.054
5	.63 - .69	red	.039
6	.69 - .75	red/near IR	.043
7	.76 - .90	near/IR	.036
8	.90 - 1.05	near IR	.110
9	6.20 - 6.90	water vapor	.40/.20
10	10.32 - 12.02	window (cold)	.15/.10
11	10.32 - 12.02	window (cold)	.15/.10
12	12.20 - 12.56	water vapor	.75/.40

(1) NE R (mw/ster/m<sup>2</sup>/cm<sup>-1</sup>) for 1-8, NE T (°C) for 9-12.

Table 2.1.2 HIS Data Products

<u>Product</u>	<u>Resolutions</u>
Surface Skin Temperature (°C)	1 km, 4 km, 40 km
Total Precipitable Water Vapor (cm)	1 km, 4 km, 40 km
Vertical Temperature Profile	4km, 40 km
Vertical Water Vapor Profile	4 km, 40 km
Total Ozone Concentration	4 km, 40 km
Tropopause Height	4 km, 40 km
Cloud Distribution (Vertical)	4 km, 40 km

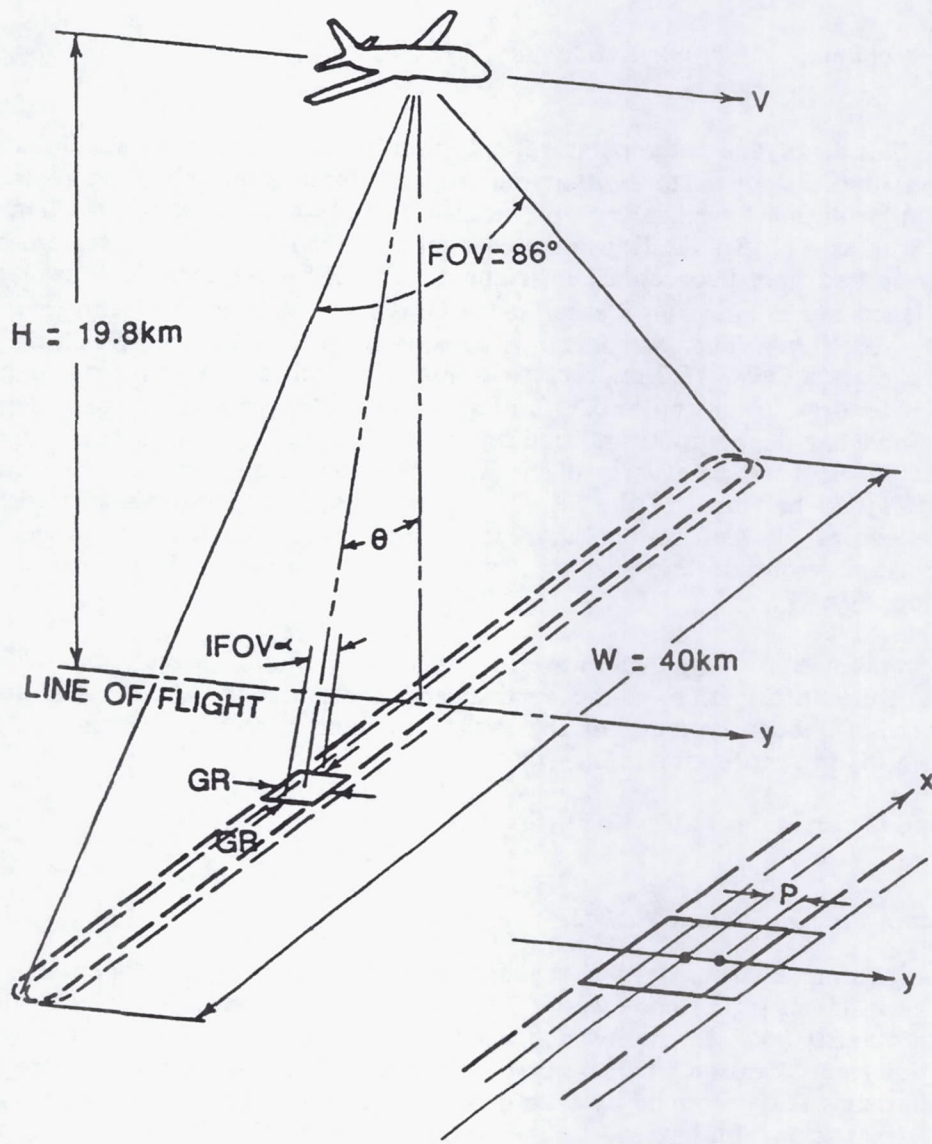


Fig. 2.1.2. Scanning geometry for the MAMS instrument onboard a NASA U-2C/ER-2 aircraft. Lower insert shows position of the center of the nadir ifov for two adjacent scans.

It is expected that the MAMS moisture fields will be used in numerical cloud models to ascertain the sensitivity of the convective response to small scale moisture variations. These small scale structures can be compared to VAS moisture as well as in situ aircraft measurements (see 5.1.3) and the SPACE rawinsonde network.

### 2.1.2 High Resolution Interferometer Sounder (HIS)

The HIS is an advanced temperature and humidity sounder which uses high spectral resolution measurements of earth emitted radiance to obtain soundings with significantly higher vertical resolution than has been previously possible with IR sounders. The instrument serves both as a NASA facility to support sounding and mesoscale research, and as a prototype for an advanced spacecraft instrument. The HIS instrument was developed by the Space Science and Engineering Center at the University of Wisconsin with joint support from NASA and NOAA. The instrument is capable of measuring the upwelling infrared spectrum of radiation (3.7 - 16.7 microns) with high spectral resolution (resolving powers in excess of 2000 and resolutions up to 0.35/cm) and radiometric precision (< 0.1 degrees Celsius noise equivalent temperature and calibration reproducibility). Such resolution allows measurement of the fine scale vertical structure of temperature, water vapor and other gases. The HIS will be flown in the SPACE field program on joint missions with MAMS. From an altitude of 20 km, water vapor and temperature data can be provided at approximately 2 km resolution and spacing. Table 2.1.2 summarizes HIS data products to be collected under SPACE.

The combination of MAMS and HIS joint flights should provide detailed temperature and moisture information in the vertical and horizontal for the SPACE area. This data will be useful quantitatively to the diagnostic budget studies (Section 3.2) and to characterizing the pre-storm environment.

## 2.2 Lightning Observations (LIP, LRP)

### 2.2.1 Lightning Instrumentation Package

The Lightning Instrumentation Package (LIP) is a recently developed sensor array designed to be installed in the nose section of the ER-2 and to make measurements in conjunction with other remote sensing instruments. The objectives include the measurement of lightning activity and location in storm systems and to relate these measurements to other storm characteristics as determined by both ground based sensors and other sensors onboard the ER-2. Of particular interest will be the intercomparisons of lightning activity and passive microwave radiances. This should provide us with an opportunity to evaluate the role of ice in the electrification process and in the microwave signature. Cloud top characteristics will also be closely studied as a function of lightning location and initial occurrence. Figure 2.2.1 gives a schematic of the sensing process.

The LIP sensors include:

- a. slow/fast electric field change meter
- b. dual wavelength, time resolved radiometers
- c. CCD TV camera
- d. linear optical lightning array

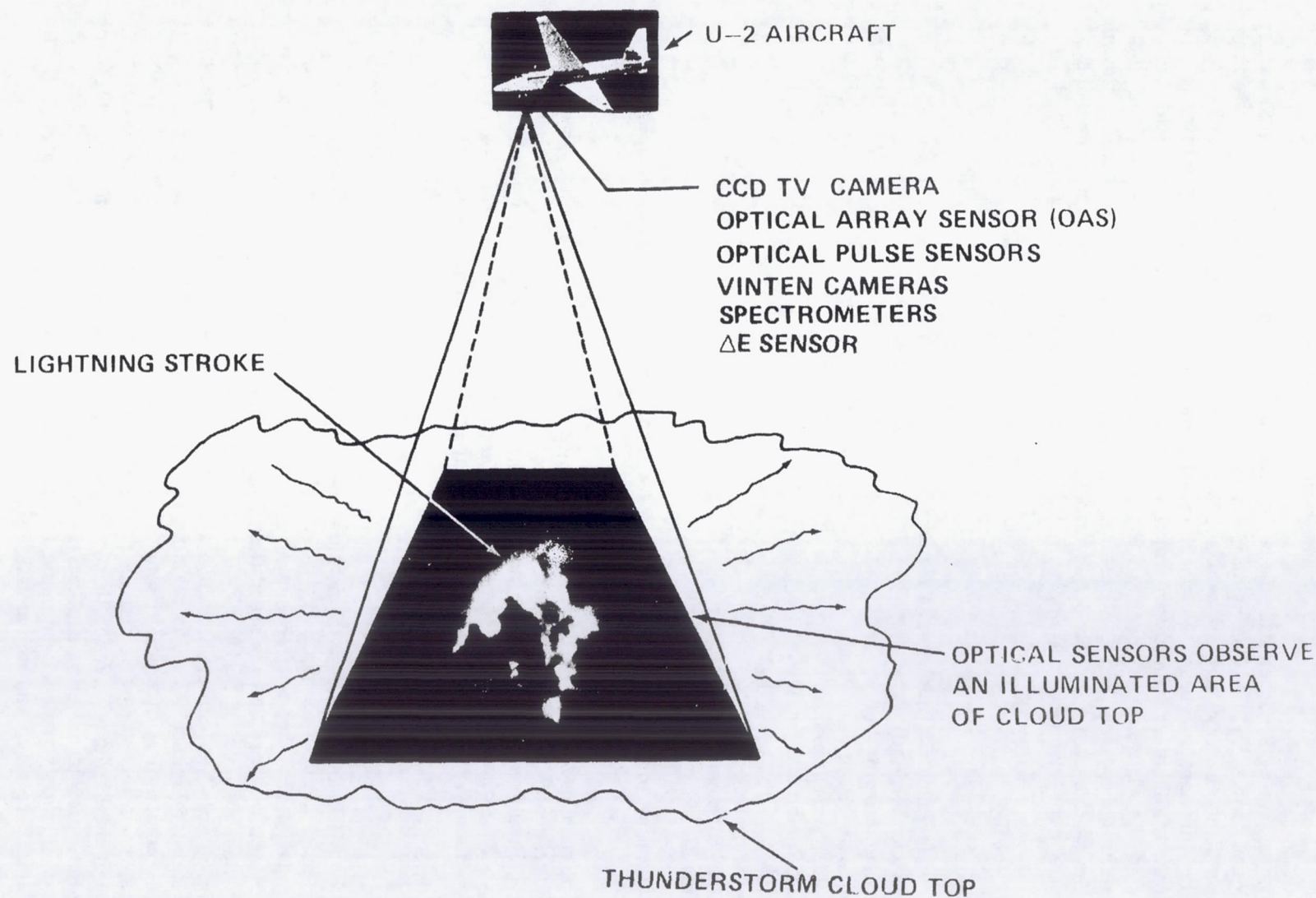


Fig. 2.2.1. A schematic of lightning observations from the U-2C.

### *2.2.2 Lightning Research Package*

The Lightning Research Package (LRP) is a multi-instrument, multi-mission package installed on a NASA U-2C. The primary objective of the LRP is to study the physics of lightning and the electrical environment above the tops of thunderstorms. It will be used extensively with ground based electrical measurements, electric field soundings, T-28 penetrations, and Doppler radar measurements. The conductivity and electric field sensors will provide the first measurements of electric currents flowing over the tops of thunderstorms since the early 1950's. These currents will be compared with currents flowing beneath the storms as a function of storm development. Additional experiments include the correlation of electrical activity with the storm kinematics, precipitation and flow fields.

The LRP sensors include:

- a. slow/fast electric field change meters
- b. electric field mills
- c. conductivity probes
- d. wide angle optical detector
- e. optical pulse sensor
- f. broad band spectrometer
- g. high resolution spectrometer
- h. optical array sensor
- i. CCD TV camera
- j. time lapse cameras

### **2.3 Investigating the Multifrequency Microwave Signature of Clouds and Precipitation (MPR)**

The passive 37 and 18 GHz dual polarization signatures of clouds and precipitation will be investigated for the first time from high altitude with the ER-2 flights of the Microwave Precipitation Radiometer (MPR). The MPR is a predecessor to the Advanced Microwave Precipitation Radiometer (AMPR) that will carry more channels and have a viewing geometry suitable for the unambiguous interpretation of radiometric data.

#### *2.3.1 Justification*

The MPR and AMPR will measure radiances at wavelengths sufficiently long to penetrate most clouds and sense the attenuation due to precipitation size hydrometeors. Modeling has shown that at frequencies much higher than 37 GHz, the attenuation by cloud becomes so severe that the precipitation attenuation is generally not observed because of the obscuring effects of the cloud. If the cloud is high enough (such as a thunderstorm anvil) the liquid water content is reduced but the emission due to nonprecipitating ice is still sufficient to reduce 92 GHz brightness temperatures by 30 degrees, while 37 GHz brightness temperatures are reduced only 1 degree, and 18 GHz is essentially unaffected. Therefore, the lower microwave frequencies that the MPR and AMPR will address give our best hope of measuring attenuation that is due to precipitation size hydrometeors. Over the ocean, polarization information is necessary to evaluate the relative importance of the scattering and emission signals. Eventually, two low frequencies will be used to determine the separability of the cloud and rain emission signals over the ocean.

### *2.3.2 MPR Data Analysis*

The primary issues that will be addressed with the MPR are (1) the cloud penetration ability of these frequencies to enable the isolation of the precipitation signal, (2) an analysis of the origin, strength, and horizontal extent of the ice scattering mechanism which has been found in the very coarse resolution Scanning Multichannel Microwave Radiometer (SMMR) measurements (Spencer et al., 1983a; Spencer et al., 1983b; Spencer, 1984), (3) measurement of the relative strengths of scattering and emission effects of oceanic rain systems (Wilheit et al., 1977) which is only achievable with polarization information (Spencer, 1986), and (4) investigate the origin of the polarization anomalies that have been found at 37 GHz in SMMR observations of convective storms (Spencer and Santek, 1985) and have been theoretically modeled (Wu and Weinman, 1984).

Because the MPR will also be flying with the Advanced Microwave Moisture Sounder (AMMS-Wilheit et al., 1982) we will have the unprecedented opportunity of comparing the signatures of clouds at the frequencies of 18, 37, 92, and 183 GHz to help verify theoretically derived cloud absorption coefficients.

### *2.3.3 Impact*

This work will impact the eventual design and use of radiometers envisioned for the measurement of global precipitation from space as part of either a dedicated rain measurement mission or as part of the Earth Observing System (EOS). Within the NASA Geostationary Platform activity, very large antennae are planned which could facilitate high resolution observations at even low microwave frequencies.

## **2.4 Precipitation, Sounding and Cloud Structure (AMMS, MCR, CLS, MTS, HIS, MPR)**

The following three sections outline the type of experiments and use of the MCR, CLS, MPR, MTS, AMMS and HIS sensors to be flown on the ER-2 during SPACE.

### *2.4.1 Precipitation*

There will be a focus on a precipitation effort involving high frequencies (90 and 180 GHz) that have yet to fly on any satellite platform and have great potential in terms of detecting precipitation and giving an indication of its intensity. These high frequencies are the focus of our research for the following reasons: 1) Convective precipitation cores are clearly delineated at 92 and 183 GHz. 2) Convective rain rate has been linked to brightness temperatures at these frequencies through both the aircraft observations and modeling results. 3) There is even a preliminary indication that stratiform precipitation can be detected in this manner. 4) High-frequency microwave observations are less sensitive to surface effects than the lower frequencies (e.g., 37 GHz). 5) For the same antenna size, better resolution is possible at the higher frequency. 6) The 183 GHz channel is the only serious current possibility for geosynchronous satellites (3 m antenna-20 km resolution).

The current and future approach in this work has been to combine the aircraft observations, radiative transfer modeling, and cloud numerical modeling to determine the relationships between rain, cloud and rain water, cloud ice, and the upwelling radiance under a variety of ambient and cloud conditions. Key field experiments in the past to provide aircraft data bases have been the Florida 1979 flights, the CCOPE Montana 1981 flights, and the spring 1984 Midwest flights. The upcoming 1986 SPACE flight will provide an additional data base with extensive ground truth from radar and rain gauge installations. With these results, comparison to quantitative rain conditions under a variety of circumstances will be available.

Flying the Advanced Microwave Moisture Sounder (AMMS) [which will provide the 90 and 180 GHz observations] and the Microwave Precipitation Radiometer (MPR) [37 and 18 GHz] in conjunction with other instrumentation, such as the Multi-channel Cloud Radiometer (MCR) and the Cloud Lidar System (CLS), will allow us to understand cloud conditions in relationship to the microwave observations and precipitation.

#### *2.4.2 Temperature and Moisture Sounding*

Microwave temperature and moisture sounding is the next major step in sounding from geosynchronous orbit. Candidate frequencies for temperature sounding are at 118 and 183 GHz for moisture. Extensive work has already been done in the moisture sounding area at 183 GHz. A 118 GHz sounding instrument, the Microwave Temperature Sounder (MTS), is to be intergrated into the package on the ER-2. The MTS is an MIT instrument with Dr. D. Staelin as principal investigator. Aircraft observations with both the MTS and AMMS will permit a combined approach toward temperature and moisture retrieval techniques. Upcoming flights are planned in early 1986 as part of the GALE Program. What is critical in this effort is to have the MTS integrated onto the ER-2 so that observations can be made with a combination of the MTS, the AMMS, and other instruments so that sounding of the total depth of the troposphere and the very lowest part of the stratosphere can be made from the high-altitude aircraft. With the package integrated onto the ER-2, this will allow temperature and moisture sounding retrievals to be done as a part of the SPACE Program and in future efforts, including STORM-Central.

An advanced infrared temperature sounder has also been developed and has previously flown on a U-2 aircraft. The High-resolution Interferometer Spectrometer (HIS) is a University of Wisconsin-developed instrument (See section 2.1). Current modification of the ER-2 will allow the HIS to be added to the ER-2 payload. In combination with the MTS, this gives the combination of both infrared sounding and microwave sounding. The addition of the MCR gives visible near-infrared and infrared imaging. This group of instruments, incorporating both infrared and microwave sounding techniques and visible and infrared imaging, provides a simulation of future geosynchronous missions.

The existence of a lidar system on a package which includes passive sounders gives rise to fundamentally new and unique approaches toward atmospheric sounding development. First, any questions regarding cloud contamination by cirrus or very thin cirrus can be determined by a comparison of the radiances and retrieved temperatures in comparison to the precise lidar observations. Second, the combination of the lidar with either the MTS and/or the HIS provides a simulation of a low-orbiter sounding package incorporating a lidar in which the lidar would be used to define tropopause height, boundary layer height, and potentially other inversion levels. Currently, the largest errors in passive temperature retrievals are for the locations and magnitude of temperature inversions.

Several studies, both published and ongoing, have indicated that a direct input of inversion levels can improve temperature sounding retrievals. In the case of water vapor sounding, an initial improved estimate of the water vapor vertical distribution should be possible. The combination of sounding instruments onboard the ER-2 in SPACE will provide a data base for multi-sensor research which will be supported by extensive ground-based and in-situ observations.

#### *2.4.3 Storm Structure*

The structure and evolution of severe thunderstorms have been studied using satellite observations. The cloud top-observed features provide information on storm growth, intensity, and, indirectly, the evolution of the storm internal structure. Therefore, studies have been undertaken toward better understanding of the interpretation of satellite observations and applying this knowledge to the detection of severe storms. An approach taken by investigators at Goddard has been to combine the unique observation capability of the high-altitude aircraft instrument package with combined satellite, radar, and, when available, insitu observations. Recent advances have included a lidar-derived analysis of the emissivity structure of storm tops. Previous flight experiments have provided an extensive series of observations. However, due to difficulty in obtaining a representative variety of storm conditions with good aircraft, radar, and in situ data, additional data sets are required. The available observations cases will be increased through participation in SPACE.

#### *2.4.4 Moisture Sounding*

Present methods for measuring atmospheric moisture include: radiosondes, in situ aircraft, passive satellite observations, and meteorological towers. All of these have limitations either in their vertical extent and resolution or temporal resolution. An alternative to these traditional methods is the Raman lidar system. The Raman lidar is able to measure atmospheric moisture with high temporal and altitude resolution much like a meteorological tower, but up to altitudes of 4-5km. The present system is limited to nighttime operation (Melfi and Whiteman, 1985).

Under the SPACE program the Raman lidar system will be used primarily to examine post-storm moisture structure. Such measurements are important in determining how the storm environment redistributes the environmental moisture. During SPACE, the expected combination of the continuous Raman lidar moisture measurements with a co-located continuous wind profiler from Penn. State University will also allow examination of moisture fluxes. In addition, it is expected that rawinsonde releases from a SPACE rawinsonde site will allow intercomparison of the two moisture techniques. The high temporal moisture resolution from the Raman lidar which can be related through wind measurements to high spatial resolution measurements will also complement the high resolution spatial moisture measurements from the MAMS sensor on the high-altitude aircraft.

### **3.0 SCIENTIFIC OBJECTIVES**

In addition to the remote sensing objectives above, the SPACE program is also designed to address several basic science questions relating to the initiation, structure, physical properties and organization of convection. Although the science objectives are separated here from the remote sensing objectives, this separation is largely for convenience of discussion. In reality many of the science objectives listed below are actually intended to increase physical understanding of atmospheric processes to better interpret remotely sensed data or define appropriate remote sensing strategies. At the same time, remote sensing objectives in the long term are devoted to providing data which can hopefully help unravel the multi-scale complexities of the convection.

Science objectives under SPACE include:

- o Defining the role of moisture variability in the pre-storm environment in producing preferred areas of convection.
- o Defining the role of boundary layer forcing in the pre-storm environment in initiating convection.
- o Quantifying scale interaction especially upscale transfer through diabatic feedback in convective complexes.
- o Developing improved convective cloud and precipitation relations in order to define Visible/IR rain estimation techniques.
- o Increasing understanding of cloud electrification through aircraft in situ measurements, radar analyses and remote sensing of convective elements.
- o Better defining the environment and mechanisms leading to the merging of convective elements into larger convective systems.
- o Describing internal cloud dynamic and microphysical structure to improve remote sensing retrieval algorithms and interpretation of remotely sensed data.
- o Evaluating and improving numerical models in order to clarify the role of physical processes and to use the models as surrogate atmospheres to test remote sensing retrieval algorithms.

The following sections give a more thorough discussion of these objectives.

### 3.1 Pre-Storm Environment

One of the major objectives of the SPACE field program is to observe the pre-storm environment in order to define atmospheric variables or structure which precede, initiate or organize convection. By defining the variables and the scales of variables important to convection, remote sensing strategies can be developed or refined to provide better operational and research data. The SPACE study area should provide a rich testing ground to evaluate the pre-storm environment.

The study of the pre-storm environment will concentrate on two areas:

- o small scale (1-50 km) variability in moisture which could lead to preferred areas for the initiation or enhanced development of convection.
- o mesoscale convergence in the pre-storm environment which can lead to initiation or organization of convection.

#### 3.1.1 Moisture Variability

Sounding products and moisture imagery have been available from VAS over the last five years. Evaluations of VAS retrievals (Jedlovec, 1985; and others) have indicated that a quantitative description of the atmosphere's thermal and moisture structure seems limited to the larger mesoscales of motion (i.e., features with wavelengths greater than 100-200 km). Smith *et al.* (1984) have indicated some hope of finer resolution of the moisture fields with VAS water vapor imagery. One of the remote sensing objectives using the MAMS instrument (see section 2.1) will be to further verify and define this variability. While the mechanisms producing or maintaining these moisture gradients are not clear at the present, such variations may be related to preferred areas of convection. The combined observational study of the moisture fields with the evolving convection should clarify such relationships if they exist. Also, sensitivity studies using cloud scale models should clarify the impact of moisture variations on convective response.

As mentioned above, mechanisms responsible for producing small scale variations in pre-storm moisture are unclear. The combined use of synoptic scale observations and satellite data with the meso-beta and meso-alpha observations in the SPACE network should provide clues as to whether the variations are locally generated or reflect fine scale advective features. Regional scale models (LAMPS - Perkey and Krietzberg (1976) and MASS - Kaplan (1982)) could also provide indications of whether the small scale moisture features represent differential moisture advection from large scale sources such as the Gulf of Mexico.

#### 3.1.2 Mesoscale Convergence

Modeling and observation studies (Pielke (1974), Ulanski and Garstang (1978)) have indicated that mesoscale convergence is correlated with or precedes convective activity. Chen and Orville (1980) in a cloud model study showed that convergence imposed on dry thermals, shifted the maximum energy to longer wavelengths and enhanced the intensity of the moist convection. There are a plethora of possible mechanisms for producing mesoscale convergence and one of the objectives of this program is to evaluate the relative impor-

tance of the mechanisms in order to prioritize remote sensing capabilities.

Boundary layer thermal inhomogeneities can give rise to sustained convergence. Figure 3.1.1 gives a schematic of possible thermal forcing mechanisms in the SPACE field area. These thermal forcing mechanisms could produce the convergence initiating and organizing convection. It is expected that numerical models, using SPACE input data, will play a major role in examining the thermal forcing mechanisms. Also, VAS and MAMS data can provide skin temperatures in clear areas which may be used in numerical model investigations. Surface stations (e.g. PAM and other mesonets) will provide data to evaluate this remotely sensed data. The surface pyranometer network should also provide pre-storm variations in insolation due to cloud shading or haze.

While the radar systems will emphasize operations under periods of active convection it is expected that clear air scans in the pre-storm environment may yield useful information on the scale and change of scale of dry thermals. Doviak and Zrnic (1984) describe the use of Doppler in providing information on pre-storm convergence patterns out to a range of approximately 100 km. It is expected that sufficient backscatter will be available in SPACE to provide similar data.

Mechanical forcing can also lead to convergence. Uccellini (1975) in an observational and simple model study indicated that subsynoptic scale gravity waves can provide the convergence necessary to initiate convection. Figure 3.1.2 from that study gives pressure perturbations in conjunction with radar summaries indicating a relation between gravity wave convergence and convection. Other mechanisms such as forced lifting over terrain and flow deacceleration over a change in surface roughness can also produce surface convergence. Figure 3.1.3 gives a schematic of mechanical forcing which might be active in the initiation of convection in the pre-storm environment. The role of short-wave baroclinic systems can also not be discounted in producing convergence and destabilization in the pre-storm environment. In fact, it is likely that the strongest early summer convection may be due to baroclinic systems skirting the SPACE area. It is expected that the combined use of the SPACE observational data with numerical models can begin to unravel the relative magnitudes of the forcing mechanisms operating during the SPACE operational days.

### **3.2 Relationships Between Bulk Convection and Its Environment**

The SPACE experiment is designed to sample scales of motion ranging from cloud-scale circulations to the background convective environment. Of prime interest in this experiment is to quantify the scale-interactions and to understand what small-scale processes future remote sensing systems will be required to measure. Two important areas of study will be the effects of the ensemble convection on the environment and how the environment responds dynamically to this forcing.

#### *3.2.1 Diabatic Processes and Vertical Transports in MCS's*

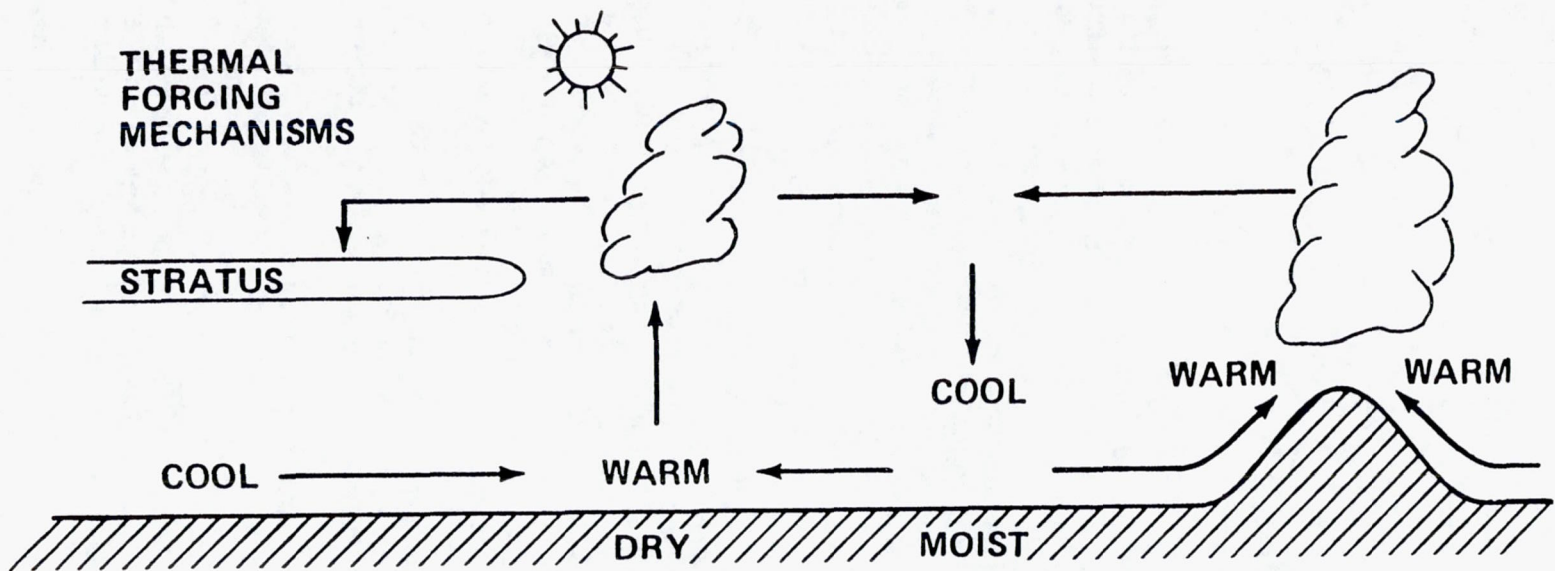
It is well known that MCSs may contain both deep convection and stratiform rain during various phases of their life cycles (Cheng and Houze, 1979). Circulations ranging from strong buoyant plumes to widespread gradual ascent and descent suggest different modes of processing moisture. Corresponding differences in vertical profiles of condensation and evaporation as well as heat, mass and momentum transport can, in general, be expected. Since MCS's frequently appear to be strongly driven by thermodynamic forcing,

an analysis of the heat and moisture balance in several COHMEC cases is planned with the following objectives in mind:

- 1) determine the vertical profiles of heating and drying produced by convective systems in the SPACE rawinsonde network and relate these effects to the observed precipitation distribution, cloud structure (convective vs. stratiform) and system life cycle.
- 2) determine the characteristic moisture balance (including transports of condensate) on scales ranging from meso-gamma to meso-alpha.
- 3) use these results and subsequent kinematic and thermodynamic retrievals from Doppler radar analyses to evaluate and improve parameterizations of moist processes for use in mesoscale and large scale numerical models.

The primary observations required are the rawinsonde measurements made in the meso-gamma and meso-beta networks, rainfall observations from the gauge and radar networks and surface and PBL measurements. It is anticipated that a compositing approach will be effective since it will minimize the impact of missing data, insure use of instances in which convection incompletely fills the rawinsonde network and allows stratification according to life cycle. While these conventional measurements form the core of the required data, remote sensing platforms will also play an important role. VAS soundings serving as an additional source of thermodynamic data and cloud track winds are expected to be incorporated into the analyses in many instances.

While analysis of the rawinsonde data can provide bulk thermodynamic (and dynamic) effects of the convection, some cloud model(s) must be used to interpret the physical processes responsible for these bulk effects (Yanai et al. 1973). In the past, 1-D models of convection have been used with a number of critical assumptions to diagnose the importance of processes such as convectively-induced environmental subsidence, detrainment of heat and moisture and cloud evaporation (Figure 3.2.1.). In COHMEC, kinematic and thermodynamic Doppler radar retrievals and satellite-derived cloud population statistics will be used to examine the validity of cloud model assumptions concerning vertical mass flux profiles, thermodynamic properties and bulk microphysical processes. Subsequent changes to parameterization methods can be evaluated by analyzing the extent to which parameterized heating and drying explains the bulk effects diagnosed from the budget calculations.



24

Fig. 3.1.1. A schematic of thermal forcing mechanisms for initiating convection which may be operating in the SPACE area.

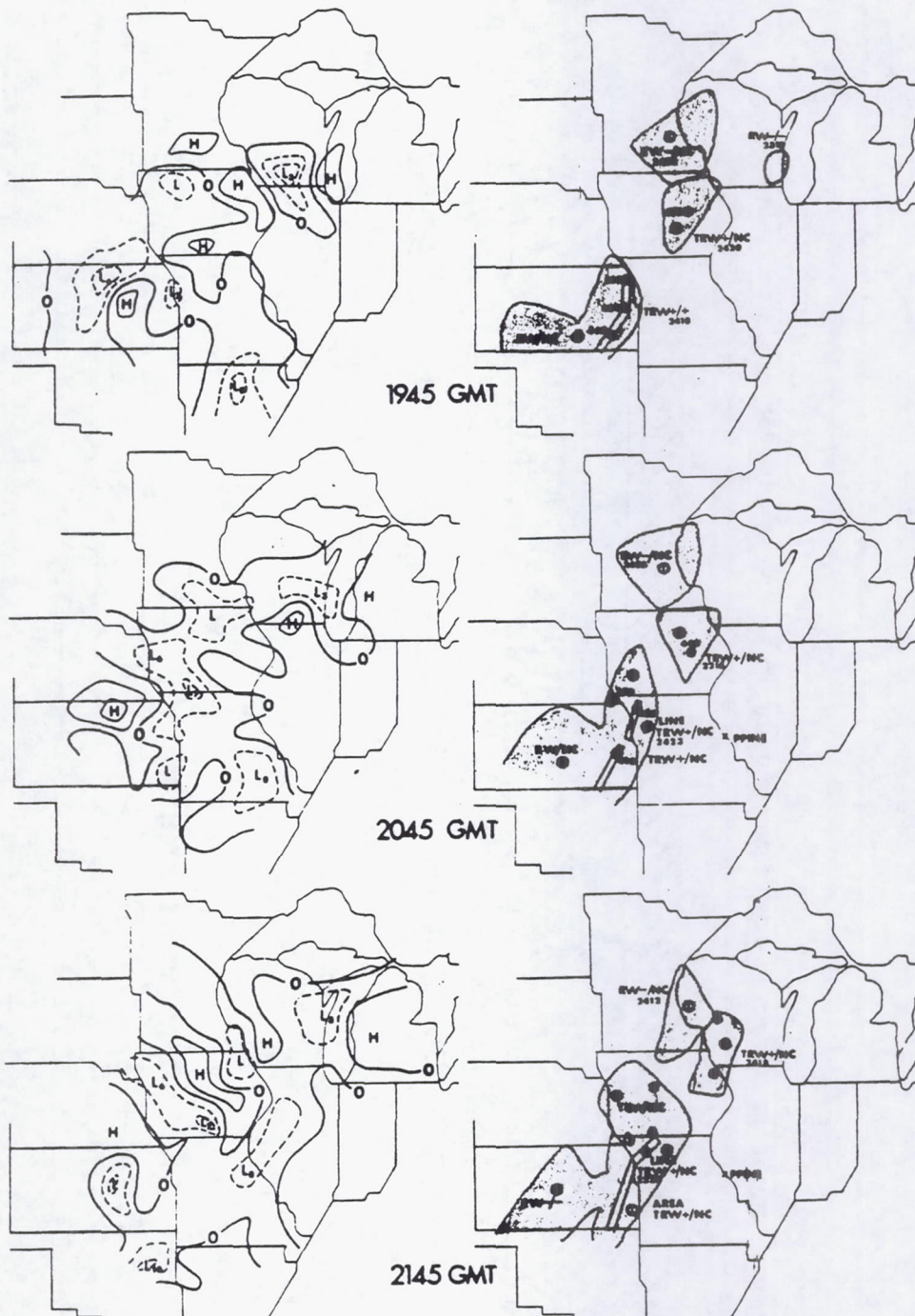


**Fig. 3.1.2. Pressure perturbations attributed to gravity wave propagation with corresponding radar summaries. From Uccellini (1975).**

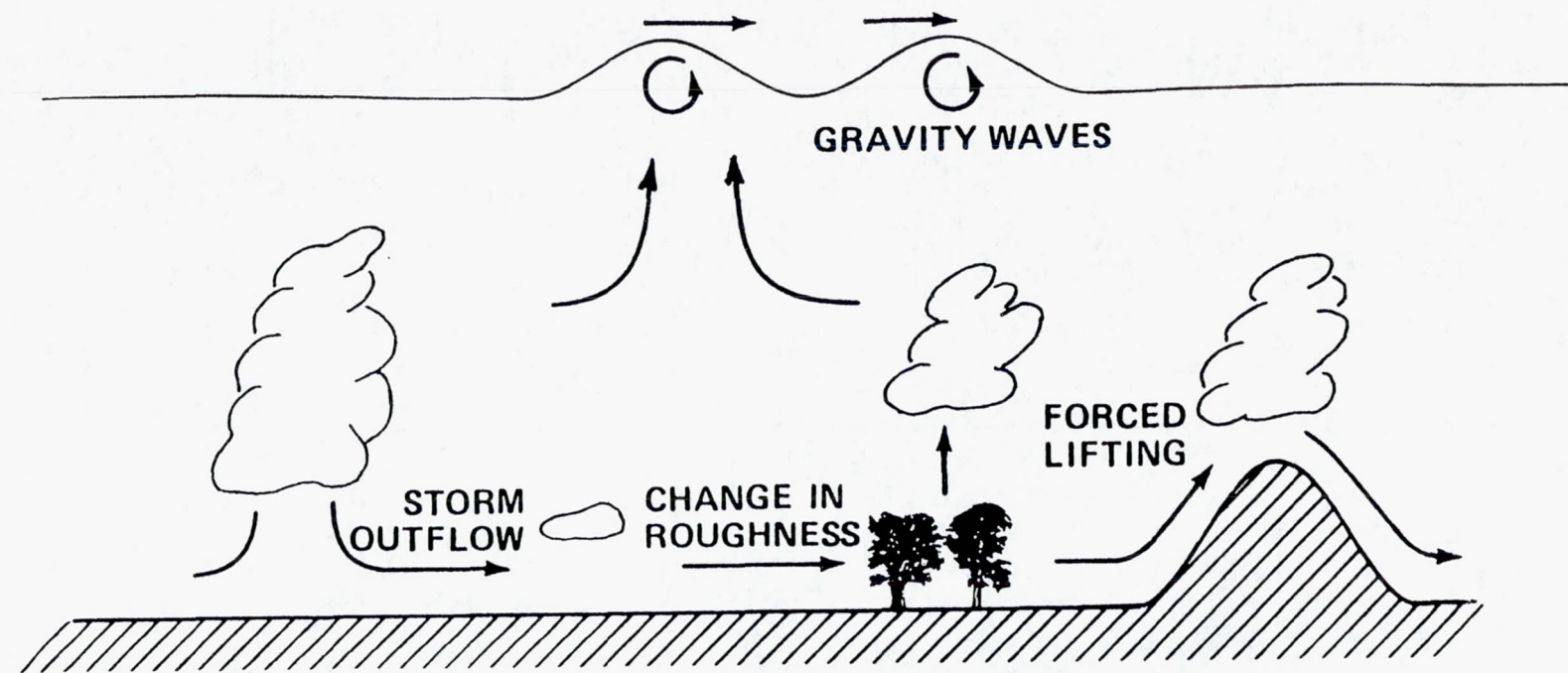


Fig. 3.1.3. A schematic of mechanical forcing mechanisms which may be operating in the SPACE area.

### *3.2.2 Dynamics of MCS Environments*

Scale analysis of mesoscale disturbances indicates that their Rossby number is typically of order 1, i.e. the flow is substantially ageostrophic (Atkinson, 1981). This presents a fundamental difficulty in observing dynamical processes in MCS environments since departures in wind and temperature from geostrophy are crucial to understand but difficult to measure with conventional rawinsonde observations. Consequently, higher order properties such as kinematic parameters and energy transfers are poorly understood since they are derivatives or covariances involving these departures from a balanced state.

During COHMEX a combined numerical and observational approach will be used to obtain a more quantitative description of the evolving MCS environment, its departure from a balanced state and its interaction with the ensemble convection. Several mesoscale models (e.g. LAMPS, MASS and SSM) will be available for producing simulations of the flow with domains approximately 1000 km on a side and grid resolutions of 20 to 50 km. These simulations will provide internally consistent data sets necessary to study departures from geostrophy with high space and time resolution. Numerous researchers (e.g. Robertson and Smith, 1983; Kalb, 1985) have used mesoscale models to investigate the interaction of organized convection and its environment.

The meso-beta rawinsonde network with approximately 75-100 km station spacing will permit complementary analyses of the environmental influence on, and response to, developing convective systems. Precipitation measurements from raingauges and digital radar and surface/PBL observations will be used to evaluate the thermodynamic forcing of the MCS cloud field on the environmental mass and motion fields as measured by the rawinsonde network. While the observational set data may have shortcomings related to area coverage and representative sampling, it complements numerical simulations which, although having internal consistency, may have incomplete physics. Comparisons of diagnostics with observational data to model simulations will facilitate critiqing the realism of the model runs from which detailed data sets will be generated for diagnostic study.

Through this combined numerical/observational approach the dynamics of the environment in which the convection is embedded can be addressed:

- 1) Do the divergence field and the mass perturbations associated with the bulk convection need to be incorporated into the balance equation to diagnose a more realistic environmental streamfunction fields (Paegle *et al*, 1983)?
- 2) What role does convection play in producing exchanges between divergent and rotational momentum field?
- 3) Can satellite measurements (mass field, water vapor distributions, tracer winds) provide additional information about non-geostrophic processes not resolvable by conventional observations?

### 3.3 Precipitation Processes and Electrical Activity

One of the unique aspects of the COHDEX experiment is the combination of radar measurements with satellite and airborne remote sensing instruments. The radar measurements coupled with the high density rain gauge network should be able to provide valuable information on rainfall rates which can then be used to evaluate remote sensing rainfall estimation techniques. The dynamic information supplied by the Doppler coverage also allows insight into internal convective structures which can be used to relate aircraft or satellite imagery to precipitation. In addition, cloud penetration by aircraft in conjunction with radar analyses can be used to relate cloud microphysical properties to precipitation processes and cloud electrification. The following two sections stress the importance of these measurements to the understanding and interpretation of remotely sensed data.

#### 3.3.1 Convective Cloud and Precipitation Relations and the Development of Visible/IR Rain Estimation Techniques

The objective of this study is to determine the relations of satellite-observed convective cloud observations to rainfall (observed by radar and rain gauge) in various synoptic situations in order to assess the potential and limitations of estimating convective rain from geosynchronous visible and IR observations.

The approach is to use high-quality radar data sets in conjunction with short-interval GOES data (if available) to first study the cloud/rain evolution and relations [e.g., as in Negri and Adler (1981)]. Second, apply precipitation-from-cloud-observation algorithms already developed or being developed (Negri *et al.*, 1984; Negri and Adler, 1984) and use the high-quality radar precipitation and rain gauge data to assess the accuracy of the techniques on various time and space scales and under varying synoptic conditions. The clarification of cloud-rain relations under differing synoptic conditions (stability, moisture, and shear) will be examined using an approach similar to that proposed by Adler and Mack (1984).

Because of the importance of precipitation information and the fine time resolution needed to accurately estimate rainfall (especially in convective situations), a number of investigators have attempted to obtain precipitation information from geosynchronous satellite data [which, unlike low-earth orbit (LEO) satellites, have reasonable time resolution (30 min)], even though the radiances from the visible and IR channels "see" only clouds and not precipitation. Because even the next generation operational satellite (GOES-Next) will be limited to visible and IR portions of the spectrum, it is incumbent to understand the potential and limitations of estimating precipitation from such data in various climatological and synoptic conditions. The COHDEX Project will provide a key data set in this regard to combine with the FACE (south Florida, summer) and SESAME (Midwest, spring) already being examined.

#### 3.3.2 Precipitation Processes and Electrical Activity

##### a. Lightning and the Thunderstorm Life-cycle

Precipitation processes appear to play an important role in the electrification of

thunderstorms (e.g., Latham, 1981; Illingworth, 1985). Not coincidentally, many storms are observed to produce lightning discharge rates in proportion to the rainfall rates observed at the ground (Piepgrass *et al.*, 1982). However, there are a number of instances when surface rainfall displays little correlation to the lightning discharge rates including weak convective situations when little or no lightning occurs at all.

It is the objective of this experiment to study the relationship between precipitation processes and measurable characteristics of lightning activity such as the nature of the initial discharge, the type and fraction of discharges (intracloud or ground), the number of component strokes of ground discharges, flash duration, polarity, frequency, spatial distribution, and peak currents. The lightning characteristics will be compared with storm echo tops, volumetric reflectivity structures, liquid water content, storm volume and mass, and surface rainfall patterns.

Multiple parameter radar measurements from the NCAR radars will be used additionally to derive kinematic, thermodynamic, and microphysical properties of the observed thunderstorms. Detailed microphysical structure will be examined with the aid of 1-D and 2-D cloud models. The time rate of change of the lightning and lightning activity is related to other storm attributes as a function of storm life-cycle. Figure 3.3.1 shows a comparison between the flashing rates of three storms and their precipitation attributes determined from the NEXt generation weather RADar (NEXRAD) algorithms. Figure 3.3.2 shows the evolution of precipitation and lightning fields during a mesoscale convective complex episode.

#### *b. Storm Attributes and the Environment*

Lightning activity, rainfall rates, storm intensity and duration will be studied in conjunction with the evolution of the important factors in the environment which influence the evolution of thunderstorm characteristics. These factors include the available buoyant energy feeding the storm, wind shear, boundary layer forcing, and low level moisture convergence.

These studies require observations from many of the remote sensing systems that are expected to collect data during the SPACE field program. Of primary importance are lightning data sets collected by the four-station lightning detection and location network, mobile storm electricity laboratory, and U-2C/ER-2 lightning instrumentation packages; microphysics data from penetrating aircraft; surface rainfall measured by the TVA rain-gauge network and Portable Automated Mesonet (PAM) stations; rawinsonde measurements in the meso-beta and meso-gamma networks; and radar data collected by the RADAP II/ICRAD system, NCAR and FAA Doppler radars. Volumetric radar data collected throughout the thunderstorm life-cycle is of vital importance to these studies.

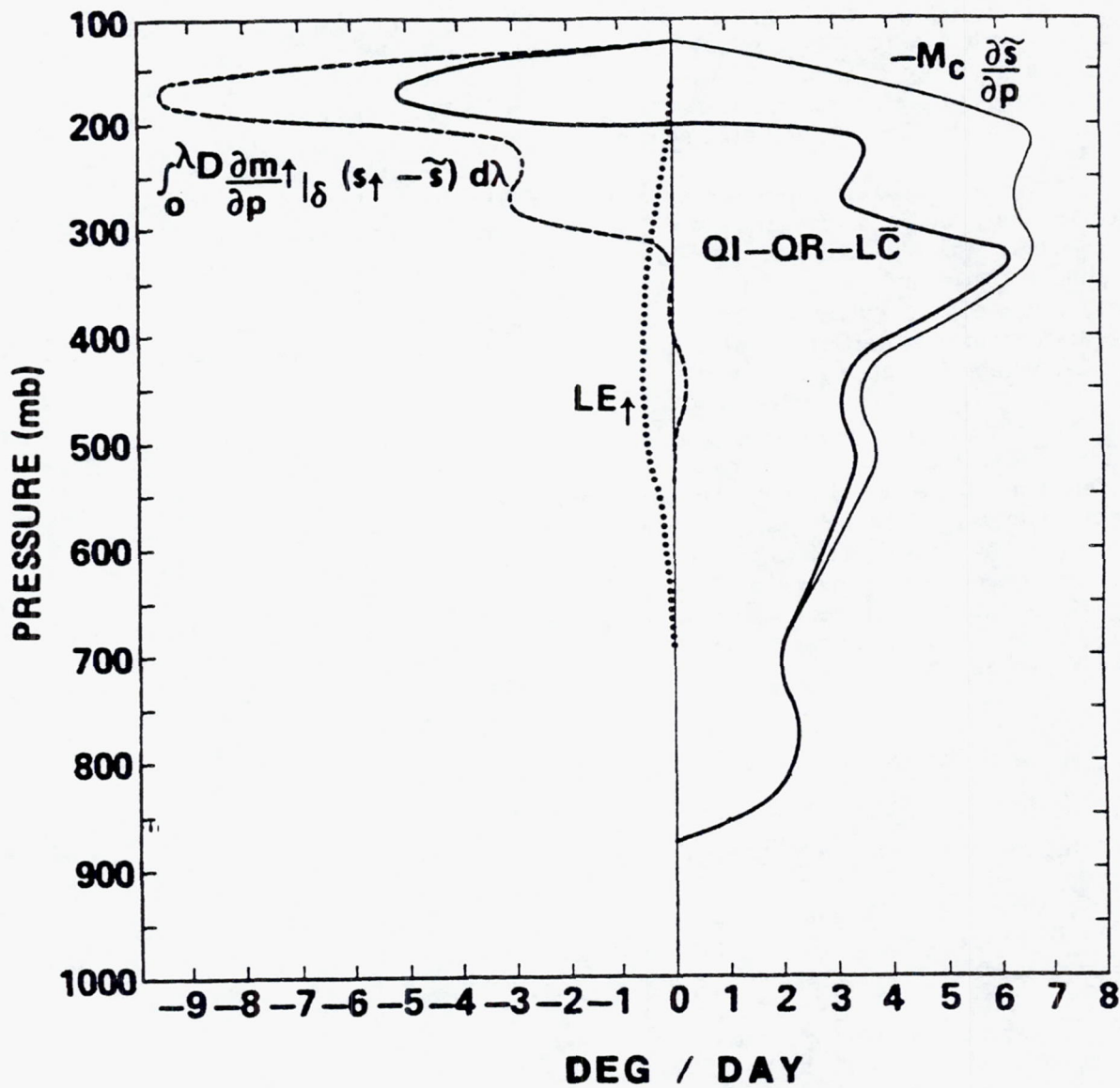


Fig. 3.2.1. Components of convective diabatic heating in deg/day diagnosed for the SESAME network at 21 GMT 10 April 1979. Heavy solid line is total heating rate, thin solid line, compensating mass flux; dashed line, detrainment of excess dry static energy; dotted line, evaporation of detrained condensate.

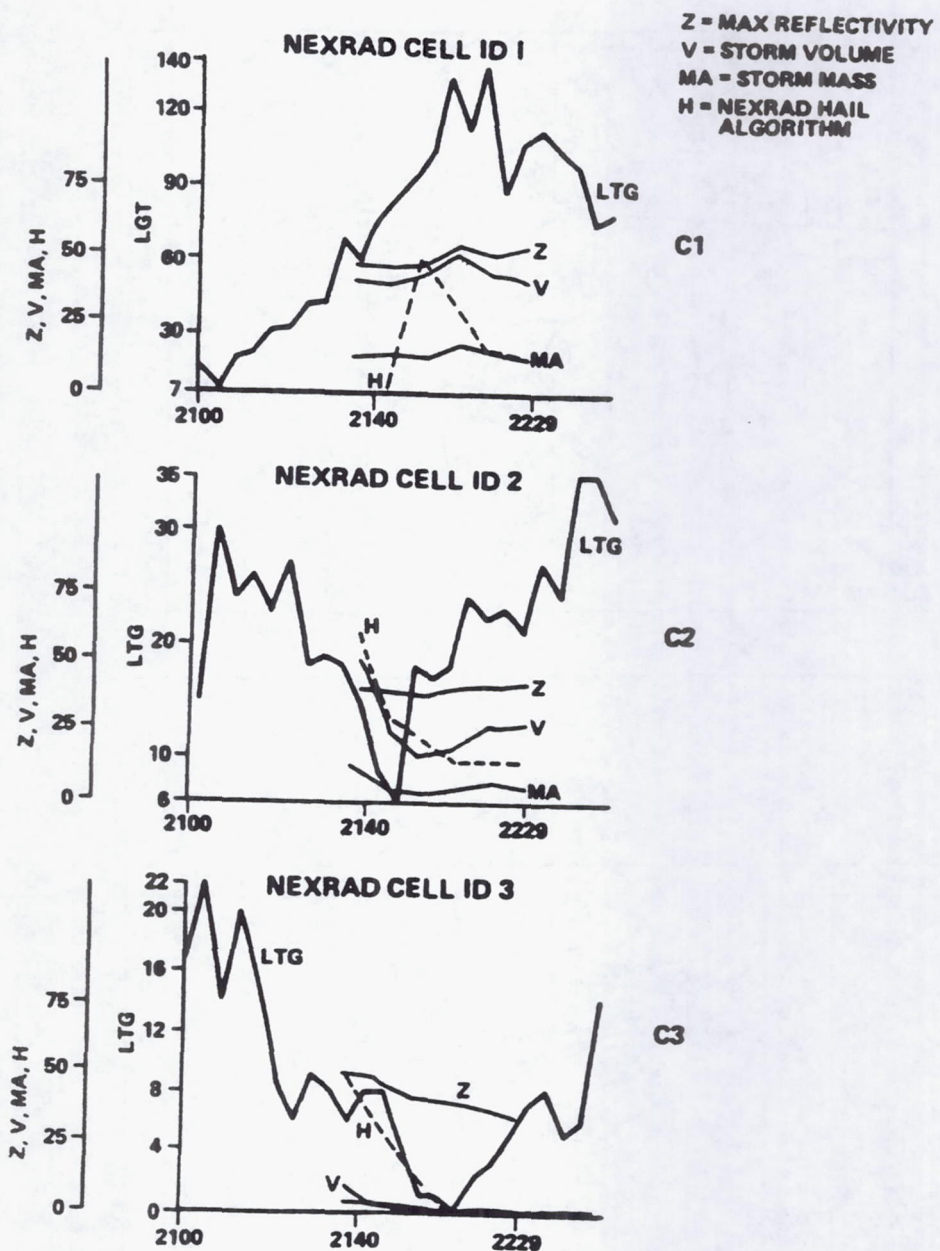


Fig. 3.3.1. A comparison of lightning flashing rates and precipitation attributes from NEXRAD algorithms.

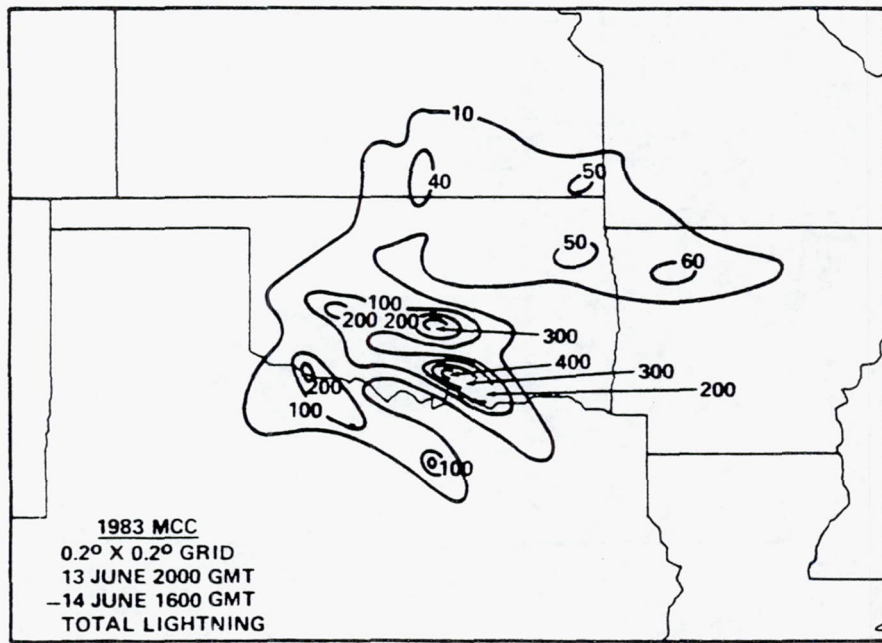
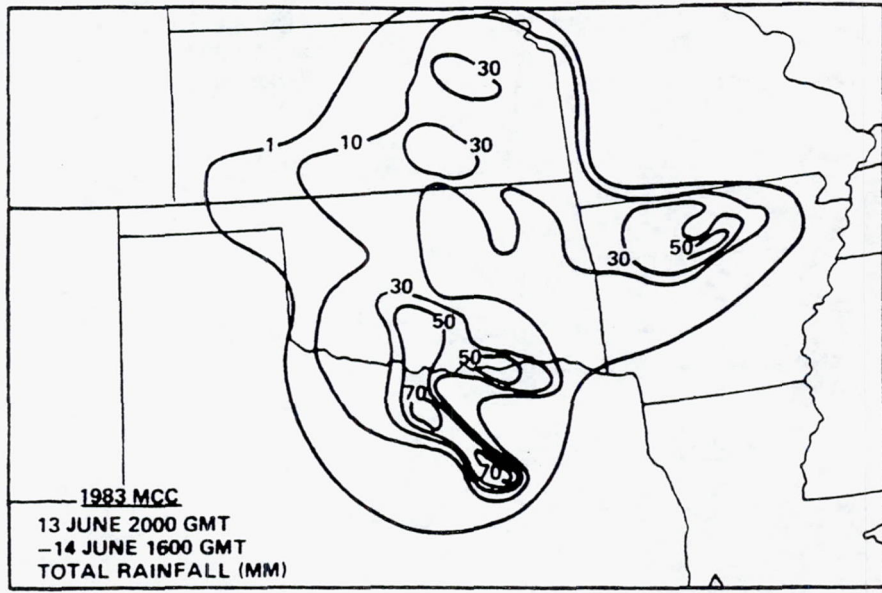


Fig. 3.3.2. An evaluation of precipitation and lightning in a mesoscale convective complex.

### **3.4 Numerical Modeling**

There are three major objectives for the numerical modeling component of SPACE :

- o Unravel the complex physical mechanisms leading to the initiation and organization of convection. By isolating and defining the physical mechanisms (and scales of these mechanisms) remote sensing strategies can be directed or refined to observing the variables most critical to the development of convection.
- o Evaluate the abilities of a hierarchy of models to simulate features observed under the SPACE field program. By increasing confidence in or improving numerical models, the models can be used as surrogate atmospheres to evaluate remote sensors.
- o Complement remote sensing data to provide better interpretation and improve retrieval algorithms.

The numerical modeling component of SPACE will utilize the rich observational data base for initialization or verification of a hierarchy of models ranging from regional scale to cloud scale. The following outlines the types and scales of models to be used. Table 3.4.1 summarizes the models and characteristics while Figure 3.4.1 schematically illustrates the horizontal domains of the models.

#### *3.4.1 Regional Scale Models (Meso-Alpha)*

While much of the focus of the SPACE program is on the convective scale, synoptic and regional scale circulations may provide meso-beta and meso-gamma structure important to the initiation and development of convection. For example, advective processes on the scale of 100 - 300 km such as low level jets may produce moisture tongues or differential temperature advection leading to preferred area of convection. Three major regional scale models are likely to be utilized on the SPACE data set - the LAMPS model (Perkey and Krietzberg, 1976), the MASS model (Kaplan (1982)) and the University of Wisconsin, sub-synoptic model (Diak et al., 1986). It is likely that the University of Wisconsin model will be used in a real time mode for operational forecasts under SPACE.

#### *3.4.2 Mesoscale Boundary Layer Models (Meso-Beta, Meso-Gamma)*

Because it is expected that many of the convective case days under the SPACE field program will not be highly synoptically forced, boundary layer forcing mechanisms may be significant. (This is discussed fully in section 3.1). In order to evaluate and isolate these mechanisms a high resolution boundary layer model is useful. It is expected that the Colorado Hydrostatic Boundary Model (Pielke (1974) and McNider and Pielke (1981)) will be utilized along with the MASS model (Wong (1982)) to examine the pre-storm boundary layer environment.

Table 3.4.1 Summary of numerical models and relation to SPACE objectives

Model	Typical Horizontal Domain/Resolution	Highlight	SPACE Objective
LAMPS	3000 km/50 km	Cumulus parameterization	Moisture variability (3.1) Diabatic feedback (3.2)
MASS	3000 km/50 km	Cumulus parameterization multi-scale	Scale interaction (3.1 and 3.2)
U. of Wisconsin (SSM)	5000 km/150 km	Cumulus parameterization surface variations	Real Time Operation
CSU Hydrostatic Model	400 km/8 km	High resolution boundary layer, surface energy budget	Boundary layer forcing (3.1)
MASS	500 km/10 km	Boundary layer parameterization with cumulus parameterization	Boundary layer forcing (3.1)
South Dakota	20 km/200 m	High resolution, microphysics	Moisture variability (3.1) Precipitation processes (3.3)
Tao and Simpson	75 km/1 km	multi-cell clouds	Cumulus mergers (3.5)

55

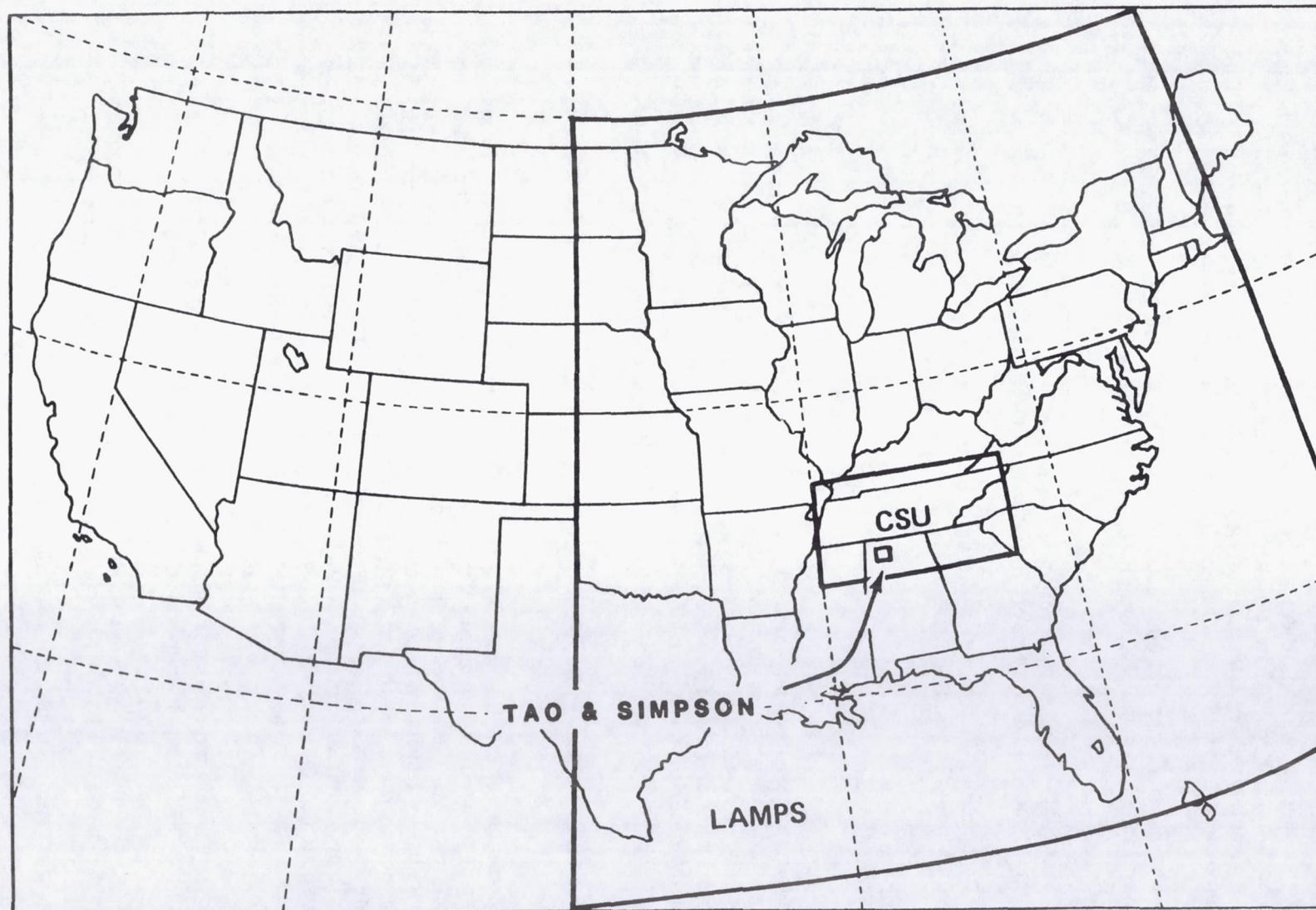


Fig. 3.4.1. A schematic of model domains applied to the SPACE area. MASS and SSM are also likely to be run for similar domains.

#### *3.4.3 Cloud Scale Models*

Many of the remote sensing objectives in section 2.0 and science objectives in this section are related to and supported by cloud scale modeling. Cloud models can assist in interpretation of remotely sensed data and test sensitivity to observed parameters. The following lists three areas related to cloud modeling and the cloud model expected to be used.

- (1) Internal structure and diagnostic studies of convection (Section 3.2). Tao and Simpson Model (Tao and Simpson (1984)), South Dakota Model (Orville and Kopp (1977)).
- (2) Sensitivity of cloud scale response to small scale variations in moisture (Section 2.1 and 3.1) South Dakota Cloud Model (Orville and Kopp (1977)).
- (3) Organization of convection through cumulus merging (Section 3.5). Tao and Simpson Model (Tao and Simpson (1984)).

#### *3.4.4 Multi-Scale Models*

As computer systems have increased in capacity and speed the ability to address meso-beta, meso-gamma and cloud scale interaction is becoming a reality. In fact two major modeling systems - RAMS - being developed at Colorado State University and MASS-TASS - being developed by Kaplan and Procter (personal communication) should allow horizontal resolution on the order of 1 km with domains (continuous or nested) up to 1000 km. The SPACE data coverage area should provide a unique testing ground for these multi-scale models.

### **3.5 Convective Structure and Evolution**

Interpretation of satellite imagery of convective storms is still in its formative stages. Better understanding is needed of the dynamic internal structure of clouds and the cloud microphysics in the expected low shear environment of SPACE in order to parameterize radiative transfer models or to define retrieval algorithms for precipitation. While thunderstorm structure within high shear environments has received considerable attention during recent years (e.g. Klemp *et al* (1981); Foote and Frank (1983); Weisman and Klemp (1984)) precipitation structure within low shear environments remains nebulous. Also, the interaction of cumulus fields in producing cumulus mergers and the role of storm outflows in the initiation of new convection needs to be better defined. Thus two objectives under SPACE are:

- o Use conventional radar and Doppler radar to define the internal structure and microphysics of observed convection within a low shear environment.
- o Use combined satellite imagery and radar analyses to increase understanding of cumulus mergers and to provide data for comparisons with numerical models.

The following discusses these objectives in more detail.

### *3.5.1 Internal Convective Structure*

Compared to the studies of Great Plains thunderstorms, there has been relatively few studies of thunderstorm structure in a moist subtropical environment. In the past, most descriptive models and cloud numerical models have concentrated on the role of vertical wind shear in determining the intensity, structure and lifetime of thunderstorms (e.g. Newton and Fankhauser (1975) and Weisman and Klemp (1982). It is expected that many of the convective cases under SPACE will be in low shear environments. Under these conditions, convergence, moisture and temperature profiles may be the key parameters in determining the intensity and lifetime of convection. The structure of individual convective cells and cloud microphysics may also be much different in the low shear environments. It is an objective under SPACE to evaluate differences in structure and microphysics of storms in order to support remote sensing interpretation and retrieval algorithms.

### *3.5.2 Cumulus Population and Mergers*

In the SPACE field program, interaction among the cumulus field either by outflow initiating new detached convection or through merger of individual cumulus clouds may be the method for maintaining or organizing convection into longlived convective systems. Merged cumulus systems have in fact been found to produce over 80 percent of the precipitation in subtropical areas. Mergers have been studied by radar and aircraft over south Florida by Simpson et al (1980), who proposed a merging mechanism involving downdraft outflows as illustrated in Fig. 3.5.1 (a) and (b). Recently Tao and Simpson (1984) evolved a numerical model which is able to simulate cumulus interactions. Preliminary results with a two-dimensional version of the model clearly show how the intersection of two or more cumulus outflows initiates first a "bridge cloud" and then a large merged system as illustrated in Fig. 3.5.2 (a),(b),and (c). An objective under SPACE is to evaluate this merging mechanism and provide data to initialize and further test the numerical model. The Doppler radar coverage in COHMEC should provide a valuable source of data in testing the merger hypothesis and the numerical model. Soundings, wind profiles, lifting or convergence and the scale and magnitude of initial perturbations in the buoyancy field all needed for the cloud model should be available from the COHMEC data set.

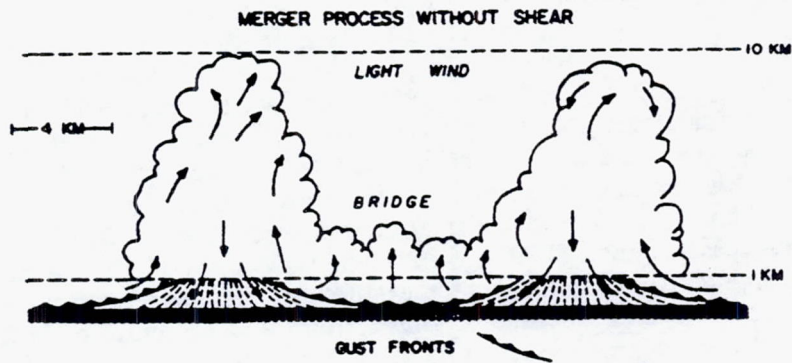


Fig. 3.5.1a. Schematic illustration relating downdraft interaction to bridging and merger in case of light wind and weak shear.

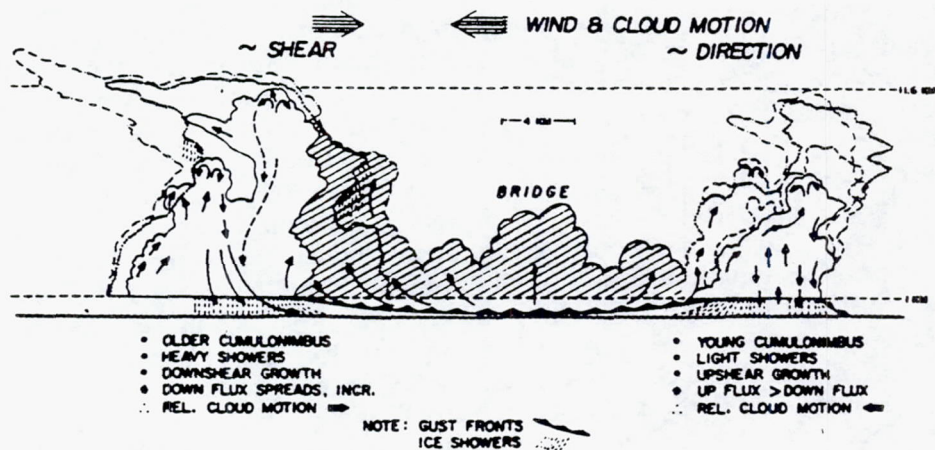


Fig. 3.5.1b. Schematic illustration relating downdraft interaction to bridging and merger in case of moderate shear opposite to wind direction through most of the vertical extent of cloud layer. Younger cumulonimbus on right has predominate upmotions, moves faster than the wind. Older cumulonimbus on left has predominate downmotions, moves slower than wind so clouds move and propagate toward each other. Interaction of downdrafts enhances bridge development.

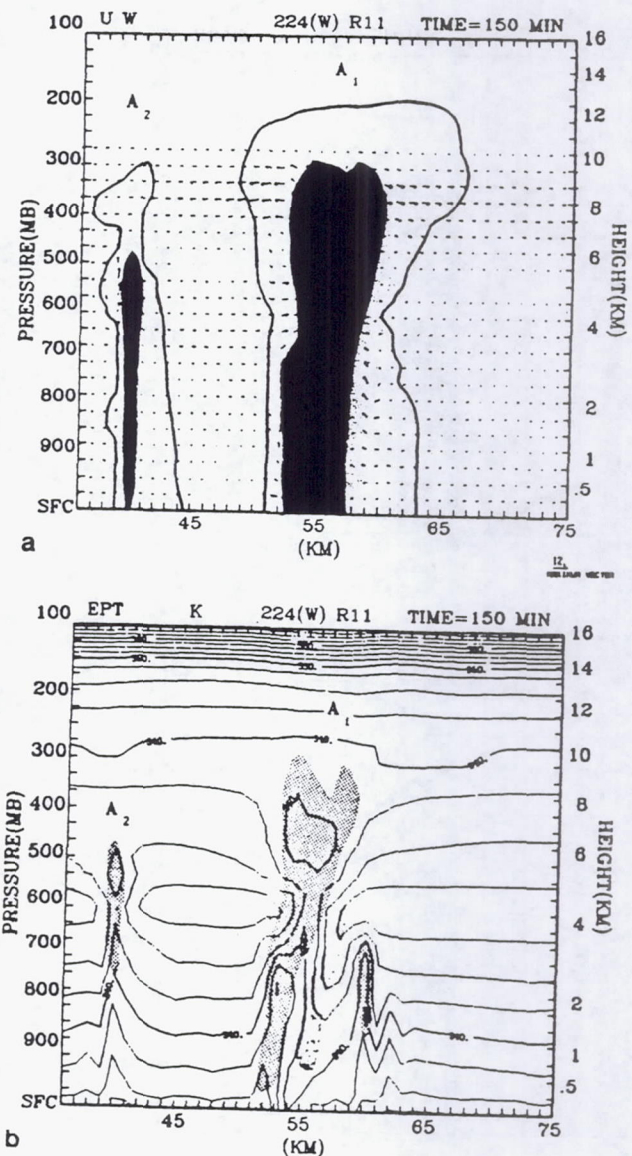


Fig. 3.5.2a. (a) The vertical cross section at  $t = 150$  min showing the vector wind fields with liquid water contents contours superimposed (maximum vector = 12 m/s). The heavy solid lines indicate the cloud boundaries and shaded areas indicate the heavy concentration of liquid water content ( $> 1$  g/kg). For a better illustration, this picture only shows the wind vectors in the low and middle troposphere. (b) The vertical cross section of equivalent potential temperature field (K). In the light shaded area  $w < -2$  m/s and in the dark stippled area  $w > 2$  m/s. Contour interval is 2.5 K.

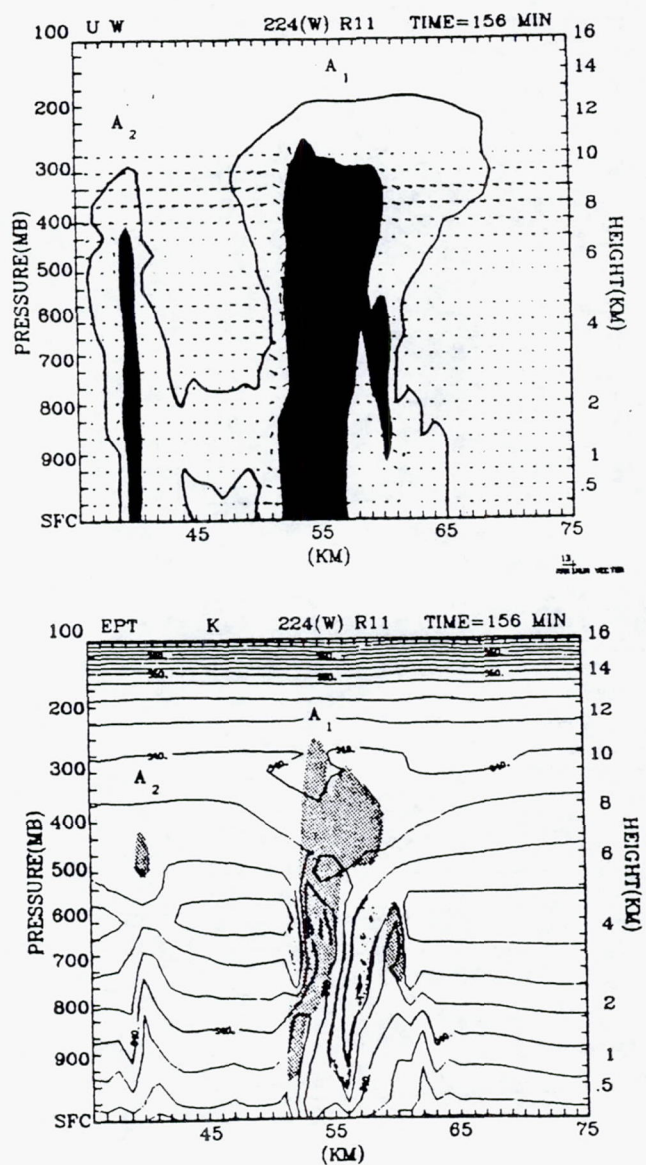


Fig. 3.5.2b. As in Fig. 3.5.2a except at  $t = 156$  min (maximum vector = 13 m/s).

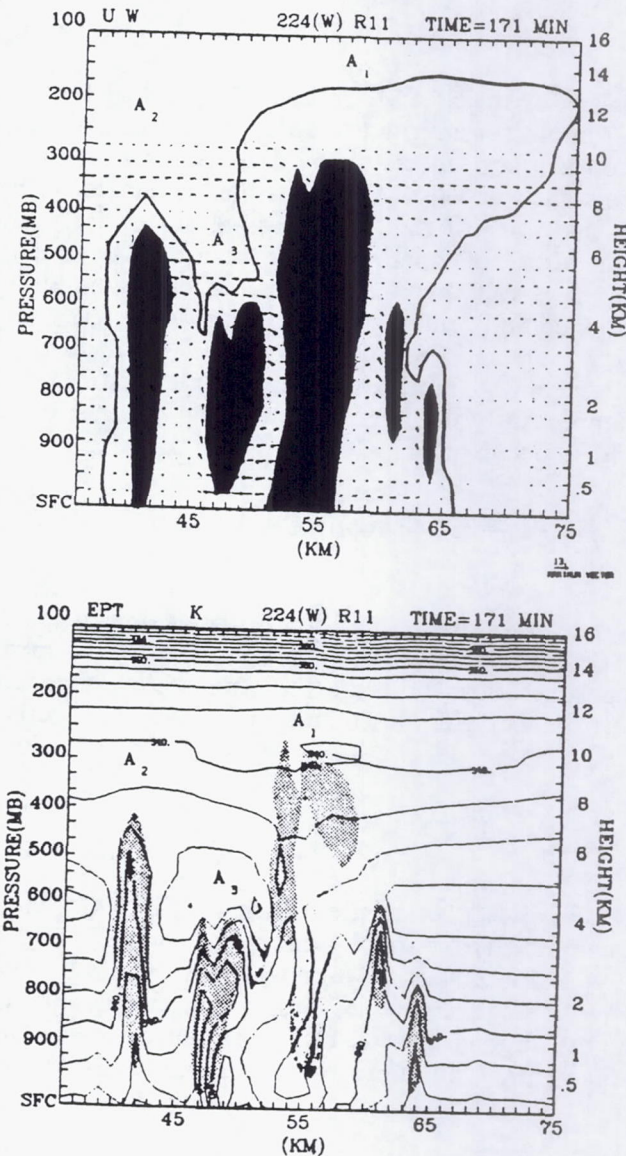


Fig. 3.5.2c. As in Fig. 3.5.2a except at  $t = 171$  min (maximum vector = 13 m/s).

## 4.0 EXPERIMENT DESIGN

The experiment design for the SPACE portion of COHDEX is configured as closely as possible to address the remote sensing and science objectives given previously in Chapters 2 and 3. It is the complimentary aspects of the diverse observing system and objectives which makes field programs such as COHDEX possible. Practically, however, the design works under the constraint that some of the objectives are not entirely mutually supportive and some compromises in terms of operation and focus of the observing systems are necessary. Never-the-less, it is felt that the design and operation of the experiment can fulfill the needs for the science and remote sensing objectives. The following sections outline in general the observing systems in SPACE and their relation to the objectives. Chapter 5, which follows, will specify in more detail the characteristics and scheduling of the observing systems. Most importantly the first section below outlines the type of experimental days which are expected to occur during COHDEX.

### 4.1 Regional Climatology and Expected Synoptic Conditions

Types of weather expected during the SPACE operational period vary considerably and are dictated generally by climatology and specifically by prevailing synoptic conditions. The following subsections describe the Huntsville region climatology and exemplify the synoptic patterns associated with different types of convective patterns.

#### 4.1.1 Climatology

The Huntsville area receives precipitation during all months, but rainfall associated with convection is most common from April through September (Fig. 4.1.1). Actual thunderstorm days peak in July, and a total of 20 thunderstorms would be expected from June 1 to July 31. Although severe weather in the form of tornadoes and hail is most common during the spring season, the summer season also experiences severe weather primarily in the form of small hail, damaging thunderstorm winds, and locally heavy rainfall (Storm Data).

Table 4.1.1 provides additional information for the spring and summer months. From late spring to early summer, surface dewpoints rise steadily, reaching a peak of approximately 70 F in July and August. Surface winds contrastingly decrease during this period as synoptic-scale influences diminish. The emergence of the subtropical high by middle summer is typically associated with more uniform low-level conditions, and much weaker flow aloft. Precipitating convection correspondingly exhibits smaller scales during this period as synoptic-scale forcing subsides. Some scenarios illustrating variations in convective cloud structure and organization under different degrees of synoptic-scale forcing are given in the following subsections.

#### 4.1.2 Strong Synoptic-scale Forcing (6/7/85)

The 7 June 1985 case was one in which appreciable synoptic-scale forcing, in the presence of unstable air, produced widespread convection and associated severe weather.

At 500 mb a shortwave trough embedded within 30 knot northwesterly flow passed over western Alabama by early evening (Fig. 4.1.2a). Low-level air was markedly unstable (Fig. 4.1.2b) as evidenced by over 60 severe weather reports (Storm Data) as the system moved through. At the surface both a well defined cold front and more diffuse warm front (Fig. 4.1.2d) triggered widespread convection as shown in the 2100 GMT visible satellite image in Fig. 4.1.2c.

#### *4.1.3 Synoptic-scale or Meso-scale Forcing at Low Levels (7/4/85)*

It is expected that in many cases upper level forcing by PVA may be small compared to forcing provided by thermal boundaries from old fronts or previous outflow boundaries. The 4 July 1985 case exemplifies such a situation. Here, the 500 mb chart in Fig. 4.1.3a indicates a short-wave trough over Alabama. Air is quite unstable (LI of -5) and wind shear is weak over the lowest 6 km (Fig. 4.1.3b).

The visible satellite image in Fig. 4.1.3c indicates several outflow boundaries which are apparently influencing convective cloud initiation and intensity. Surface flow patterns three hours later at 0000 GMT 4 July (Fig. 4.1.3d) indicate a net mass convergence over eastern Alabama. Several well-defined meso-beta scale convective systems are visible over the region in Fig. 4.1.3c, including a cluster of several over northern Alabama and central Tennessee.

#### *4.1.4 Negligible Synoptic-scale Forcing (7/18/85, 7/19/85)*

When both upper air troughs and low-level boundaries are absent, convection appears to be strongly influenced by local forcing. On two consecutive synoptically-undisturbed days (18 and 19 July 1985) convection appeared to be influenced by local effects (Figs. 4.1.4c,e), and tended to assume smaller horizontal dimensions and smaller area coverage. Synoptic-scale features on both days were influenced by an upper level ridge (Fig. 4.1.4a) over the Southeast, which produced weak easterly flow over northern Alabama. At the surface, relatively homogeneous features can be seen in Fig. 4.1.4d. Very weak frontal boundaries are located well to the northwest and to the east. Soundings plotted in Fig. 4.1.4b show small to moderate CAPE and small vertical wind shear.

It is expected that environments such as this will typify conditions during the COHMEC operational period from June 1 to July 31 (e.g., Purdom and Marcus, 1982). Cloud development may be largely determined by local forcing, mature clouds may be relatively small and isolated, but subsequent merging may occur as individual convective cell outflows begin to interact. Peak activity and intensity is likely to occur in late afternoon and early evening. More widespread and intense convective activity is expected primarily when synoptic scale features such as short-wave troughs, active fronts or old frontal boundaries are present.

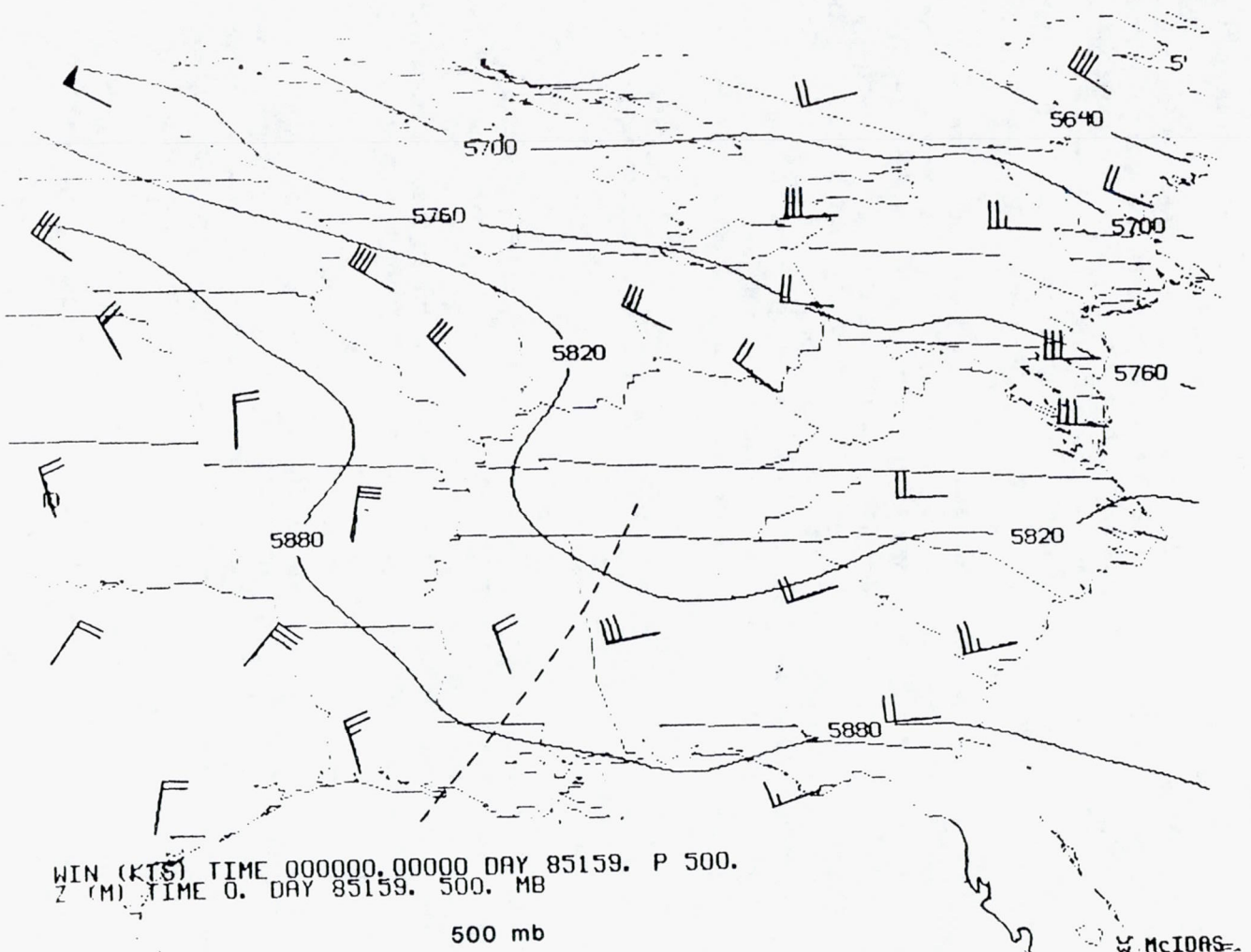


Fig. 4.1.2a. The 500 mb weather chart for 00Z, 8 June 1985.

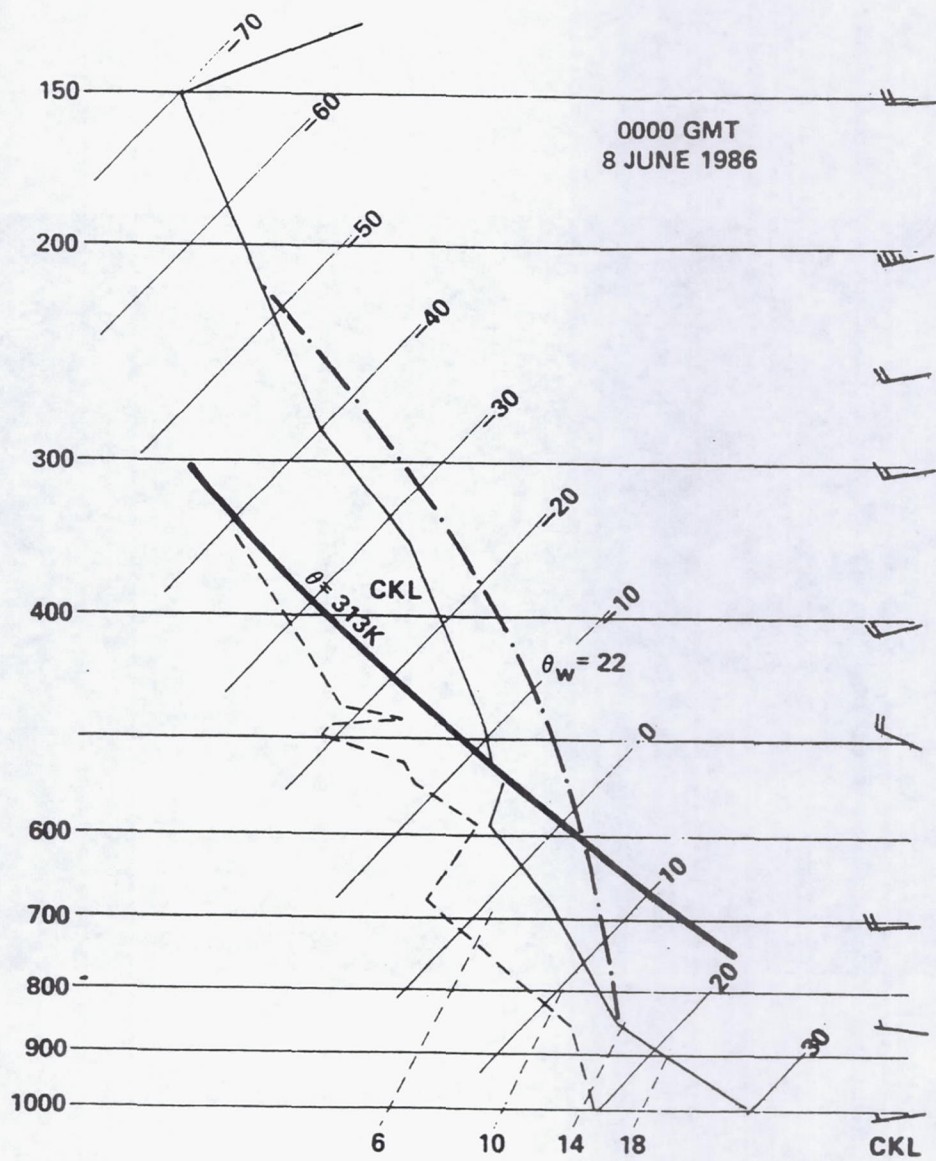


Fig. 4.1.2b. The sounding for 00Z, 8 June 1985.

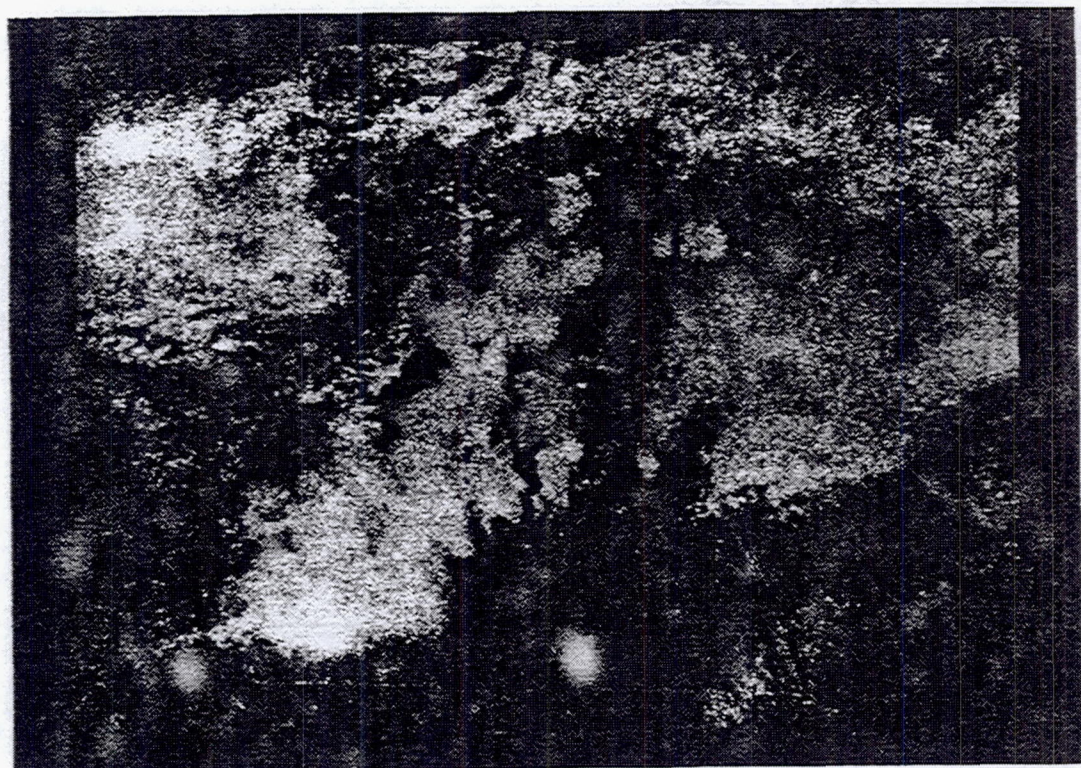


Fig. 4.1.2c. The regional visible satellite image (2 km resolution) for 21Z, 7 June 1985.

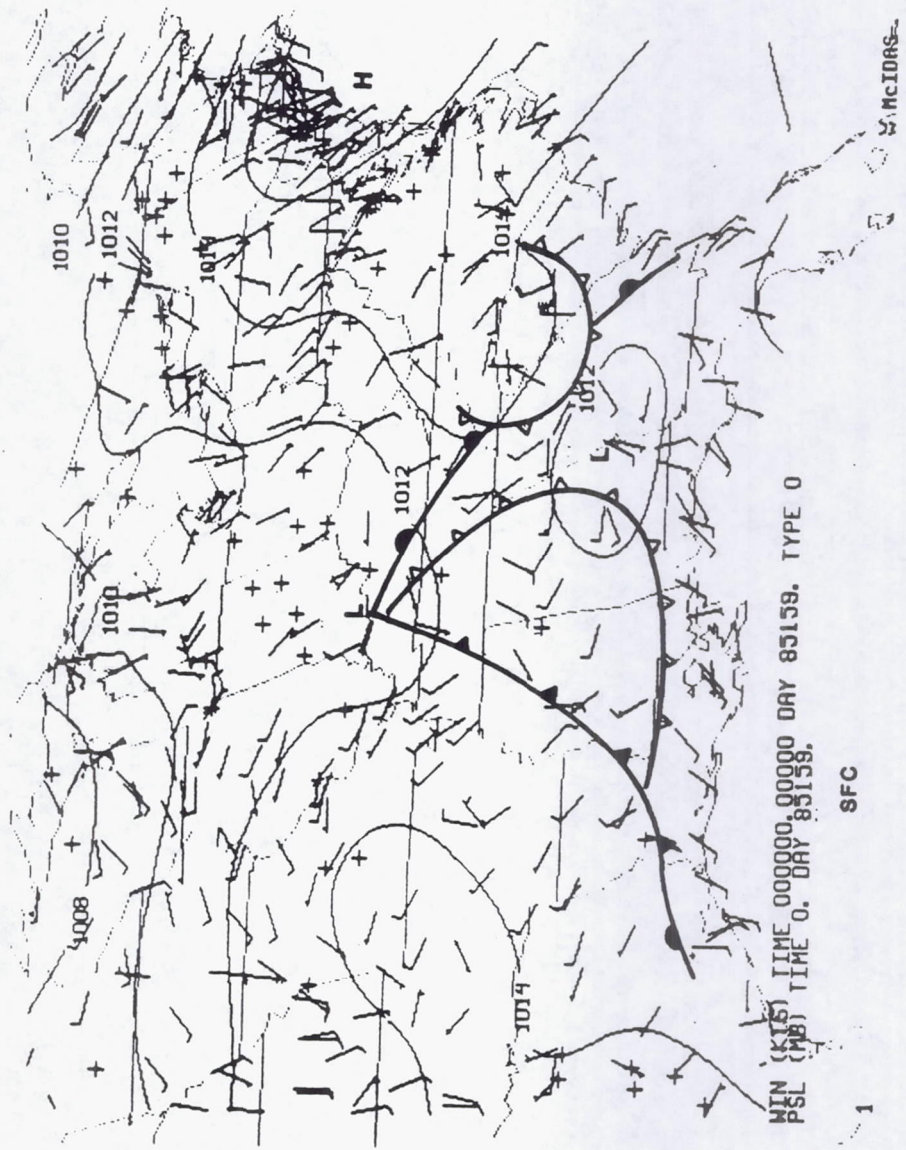


Fig. 4.1.2d. The surface chart for 00Z, 8 June 1985.

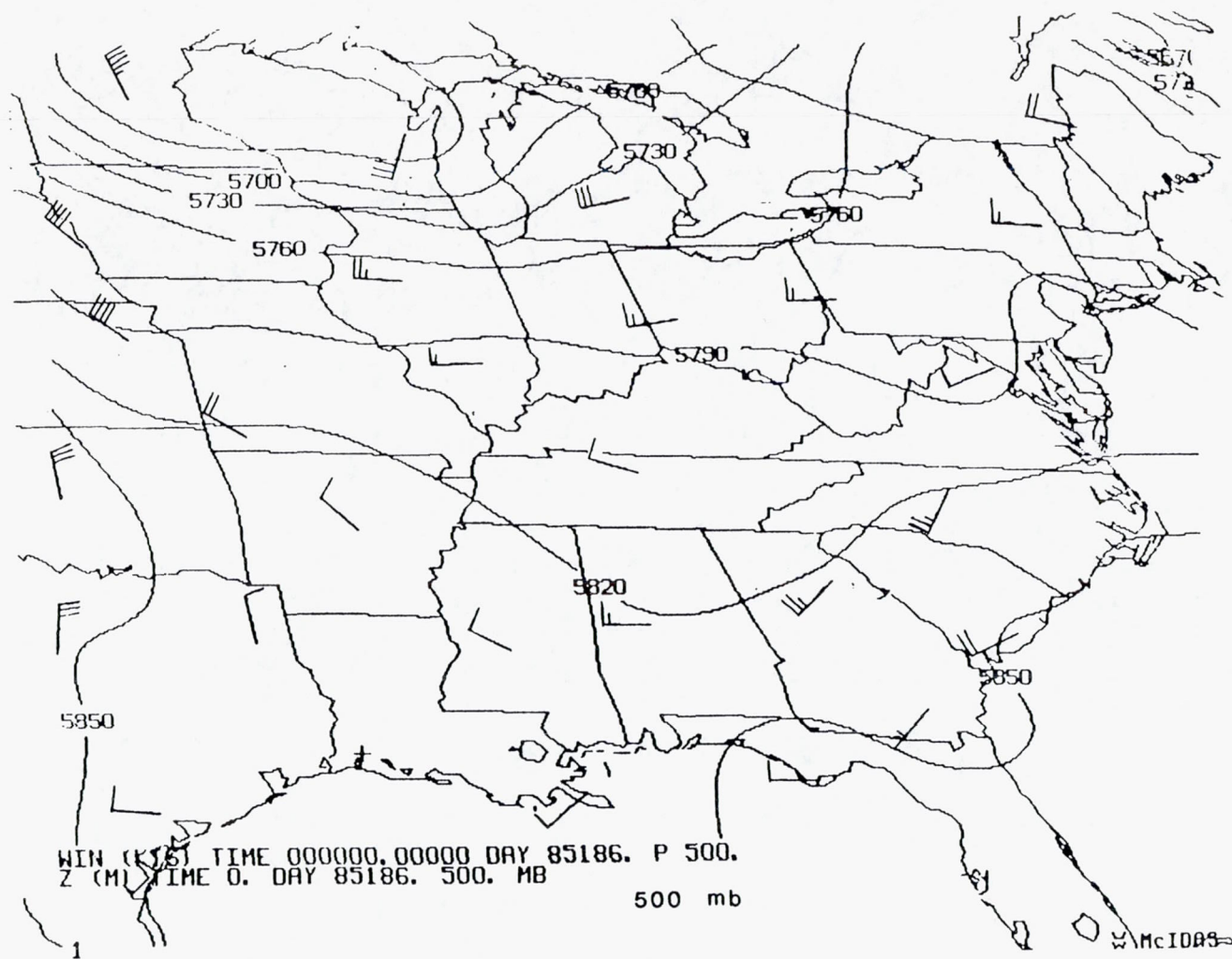


Fig. 4.1.3a. The 500 mb weather chart for 00Z, 5 July 1985.

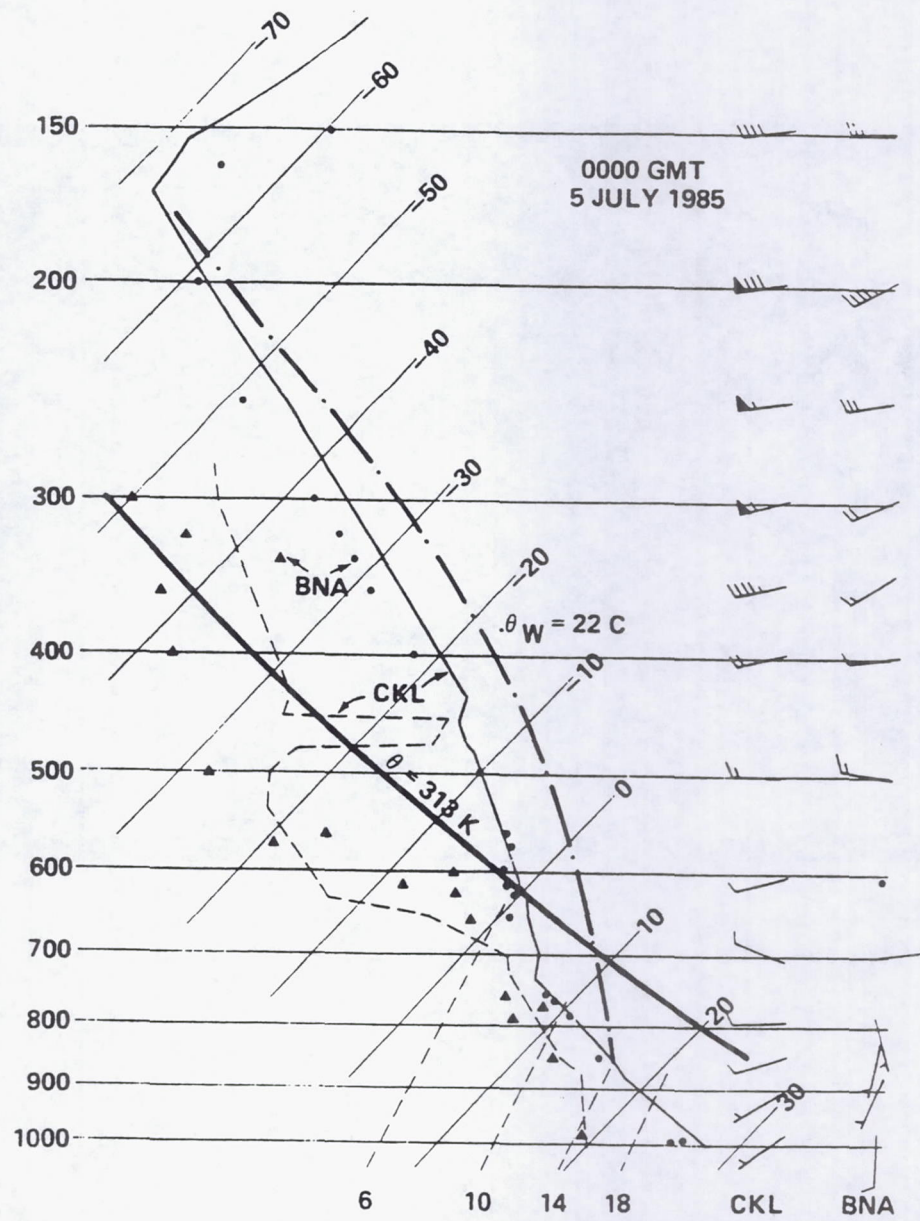


Fig. 4.1.3b. The sounding for 00Z, 5 July 1985.

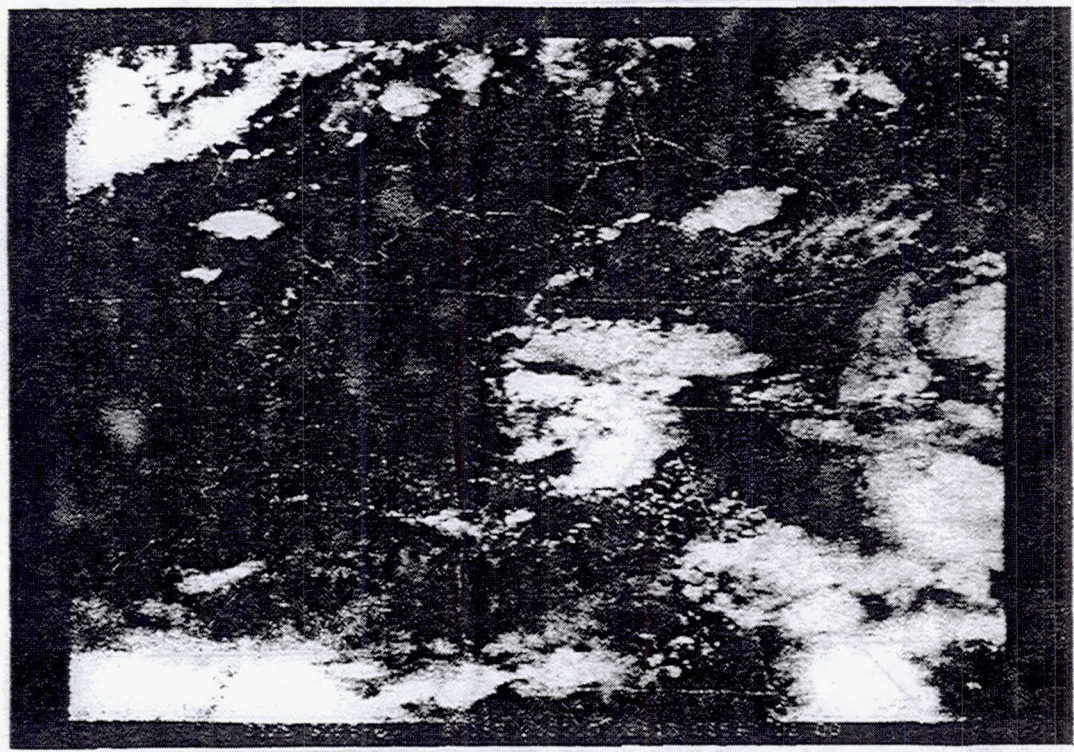
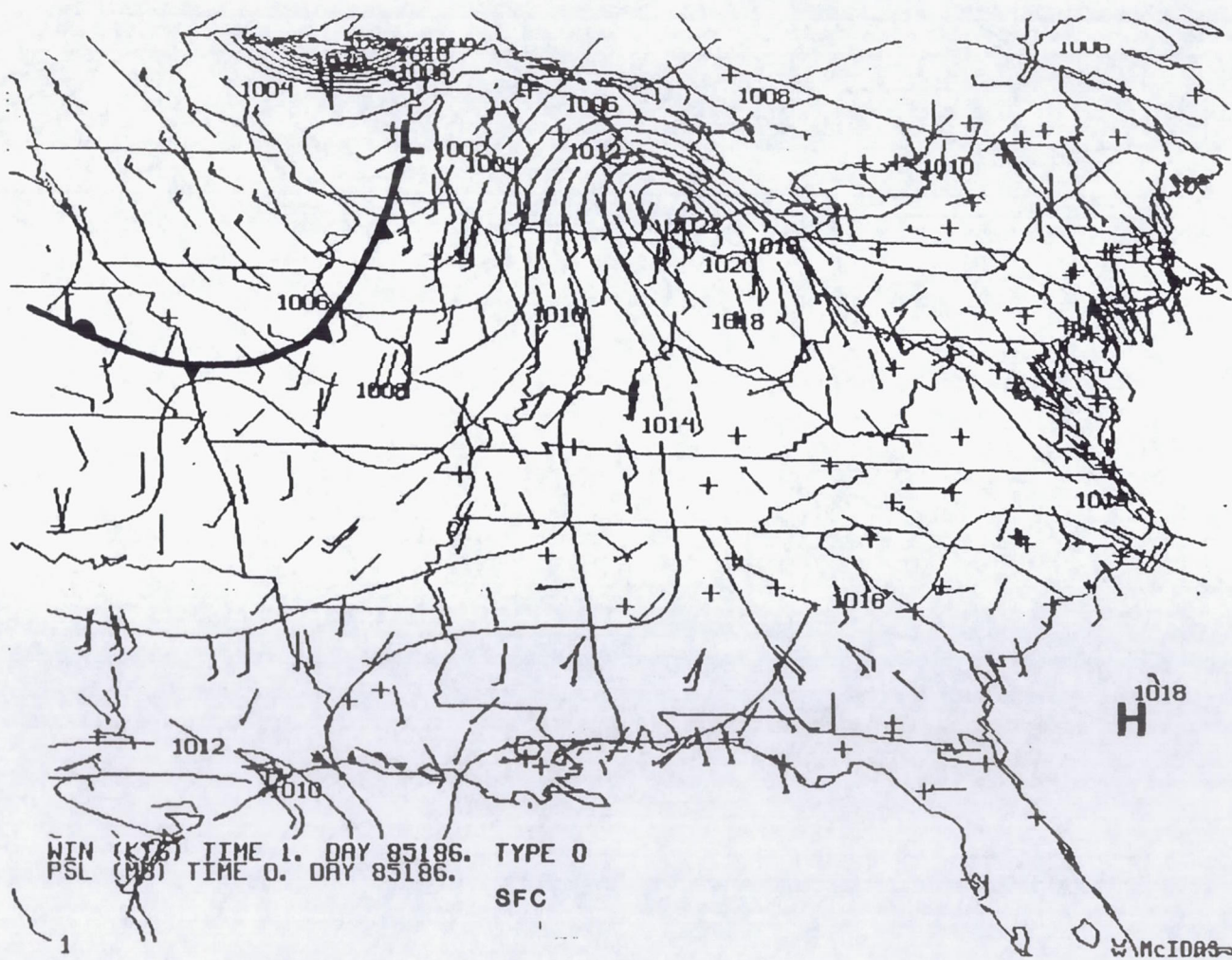


Fig. 4.1.3c. The regional visible satellite image (2 km resolution) for 21Z, 4 July 1985.



**Fig. 4.1.3d.** The surface chart for 01Z, 5 July 1985.

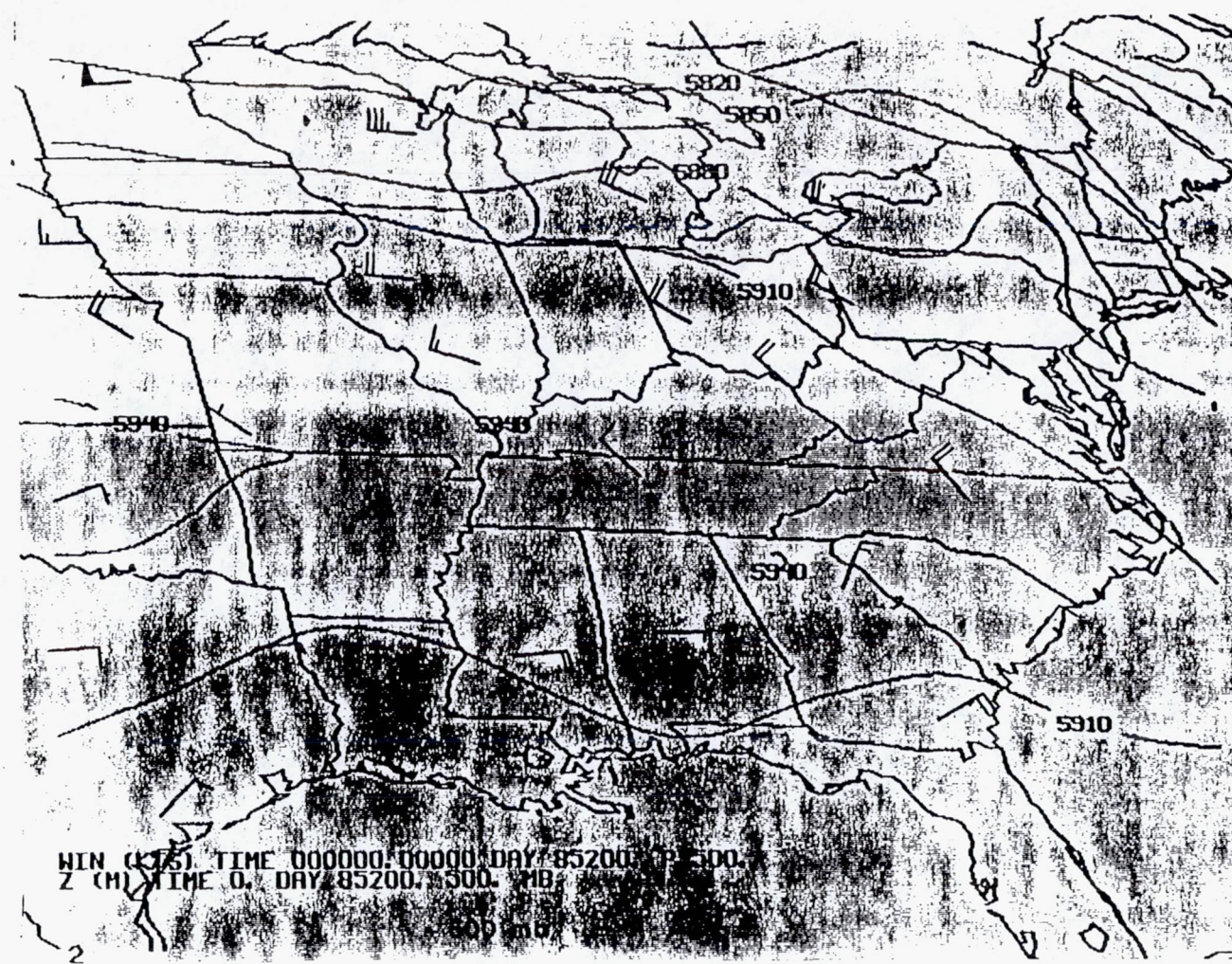


Fig. 4.1.4a. The 500 mb weather chart for 00Z, 19 July 1985.

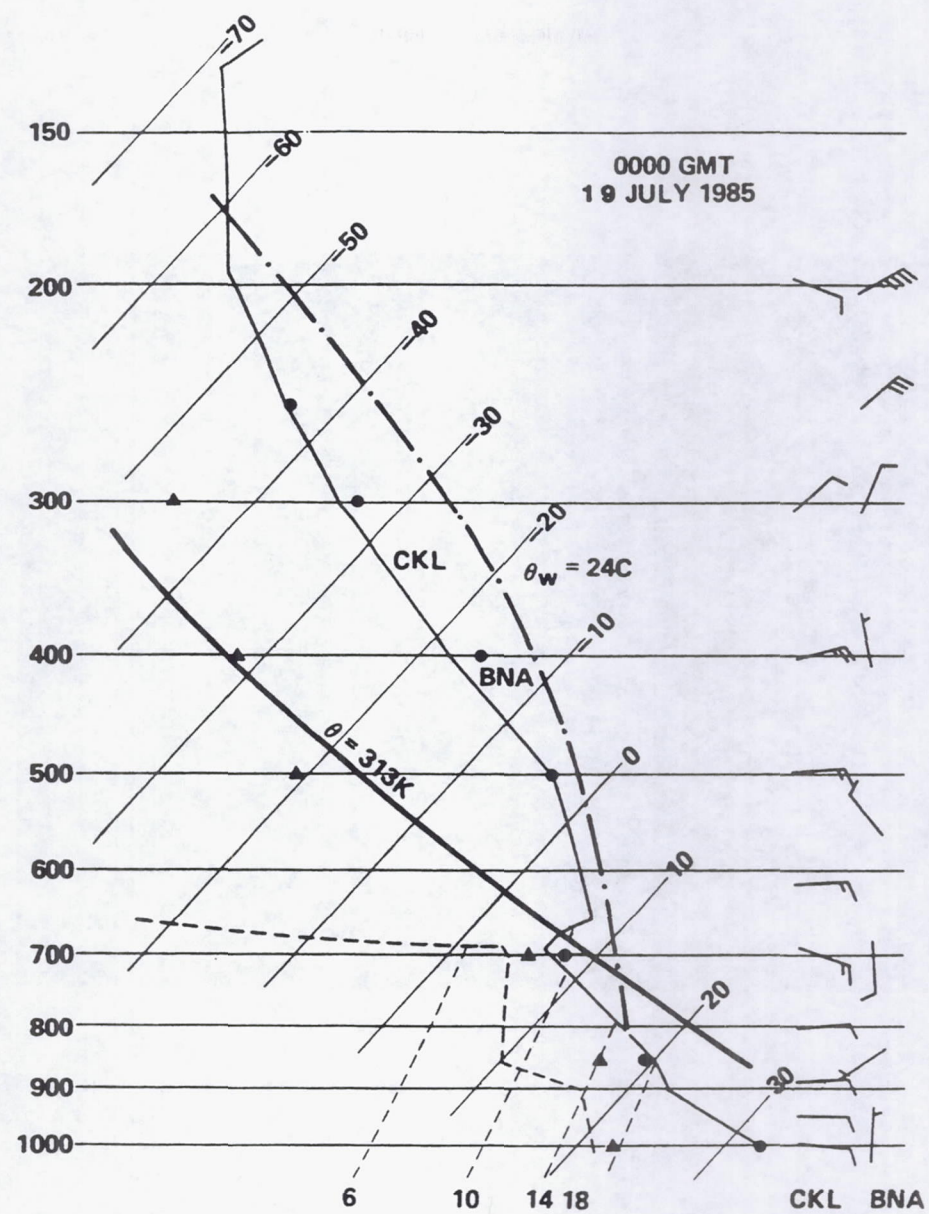


Fig. 4.1.4b. The sounding for 00Z, 19 July 1985.

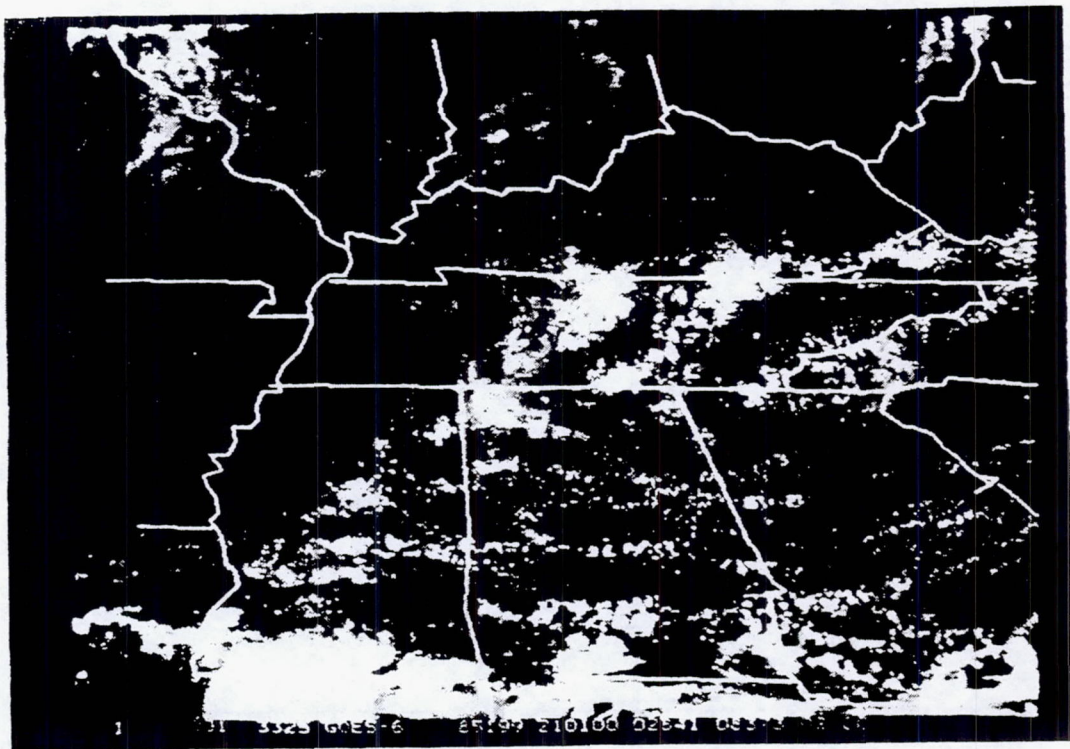


Fig. 4.1.4c. The regional visible satellite image (2 km resolution) for 21Z, 18 July 1985.

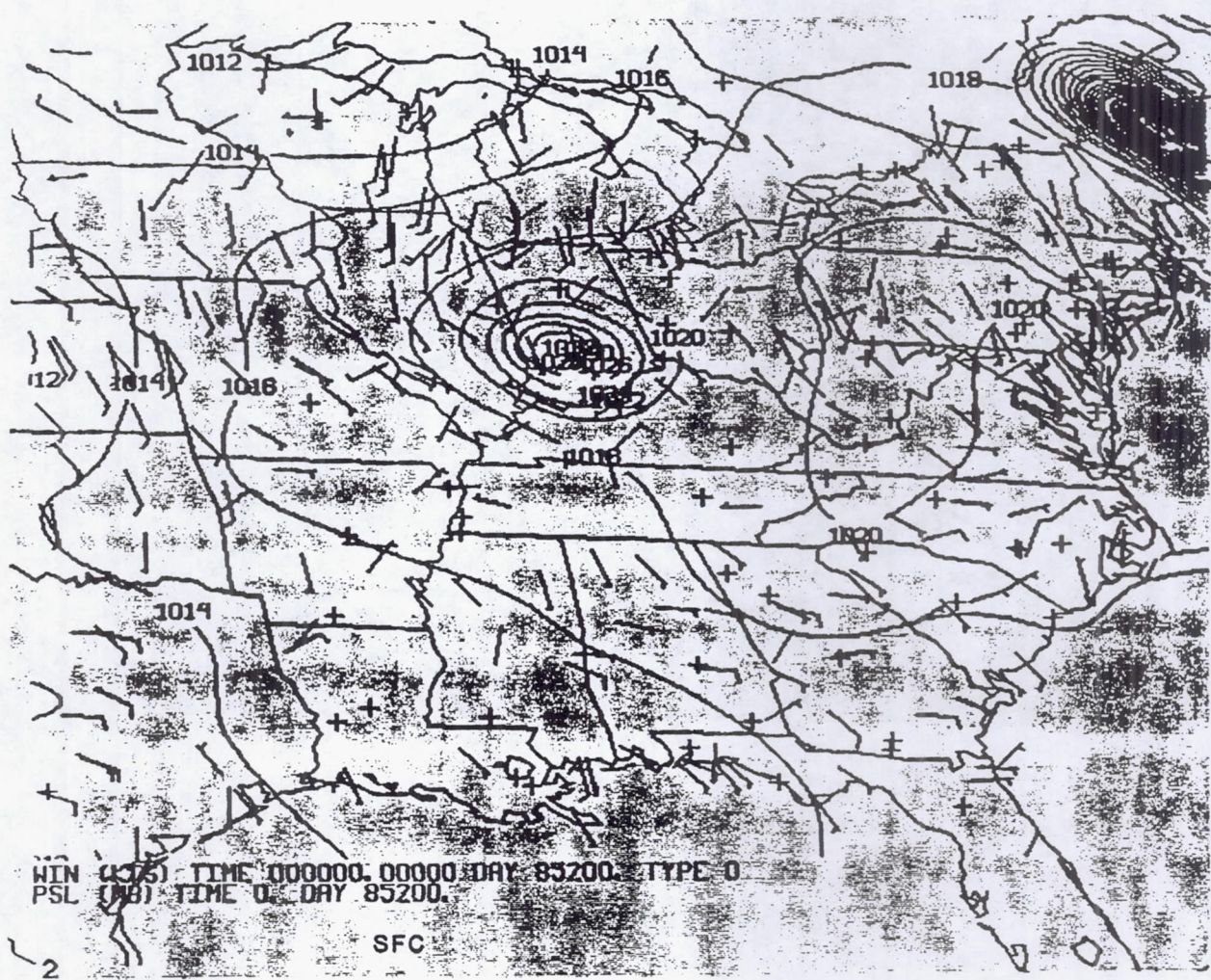


Fig. 4.1.4d. The surface chart for 00Z, 19 July 1985.

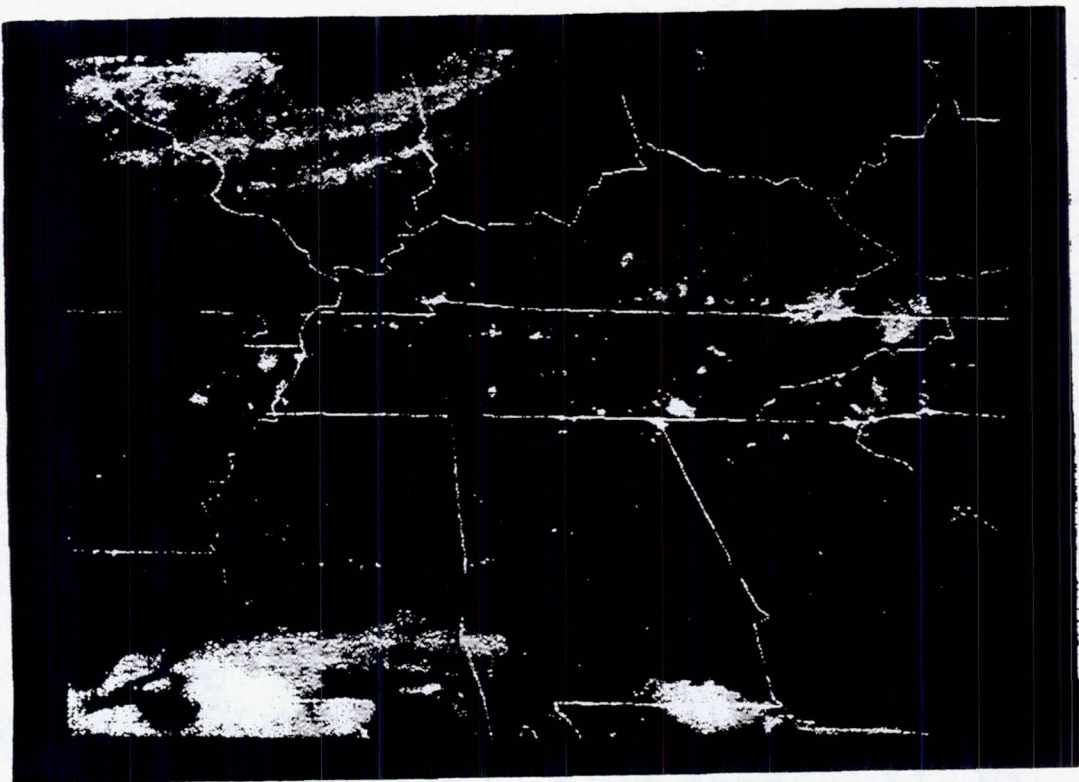


Fig. 4.1.4e. The regional visible satellite image (2 km resolution) for 21Z, 19 July 1985.

## 4.2 Upper Air Network

The design of the upper air network is intended to address four major areas:

- o Provide ground truth for temperature and moisture sensing instruments such as MAMS, MTS and HIS (Sections 2.1, 2.3, 2.4).
- o Provide mass and moisture budgets in support of diagnostic studies of the dynamic and thermodynamic impact of convection (Section 3.2).
- o Provide data to initialize and verify numerical models (Section 3.4).
- o Provide background environmental conditions for analysis of the initiation, structure and evolution of convection (Section 3.1 and 3.5).

### 4.2.1 *Ground Truth for Remote Sensors*

As covered in Chapter 2 one of the main areas of emphasis in SPACE is to evaluate and test remote sensors. The upper air network should be able to produce two to three soundings at each station during the U2-C and ER-2 overflight times. This will provide baseline data for evaluation of sensor performance and retrieval algorithms (Menzel et. al. 1981). Also, integrated parameters such as total precipitable water or stability indices can be derived from the rawinsonde sounding data for comparison with the aircraft or satellite based soundings (Jedlovec (1985)).

Jedlovec (1985) has shown that relatively high spatial resolution rawinsonde soundings can be made most useful in comparison to remotely sensed data by conversion through objective analysis techniques to mesoscale grids. These grid based values can then be compared to remote sensing images for structure integrity or more quantitatively in terms of absolute error as a function of retrieval methods or layer intervals. These techniques using the rawinsonde data should be most useful in evaluating HIS and MTS sounder data.

#### *4.2.2 Mass, Momentum and Moisture Budgets*

In both the pre-storm and storm environment the rawinsonde network should provide data on the areas of mass, momentum and moisture convergence. The rawinsonde configuration in terms of triangles (see Section 5.3) is meant to maximize the spatial information for such budget parameters. This data can then be used in diagnostic models to evaluate the role bulk parameters such as moisture and mass convergence have on convection and in turn the role bulk diabatic heating (through precipitation measurements) may play in the mass and momentum budgets (see Section 3.2).

#### *4.2.3 Initialization and Verification of Numerical Models*

The high resolution, high frequency rawinsonde network will provide data not normally available in an operational mode to initialize and verify models. For example, the entire heating sequence from sunrise to sunset which is so important for air mass convection is normally completely missed by operational rawinsonde networks.

The prognostic mesoscale and cloud models to be used for analysis under SPACE need initial fields. The rawinsonde network as configured can provide the thermodynamic and windfield data to provide high resolution initialization.

Aside from initialization, the rawinsonde network will be able to provide needed verification as the numerical models are integrated in time. Such verification is necessary to evaluate the physical processes which are parameterized in the numerical models and the fidelity of the total simulation.

#### *4.2.4 Background Environmental Conditions*

Traditional methods for evaluation of convective potential and evolution are intimately tied to analysis of standard rawinsonde information (e.g. determination of convective instability, energy availability, stability indices, shear analyses, ect.). While the SPACE program will be utilizing new technologies for studying convection, the more standard rawinsonde data will be a valuable tool to describe the background environmental conditions in which the convection is initiated and the influence the convection has on the environment.

### **4.3 Associated Radar Network**

Radar systems available for the SPACE program can be partitioned into two categories:

- (1) radars devoted to large-scale scanning over the meso-beta scale SPACE network and adjacent areas, and
- (2) Doppler radars devoted to scanning limited areas within the MIST/FLOWS mesonet.

Large-scale radar coverage will be provided by the standard NWS radar network (Fig. 4.3.1). Data from selected NWS radar sites will be available as Kavouras image products (see section 5.2.2) accessed in near real time during field operations. Such data will provide documentation on the origin and evolution of convective systems which affect the SPACE experimental area (Fig. 4.3.1).

Over the meso-beta scale SPACE network, quantitative information will be available from the Radar Data Processor (RADAP- see Section 5.2.1) installed on the BNA radar, whose location is given in Fig. 4.3.2. This system will document the gross three-dimensional structure and evolutionary characteristics of convective systems, and will thereby fulfill some of the scientific data requirements outlined in Sections 3.2 and 3.3. Specifically, the RADAP data will provide (a) a source of verification in the special programs relating satellite observables and precipitation within clouds (Section 3.3); and (b) estimates of instantaneous and total precipitation needed for cloud water budget studies.

NCAR's CP-2 multiparameter radar (Fig. 4.3.2) will function as a second large-scale scanning radar and will provide invaluable high-resolution information on cloud horizontal and vertical structure. Its dual wavelength and dual polarization capability allow inferences on precipitation size and phase (e.g. Doviak and Zrnic, 1984). This microphysical information, in conjunction with CP-2's Doppler capability, will supply valuable data on convective cloud internal structure. The CP-2 data, combined with other remote sensing and in situ measurements, will allow investigators to address specific scientific questions regarding relationships between electrical activity and microphysics within clouds (Section 3.3).

The meso-gamma scale MIST/FLOWS Doppler radar network (Fig. 4.3.3) will provide information on cloud and planetary boundary layer structure over a 65 km by 50 km region over the southern SPACE network. Although these radars will be controlled by MIST/FLOWS PI's during field operations, it is expected that valuable high resolution data on cloud internal flow structure will be available to SPACE researchers. Analyses of these data will document internal structures of convective clouds and relate convective cloud flows to measured or inferred microphysical processes and electrical activity.

It is also over the MIST/FLOWS mesonet that detailed multiple Doppler scans of PBL structure (section 3.1) will be conducted. Such Doppler analyses will provide detailed information on PBL flows (e.g., Kropfli and Hildebrand, 1980) and on horizontal/vertical variability in these flows. Thus, these observations will provide some ground truth check on the planned mesoscale numerical modeling activities outlined in section 3.1.

#### 4.4 Surface Network

The combined surface network under the COHMEX program is probably one of the most extensive networks ever utilized in a field program. Section 5.4 gives a detail description of the locations and operation of the network. In general, the network can be divided into two sections. The first is a sub-cloud scale network located in the MIST observing area with surface station spacing on the order of 2 km. The second is a larger scale surface network (meso-beta) encompassing the upper air rawinsonde network with spacing on the order of 75 km.

The surface networks will provide surface estimates of mass, moisture and momentum convergence in support of budget and diagnostic studies of convection and numerical model evaluations (sections 3.2 and 3.4) The surface network will complement the rawinsonde network in that the surface stations will provide almost continuous time coverage of pre-storm and storm convergences compared to the three-hour intervals from the rawinsondes. The surface wind information will also be extremely useful in describing interaction of outflow among the larger scale convective systems leading to mergers or new convection (section 3.5).

The surface temperature and moisture measurement at the sites will provide ground truth support of the aircraft and satellite based sensors for skin temperature and low level moisture. The PAM sites will also be providing data in real-time to assist in direction of other observing systems.

One of the unique aspects of the meso-beta network is the addition of pyranometers (for measuring global and diffuse radiation) to the normal complement of wind, temperature and moisture sensors. The pyranometer measurements will allow better evaluation of surface energy budgets in the numerical models as well as address boundary layer forcing mechanisms such as cloud shading.

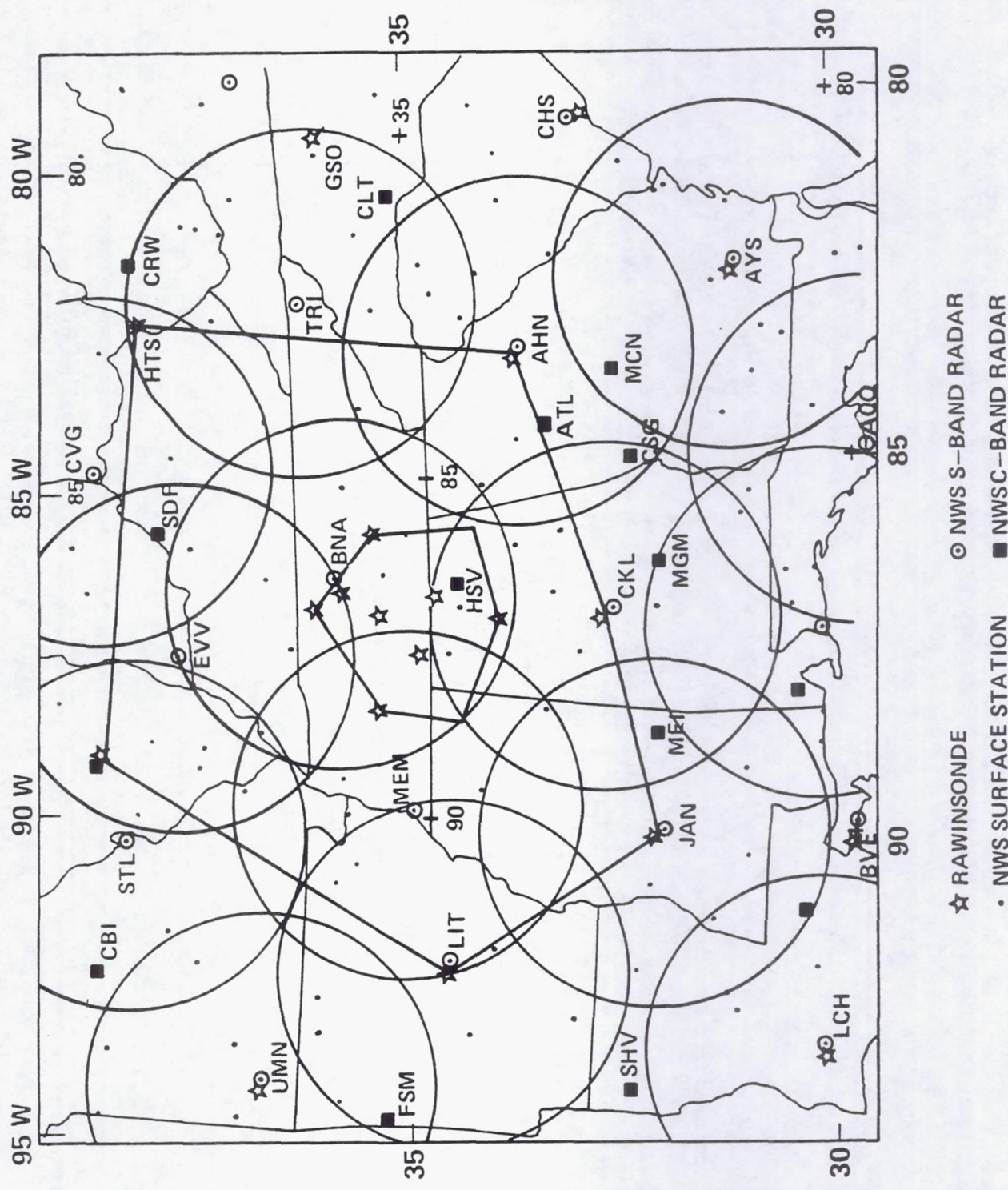
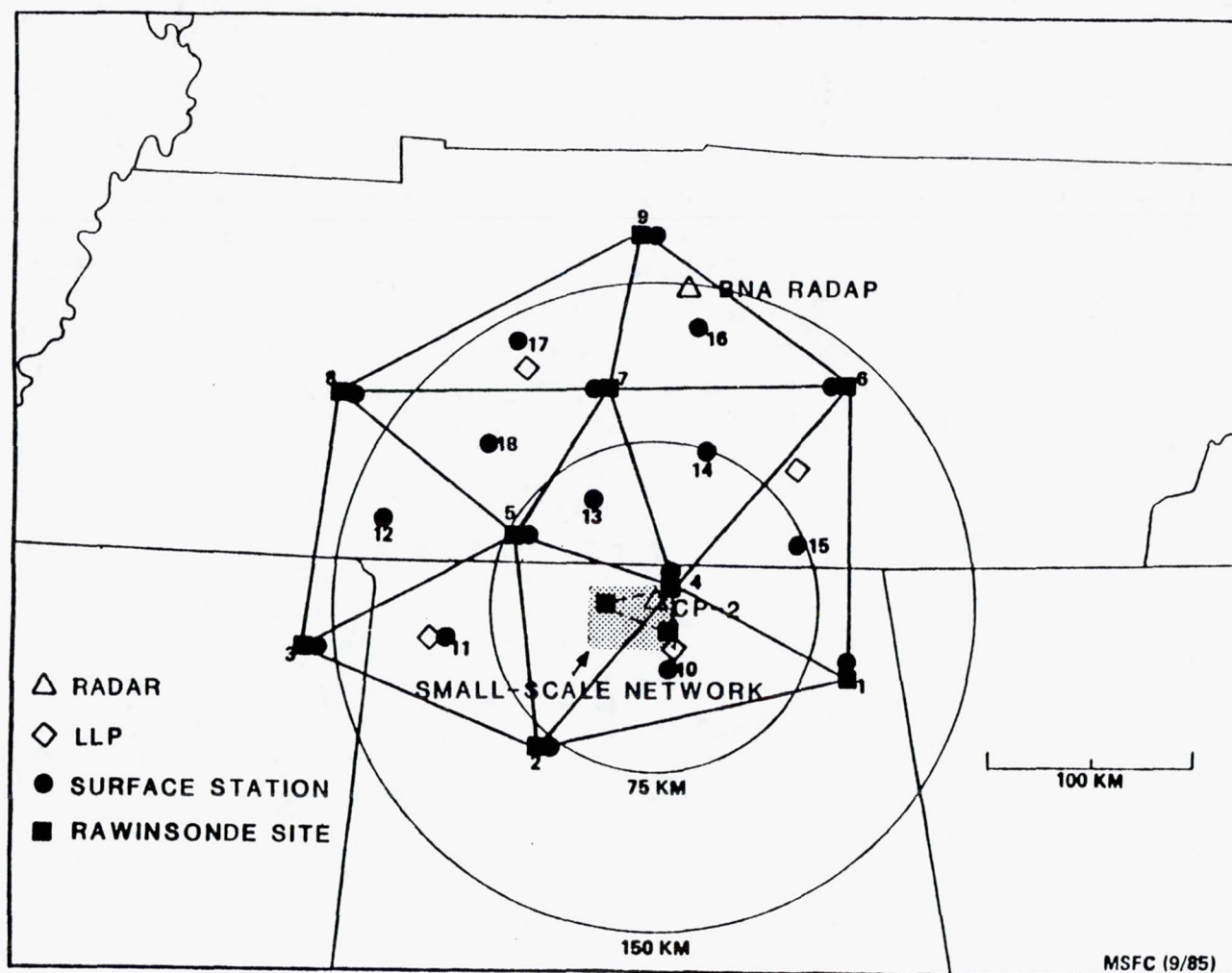


Fig. 4.3.1. Locations of National Weather Service radars relative to the SPACE meso-alpha and meso-beta observational networks.



**Fig. 4.3.2.** Locations of designated large-scale scanning radars BNA and CP-2 relative to the SPACE meso-beta observational network.

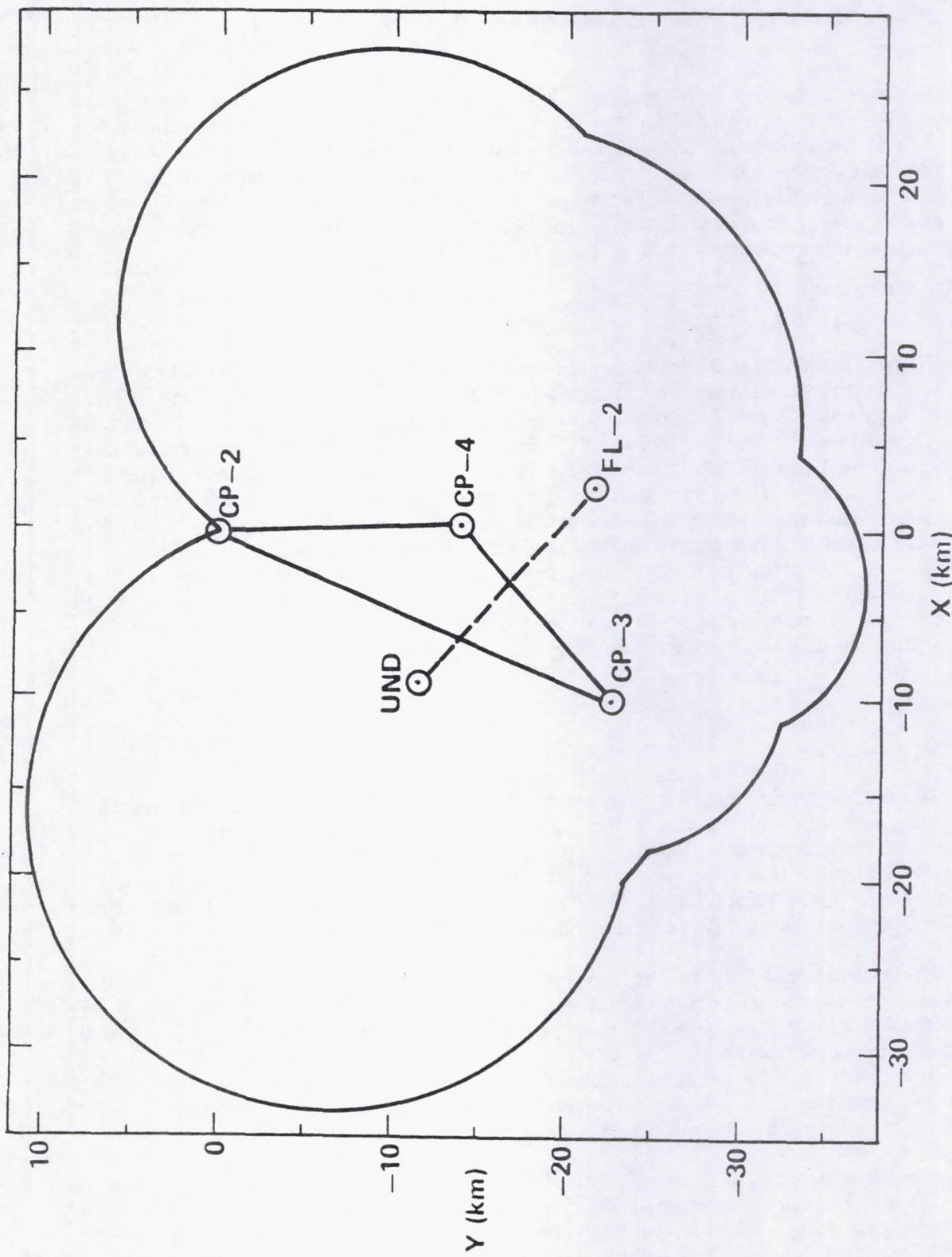


Fig. 4.3.3. Effective area of multiple Doppler radar coverage, defined by 45-deg beam intersections of various dual Doppler combinations. This meso-gamma region is stippled in Fig. 4.3.2.

## 5.0 SPECIAL OBSERVING PROGRAMS AND FACILITIES

The core of the COHDEX program is the special temporal and spatial observations which will be made. Some of the observing facilities are unique in their scale and magnitude such as the number of Doppler and special radars which will be employed or the number of surface mesonet stations. Other systems such as the remote sensors are unique in that they are innovative pieces of hardware which may provide insight into convective processes not here-to-fore available. The following sections list and discuss the special observing systems to be operating under SPACE and COHDEX.

### 5.1 Aircraft Systems

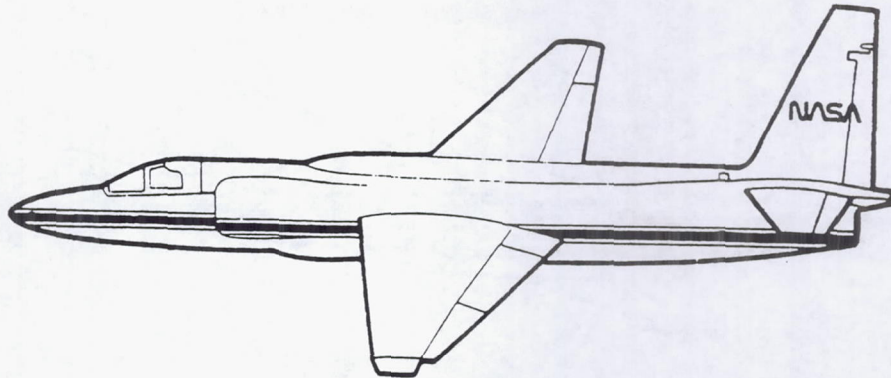
There are a number of instrumented aircraft participating in the COHDEX field program. The aircraft primarily associated with the NASA/SPACE portion of the experiment are the South Dakota School of Mining and Technology (SDSM&T) T-28 and the NASA/Ames Research Center (NASA/ARC) ER-2 and U-2C. The high altitude ER-2 and U-2C aircraft will provide cloud top observations of storm structure, precipitation, and lightning during active thunderstorms, and temperature and water vapor soundings of the pre-storm environment. The T-28 will provide in situ hydrometeor observations, electric field measurements, and standard meteorological observations during penetrations into thunderstorms. The specifications and instrumentation on these aircraft platforms will be briefly reviewed in sections 5.1.1 - 5.1.3. Other aircraft which may participate in the COHDEX field program are two NOAA P-3's, the University of North Dakota Citation, the FAA Convair 580, and the Colorado State University Cessna 207.

#### 5.1.1 NASA/ARC ER-2

The NASA/ARC ER-2 is a high altitude aircraft which will overfly thunderstorms and/or take soundings during COHDEX. Deployment of the ER-2 will begin on June 2 and continue for six weeks following the first flight which will probably occur around June 4-6. During the first three weeks, the ER-2 operations will be directed by NASA/Goddard Space Flight Center (GSFC), while NASA/Marshall Space Flight Center (MSFC) will control the operations during the second three weeks period.

The general specifications of the ER-2 are outlined in Figure 5.1.1a. Two large wing pods (known as super pods), a small pod, and a nose cone area, along with the Q-bay instrumentation area allow the ER-2 to be extensively instrumented. This capability is being utilized to great advantage for the COHDEX field program. Table 5.1.1a lists the sensor systems that will be installed on the ER-2 during the two periods and Figure 5.1.2 shows the locations of these instrument packages on the aircraft platform. All of these sensor systems are described in detail in section 2 of this report.

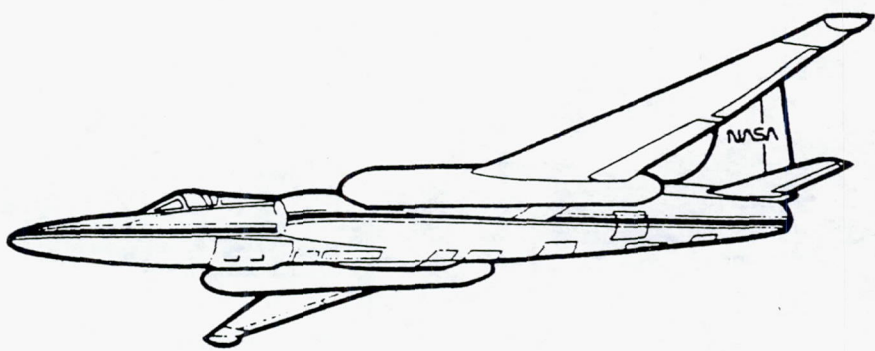
The ER-2 will be based out of Wallops Island, Virginia for the entire deployment, so that it will require approximately 1 hr. 40 min. to reach the SPACE operations area. Two examples of pre-storm flight patterns are shown in Figures 5.1.3 (a) and (b). Figure (c) illustrates "target of opportunity" flight lines or tracks employed in overflying active thunderstorm. Specific details on the operations of the ER-2 (and U-2C) aircraft during COHDEX can be found in the COHDEX High Altitude Aircraft Operations Plan.



## U - 2 C Specifications

<b>Description:</b>	Crew: One Pilot Length: 49 feet, 9 inches Wingspan: 80 feet, 2 inches Engine: One J75-P-13B Base: Ames Research Center, Moffett Field, CA
<b>Performance:</b>	Altitude: 65,000 feet (Cruise), 70,000 feet (Maximum) Range: 2500 nautical miles Duration: 6.5 hours Speed: 392 to 400 knots True Air Speed Payload: 750 lb Q-bay; 100 lb. Canoe; 300 lb. Wing Pods
<b>Accommodations:</b>	Q-Bay Instrumentations Area and Payload Pallets (Pressurized) Wing Mounted Instrumentation Pods (Unpressurized) Nose Cone Instrumentation Area (Unpressurized) Zenith and Nadir Viewing Capability
<b>Support:</b>	Inertial Navigation Time Code Generator

Fig. 5.1.1b. General specifications of the U-2C.



## ER-2 Specifications

<b>Description:</b>	Crew: One Pilot Length: 62 feet, 1 inch Wingspan: 103 feet, 4 inches Engine: One Pratt and Whitney J75-P-13B Base: Ames Research Center, Moffett Field, CA
<b>Performance:</b>	Altitude: 70,000 feet (Cruise) Range: 3000 nautical miles Duration: 8 hours (Nominal 6.5 hours) Speed: 410 knots True Air Speed Payload: 600 lb. Nose; 750 lb. Q-bay; 1500 lb. Wing Pods
<b>Accommodations:</b>	Q-Bay Instrumentations Area and Payload Pallets (Pressurized) Wing Mounted Instrumentation Pods (Pressurized) Nose Cone Instrumentation Area (Pressurized) Zenith and Nadir Viewing Capability
<b>Support:</b>	Inertial Navigation Time Code Generator

Fig. 5.1.1a. General specifications of the ER-2.

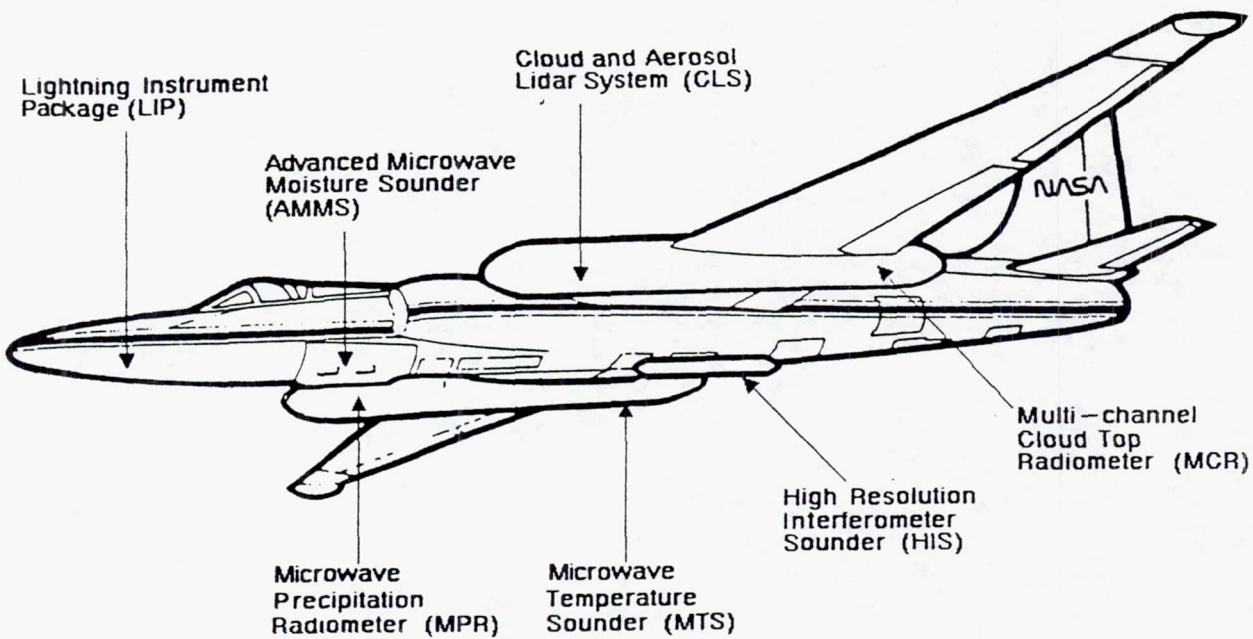
(a) Aircraft Instrument Systems : NASA ER-2

	<u>SENSOR</u>	<u>MEASUREMENT</u>
First Period (under GSFC direction)	Cloud and Aerosol Lidar System (CLS)	Cloud top structure, Tropospheric structure
	Multi-channel Cloud Top Radiometer (MCR)	Cloud top temperature, microphysics, structure (visible and IR channels)
	Microwave Temperature Sounder (MTS)	Temperature soundings (118 GHz)
	Advanced Microwave Moisture Sounder (AMMS)	Moisture soundings, precipitation (90, 183 GHz)
	Microwave Precipitation Radiometer (MPR)	Precipitation (18, 37 GHz)
	High Resolution Interferometer Sounder (HIS)	Temperature and moisture soundings
	Lightning Instrumentation Package (LIP)	Lightning imaging, optical pulse emissions, electric field changes
	Vinten Time Lapse Cameras	Cloud top and lightning imaging
Second Period (under MSFC direction)	MTS	
	AMMS	
	MPR	
	HIS	
	LIP	
	Vinten	
	Multispectral Atmospheric Mapping Sensor (MAMS)	Water vapor, cloud and surface imaging (visible and IR channels)

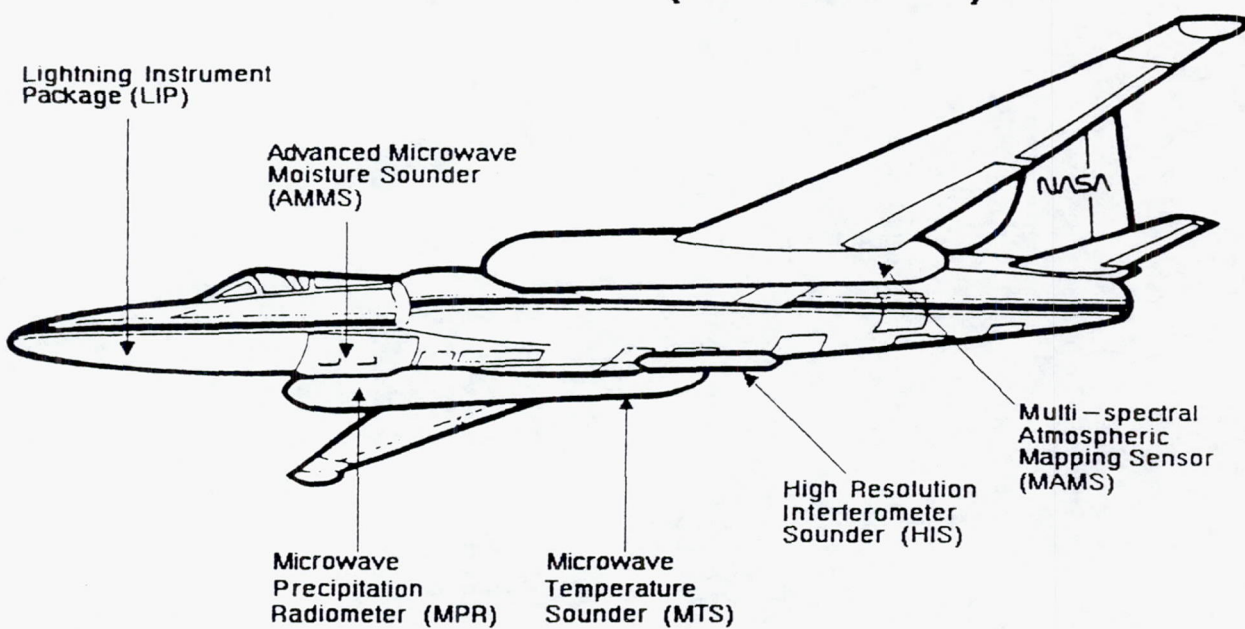
(b) Aircraft Instrument Systems : NASA U-2C

	<u>SENSOR</u>	<u>MEASUREMENT</u>
Storm Configuration	Lightning Research Package	Electric fields and field changes, conductivity, optical pulse emissions, lightning spectra, lightning and cloud imaging
Pre-storm Configuration	Multispectral Atmospheric Mapping Sensor (MAMS)	Water vapor, cloud and surface imaging (visible and infrared channels)
	High Resolution Interferometer Sounder (HIS)	Temperature and moisture soundings

Table 5.1.1. (a) The sensor systems installed on the ER-2 during the first and second observational period. (b) The configuration of instrument systems for the U-2C.



**ER – 2 Platform (First Period)**



**ER – 2 Platform (Second Period)**

Fig. 5.1.2. The location of remote sensor instrument packages on the ER-2 during the first and second observing periods.

17

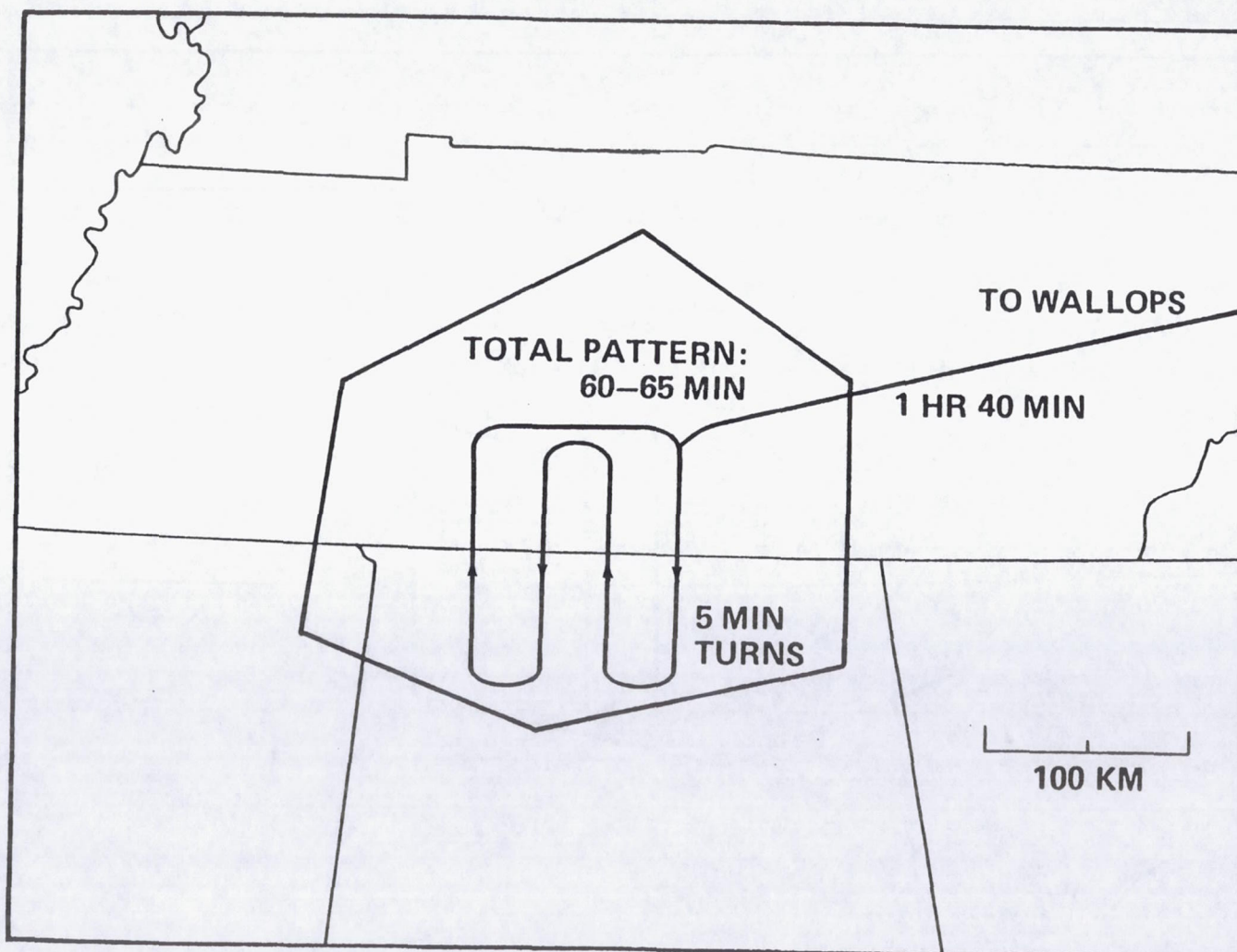


Fig. 5.1.3a. Possible pre-storm flight pattern for use with MAMS and HIS.

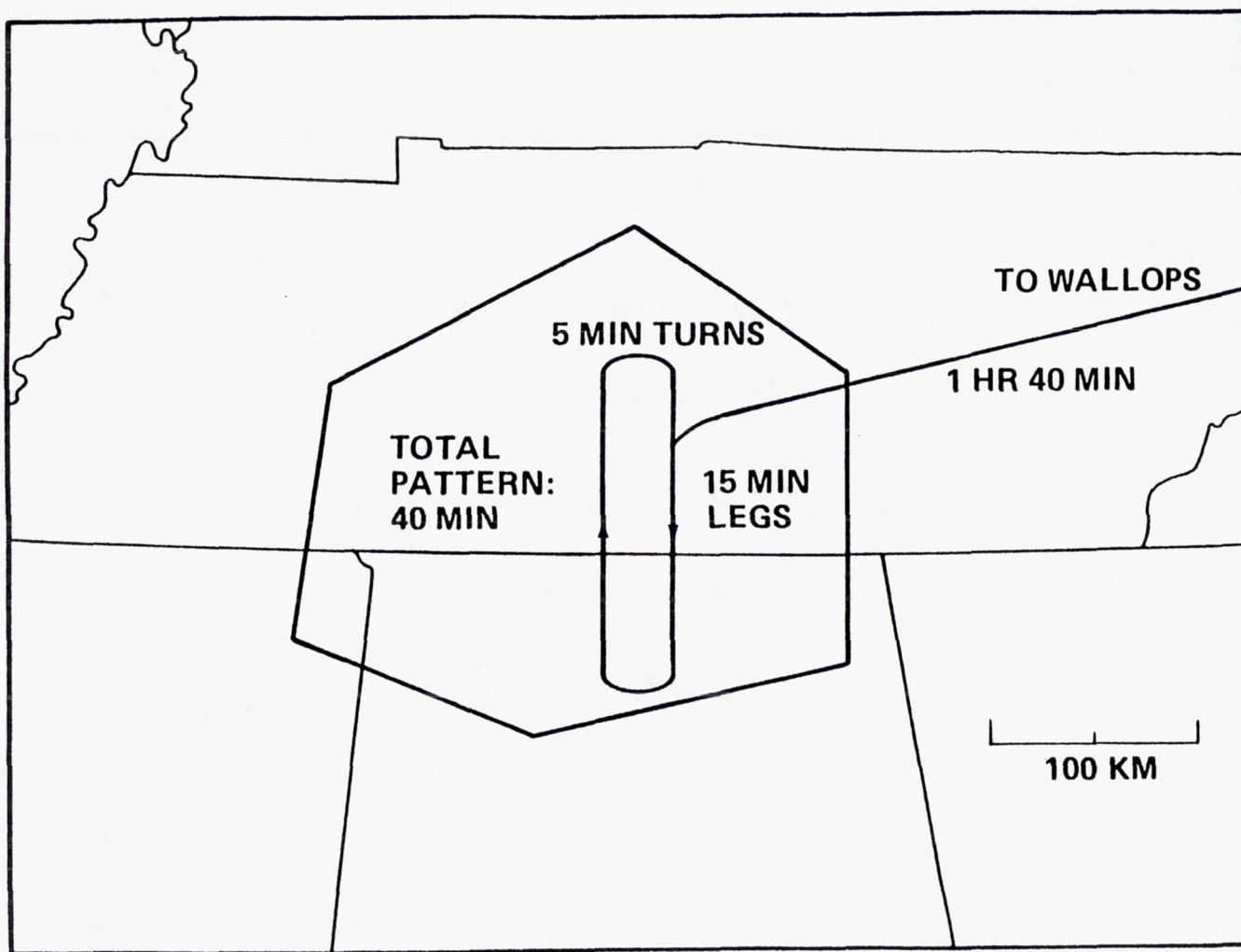


Fig. 5.1.3b. Pre-storm "racetrack" flight pattern for MAMS and HIS.

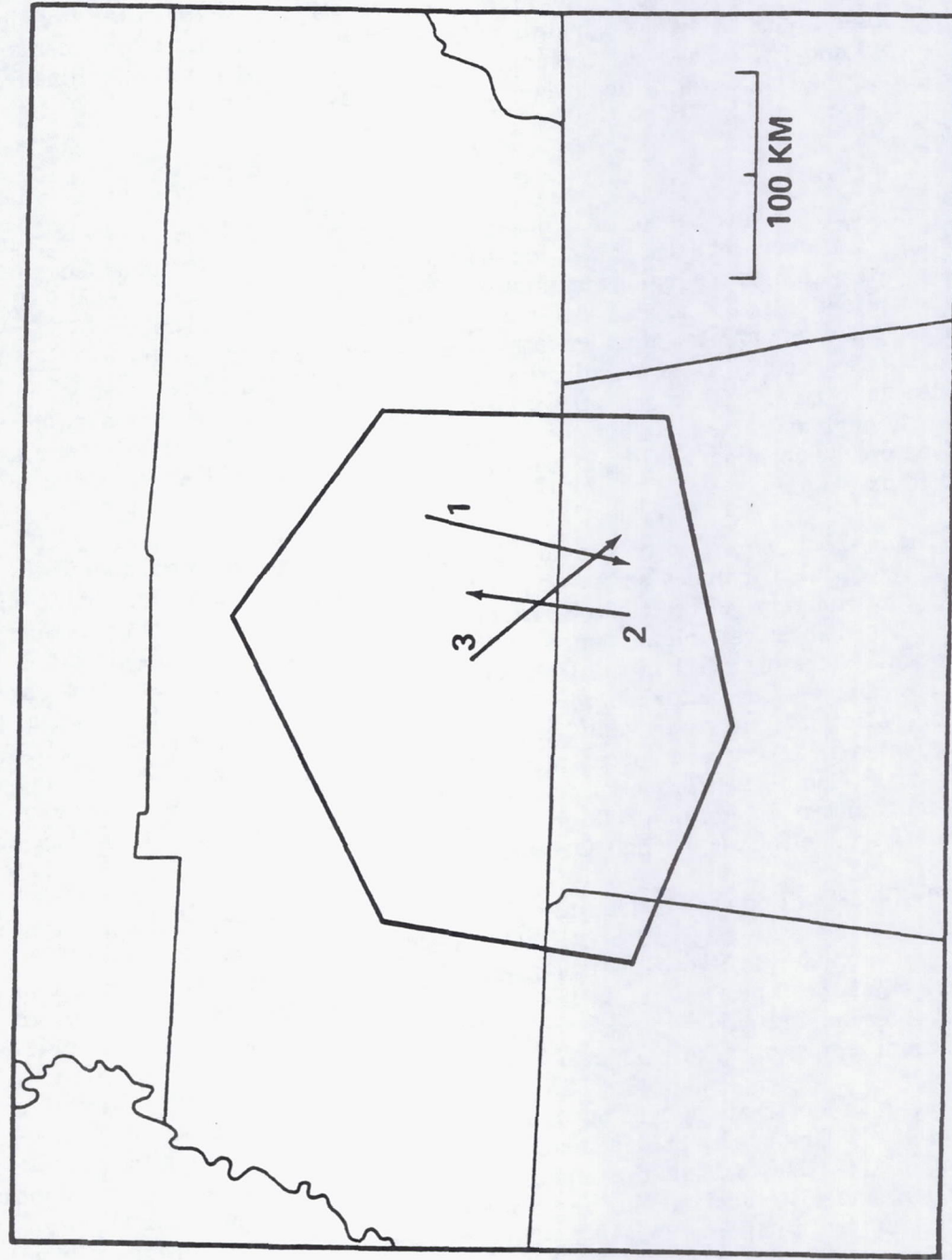


Fig. 5.1.3c. Example of three storm "target of opportunity" flight lines.

### 5.1.2 NASA/ARC U-2C

One, perhaps two, U-2C aircraft will also be deployed for six weeks starting June 2 during which time the flight operations will be under the direction of MSFC. Figure 5.1.1b outlines the specifications of the U-2C. The U-2C has a Q-bay instrumentation area and supports the small pod, therefore, the aircraft will be configured for either thunderstorm electrical observations using the Lightning Research Package or pre-storm measurements using MAMS and HIS. Table 5.1.1b summarized these two configurations. Finally, just as for the ER-2, the U-2C will be deployed from Wallops Island, Virginia.

### 5.1.3 T-28

The South Dakota School of Mines and Technology T-28 (Fig. 5.1.3) is a single engine military trainer that has been modified, armored, and instrumented to permit measurements within active regions of thunderstorms. The aircraft is capable of flights of about 2 hours duration and can operate effectively at altitudes up to 6-7 km MSL. Meteorological directions for thunderstorm penetrations are provided by a ground-based meteorologist working in close coordination with the pilot. Flights have intentionally been performed in regions with radar reflectivity factors up to 55 dBz without substantial damage, although airframe icing has occasionally required that the aircraft descend to melt the ice before performing additional penetrations. Lightning strikes have caused little concern in past flights.

The T-28 is equipped to provide data as described by Johnson and Smith (1980). The data system now includes an on-board minicomputer to control the data acquisition and recording functions. The research instrumentation consists of sensors to measure basic aircraft performance variables, atmospheric state variables, vertical velocities, and hydrometeors. Measurements in the first three categories include: temperature, pressure, aircraft position, heading, and airspeed. Hydrometeor measurements include: cloud liquid water concentration (hot wire), cloud droplet sizes and concentrations (PMS FSSP), and precipitation particle sizes and concentrations (foil impactor, PMS 2D-C Probe, and a hail spectrometer). Combined size measurements from these sensors cover a range from 3 to 50 microns in diameter. In addition field mills furnished by NASA will be installed on the T-28 for the first time for use during COHDEX.

The T-28 will be used to acquire a data set of observations from the interiors of mature thunderstorms during the 1986 COHDEX field program. The specific data set to be acquired will include: 1) Hydro-meteor spectra from cloud droplet through hailstone sizes, 2) vertical wind speed profiles across the storms, and 3) electric field measurements from the storm interiors and environment. Also available are observations of cloud liquid water concentration, temperature, turbulence and other quantities.

The T-28 observations will be useful for supporting many tasks under the general objectives of SPACE such as: (1) Understanding the processes controlling the production of precipitation; (2) Describing the structure of small convective systems producing precipitation; and (3) Understanding the interrelationships between electrical activity and the process of precipitation. In MIST, they may prove vital in determining whether or when microbursts are driven by evaporation or by precipitation loading and cooling (due to melting). The observations would also provide supporting data for the remote sensor experiments involving MAMS, AMPR and LIP. Finally, they will be important in providing checks for Doppler radar observations and numerical modeling results during the analysis phase of the project.

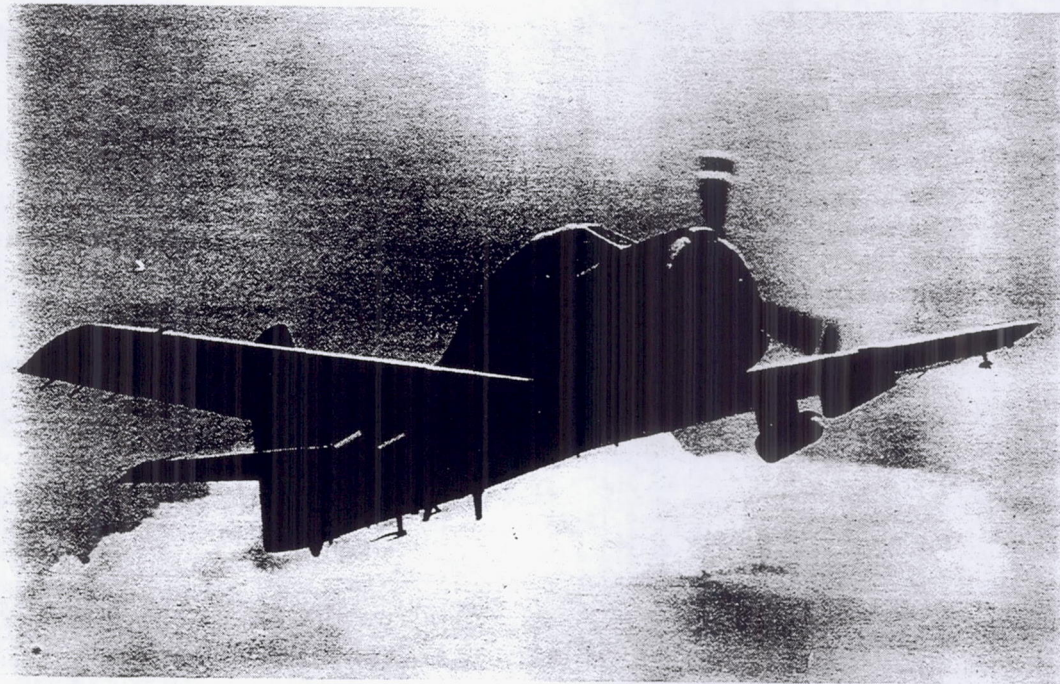


Fig. 5.1.3. A photograph of the T-28 which will be flown during SPACE.

## 5.2 Radar Systems

The radar systems (see fig 4.3.2 and 4.3.3 for location) will perform a variety of tasks during the SPACE field program. The primary function will be to document the small-scale and large-scale precipitation structure of convective systems. Doppler radars will additionally provide air motion information within precipitating clouds, and within the prestorm clear air PBL. Specific tasks performed by each individual radar system are elucidated below.

### 5.2.1 RADAP II/ICRAD

The NWS radar located in the northern SPACE region at BNA (Fig. 4.3.2) will be equipped with an updated Radar Data Processor, or RADAP II. The equipment comprising RADAP II consists of the BNA WSR-57 radar system, the RADAP II processing system, and interfacing devices. The heart of the RADAP II processing system is a Data General NOVA series minicomputer with 32,000 words of memory. The computer receives radials of radar data from the Digital Video Integrator and Processor (D/VIP) via the Isolation Distribution Equipment (IDE) and translates the 8-bit values into internal RADAP II levels ranging from 0 to 15. It then processes the data into various products, archives the radial data, and outputs the products either automatically or on command.

Data are then transferred to an Interactive Color Radar Display (ICRAD) processor located at NASA/MSFC for display. ICRAD consists of a Northstar Horizon microcomputer having one 5-1/4 in floppy and one 15 Mbyte Winchester hard disk, a set of color graphics generator boards (6 bit planes, 512 by 480 pixels per plane), a color monitor and a keyboard for operator I/O.

RADAP II acquires observations at some base elevation every 10 min. These observations consist of reflectivity intensity and its by-products, separated by every 2 deg in azimuth and 1 n mi in range from 10 n mi to 125 n mi. Additionally, RADAP II is capable of conducting a tilt sequence volume scan (every 10 min) in which elevation is incremented every 2 deg starting from base up to 22 deg. These data are then processed to produce maps of echo height, vertically-integrated liquid water, storm structure and estimates of severe weather probability.

The ICRAD option allows enhanced color graphics display of all RADAP II products. Some options include time lapse looping, overlaying of two products, and determination of echo movements.

### 5.2.2 Kavouras

Additional information on large-scale precipitation patterns will be provided at NASA by a Kavouras RADAC system, which allows user access to real-time color radar displays from any one of the NWS radars included in Fig. 4.3.1. Although such information will be most valuable for nowcasting and operational decision-making purposes, displays can be stored as images on disk, or on video tape, and later used as first-look analysis products. Microfilm from each NWS radar site, available from NCDC, will probably serve as the primary source for construction of large-scale radar data composites.

### *5.2.3 CP-2*

The NCAR CP-2 radar is a dual-wavelength, dual polarization system capable of measuring several parameters (Table 5.2.1) which include Doppler velocity, reflectivity factor (S-and X-band) differential reflectivity, X-band depolarization ratio, and dual-wavelength ratio. Such measurement capabilities make CP-2 a valuable tool to remotely sense general characteristics of precipitation, including precipitation phase, concentration, general size and shape. Characteristics of CP-2 radar hardware are given in Table 5.2.2.

CP-2 measurements can be acquired in one of two modes, Doppler or multiparameter. In the Doppler mode, recorded parameters include X-and S-band reflectivity factor, Doppler velocity and Doppler variance. In the multiparameter mode, additional parameters shown in Table 5.2.1 are recorded, but both the scanning rate and Nyquist velocity are reduced to half.

General usage of CP-2 will involve sector scanning in the multiparameter mode, with two general scenarios likely. The first will involve complete scanning over some sector including a storm or set of storms, possibly being probed by aircraft. The second will involve closer coordination with other Doppler radars scanning cells over the MIST network. For both scenarios, it is desirable to scan the entire cloud depth from ground to cloud tops.

### *5.2.4 Other Doppler Radars*

Four other Doppler radars (two pairs) will scan storms primarily within the small-scale MIST/FLOWS region. Radar characteristics and recorded parameters are given in Tables 5.2.1 and 5.2.2. Although each pair will be controlled independently, some degree of scanning coordination will occur. The NCAR Doppler pair (CP-3, CP-4) will typically be coordinated with CP-2 to conduct scans of convective clouds within or near the Doppler network. Such scans will by necessity have greatest resolution in the lowest several kilometers. The FLOWS radars will similarly focus on resolving thunderstorm outflows at low levels, in addition to conducting NEXRAD-type full volume scans. In order to fully satisfy the SPACE scientific objectives, it would be highly desirable to uniformly sample storms, from ground to cloud top, with cycle times of 4 min or less.

Table 5.2.1 Recorded (R) and displayed (D) data fields  
from each Doppler radar

Data type	CP-2					
	S-band	X-band	CP-3	CP-4	FL-2	UND
Log power, hzn	R,D	R,D	R,D	R,D	R,D	R,D
Differential log power	R,D	-	-	-	-	-
Linear depolarization	-	D	-	-	-	-
Log power, vertical	-	R,D	-	-	-	-
Linear power, hzn	R,D	-	-	-	-	-
Coherent power, hzn	R,D	-	-	R	R,D	-
velocity, hzn	R,D	-	R,D	R,D	R,D	R,D
velocity, vrt	R,D	-	-	-	-	-

Table 5.2.2 Doppler radar hardware and recording characteristics

Parameter	CP-2	CP-3/4	FL-2	UND
Wavelength (cm)	10.68/3.20	5.45(5.49)	10.6	5.38
Peak power (kw)	1000/23	400	1100	250
Pulse duration ( s)	1.0	1.0	-	-
Average power (w)	960/73	250	-	-
Pulse repetition freq. (Hz)	750-1500	750-1667	700-1200	250-1100
Antenna diameter (m)	8.53/2.5	3.66	8.53	3.66
System gain (dB)	42.2/44.5	41.0/42.4	-	-
Beamwidth (deg)	0.97/0.95	1.02(1.11)	0.97	0.99
Noise power (dBm)	-110/-93	-109	-107	-
Minimum reflectivity at 25 km (dBZ )	-22/-17	-12	-19	-12
No. samples	32 - 1024	32 - 512	-	32-128
No. range gates	256 - 1024	512	-	-
Azimuth scan rate (deg/s)	0-18	0-27	-	0-24
Elevation increment (deg)	0.1	0.1	-	-
Range gate spacing (m)	50 - 2000	150 - 2000	-	-
Pulse width ( s)	.2-1.5	1.0	0.65	0.6
Pulse repetition period	1042	800	-	-
Max. unambiguous range (km)	156	120	-	-
Max. unambiguous velocity (m/s)	25.7	19.5	-	-

### **5.3 Sounding Systems**

Soundings will be taken from a combination of three rawinsonde networks, as shown in Figure 5.3.1. The details in the operation of each network are described below.

#### *5.3.1 Meso-Alpha Rawinsonde*

The meso-alpha rawinsonde network consists of seven (7) existing NWS stations in the SPACE operational area as shown in Figure 5.3.1. Station spacing for this network is approximately 400-500 km. These stations, identifiers, and locations are listed in Table 5.3.1. Radiosondes will be released at 3-h intervals on five operational days during the period April 15 through June 30. Special soundings will be taken from 1500 to 0600 GMT on operational days. In addition to these special soundings, standard NWS soundings taken at 0000 and 1200 GMT will be processed and archived to the data base. A lead time of at least 24 hours is required to activate this network.

#### *5.3.2 Meso-Beta Rawinsonde*

The meso-beta-scale rawinsonde network consists of nine special NASA stations located in Central Tennessee, Northern Alabama, and Northeastern Mississippi as shown in Figure 5.3.2. The spacing of these stations is approximately 100-150 km. These stations, identifiers, and locations are listed in Table 5.3.2. Radiosondes will be released at 3-h intervals from 1500 to 0300 GMT on approximately 20-25 operational days during the period April 15 through July 31. At least eighty percent of these operational days are expected during the period June 1 through July 31. The operation of this network will remain quite flexible to permit extended operation or early termination due to evolving conditions or circumstances. Partial network operation or 1 1/2 hour soundings may be initiated and terminated as dictated. A lead time of twelve to twenty-four hours are required to activate this network.

#### *5.3.3 Meso-Gamma Rawinsonde*

The meso-gamma-scale rawinsonde network consists of three stations: a special NASA station, an existing station operated by the US Army, and a meso-beta network station. The station spacing for this network is approximately 40-50 km. These stations surround the MIST/ FLOWS radar and mesonet stations and are shown in Figure 5.3.3. These stations, identifiers, and locations are listed in Table 5.3.3. Radiosondes will be released at 3-h or 1 1/2-h intervals for approximately eight operational days during the period June 1 through July 31. The operation of this network is solely dictated by convective activity within the MIST/FLOWS area, and will be initiated or terminated with relatively short notice. Activation time for this network is 2-3 hours.

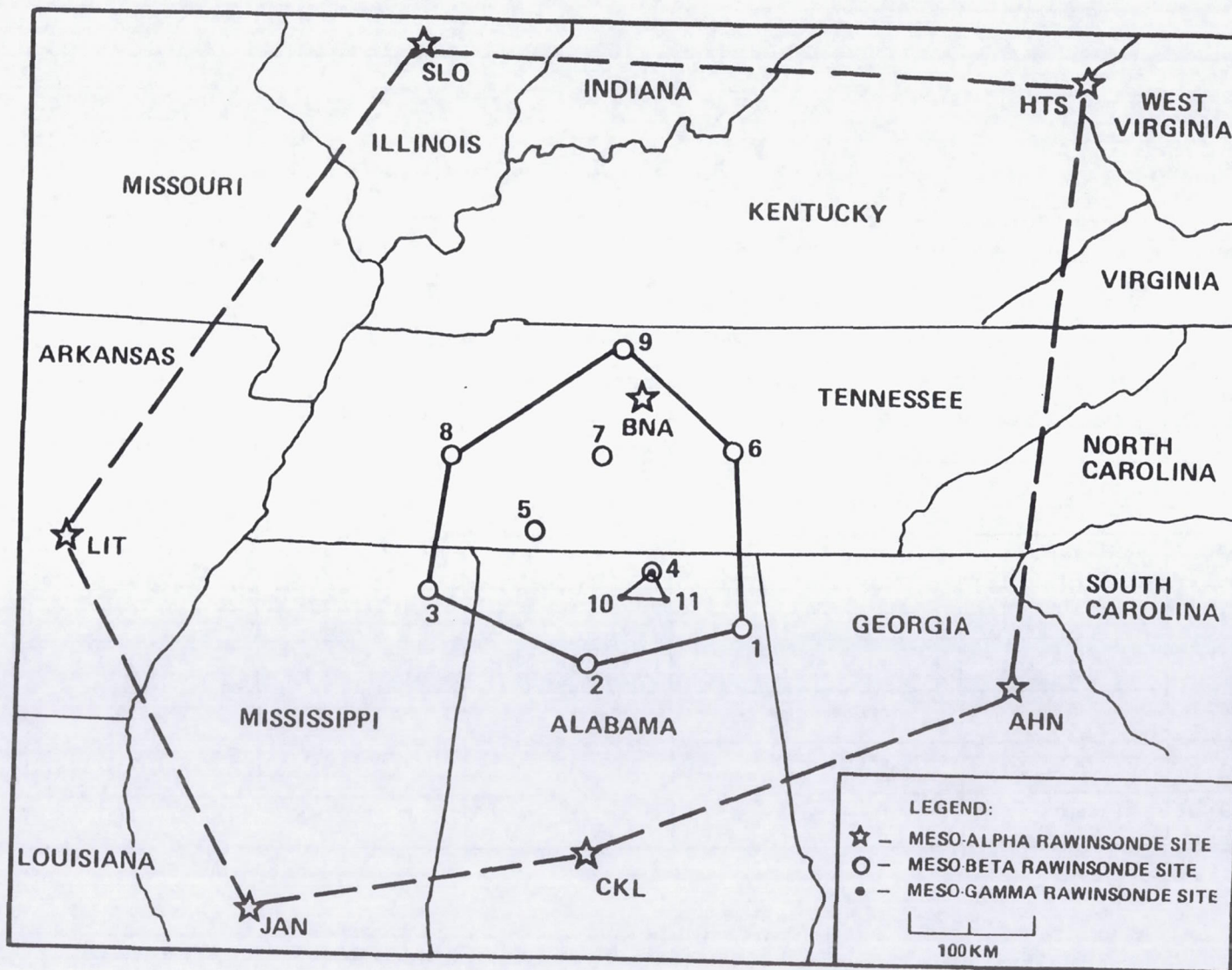


Fig. 5.3.1. The SPACE rawinsonde sounding network.

Table 5.3.1 SPACE MESO-ALPHA RAWINSONDE STATION LOCATIONS

SITE NO.	SITE IDENTIFIER	LOCATION	LATITUDE	LONGITUDE	ELEVATION FT (M) Above MSL
72229	CKL	Centerville, AL	32° 00' 00"	87° 13' 48"	459 (140)
72235	JAN	Jackson, MS	32° 19' 48"	90° 04' 48"	328 (100)
72311	AHN	Athens, GA	33° 56' 24"	83° 19' 12"	807 (246)
72327	BNA	Nashville, TN	36° 15' 00"	86° 34' 12"	590 (180)
72340	LIT	Little Rock, AR	34° 44' 24"	92° 14' 24"	260 (79)
72425	HTS	Huntington, WV	38° 21' 36"	82° 32' 24"	807 (246)
72433	SLO	Salem-Leckrone, IL	38° 39' 36"	88° 58' 48"	574 (175)

83

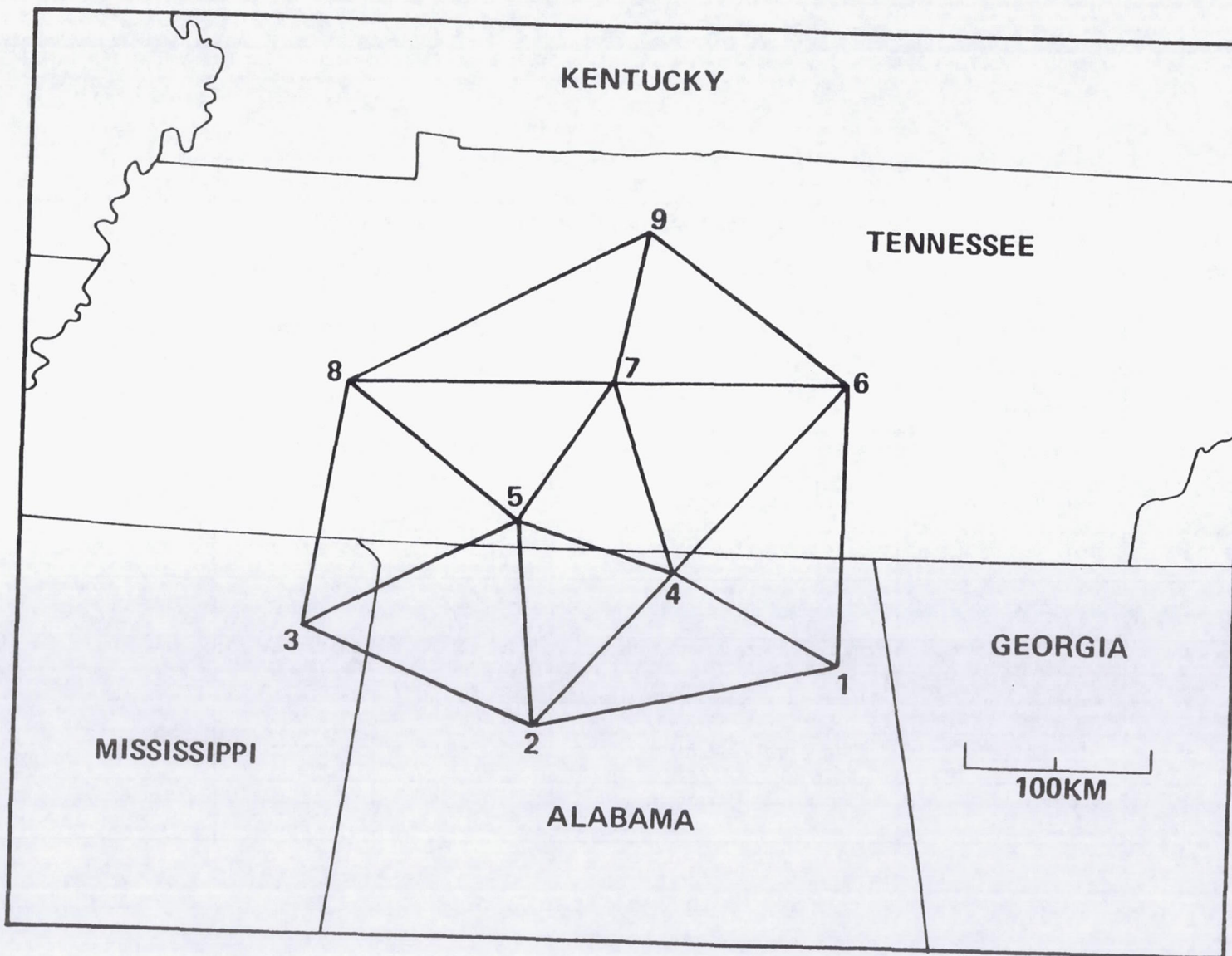


Fig. 5.3.2. The SPACE meso-beta scale rawinsonde sounding network.

Table 5.3.2 SPACE MESO-BETA RAWINSONDE STATION LOCATIONS

SITE NO.	SITE NAME	LOCATION	LATITUDE	LONGITUDE	ELEVATION FT (M) Above MSL
1	Rainsville, AL	Private Residence	34° 27' 24"	85° 51' 39"	1230 (375)
2	Double Springs, AL	Winston County Airport	34° 08' 37"	87° 20' 16"	750 (229)
3	Booneville, MS	Booneville/Baldwyn Airport	34° 35' 37"	88° 38' 52"	385 (117)
4	Hazel Green, AL	Private Residence	34° 52' 02"	86° 42' 27"	815 (248)
5	St. Joseph, TN	St. Joseph Airstrip	35° 01' 33"	87° 28' 49"	810 (247)
6	McMinnville, TN	Warren County Airport	35° 42' 12"	85° 50' 21"	1040 (317)
7	Columbia, TN	Middle Tennessee Agricultural Exper. Station	35° 42' 55"	86° 57' 48"	722 (220)
8	Lexington, TN	Franklin-Wilkins Airport	35° 39' 05"	88° 22' 58"	505 (154)
9	Springfield, TN	Springfield Airport	36° 32' 40"	86° 55' 06"	710 (216)

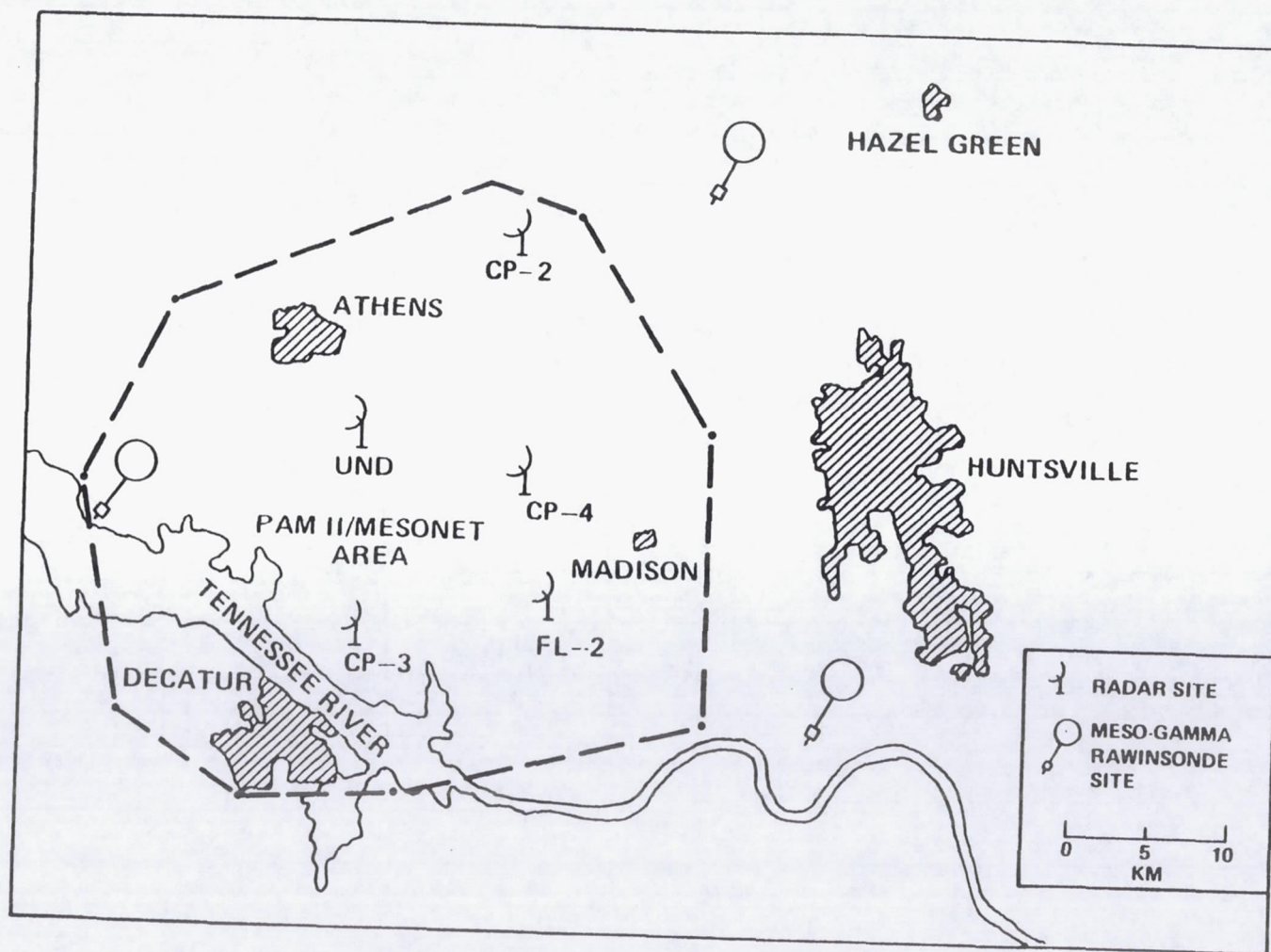


Fig. 5.3.3. The SPACE meso-gamma scale rawinsonde sounding network.

Table 5.3.3 SPACE MESO-GAMMA RAWINSONDE STATION LOCATIONS

SITE NO.	SITE NAME	LOCATION	LATITUDE	LONGITUDE	ELEVATION FT (M) Above MSL
4	Hazel Green, AL	Private Residence	34° 52' 02"	86° 42' 27"	815 (248)
10	Athens, AL	Private Residence	34° 42' 35"	87° 05' 22"	655 (200)
11	Redstone Arsenal, AL	Test Area I	34° 36' 36"	86° 37' 54"	570 (174)

## 5.4 Surface Mesonet Systems

A unique aspect of COHDEX will be the most dense network of surface mesonet stations ever assembled for a field experiment. Ninety-two mesonet surface stations will be incorporated within the COHDEX area, with seventy-four stations contained in an area of 1300 square km. Three types of surface mesonet stations comprise the network as described below.

### 5.4.1 Portable Automated Mesonet System (PAM II)

This second generation portable automated surface mesonet system (PAM II) was designed and built by NCAR to provide high time resolution measurements of standard meteorological variables. The configuration and dimensions of a PAM II station are shown by the schematic in Figure 5.4.1. Fifty stations in the SPACE/MIST experiment area will provide one-minute averages of pressure, temperature, dew point, wind velocity, and precipitation. In addition, nine of these stations located in the SPACE experiment area will provide one-minute averages of horizontal global insolation. Sensor type, accuracy, and resolution are given in Table 5.4.1.

The stations will transmit data via satellite to base stations at Boulder, Colorado and the MIST operations center in near real time. Remote displays of the network will be provided in SPACE and FLOWS operation centers as well. This real-time display of the network will assist directing aircraft, radar, and other operations as well as providing an operational status of each station for maintenance purposes.

Forty-one PAM II stations will be located in the MIST area as shown in Figure 5.4.2. Station spacings for this network will be on the order of 2-10 km. The coordinates of these locations are listed in Table 5.4.2. A second network of nine additional stations will be located within the SPACE meso-beta rawinsonde network as shown in Figure 5.4.2. For this network, station spacing is approximately 60 km. These locations are listed in Table 5.4.3. Because of the spatial scale variation between networks, a two-page real-time display will be available to monitor all fifty stations.

### 5.4.2 NASA Mesonet System (NAMS)

A network of nine NASA automated mesonet stations (NAMS) will be located within the SPACE experiment area. One station will be co-located at each meso-beta rawinsonde station as shown in Figure 5.4.2. Each station will record 5-min averages of temperature, dew point, wind velocity, peak gust, precipitation, horizontal direct insolation, diffuse insolation, and reflected surface insolation. Table 5.4.4 describes the types of sensors, accuracy, and resolution for each parameter.

The configuration dimensions of a NAMS station are shown in Figure 5.4.3. Data will be stored in a remote weatherproof designed data logger and downloaded to floppy disk using a portable Apple II-C personal computer. This data will be reviewed on-site for operational status, and transferred to the SPACE Operations Center for analysis and archiving.

### *5.4.3 FAA Mesonet Station Network*

Thirty FAA Mesonet Stations will be located in the MIST/FLOWS experiment area as shown in Figure 5.4.2. The locations and coordinates of these stations are given in Table 5.4.5. Station spacing for this network is on the order of 2-10 km. Each station will be recording 1-min averages of temperature, dewpoint, wind velocity, precipitation, and pressure. Table 5.4.6 lists sensor type, accuracy, and resolution. Data will be transmitted via satellite to the FLOWS Operations Center for review and archiving.

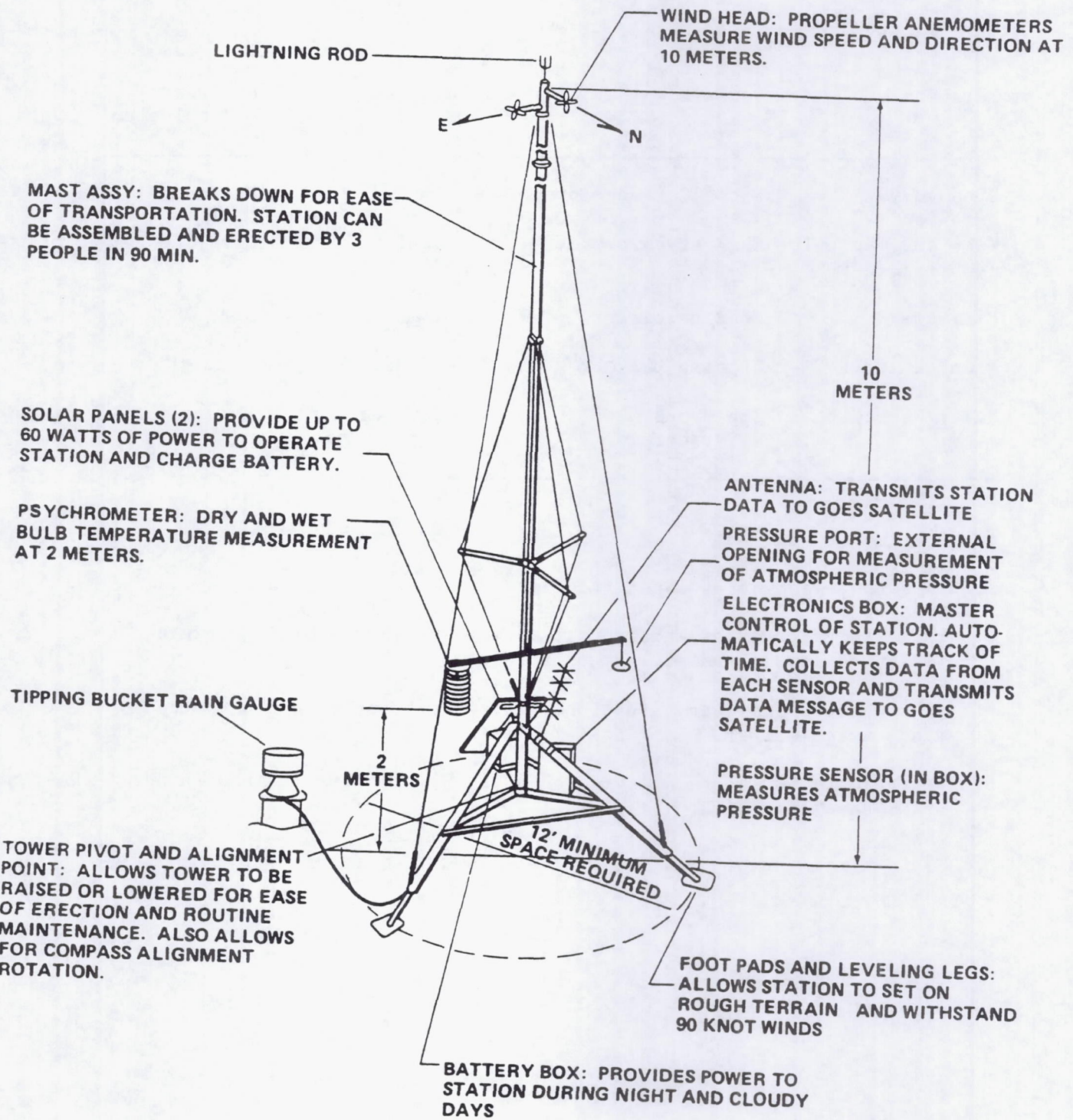


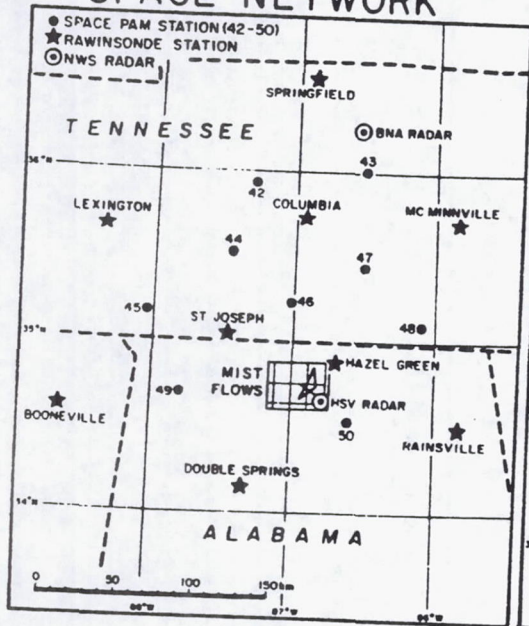
Fig. 5.4.1. Schematic of NCAR PAM tower and sensors.

Table 5.4.1 PAM II Mesonet Parameter Specifications

Parameter	Sensors	Accuracy <sup>1</sup>	Recorded Resolution
Wind (u,v)	Propeller anemometers	$\pm 1 \text{ m s}^{-1}$	$0.1 \text{ m s}^{-1}$
Wet- and wet bulb temperature	NCAR psychrometer	$\pm 0.25^\circ\text{C}$ <sup>2, 3</sup>	$0.05^\circ\text{C}$
Pressure	NCAR barometer	$\pm 1 \text{ mb}$	$0.02 \text{ mb}$
Precipitation	Tipping buckets	$\pm 15 \text{ percent}$ <sup>4</sup> ,	$0.25 \text{ mm}$
Solar Radiation <sup>5</sup>	Eppley PSP Pyranometer	$\pm 2.0 \text{ percent}$	$1 \text{ w m}^{-2}$

1. 2 sigma bounds.
2. This is an estimate. Specific tests are in progress.
3. Plus radiation errors that at times may exceed 05. C depending on radiation levels and siting conditions.
4. Plus the 0.25 mm quantizing interval. The figures do not include wind caused errors.
5. Solar radiation to be measured on nine (9) stations located in the SPACE PAM II network.

## SPACE NETWORK



## MIST/FLows NETWORK

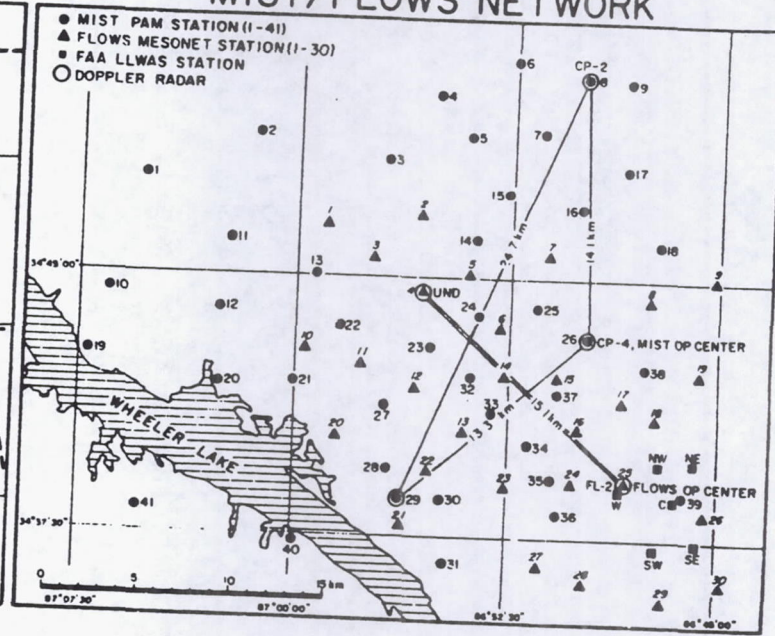


Fig. 5.4.2. (left) Locations of SPACE network surface stations.  
(right) Locations of MIST and FLOWS surface stations.

Table 5.4.2 PAM II Mesonet Site Location

Site No.	Latitude (dms)	Longitude (dms)
1	34 47 35	87 05 18
2	34 49 11	87 01 28
3	34 48 24	86 56 52
4	34 50 20	86 55 14
5	34 49 08	86 54 02
6	34 51 18	86 52 30
7	34 49 14	86 51 28
8	34 50 56	86 49 56
9	34 50 47	86 48 22
10	34 44 31	87 06 30
11	34 46 08	87 02 38
12	34 44 01	87 02 38
13	34 45 10	86 59 01
14	34 46 05	86 53 44
15	34 47 40	86 52 40
16	34 47 05	86 50 00
17	34 48 32	86 48 30
18	34 46 51	86 47 00
19	34 42 38	86 07 07
20	34 41 53	87 02 38
21	34 41 55	87 00 00
22	34 43 36	86 58 27
23	34 42 59	86 55 18
24	34 43 56	86 53 40
25	34 44 12	86 51 32
26	34 43 17	86 49 43
27	34 41 17	86 56 33
28	34 39 29	86 56 38
29	34 38 37	86 56 17
30	34 38 35	86 54 46
31	34 36 46	86 54 40
32	34 42 06	86 53 51
33	34 41 03	86 53 07
34	34 40 15	86 15 47
35	34 39 22	86 50 58
36	34 38 04	86 50 41
37	34 41 42	86 50 46
38	34 42 26	86 47 45
39	34 38 47	86 46 07
40	34 37 16	86 59 52
41	34 38 14	86 05 25

Table 5.4.3 SPACE PAM II Network Locations

SITE NO.	SITE NAME	LOCATIONS	LATITUDE (dms)	LONGITUDE (dms)	ELEVATION Above MSL FT(M)
42	Bon Agua, TN	Hickman County School	35 55 33	87 19 17	900 (274)
43	Smyrna, TN	Smyrna Airport	36 00 27	86 31 18	520 (158)
44	Hohenwald, TN	Lewis National Monument	35 30 20	87 28 08	910 (277)
45	Center Star, TN	Private Residence	35 09 34	88 03 36	720 (219)
46	Pulaski, TN	TVA Communications Facility	35 13 08	87 01 18	985 (300)
47	Shelbyville, TN	Liberty School	35 25 48	86 30 33	800 (244)
48	Rowe Gap, TN	Private Residence	35 05 50	86 05 24	1860 (567)
49	Pride, AL	Private Residence	34 40 08	87 48 34	810 (247)
50	Lacys Springs, AL	Private Residence	34 29 10	86 33 30	1195 (364)

Table 5.4.4 NAMS Parameter Specifications

Parameter	Sensors	Accuracy	Recorded Resolution
Wind Direction	Climet 012-1	$\pm 1$ deg	0.1 deg
Wind Speed	Climet 011-1	$\pm 1$ %	0.05 mph
Peak Wind Gust	(stored by logger)	$\pm 1$ %	0.05 mph
Dry-and wet-bulb temperature	Yellow Springs Instruments linear Thermistor YSI 44203	$\pm .15$ °C	0.05 °C
Precipitation	Weather measure Tipping Bucket P501-I	0.10 mm	0.10 mm
Solar Radiation (direct, diffuse, and reflected)	Eppley PSP Pyranometers (3)	$\pm 2.0$ %	1 w/m <sup>2</sup>

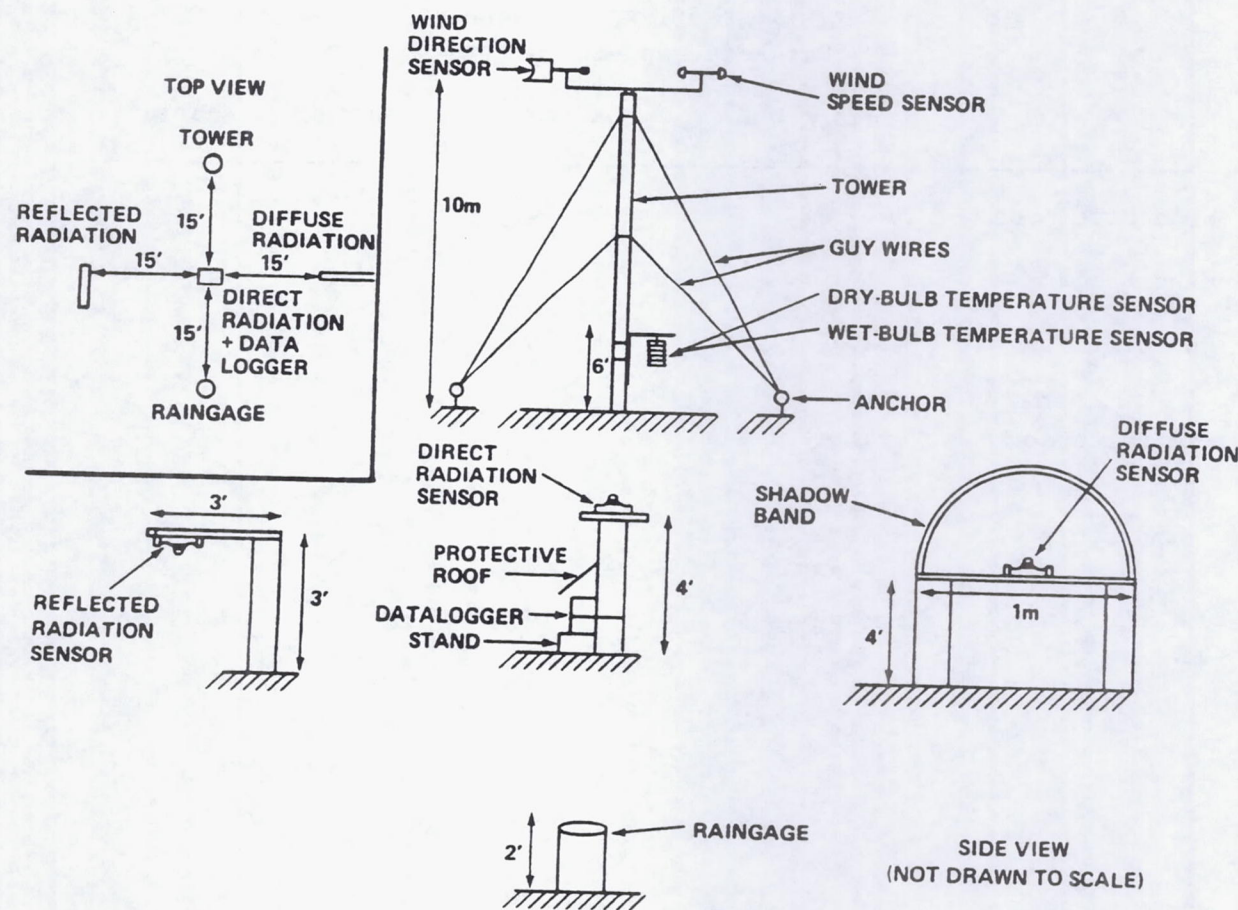


Fig. 5.4.3. Diagram of the NASA mesonet stations.

Table 5.4.5 FLOWS Mesonet  
Parameter Specifications

Parameter	Sensors	Range	Accuracy	Resolution
Wind Direction	MRI 1022	0-360°	2.5°	.4°
Wind Speed	MRI 1022	.2-54 m/s	-	.05 m/s
Humidifiers	Weathertronics 5121-99	0-100%	3%	2%
Precipitation	Belfort Instr. 5915 R	0-300 mm	-	.3 mm
Temperature	Weathertronics 5121-99	-30-+50°C	.2	.1°C
Pressure	Weathertronics 7115	200 mb	-	.1 mb

Table 5.4.6 FLOWS MESONET NETWORK SITE LOCATIONS

Sta. #	El. (ft.)	Lat. DDMSS	Long. DDMSS	SLF (DCP)
1	694	344625.0 N	865908.6 W	252
2	704	344634.9 N	865545.0 W	255
3	582	344535.5 N	865714.2 W	247
4	663	344435.1 N	865531.1 W	240
5	650	344502.5 N	865343.1 W	236
6	631	344338.8 N	865239.5 W	229
7	700	344540.1 N	865113.7 W	254
8	735	344424.6 N	864737.8 W	267
9	770	344507.5 N	864522.5 W	279
10	650	344259.6 N	865923.6 W	236
11	632	344238.3 N	865736.0 W	229
12	621	344151.7 N	865544.3 W	225
13	603	344031.7 N	865354.0 W	219
14	602	344224.4 N	865234.5 W	218
15	618	344202.3 N	865044.2 W	224
16	595	344028.0 N	864946.6 W	216
17	670	344126.8 N	864838.2 W	249
18	685	344057.3 N	864728.0 W	253
19	697	344225.3 N	864544.6 W	251
20	575	344019.3 N	865833.8 W	209
21	588	343744.3 N	865603.0 W	213
22	595	343913.9 N	865535.3 W	216
23*	585	343823.5 N	865242.0 W	212
24	600	343902.1 N	865034.1 W	218
25	636	343907.4 N	864313.5 W	231
26	630	343804.5 N	864546.4 W	229
27	562	343636.0 N	865124.9 W	204
28	586	343616.0 N	864941.4 W	213
29	570	343545.4 N	864631.9 W	207
30	620	343603.7 N	864451.7 W	225
FL2	632	343912.5 N	864819.0 W	229
UND	660	344433.1 N	865536.6 W	239
NWS	618	343830.0 N	864600.8 W	224

\* This station may have to be moved, since the landowner does not want it on their land.

## 5.5 Lightning Detection System

The lightning detection and location system at MSFC uses four radio direction finding systems linked to a central computer to determine the location, time, number of component return strokes, polarity, and signal intensity of lightning discharges to ground in real-time. The basic system is manufactured by Lightning, Location, and Protection (LLP), Inc. of Tucson, Arizona. The locations of the 4 direction finders are shown in Figure 5.5.1. A description of the technique used to detect the lightning discharges to ground can be found in Krider et al (1976). A discussion of the accuracy and other system measures of performance can be found in Hiscox et al (1984) and Mach et al (1986).

### 5.5.1 Real-time Displays

The real-time lightning locations can be accessed and displayed in three ways.

- (1) The Modular Lightning Information and Display system (MLIDS) developed at MSFC (Goodman, 1985) can be used to access the lightning data directly at the COHDEX Operations Center or an approved user can call in to the MSFC Develcon Data Switch to access the lightning data remotely. Only two dial-up phone line connections can be made simultaneously.
- (2) A direct line exists between the Harris/6 MCIDAS and the lightning network central processor. The user can overlay the lightning locations with standard meteorological data sets (surface and upper air), satellite images, and radar data from one of the MCIDAS work stations.
- (3) A direct line exists between the MSFC EADS (engineering analysis and data system) computer network (including the IBM 4381 MCIDAS) and the lightning network central processor. This system will also allow access to the data sets listed in (2) above. The primary reason for using the IBM 4381 MCIDAS for lightning data analysis includes a capability to grid and contour the lightning data, and perform statistical analyses.

### 5.5.2 Data Archive

The data are archived in three ways. The primary archive is through the use of a Microstreamer 1600 bpi, 9-track tape drive. All raw lightning data, including the real-time solutions and individual direction finder data are recorded continuously on this machine. Daily lightning plots and lightning summaries are archived in a ring-binder for easy reference. The lightning data on the Harris and IBM 4381 MCIDAS systems are archived in MCIDAS SDS and MD file formats on tape. Each system allocates 10 days of disk storage for immediate recall. This includes the present day and the previous nine days on which lightning occurred.

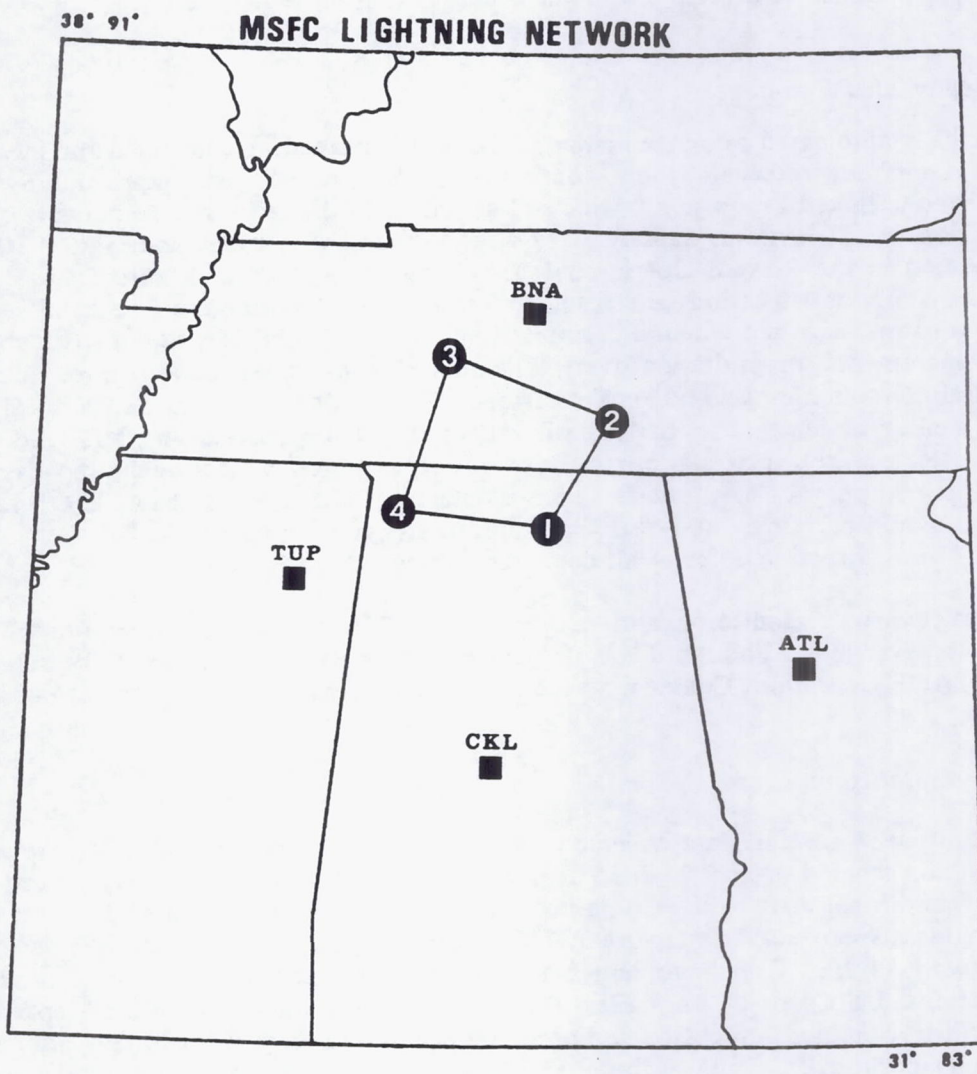


**Fig. 5.5.1.** The location of the MSFC four radio direction finding systems.

## **5.6 Raingage Systems**

A series of raingage networks currently exists in the SPACE Operational Area, and data is obtained and archived by various agencies on a routine basis for various time increments and periods. A description of these networks is presented below.

### *5.6.1 TVA Automated Raingages*

The TVA automated raingage system, originally designed and installed for monitoring rainfall runoff and reservoir levels, consists of an Automated Data Acquisition System (ADAS) telephone linked raingage network and a VHF radio linked raingage network. The western portion of this system, namely sixty-four (64) ADAS stations and eight VHF stations are located in the SPACE Operational Area, and are shown in Figure 5.6.1. These stations, identifiers, and locations are listed in Table 5.6.1. Each of the 64 ADAS stations (capable of storing 5-min incremental precipitation data), and the VHF stations (capable of storing 2-h incremental precipitation data), will relay this information every three hours to TVA's central computer in Knoxville, Tennessee. This data will be transmitted to SPACE Operations Center at least on a daily basis where it will be plotted and analyzed. Individual or selected groups of stations may be interrogated on a near real time basis by TVA's central computer if requested, and the data transmitted to the SPACE Operations Center. This would permit a quasi-real time rainfall analysis for operational decisions. TVA will retain copies of all data transmitted.

The network is monitored and maintained by TVA's reservoir operations branch throughout the system. Although TVA retains responsibility for scheduling the repair of raingages, SPACE Operations Center may request the priority repair of important raingages.

### *5.6.2 Supplemental Raingages*

In addition to rainfall data collected by the mesonet stations and TVA's automated raingage system, other 1-h and 24-h incremental precipitation data routinely recorded in the SPACE Operational Area will be obtained and archived. Figure 5.6.2 denotes the NWS and TVA cooperative observer network (24-h manual gage readings) and NWS recording raingage network (1-h). Other supplemental raingage data recorded by Agricultural Experiment Stations, US Corps of Engineers, Department of the Interior, and the Department of Energy will be obtained, processed and archived to the data base. Up to five additional recording raingages may be deployed by NASA to supplement areas of sparse data coverage.

## **5.7 Meteorological Satellite Systems**

The Cooperative Institute for Meteorological Satellite Studies (CIMSS) at the University of Wisconsin will provide polar and geostationary satellite imagery and retrieved products during the COHDEX period. Nowcasting support will be available during the field program itself, and afterwards, special research quality data sets will be prepared for investigators. Data will be provided both from geostationary (GOES) and polar orbiting (NOAA, DMSP, and NIMBUS) platforms.

Table 5.6.1 Automated TVA Raingage Network

No.	Station	<u>Latitude</u> (dms)	<u>Longitude</u> (dms)
<u>ADAS STATIONS</u>			
1	Albertville	34 14 09	86 11 08
2	Altamont	35 25 54	85 43 00
3	Anderson	35 00 10	85 53 50
4	Arkdell	34 58 11	87 23 50
5	Athens	34 47 26	86 57 56
6	Big Sandy	36 14 03	88 05 51
7	Bruceton	36 02 34	88 15 40
8	Cavvia	35 50 29	88 14 12
9	Cedar Creek	34 33 09	87 59 08
10	Centerville	35 48 38	87 26 17
11	Clifton City	35 22 22	87 59 02
12	Coalmont	35 20 42	85 41 47
13	Collinwood	35 09 46	87 44 42
14	Columbia	35 39 49	87 02 00
15	Columbus City	34 28 35	86 13 24
16	Crawfish Creek	34 49 06	85 32 08
17	Danville	34 24 48	87 05 32
18	Dime	34 20 02	87 39 02
19	Dunlap	35 21 48	85 22 50
20	Dunn	35 11 52	87 19 28
21	Elkton	35 02 11	86 53 15
22	Falkville	34 22 26	86 54 46
23	Fayetteville	35 09 08	86 34 55
24	Flat Rock	34 46 04	85 42 02
25	Flintville	35 03 50	86 24 49
26	Geraldine	34 19 21	85 59 58
27	Grove Oak	34 25 35	86 01 20
28	Henagar	34 37 37	85 45 10
29	Hodges	34 23 36	87 53 11
30	Hohenwald	35 32 39	87 32 56
31	Kensington	34 43 00	85 25 40
32	Lewisburg	35 27 33	86 47 55
33	Lexington	35 38 29	88 22 48
34	Lim Rock	34 40 45	86 11 20
35	Linden	35 37 17	85 50 03
36	Lynchburg	35 16 09	86 23 08
37	Lynchville	35 22 26	87 01 06
38	McEwen	36 06 25	87 38 13
39	Milledgeville	35 21 28	88 22 24
40	Montgomery	35 27 55	88 09 17
41	Morgan	34 34 16	87 03 31
42	Morrison	35 36 57	85 53 36

Table 5.6.1 (Continued)

43	Mount Pleasant	35 31 55	87 12 19
44	Mount Rozell	34 55 48	87 07 19
45	North Huntsville	34 49 00	86 39 33
46	Oakland	34 51 42	87 46 43
47	Only	35 48 38	87 42 14
48	Paris Landing	36 25 28	88 07 43
49	Parsons	35 36 54	88 07 20
50	Pence	34 26 44	86 45 39
51	Petersburg	35 19 36	86 39 14
52	Pulaski	35 11 20	87 01 54
53	Rainsville	34 30 24	85 50 47
54	Red Bay	34 26 59	88 06 03
55	Russellville	34 29 43	87 44 09
56	Salem	35 05 10	86 15 10
57	Sewanee	35 11 49	85 55 05
58	Town Creek	34 39 38	87 24 19
59	Unionville	35 37 16	86 35 11
60	Waynesboro	35 19 57	87 41 28
61	Whitesburg	34 34 18	86 33 29
62	Whitewell	35 12 32	85 31 10
63	Williamsport	35 41 38	87 12 43
64	Wright	34 57 21	87 57 13

VHF STATIONS

65	Bone Cave	34 40 58	88 01 42
66	Estill Springs	35 17 08	86 06 20
67	Hyt op	34 53 29	86 05 36
68	Manchester	35 28 16	86 04 54
69	Moulton	34 24 13	87 18 58
70	Normandy	35 25 55	86 14 32
71	Shelbyville	35 28 10	86 27 56
72	West Point	35 05 59	87 33 58

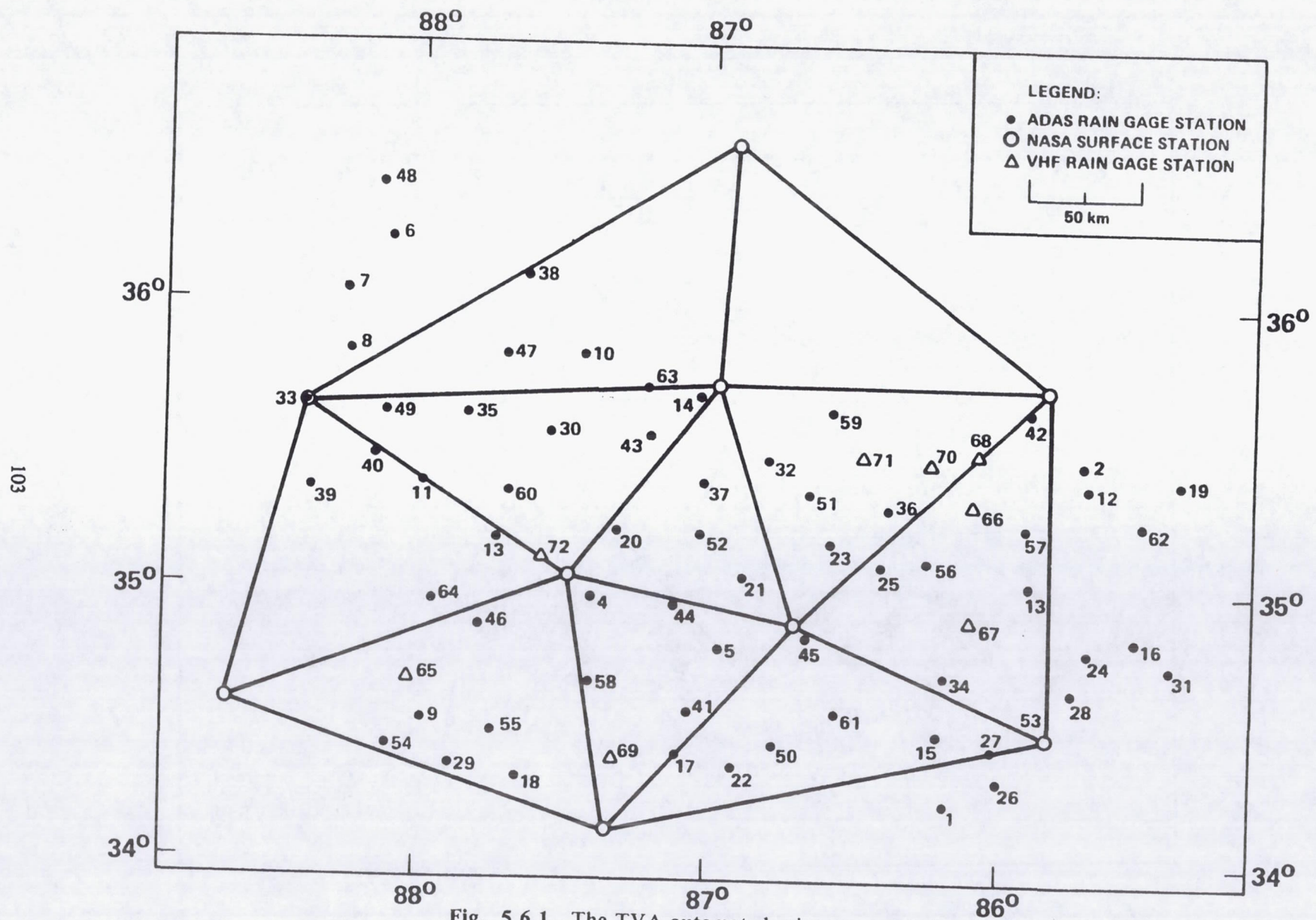


Fig. 5.6.1. The TVA automated raingage network.

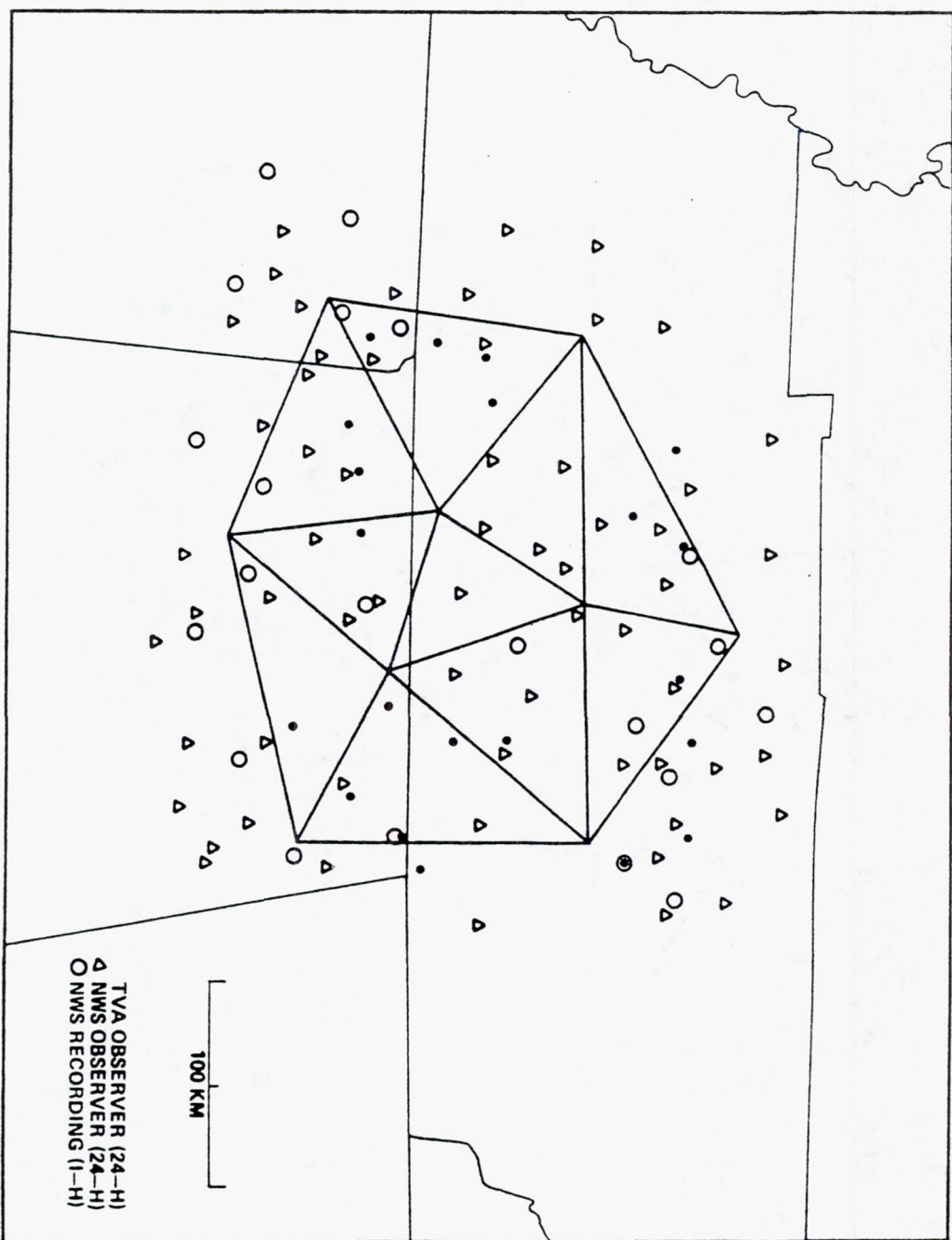


Fig. 5.6.2. The NWS and TVA cooperative observer雨量計 network.

### *5.7.1 Geostationary Platforms*

Final details of GOES/VAS scheduling during COHDEX were not available at the time of this writing; however representative information is provided in Tables 5.7.1 and 5.7.2. Although no major changes are expected, one likely modification to the Processor Data Loads (PDLs) of Table 5.7.2 will be to change latitudinal coverages of the Dwell Sounding (DS) modes so that as much of the COHDEX region as possible either is in a northern or southern sector, not split between them. Operational needs require GOES to obtain visible and infrared imagery each half hour, and full disc versions are mandated at 3 h intervals. Thus, sounding quality (DS) radiances must be gathered in ten minute segments between operational scans. Although these or similar schedules will be the default during much of Summer 1986, copied rapid scanning requirements of the National Severe Storms Forecast Center and the National Hurricane Center will have highest priority.

During the field program, CIMSS will prepare satellite - derived products needed to predict and monitor conditions on days of intensive data collection. This effort will be similar to the support provided to the National Severe Storms Forecast Center and the National Hurricane Center. That is, VAS retrievals will be made over cloud-free areas of the eastern two-thirds of the nation at spacings of approximately 80 km and intervals of approximately three hours. Precipitable water and stability imagery at 7 km resolution also will be provided. Details of the three procedures can be found in Smith *et al.* (1985). There will be a special effort to achieve dense sounding coverage over the COHDEX domain.

After the field program phase is completed, five to ten days will be selected for the preparation of special research quality data sets. Except for breaks at 3 h intervals due to required full disc scanning, the sounding products on many days are expected to be available every 1 h during the morning and afternoon period. Sounding spacing will be no greater than 80 km in cloud free areas, and their spacing on some days may be substantially less. Once again, precipitable water and stability products at 7 km resolution will be provided. Coverage will encompass all of the COHDEX domain and a large portion of the eastern United States, depending of course on cloud cover. Through use of the latest available techniques, every effort will be made to produce the highest quality products for research use.

In addition to the sounding products, winds will be derived three times per day (1200, 1800, and 0000 GMT) by means of cloud tracking, tracking of water vapor image features, and calculation via thermal wind relationships. The thermally - derived winds accompany the retrieval process; however, loops of high resolution VISSR images are used in the the cloud and vapor tracking procedures. These techniques are described in Velden *et al.* (1984) and Stewart *et al.* (1985).

### *5.7.2 Polar Orbiting Platforms*

Anticipated activities for the polar orbiters are given in Table 5.7.3. Nimbus 7 will provide ozone measurements whereas NOAA-10, DMSP, and NOAA-9 will provide high resolution imagery and sounding products eight times daily. Gaps in GOES sounding coverage due to high cloudiness can be reduced by incorporating TOVS microwave data in the VAS retrieval process (Smith and Woolf, 1984). Thus, satellite - derived profiles will be specified from combined TOVS and VAS radiances whenever possible in cloudy regions. Furthermore, AVHRR data may be used to enhance VAS soundings in partly cloudy regions. Finally, cloudiness estimates will be produced at nominal 90 min intervals using both VAS and the AVHRR when available.

Table 5.7.1  
**ASPP RECOMMENDATION FOR NOMINAL TVAS OPERATION  
 DURING SEVERE STORM SEASON AND COHMEX**

2/12/86

**HRS-A Schedule**

<u>Time</u>	<u>PDL</u>	<u>Activity (Channels)</u>
0830 GMT	79, 70	9-10, DI(N)
0900 GMT	71	7-10, (Full Disc)
0930 GMT	79, 72	9-10, DS(N)
1000 GMT	81, 74	6-10, DS(S)
1030 GMT	79, 70	9-10, DI(N)
1100 GMT	75, 72	7-10, DS(N)
1130 GMT	87, 74	10-7-12,* DS(S)
1200 GMT	73	7-12, (Full Disc)
1230 GMT	79, 72	9-10, DS(N)
1300 GMT	81, 74	6-10, DS(S)
1330 GMT	79, 76	9-10, DI(C)
1400 GMT	75, 72	7-10, DS(N)
1430 GMT	79, 74	9-10, DS(S)
1500 GMT	73	7-12, (Full Disc)
1530 GMT	79, 72	9-10, DS(N)
1600 GMT	81, 74	6-10, DS(S)
1630 GMT	79, 70	9-10, DI(N)
1700 GMT	75, 72	7-10, DS(N)
1730 GMT	87, 74	10-7-12,* DS(S)
1800 GMT	73	7-12, (Full Disc)
1830 GMT	81, 72	6-10, DS(N)
1900 GMT	79, 74	9-10, DS(S)
1930 GMT	75, 76	7-10, DI(C)
2000 GMT	79, 72	9-10, E <sub>B</sub> (N)
2030 GMT	81, 74	6-10, DS(S)
2100 GMT	73	7-12, (Full Disc)
2130 GMT	75, 72	7-10, DS(N)
2200 GMT	79, 74	9-10, DS(S)
2230 GMT	81, 70	6-10, DI(N)
2300 GMT	79, 72	9-10, DS(N)
2330 GMT	87, 74	10-7-12,* DS(S)
0000 GMT	71	7-10, (Full Disc)
0030 GMT	79, 70	9-10, DI(N)
0100 GMT	81	6-10, Transition
0130 GMT	NORMAL VISSR	

DI - Dwell Image

DS - Dwell Sound

(N) - North

(S) - South

\*VISSR S/DB - Moisture Channel Support

02/WPM6/35

Table 5.7.2 VAS PDL RECOMMENDATIONS FOR GOES

PDL	71 MSI	73 MSI	75 MSI	77 MSI	79 MSI	81 MSI	87 MSI	70 DS	72 DS	74 DS	76 DS
	8	8	8	8	8	8	10	1	1	1	0
	7	7	7	7	9	6	7	2	3	3	3
	8	8	8	8	8	8	10	2	3	3	3
	7	7	7	7	9	6	7	2	3	3	3
	8	8	8	8	8	8	10	1	2	2	0
10	12	10	12	10	10	10	12	1	2	2	0
	8	8	8	8	8	8	10	3	4	4	0
10	12	10	12	10	10	10	12	1	2	2	0
								2	2	2	0
								1	1	1	0
								0	0	0	0
B8	S	S	S	S	S	S	S	1	1	1	0
IGFOV3											
4								S	S	S	S
5								S	S	S	S
6								S	S	S	S
7								L	L	L	L
8								S	S	S	S
9								L	L	L	L
A								L	L	L	L
S <sub>1</sub> , S <sub>3</sub>											
hs	810	810	700	700	700	700	700	6,2	6,2	6,2	6,2
cen	911	911	801	801	801	801	801	95	75	75	164
time	16.2	16.2	14.0	14.0	14.0	14.0	14.0	349	313	453	692
coverage full	full	90°N-42°S	90°N-42°S	90°N-42°S	90°N-42°S	90°N-42°S	90°N-42°S	48°-31°N	50°-35°N	36°-24°N	24°N-3°N
comment 7-10 <sup>f</sup>	7-12 <sup>f</sup>	7-10	7-12	9-10	6-10	10-7-12	DI(N)	DS(N)	DS(S)	DI(C)	

Table 5.7.3

**Satellite Activity Proposed for COMMEX IOP**

Time (GMT)	Imagery & Soundings from Polar Orbiters	Note: Underscored times indicate scheduled three- hourly radiosonde launches
0000		
0030	NOAA-10	
0100		
0130		
0200		
<u>0230</u>		
0300	DMSP	
0330		
0400		
0430		
<u>0500</u>		
0530		
0600		
0630		
0700		
0730	NOAA-9	
<u>0800</u>		
0830		
0900		
0930		
1000		
1030		
<u>1100</u>	DMSP	
<u>1130</u>		
1200		
1230	NOAA-10	
1300		
1330		
1400		
<u>1430</u>		
1500	DMSP	
1530		
1600		
1630		
<u>1700</u>	NIMBUS-7 (Ozone)	
1730		
1800		
1830		
1900		
1930	NOAA-9	
<u>2000</u>		
2030		
2100		
2130		
2200		
2230		
<u>2300</u>	DMSP	
2330		

## **6.0 OPERATIONS CENTER**

Aside from equipment and operation, the success of an atmospheric field program such as SPACE depends on three factors:

- o Forecasting
- o Communication
- o Coordination

The ability to foresee with adequate lead time periods of active convection over the SPACE network is critical to deploying rawinsonde teams, readying aircraft, and initiating the special observing programs. However, even with good forecasts the information has to be communicated to field and aircraft personnel. In addition, in a cooperative field program such as COHMEX there has to be coordination among the participants to take advantage of the complementary observations upon which much of the justification of the programs is based. The following outlines a description of the operation centers and general discussions of coordination and communication. Details of the operations and a separate operations manual will be developed in the near future.

### **6.1 Facility Description and Organization**

The operations center for the Satellite Precipitation and Cloud Experiment will be located in the MCIDAS/Image Processing Room of the Atmospheric Sciences Division, Systems Dynamics Laboratory of the Marshall Space Flight Center. This room will contain three MCIDAS terminals for data and real-time image display purposes as well as display systems for lightning strike information, Nashville radar display, and positions of research aircraft in the SPACE/COHMEX domain. Dial-in access to the SPACE computer network from remote sites will be possible for special user groups. This will allow operational use of special data sets for both field operations and aircraft operations.

Status briefings as well as forecast briefings will be held at the Marshall Space Flight Center on a twice a day basis. A morning briefing will be used to make operational plans for SPACE rawinsonde operations as well as to plan the high-altitude aircraft experiments and flight procedures. An afternoon briefing will take place for the purpose of developing a 12 and 24 hour forecast. This forecast will be used to plan SPACE operations for the next day. Both briefings will be held in a room near the MCIDAS operations center and will have both video and map displays of atmospheric conditions and operational status.

MSFC computer facilities and connections that will be used to support the field program are shown in Fig. 6.1.1. Real-time meteorological satellite data will be obtained from the Satellite data base at the University of Wisconsin. Both images and ground based data will be transferred to MSFC through 9.6 kb links. The data bases will then be exchanged between the MSFC IBM 4381, the Harris/6 and a VAX 730/785. Desired information will then be displayed on the MCIDAS terminals. The precipitation data from the TVA network will be ingested on a HP 1000F for display purposes. Kavouras radar images ICRAD system co-located with the MCIDAS display. Position information for aircraft in the program will be overlaid on the ICRAD display of radar activity or on a base chart of the local area. Communication between the aircraft home base or the aircraft will be conducted via radio and telephone links. The Marshall LLP network information will also be displayed adjacent to the ICRAD output.

## DATA TRANSFER

# SPACE NETWORK CONFIGURATION

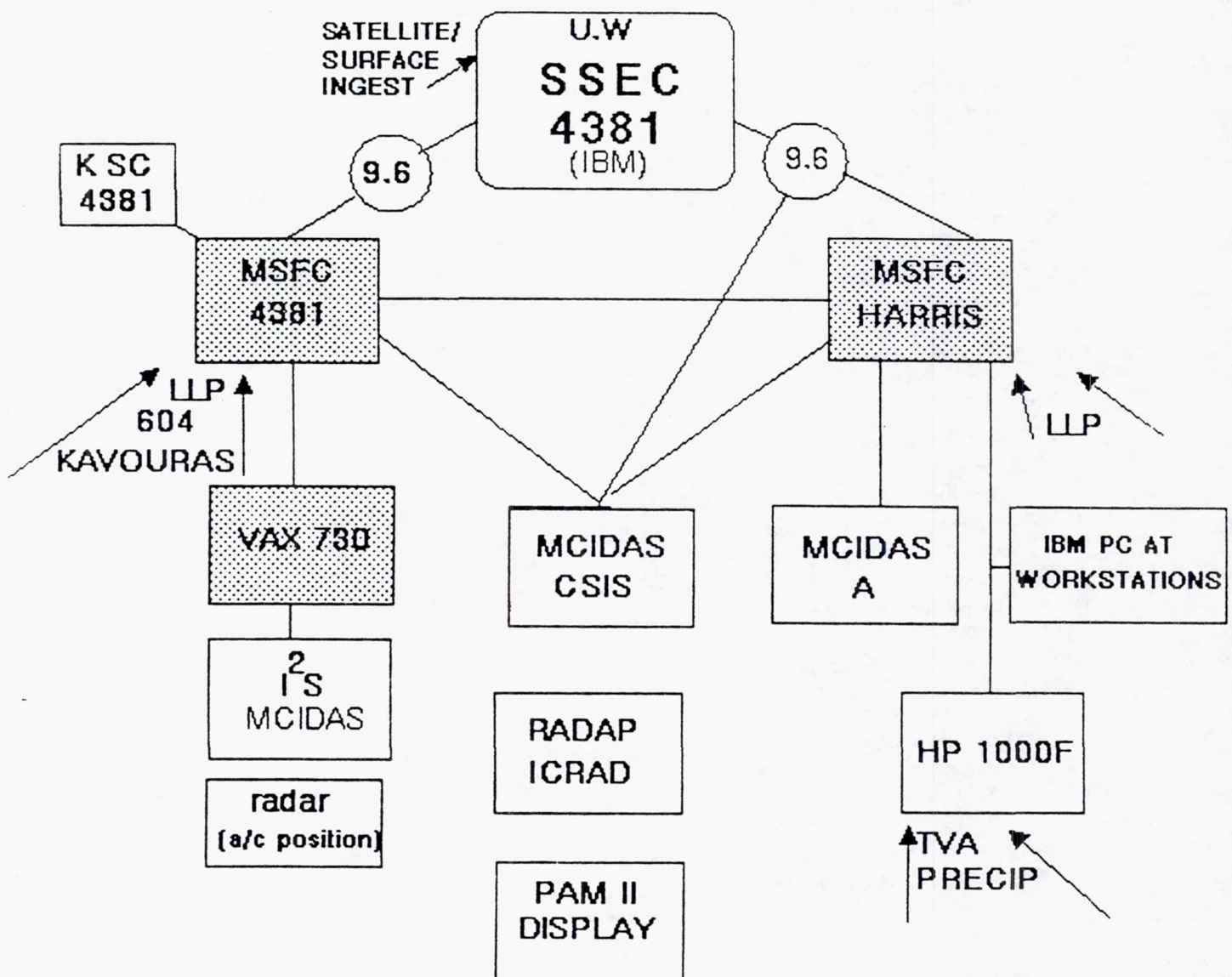


Fig. 6.1.1. Schematic of data communications and systems accessible from the operations center.

## 6.2 Operations Forecast Center

### 6.2.1 Operational Data Flow

Forecasting operations will be housed at Marshall Space Flight Center's Atmospheric Sciences Division. The function of the forecast operations group is to monitor atmospheric conditions for convective potential and disseminate forecasts which meet the special needs of scientific teams, field observers and aircraft flight operations planners.

The operations center will have access to an array of tools for observing weather developments on a wide range of spatial and temporal scales. Conventional National Weather Service (NWS) and National Meteorological Center (NMC) facsimile products will be available at MSFC and from the U.S. Army range forecast team at Redstone Arsenal. The Army forecast team will also provide a 1200 GMT rawinsonde sounding from Redstone Arsenal. NASA's MCIDAS computer facility located in the operations room will provide real-time satellite looping capabilities for visible, infrared window and water vapor imagery. The extensive real-time data management and display capabilities of MCIDAS will also allow instant access to fields of derived parameters and indices pertinent to the monitoring and forecast of regional and mesoscale scale convective activity. Standard text data is automatically ingested and may be displayed on the MCIDAS. Kavouras color radar displays from selected NWS radar sites will also be available through MCIDAS. The commercial WSI meteorological data service will serve as emergency backup to the MCIDAS system for the access of real time regional weather data. The Nashville RADAP system information will be accessed by MSFC personnel from the operations room in Huntsville. The MSFC Modular Lightning Information and Display System (MLIDS) will be located next to the RADAP and Kavouras radar display systems.

The forecast team will be comprised of three core members from MSFC's Atmospheric Sciences Division and the U.S. Army. Additional input may be provided by SPACE, MIST, and FLOWS scientists whose activities may be affected by a particular developing weather situation. Other MSFC atmospheric scientists may be consulted before finalizing of the forecast in critical situations. This input will generally be provided at or immediately prior to the morning weather briefing. Those receiving forecast information directly include representatives of the MIST and FLOWS teams, SPACE scientific personnel, and University of Alabama-Huntsville (UAH) coordinators.

Communication of forecasts to participating science teams will occur at the weather briefing meetings. The UAH coordinator will relay the forecast and "go" decisions to all field personnel and National Weather Service offices. Potential flight days will be reported directly to the Wallops Island, Virginia facility from the operations room after consultation with scientists with flight experiments. An 800 telephone line to the operations room will permit access of field personnel to forecast information; however, the primary purpose of the line is for reporting malfunctioning equipment to the operations center.

### 6.2.2 Nowcasting

A strength of the MSFC operational forecasting facility will be the ability to monitor recent weather and thus to project local changes several hours in advance. The satellite image looping capability of MCIDAS will play a major role. Image sequences may

allow, for example, a forecaster to project development of squall lines from a sudden appearance of a rope-like line of cumulus resulting from low level convergence. Regional pressure tendency patterns are easily calculated via MCIDAS and may indicate imminent convective development. Other parameters can be derived which may be related to convective development (such as a surface divergence of equivalent potential temperature). The RADAP and lightning display system (MLIDS) will provide accurate estimates of precipitation system locations, intensities and movements.

#### *6.2.3 Operational Briefings*

Weather analysis and forecast preparation will begin at 6:00 A.M. by a MCIDAS operator following a pre-planned itinerary of key-ins and information display formats. The NASA and Army meteorologists will separately begin data analysis and forecast preparations around 6:30 A.M. The purpose of the morning forecast is to:

- (a) confirm or retract a previous days "go" decision,
- (b) decide on the current day's meso-beta launch,
- (c) tentatively set a new 24 hour forecast.

At 8:00 A.M. the morning weather briefing is held for NASA and UAH coordinators, and representatives of each science team having a critical interest in the day's weather.

The weather conditions will be monitored continually throughout the day and information relayed to program coordinators. Preparation and discussion for the next day forecast begins at 1:30 P.M. and continues until 4:00 P.M. The purpose of this forecast is to decide on whether to plan for a regional or meso-beta rawinsonde launch for the next day. The forecast will be issued at a 4:00 P.M. briefing.

#### *6.2.4 Long Range Outlooks*

Long range forecasts will be based primarily on National Meteorological Center model products. Synoptic and regional scale forecasts must continually anticipate weather conditions 24 to 48 hours in advance in order to advise field crews on the likelihood of a launch day. Research aircraft based at Wallops Island, Virginia require 24 hours notice for flight to North Alabama. Regional National Weather Service sites also require 24 hours notice prior to a regional 3 hourly rawinsonde launch phase. Longer range forecasts are also necessary to plan for equipment maintenance.

### **6.3 Coordination and Communication**

The following describes planned coordination among the COHMEX programs and facilities.

### *6.3.1 Coordination with COHMEC Operation Centers*

Operational coordination with the MIST and FLOWS components of COHMEC will take place at three levels. After the field portion of the experiment has begun, a weekly meeting should take place between the three program elements. This should take place at the end of each week on a non-operational day. At this time the operational and scientific objectives that have been met during the past week would be reviewed and levels of cooperation desired from each COHMEC group to help the other efforts meet their objectives will be outlined. A working operational agreement can thus be reached for each one week period based on past and expected activities.

At the beginning of each operational day, experiment coordination can be carried out at the morning status and forecast briefing. At that time, special operational support can be requested for both the current operational day and that support anticipated for the following day presented for consideration.

There will be a SPACE coordinator at each of the COHMEC operation centers for detailed coordination of radar and aircraft activities. It will be the responsibility of the on-site coordinator to communicate information between the SPACE operations group and the MIST and FLOWS groups during an operational day. MIST and FLOWS groups can also communicate directly with the SPACE operations center.

### *6.3.2 Air Traffic Coordination*

Details for the aircraft coordination during COHMEC are at this time still being finalized. However, we can say that, in general, in-flight vectoring of aircraft to storm locations will be accomplished via ground-to-air communications from local control points (an exception to this being that the ER-2 and U-2C may at times receive directions from their Wallops Island, VA home base). Table 6.3.1 indicates possible on-site control points for the COHMEC aircraft. We have also shown in this table that a highly equipped NASA communications vehicle may be made available for use during the SPACE/MIST time period. This vehicle could then be employed as an alternate or primary control point for any of the COHMEC aircraft. One complication to the aircraft operations may arise because the COHMEC network straddles air space controlled by the Atlanta and the Memphis Air Traffic Control (ATC) centers.

Fig. 6.3.1 outlines the lines of communication which may be implemented to keep the ATC centers fully aware at all times of ongoing COHMEC aircraft operations. In this arrangement, each of the local control points would report to a single COHMEC liaison person, who would then brief a designated liaison person or dedicated controller at the ATC centers.

Some issues that are presently receiving attention include:

- o determine if one ATC center can control COHMEC aircraft
- o determine if a dedicated controller for COHMEC can be made available at the ATC center(s)
- o dynamic allocation of blocks of air space during the experiment

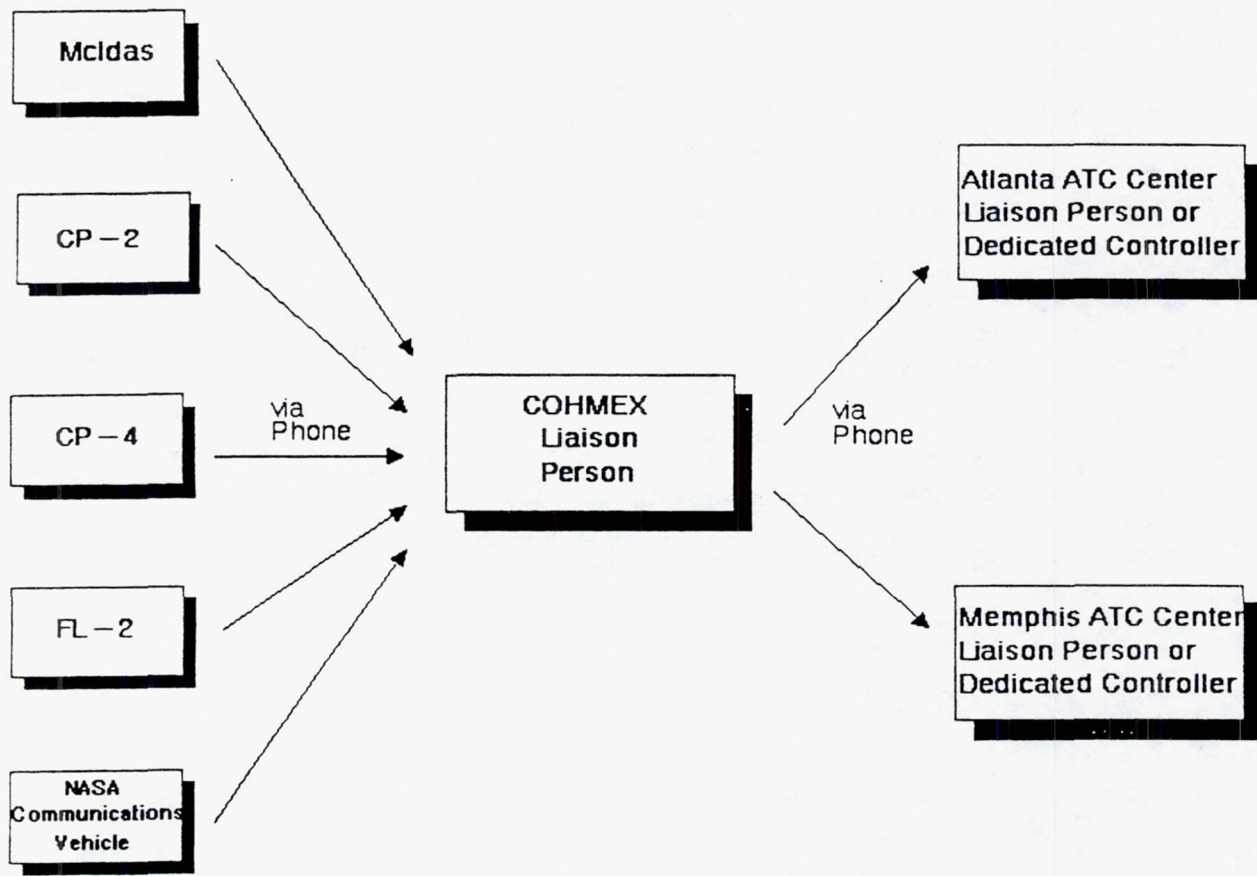


Fig. 6.3.1. The lines of communication from the local aircraft control points to the ATC centers.

TABLE 6.3.1

<u>Local Control Point</u>	<u>Aircraft</u>	<u>Aircraft Positions Available</u>
Mcidas	ER-2, U-2C, possibly T-28	Yes (via RADAP)
CP-2	T-28	Yes*
CP-4	P3, Cessna 207	Yes*
FL-2	Convair 580, Cessna Citation	Yes
NASA Communications Vehicle (access to Mcidas)**	all aircraft – as alternate or primary control point	Yes (via RADAP)

\* Software for displaying aircraft locations on CP-2 and CP-4 still under development

\*\* Efforts to obtain NASA Communications Vehicle for COHMEC underway

- o obtain unique experimental call signs (e.g. COHMEX1, COHMEX2, etc.)
- o obtain block of transponder ID numbers for use during the experiment
- o transmit official notification to the VFR community about the COHMEX operations

It is expected that a detailed aircraft coordination plan will become available in early May following the final aircraft coordination meeting on April 28. Comments and/or questions on the aircraft coordination activities should be directed to:

Mr. Albert Paradis  
MIT Lincoln Laboratories  
RM V115  
244 Wood St.  
Lexington, MA 02173  
(617) 863-5500 ext. 3547

#### 6.3.3 Radar Coordination

Radar coordination involves critical communication and collaboration in several areas:

- o Coordination of radar scans such that scientific objectives are optimized for all three COHMEX programs;
- o Coordination with aircraft and other mobile platforms;
- o Coordination between radar operations and the SPACE operations center.

Close radar coordination among the SPACE, MIST and FLOWS experiments involves careful planning prior to experimental operations. The scientific interests in both the MIST and FLOWS program are related to microbursts and associated wind shear at low levels (the lowest several kilometers), whereas SPACE scientific interests generally encompass the entire cloud depth from surface to cloud top.

From the SPACE standpoint, it is therefore critical to scan the entire cloud depth uniformly. Such scanning would also seem beneficial to MIST objectives, since cloud processes at low levels may be directly or indirectly related to processes and structure at upper levels. Moreover, accuracy in Doppler-derived vertical motion estimates can be improved considerably when a second boundary condition at cloud top and downward integration are utilized.

Radar coordination also involves a differentiation in types of scans to be conducted. Because both meso-beta and meso-gamma scales are of interest, scans devoted to one generally preclude complete scanning of the other. For example, high spatial resolution scans are required to satisfy MIST/FLOWS objectives and cloud-scale aspects of SPACE objectives. However, relatively high-resolution scans (by CP-2 in particular) over meso-beta scales are required to meet a number of other SPACE scientific objectives (see Section 3). Therefore, the radar coordination effort should include a pre-determined menu which differentiates high-resolution MIST-type scans (which are also of great interest to SPACE) from larger-scale SPACE scans. The selection may be obvious when convection is either within or far from the MIST/FLOWS network, but "gray" cases will obviously exist.

Several SPACE-related experiments will investigate the prestorm PBL structure. To meet these objectives, it is desirable to conduct both sectorized multiple Doppler scans and VAD scans so that high horizontal and vertical resolution of PBL flows can be attained.

Another critical coordination component involves communication between CP-2 and the NASA aircraft (T-28, U-2 and the ER-2) and the ground-based mobile laboratory. Decisions on locations of aircraft flights will be made from CP-2 and the SPACE operations center. Because supporting aircraft greatly accentuate Doppler radar analyses, such coordination will likely impact other radar operations. For example, T-28 cloud penetrations will be of great interest to MIST researchers, and every effort should be made to maximize coordination between T-28 flights and multiple Doppler radar scans. Similarly, data from P-3 flights will certainly supplement SPACE-related analyses. Therefore, coordination among all aircraft and radars should be maximized whenever possible.

Finally, radar coordination involves collaboration among the SPACE, MIST, and FLOWS operations centers. It is expected that much of the SPACE-related coordination will be provided by a SPACE scientist located at the CP-2 radar site. Based on current conditions and discussions with CP-2, MIST, FLOWS and SPACE personnel, these scientists will provide information to the SPACE operations center which will help determine aircraft flight patterns. The CP-2 SPACE coordinator will also provide input to other CP-2 scientists concerning types of scans which would optimize SPACE scientific objectives.

#### *6.3.4 Communications and Real-time Data Transfer*

Communications between special observing system platforms and the MSFC SPACE operations center, and among special observational platforms, are outlined in Table 6.3.2. Phone communications into NASA/MSFC will be possible from any location through a specially-installed 800-line.

Real-time transfer of data into the NASA/MSFC Operations Center will consist of the following products:

- o ICRAD products arriving from the BNA RADAP site (1200/2400 baud line),
- o Kavouras radar displays accessed by phone calls to NWS radar sites,
- o PAM displays sent by phone line from the CP-4 radar site,
- o location of cloud-to-ground lightning discharges from the MLIDS system located at MSFC,
- o TVA raingage data accessed via phone from the TVA computer,
- o MCIDAS access to satellite and other 604-line weather information originating from the University of Wisconsin 4381 computer (9600 baud),
- o An optional 9600 baud line to Kennedy Space Center, used as a backup to the Wisconsin line.

In addition, FAA air traffic control (ATC) data will be accessed by the FL-2 radar.

Table 6.3.2 SPACE/COHMEC Voice Communications

Calls to From	SPACE Ops.	MIST Ops.	FLows Ops.	CP-2	CP-3	UND	BNA RADAP	Aircraft	PAM	TVA	NASA rawin	NWS rawin
SPACE Ops.		Phone	Phone	Phone	Phone	Phone	Phone	Radio (ER-2, U-2)	Phone	Phone	Phone	Phone
MIST Ops. (CP-4)	Phone		Phone	Phone Radio	Phone Radio	Phone Radio	Phone*	Radio (P-3)	Direct	Phone*	N/A	Phone*
FLOW Ops. (FL-2)	Phone	Phone Radio		Phone	Phone	Phone Radio	Phone*	Radio: Citation, Convair	Phone	Phone*	N/A	Phone*
CP-2	Phone	Phone Radio	Phone		Phone Radio	Phone	Phone*	Radio: T-28	Phone	Phone*	N/A	Phone*
CP-3	Phone	Phone Radio	Phone	Phone Radio		Phone	Phone*	none	Phone	Phone*	N/A	Phone*
UND	Phone	Phone	Phone Radio	Phone	Phone		Phone*	none	Phone	Phone*	N/A	Phone*
BNA RADAP	Phone	N/A	N/A	N/A	N/A	N/A		none	N/A	N/A	N/A	N/A
Aircraft	Radio: ER-2, U-2	Radio: P-3	Radio:Citation Convair	Radio:	none	none	none	Radio	none	none	none	none
PAM Trailer	Phone	Direct	Phone	Phone	Phone	Phone	Phone*	none		Phone*	N/A	Phone*
TVA	Phone	N/A	N/A	N/A	N/A	N/A	Phone	none	N/A		N/A	N/A
NASA rawin sites	Phone	N/A	N/A	N/A	N/A	N/A	N/A	none	N/A	N/A		N/A
NWS rawin sites	Phone	N/A	N/A	N/A	N/A	N/A	N/A	none	N/A	N/A	N/A	

Key: Phone\* = Communication possible, but not advised  
 N/A = not applicable - probably no need for such communication  
 none = direct communication not possible

## 7.0 DATA MANAGEMENT

Data management encompasses two general areas: (a) collection, archival, documentation and storage of data, and (b) documentation of daily operations during the experimental period. The primary purpose of a data management plan (DMP) is to provide a detailed outline of data management procedures before, during and after experimental operations so that data is collected, stored, and validated as quickly as possible. Additionally, effective data management allows efficient and easy access to data, both during field operations and during post experimental phases.

The following sections summarize the data management process as related to SPACE operations. Further details of data management activities and policies will be described in the SPACE DMP document.

### 7.1 Data Types

During SPACE field operations, conventional NWS synoptic data and special COH-MEX experimental data will represent two distinct types of data available. Conventional NWS data will be routinely available on a daily basis, while access to experimental data will be governed by special operations.

Data can be generally classified into the distinct levels defined in Table 7.1.1. This categorization follows that used during the GARP and GALE programs. The data levels defined in Table 7.1.1 will appear in subsequent data management documents, and are used in the following subsections.

#### 7.1.1 *Conventional Data*

Conventional NWS data are defined as those data available from routine NWS daily operations. These data include:

- o surface observations (NWS and FAA),
- o NWS soundings and pilot reports,
- o NMC analyses and numerical output,
- o NMC public forecasts and special weather bulletins,
- o precipitation observations from different sources.

During field operations, subsets of conventional data will be available over the MCIDAS system located at NASA. Cleaned-up data sets may be obtained after the fact from NCDC's Service Record Retention System (SRRS) tape, which is derived from an Automation of Field Operations and Services (AFOS) data tape. The SRRS tape will therefore serve as the primary source of level IIA conventional NWS data.

#### 7.1.2 *Special Experimental Data*

Special experimental data sets will be derived from the special observational platforms described in Section 4. Data collection, preparation and archival will be done in

Table 7.1.1 Definition of experimental data levels

Level	Definition	Examples
I	Raw measurements which require additional processing in order to be meaningful to users	Raw rawinsonde ascent trace Raw aircraft data
IIA	Data available in real-time or near real-time which have not been validated by in-field calibration or intercomparison	PAM II displays Doppler radar displays
IIB	Calibrated level IIA data subjected to quality-control and reformatting procedures. This category may include non level IIA data not available in real-time	Universal-format radar data Processed rawinsonde data
IIIA	Analyses prepared from level IIA data, including real-time operational analyses and preliminary research analyses	Synoptic or meso-scale (PAM) analysis Sounding analyses
IIIB	Research analyses of level IIB data sets, generally involving elaborate analysis techniques on multiple data sets	Multiple Doppler radar analyses combined with aircraft analyses and lightning data

many cases with the help of outside agencies such as NCAR. General data categories appear in Table 7.1.1 and are described in the following.

*a. Surface Data*

Special surface data and related observations will be available from several sources. These are:

- o PAM-II mesonet stations. These will be deployed on both MIST and SPACE scales. Data collection, validation, and archival will be done by NCAR, with probable commentary by MIST and SPACE PI's.
- o FAA mesonet stations. These will be deployed on the MIST scale. FAA will oversee data collection, validation and archival.
- o NASA mesonet stations. These will be deployed on the SPACE scale. UAH will conduct data collection, validation and archival.
- o Raingage data. These will originate from dedicated raingages operated by the TVA and NWS. NASA will collect, reduce and archive these data.
- o Lightning data. These will originate from NASA's four-station lightning network, and will be collected, reduced, and stored by NASA.

*b. Rawinsonde Data*

Special rawinsonde data will be available during declared operational periods from 9 GMD units deployed on a meso-beta scale array, and from adjacent NWS sites. All GMD rawinsonde data will be collected, reduced, checked and archived by UAH. Special NWS data derived from satellite, and NASA aircraft sensors, will be available from the University of Wisconsin and NASA, respectively.

*c. Aircraft Data*

Flight-level aircraft data will be provided by several agencies, each of which will have primary responsibility for data collection, reduction, validation and archival (see Table 7.1.2). Three aircraft, NASA's ER-2 and U-2, and the South Dakota T-28, will execute primary SPACE operations. Primary MIST/FLOWS aircraft include the NOAA P-3 and the two FAA aircraft. It is expected that significant SPACE/MIST overlap will occur for the T-28 and P-3.

*d. Radar Data*

Radar data will be collected, checked and archived by several groups. The radars are listed below.

Table 7.1.2 Institutions\* responsible for data collection, checking and archival

<u>Data Type</u>	<u>Data Collection</u>	<u>Data Checking</u>	<u>Generation of Level IIB Data</u>	<u>Data Archival</u>
PAM-II surface mesonet	NCAR	NCAR, UC, UCLA, MSFC	NCAR	NCAR, NASA, UC
NASA surface mesonet	MSFC/UAH	MSFC/UAH	MSFC	MSFC
FAA surface mesonet	FAA	FAA	FAA	FAA, MSFC
Raingage network	MSFC, TVA	MSFC	MSFC	MSFC
LLP network	MSFC	MSFC	MSFC	MSFC
Rawinsonde network	MSFC/UAH	MSFC/UAH	MSFC	MSFC
Special NWS rawinsonde	NWS	MSFC	MSFC	MSFC
U-2, ER-2 aircraft	MSFC, GSFC	MSFC, GSFC	MSFC, GSFC	MSFC, GSFC
T-28 aircraft	SDSMT	SDSMT	SDSMT	SDSMT, MSFC
P-3 aircraft	NOAA	NOAA, UC, MSFC	NOAA	NOAA, UC, MSFC
UND citation	FAA	FAA	FAA	FAA
FAA Convair 580	FAA	FAA	FAA	FAA
CSU Cessna	CSU	CSU	CSU	CSU
BNA RADAP	NWS, MSFC	MSFC	MSFC, NOAA	MSFC
CP-2	NCAR	NCAR, CSU, PSU, MSFC	NCAR	NCAR, MSFC
CP-3, CP-4	NCAR	NCAR, UCLA, UC, FSU	NCAR	NCAR
FL-2	FAA	FAA	FAA	FAA
UND	FAA	FAA	FAA	FAA
Satellite image products	UW	UW, MSFC, GSFC	UW	UW, MSFC
Derived satellite soundings	UW	UW, MSFC, GSFC	UW	UW, MSFC
Derived satellite winds		MSFC, UW	MSFC, UW	MSFC

\*MSFC-NASA Marshall Space Flight Center, GSFC-Goddard Space Flight Center, NOAA-National Oceanic and Atmospheric Administration, NCAR-National Center for Atmospheric Research, FAA-Federal Aviation Administration, UC-University of Chicago, UCLA-University of California in Los Angeles, PSU-Penn State, CSU-Colorado State, SDSMT-South Dakota School of Mines and Technology, FSU-Florida State, UW-University of Wisconsin

- o BNA RADAP. Data in the form of Interactive Color Radar Display (ICRAD) products will be accessible via phone line from the BNA RADAP II system. ICRAD products will be displayed at NASA and stored on NASA computers. Raw RADAP data will be available on 9 track tape after completion of field operations.
- o Other NWS radars. Data from regional NWS radars will be accessed by a Kavouras RADAC system at NASA, and stored as images and perhaps recorded on video cassette. Manually-digitized radar (MDR) data and other special observations may be obtained from SRRS tapes and microfilm at NCDC.
- o NCAR Doppler radars (CP-2, CP-3, CP-4). These data will be handled primarily by NCAR. [It would be desirable to conduct preliminary analyses of single and multiple Doppler during field operations.] Although NCAR will serve as the primary data archive source, a secondary source may reside on the mass store device of the NASA EADS system.
- o FAA radars (UND and FL-2). FAA will serve as managers of these data.
- o NOAA P-3 radars. These data will be archived by NOAA in the form of 9-track tapes. A secondary partial archive may be stored on the NASA EADS system.

It would be highly desirable to store all archived radar data in universal radar format (see Barnes, 1980).

#### *e. Satellite Data*

The University of Wisconsin will collect, reduce and archive all satellite products. NASA will also archive these data. Satellite data platforms will include GOES, Nimbus 7, DMSP and NOAA 9,10 satellites. Satellite products will consist of visible and IR images, derived soundings of temperature and humidity, total moisture, other derived thermodynamic parameters, and winds.

### 7.2 Data Sets

Every intense observing period (IOP) will have an associated data set, composed of data from all available observational platforms. In addition, daily operations for both IOP and inactive periods will be documented. These data sets and associated documentaries are described below.

#### *7.2.1 Documentation of Daily Operations*

The success of any meteorological experiment depends on the ability to thoroughly document daily meteorological events and the measurement of such events. It is therefore desirable to document:

- o general meteorological conditions and events over the SPACE network;
- o what portion of the event(s) may have been measured;

- o the status of individual measurement programs, including measurements taken, status of instrumentation, calibrations, and work on equipment.

In regard to the final category above, it would be desirable to document and summarize:

- o radar operations
- o surface mesonet operations
- o rawinsonde operations
- o aircraft operations

In general this involves a summary of (a) the key measurements, (b) all interesting phenomenon, (c) the scientific implications, and (d) the quality of the measurements.

#### *7.2.2 Preliminary Data Sets*

One goal of data management is to make level IIA data available to scientists as quickly as possible so that data can be critically examined. It is expected that such timely availability would have several benefits:

- o It would check data quality.
- o It would check data acquisition optimization, e.g., whether data are being acquired in the right manner to answer the fundamental scientific questions being addressed.
- o It would provide a quick start to data analysis.

#### *7.2.3 Final Data Sets*

The availability of final corrected level IIB data sets (i.e. those suitable for detailed analyses) will be dependent on the complexity of the data set and the availability of resources from which the data originate. Highly complex data sets such as Doppler radar and aircraft may require preprocessing times of 6 months or more. Level IIB data sets will include all final corrections and updates to the original data, conversion of the data to a common or universal format, and commentaries on data quality, the nature of data correction, and conversions.

#### *7.2.4 Documents*

Several documents will describe the field program operations and results. The Operations Summary will include the daily summaries and operational activities discussed in Section 7.2.1. Next, a Data Inventory will provide basic information on each particular data set, with emphasis placed on IOP's. This document will contain an inventory of all

level IIB data available, indicate data quality, and outline procedures for data access. It is expected that other specialized data archive catalogs will be produced by institutions supporting complex data gathering systems, such as NCAR for Doppler radar.

### 7.3 Data Processing

#### 7.3.1 Facilities

Data under direct management of the SPACE program will be stored and manipulated within various computers as shown in Fig. 7.3.1. Principle MSFC computers include:

- o an IBM 4381 which will ingest Kavouras images, LLP data, NWS data and other image data;
- o a Harris/6 computer which will primarily work with image products;
- o a VAX 11/730 which will serve as a mainframe for sophisticated image processing;
- o an HP-1000F which will ingest, manipulate and display surface and sounding data.

In addition, several other computers will be available for data storage and processing:

- o a Perkin-Elmer 3254 mainframe minicomputer available for image processing and NEXRAD type radar processing;
- o an HP-1000 (A-900) available for aircraft data processing and perhaps image display of radar data;
- o a VAX 11/785 (possibly) to be used for multiple Doppler radar analysis;
- o a CRAY-XMP supercomputer perhaps available for cloud and mesoscale modeling purposes.

The IBM 4381, VAX 11/730 and CRAY-XMP represent primary processors of the NASA/MSFC Engineering Analysis and Data System (EADS). These computers will also be linked directly to the MSFC minicomputers listed above, and to external computers such as a MCIDAS IBM 4381 located at the University of Wisconsin (Fig. 7.3.1). The EADS system also contains a Mass Store Device (165 Gbyte) which may be used to store voluminous radar data.

Software has either been developed or is being incorporated on these computers so that displays and various analyses can be performed as soon as data becomes available.

#### 7.3.2 Data Quality Assurance and Validation

An important data management activity during field operations is data checking and

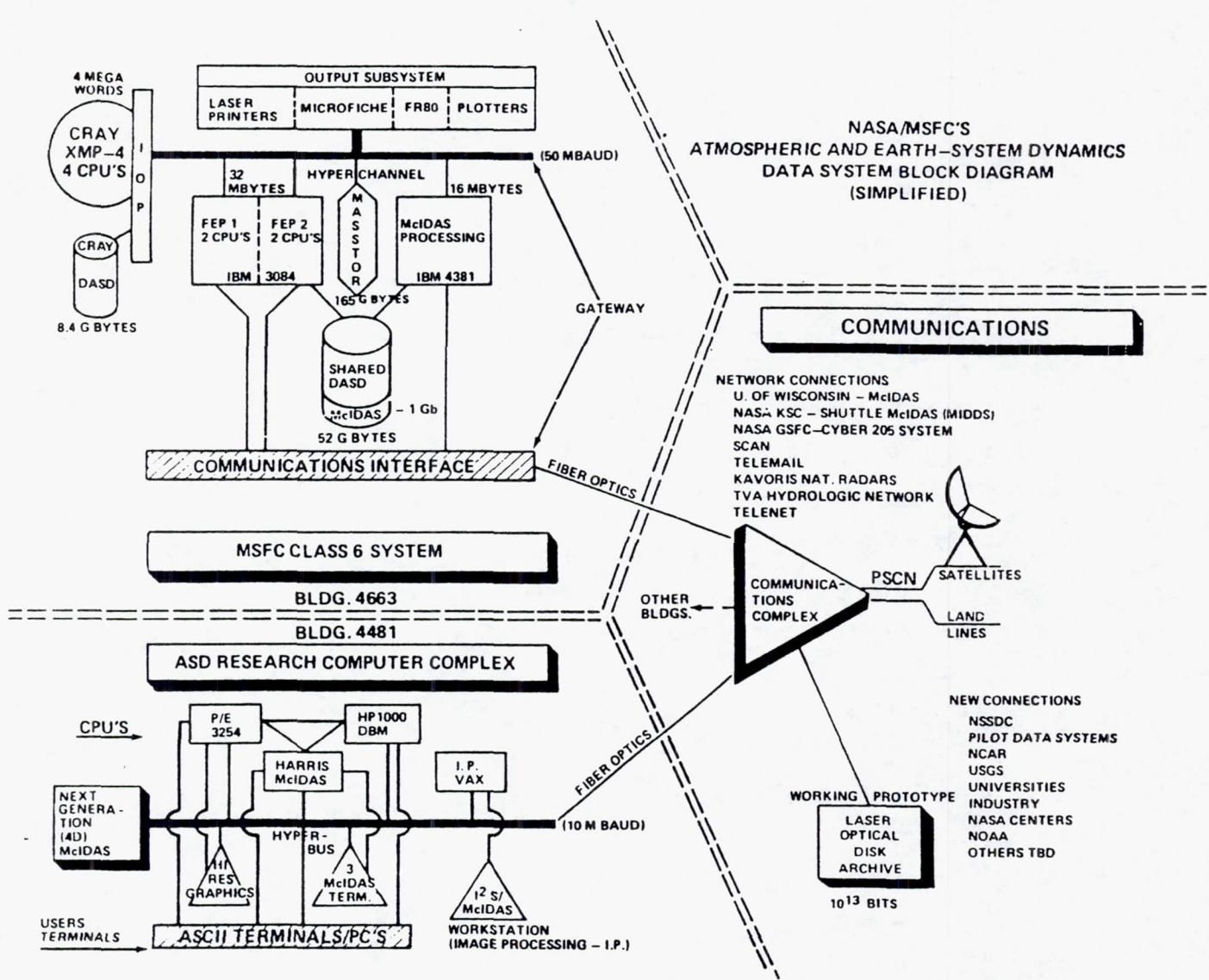


Fig. 7.3.1. General data flow and relationships among the computers within the Atmospheric Science Division of NASA/MSFC.

verification to ensure data accuracy and proper measurement strategies. It is planned to examine most forms of data at least superficially during the field program. Because detailed analyses and comparisons among independent data sets provide the most stringent test, preliminary but detailed analyses will be performed on:

- o single Doppler radar data (e.g., CP-2)
- o multiple Doppler radar (simple analyses)
- o surface data (PAM-II and NASA stations)
- o rawinsonde data
- o P-3 radar data
- o other aircraft data, including the ER-2, U-2C and T-28
- o satellite data

Much of the software required for these simple data analyses should be available by June 1. It is planned to exchange results of such analyses with other COHMEC scientists.

#### 7.4 Data Archiving and Distribution

The primary SPACE data center will be located at NASA Marshall Space Flight Center. Here, hard copies, observer notes, flight tracks, daily reports and other preliminary information will be stored in a dedicated data office during and after the field program. Much of the special experimental data will also be stored at MSFC, either on dedicated computer disks or on 9 track magnetic tape. It is expected that much of the radar, aircraft and satellite data will reside on 9 track tapes or on mass storage devices rather than dedicated computer disks.

The SPACE data management group (Table 7.4.1) will assume the responsibility of:

- o determining data formats and storage locations of final data sets, prior to the start of field operations;
- o informing potential users on the status and nature of data sets by distributing documents such as the operations summary, data inventory, and other information memos;
- o providing information on data available, and filling researchers' requests for specific data sets.

Further details on the data management process will be included in the forthcoming Data Management Plan document.

Table 7.4.1 SPACE Data Management Group

<u>Individual</u>	<u>Affiliation</u>	<u>Phone Number</u>
Paul Meyer	NASA/MSFC	(205) 453-1557 128
Kevin Knupp	UAH	(205) 895-6257
Steve Williams	UAH	(205) 895-6257

## REFERENCES

- Adler, R. F., and R. A. Mack, 1984: Thunderstorm cloud height-rainfall rate relations for use with satellite rainfall estimation techniques. *J. Clim. Appl. Meteor.*, 23, 280-296.
- Atkinson, B. W., 1981: *Meso-scale Atmospheric Circulations*. Academic Press Inc., 111 Fifth Ave., New York, New York 10003, 495pp.
- Barnes, S. L., 1980: Report on a meeting to establish a common Doppler radar data exchange format. *Bull. Amer. Meteor. Soc.*, 61, 1401-1404.
- Barnes, S. L. and D. K. Lilly, 1975: Covariance analysis of severe storm environments. *Preprints Ninth Conference on Severe Local Storms*, AMS, Boston, 301-306.
- Chen, C. H. and H. D. Orville, 1980: Effects of mesoscale convergence on cloud convection. *J. Appl. Meteor.*, 19, 256-274.
- Cheng, C. P. and R. A. Houze, Jr., 1979: The distribution of convective and mesoscale precipitation in GATE radar echo patterns. *Mon. Wea. Rev.*, 107, 1370-1381.
- Chesters, D., L. W. Uccellini, and W. D. Robinson, 1983: Low-level water vapor fields from the VISSR Atmospheric Sounder (VAS) "split window" channels. *J. Clim. Meteor.*, 22, 725-743.
- Diak, G., S. Heikkinen and J. Bates, 1986: The influence of variations in surface treatment in a 24 hour forecast with a limited area model, including a comparison with modeled and satellite-measured surface temperatures. *Mon. Wea. Rev.*, 114, 215-232.
- Doviak, R. J., and D. S. Zrnic, 1984: *Doppler Radar and Weather Observations*, Academic Press, 205-232.
- Foote, G. B., and H. W. Frank, 1983: Case study of a hailstorm in Colorado. Part III: Airflow from triple-Doppler measurements. *J. Atmos. Sci.*, 40, 686-707.
- Goodman, S. J., 1985: Real-time applications for remotely sensed lightning observations, *Preprints Conf. on Aerospace and Range Meteorology*, 27-29 Aug., Huntsville, AL, Am. Meteor. Soc.
- Hill, C. K. and R. E. Turner, 1983: NASA's AVE/VAS Program, *Bull. Amer. Meteor. Soc.*, 64, 796-797.
- Hiscox, W. L., E. P. Krider, A. E. Pifer, and M. A. Uman, 1984: A systematic method for identifying and correcting "site errors" in a network of magnetic direction finders, *Preprints Int. Conf. on Lightning and Static Elec.*, 26-28 June, Orlando, FL.
- Illingworth, A. J., 1985: Charge separation in thunderstorms : small scale processes, *J. Geophys. Res.*, 90, 6026-6032.
- Jedlovec, G. J., 1984: Mesoscale analysis of 6.7 micron image data from VISSR atmospheric Sounder (VAS) for several case studies. *Conf. on Satellite/Remote Sensing and Appl.*, AMS, Boston, 185-190.

- Jedlovec, G. J., 1985: An evaluation and comparison of vertical profile data from the VISSR Atmospheric Sounder (VAS). *J. Atmos. Ocean. Tech.*, 2, 559-581.
- Johnson, G. N., and P. L. Smith, Jr., 1980: Meteorological instrumentation system on the T-28 thunderstorm research aircraft. *Bull. Amer. Meteor. Soc.*, 61, 972-979.
- Kalb, M. W., 1985: Results from a limited area mesoscale numerical simulation for April 10, 1979. *Mon. Wea. Rev.*, 113, 1644-1662.
- Kaplan, M. L., 1982: Initial results from a mesoscale atmospheric simulation system and comparisons with the AVE-SESAME I data set. *Mon. Wea. Rev.*, 110, 1564-1590.
- Klemp, J. B., R. B. Wilhelmson, and P. Ray, 1981: Observed and numerically simulated structure of a mature supercell thunderstorm. *J. Atmos. Sci.*, 38, 1558-1580.
- Krider, E. P., R. C. Noggle, and M. A. Uman, 1976. A gated, wideband magnetic direction finder for lightning return strokes, *J. Appl. Meteor.*, 15, 301-306.
- Kropfli, R. A., and P. H. Hildebrand, 1980: Three-dimensional wind measurements in optically clear planetary boundary layer with dual Doppler radar. *Radio Sci.*, 15, 283-296.
- Latham, J., 1981: The electrification of thunderstorms, *Q. J. R. Meteor. Soc.*, 107, 277-298.
- Mach, D. M., and D. R. MacGorman, W. D. Rust, and R. T. Arnold, 1986. Site errors and detection efficiency in a magnetic direction finder network for locating lightning strokes to ground, accepted for publication, *J. of Atm. and Oceanic Tech.*
- McNider, R. T. and R. A. Pielke, 1981: Diurnal boundary-layer development over sloping terrain. *J. Atmos. Sci.*, 38, 2198-2212.
- Melfi, S. H. and D. Whiteman, 1985 : Observation of lower atmospheric moisture and its evolution using a Raman lidar. *Bull. Amer. Meteor. Soc.*, 66, 1288-1292.
- Menzel, W. P., W. L. Smith and L. D. Herman, 1981: VAS radiometric calibration: An inflight evaluation from intercomparisons with HIRS and radiosonde measurements. *Appl. Opt.*, 20, 3641-3644.
- Negri, A. J., and R. F. Adler, 1981: Relation of satellite-based thunderstorm intensity to radar-estimated rainfall. *J. Appl. Meteor.*, 20, 288-300.
- Negri, A. J., and R. F. Adler, 1984: A new technique to infer convective rainfall from satellite infrared cloud observations. *Preprints Conferences on Satellite Meteorology/Remote Sensing and Applications*, Clearwater Beach, FL, Amer. Meteor. Soc., 58-63.
- Negri, A. J., R. F. Adler, and P. J. Wetzel, 1984: An analysis of the Griffith-Woodley rain estimation technique. *J. Clim. Appl. Meteor.*, 23, 102-116.
- Newton, C. W., and J. C. Fankhauser, 1975: Movement and propagation of multicellular convective storms. *Pure Appl. Geophys.*, 113, 747-764.
- Orville, H. D. and F. J. Kopp, 1977: Numerical simulation of the life-cycle of a hailstorm. *J. Atmos. Sci.*, 34, 1596-1618.

- Paegle, J., J. N. Paegle and G. C. Dodd 1983: On the occurrence of atmospheric states that are non-elliptic for the balance equation. *Mon. Wea. Rev.*, 111, 1709-1723.
- Perkey, D. J. and C. W. Krietzberg, 1976: A time dependent lateral boundary scheme for limited-area primitive equation models. *Mon. Wea. Rev.*, 104, 744-755.
- Petersen, R. A., L. W. Uccellini, A. Mostek, and D. A. Keyser, 1984: Delineating mid- and low-level water vapor patterns in a preconvective environment using VAS moisture channels. *Mon. Wea. Rev.*, 112, 2178-2198.
- Pielke, R. A., 1974: A three-dimensional numerical model of the sea breeze over South Florida. *Mon. Wea. Rev.*, 102, 115-139.
- Piepgrass, M. V., E. P. Krider, and C. B. Moore, 1982: Lightning and surface rainfall during Florida thunderstorms, *J. Geophys. Res.*, 87, 11193-11201.
- Purdom, J. F. W., and K. Marcus, 1982: Thunderstorm trigger mechanisms over the southeast United States. *Preprints, 12th Conf. on Severe Local Storms*, AMS, 487-488.
- Robertson, F. R. and P. J. Smith, 1983: The impact of model moist processes on the energetics of extratropical cyclones. *Mon. Wea. Rev.*, 111, 724-744.
- Simpson, J., N. E. Westcott, R. J. Clerman, and R. A. Pielke, 1980: On cumulus mergers. *Arch. Meteor. Geophys. Biokl. Ser. A*, 29, 1-40.
- Smith, W. L., G. S. Wade, and H. M. Woolf, 1985: Combined atmospheric sounding/cloud imaging - a new forecasting tool. *Bull. Amer. Meteor. Soc.*, 66, 138-141.
- Smith, W. L., and H. M. Woolf, 1984: Improved Vertical soundings from an amalgamation of polar and geostationary radiame observations. *Preprints Cong. on Satellite/Remote Sensing and Application*, Clearwater Beach. Amer. Meteor. Soc., 45-48.
- Spencer, R.W., W.S. Olson, W. Rongzhang, D.W. Martin, J.A. Weinman, and D.A. Santek, 1983a: Heavy thunderstorms observed over land by the Nimbus 7 Scanning Multichannel Microwave Radiometer. *J. Climate Appl. Meteor.*, 22, 1041-1046.
- Spencer, R.W., D.W. Martin, B.B. Hinton, and J.A. Weinman, 1983b: Satellite microwave radiances correlated with radar rain rates over land. *Nature*, 304, 141-143.
- Spencer, R.W. 1984: Satellite passive microwave rain rate measurement over croplands during spring, summer, and fall. *J. Climate Appl. Meteor.*, 23, 1553-1562.
- Spencer, R.W., and D.A. Santek, 1985: Measuring the global distribution of intense convection over land with passive microwave radiometry. *J. Climate Appl. Meteor.*, 24, 860-864.
- Spencer, R.W., 1986: A satellite passive 37 GHz scattering based method for measuring oceanic rain rates. To appear in April *J. Climate Appl. Meteor.*
- Stewart, T. R., C.M. Hayden, and W. L. Smith, 1985: A note on water vapor wind tracking using VAS data on McIDAS. *Bull. Amer. Meteor. Soc.*, 66, 1111-1115.

- Szejwach, G., R. F. Adler, I. Jobard, and R. A. Mach, 1986: A cloud model-radiative model combination for determining microwave T - rainrate relations. *Preprints, Second Conf. on Satellite/Remote Sensing and Applications*, Williamsburg, VA, May 1986.
- Tao, W. K., and J. Simpson, 1984: Cloud interaction and merging. *J. Atmos. Sci.*, 41, 2901-2917.
- Uccellini, L. W., 1975: A case study of apparent gravity wave initiation of severe convective storms. *Mon. Wea. Rev.*, 103, 497-513.
- Ulanski, S. L. and M. Garstang, 1978: The role of surface divergence and vorticity in the life cycle of convective rainfall. Part I. Observation and analysis. *J. Atmos. Sci.*, 35, 1047-1062.
- Velden, C. S., W. L. Smith, and M. Mayfield, 1984: Applications of VAS and TDVS to tropical cyclones. *Bull. Amer. Meteor. Soc.*, 65, 1059-1067.
- Weisman, M. L., and J. B. Klemp, 1982: The dependence of numerically-simulated convective storms on vertical wind shear and buoyancy. *Mon. Wea. Rev.*, 110, 504-520.
- Weisman, M. and J. Klemp, 1984: The structure and classification of numerically simulated convective storms in directionally varying wind shears, *Mon. Wea. Rev.*, 112.
- Wilheit, T.T., A.T.C. Chang, M.S.V. Rao, E.B. Rodgers, and J.S. Theon, 1977: A satellite technique for quantitatively mapping rainfall rates over the oceans. *J. Appl. Meteor.*, 16, 551-560.
- Wilheit, T.T., A.T.C. Chang, J.L. King, E. B. Rodgers, R. A. Nieman, B. M. Krupp, A. S. Milman, J. S. Stratigos, and H. Siddalingaiah, 1982: Microwave radiometric observations near 19.35, 92, and 183 GHz of precipitation in Tropical Storm Cora. *J. Appl. Meteor.*, 21, 1137-1145.
- Wolfsom, M. M. , J. T. Di Stefano and B. E. Forman, 1985: The FLOWS Automatic Weather Station Network in Operation. DOT-FAA-PM-85/27.
- Wong, V. C., 1982: On the effect of the PBL parameterizations in a mesoscale numerical weather prediction. NATO Advanced Institute. *Theory, Observations, and Models*. Gascogne, France, July 13-31, 1982.
- Wu, R., and J.A. Weinman, 1984: Microwave radiances from precipitating clouds containing aspherical ice, combined phase, and liquid hydrometeors. *J. Geophys. Res.*, 89, 7170-7178.
- Yanai, M. S., S. Esbenen and J. H. Chu, 1973: Determination of bulk properties of tropical cloud clusters from large-scale heat and moisture budgets. *J. Atmos. Sci.*, 30, 611-627.

## **Appendix A**

### **SPACE Mailing List**

### SPACE MAILING LIST

<u>Name and Address</u>	<u>Telephone No.</u>
Dr. Robert Adler Mail Code 675 NASA/Goddard Space Flight Center Greenbelt, MD 20771	(301) 344-9086
Dr. James Arnold Mail Code ED-43 NASA/Marshall Space Flight Center Huntsville, AL 35812	(205) 544-1650
Mr. John Arvesen N240-6 NASA/AMES Research Center Moffett Field, CA 94035	(415) 694-5376
Mr. Dick Beranek Advanced Systems Office Mail Code PS02 NASA/Marshall Space Flight Center Huntsville, AL 35812	(205) 453-3430
Dr. Richard Blakeslee Mail Code ED-43 NASA/Marshall Space Flight Center Huntsville, AL 35812	(205) 544-1652
Dr. William Bonner NOAA W/NMC World Weather Bldg. 5200 Auth Rd. Washington, DC 20233	(202) 763-8016
Mr. David Bowdle Mail Code ED-43 UAH/Marshall Space Flight Center Huntsville, AL 35812	(205) 544-1682
Dr. V. N. Bringi Department of Electrical Engineering Colorado State University Fort Collins, CO 80523	(303) 491-5595
Dr. Marx Brooks R & D Division New Mexico Institute of Mining and Technology Socorro, NM 87801	(505) 835-5611

Mr. Dennis Buechler  
Mail Code ED-43  
USRA/Marshall Space Flight Center  
Huntsville, AL 35812 (205) 544-1687

Dr. Rit Carbone  
NCAR/FOF  
P.O. Box 3000  
Boulder, CO 80307 (303) 497-8812

Dr. Hugh Christian  
Mail Code ED 43  
NASA/Marshall Space Flight Center  
Huntsville, AL 35812 (205) 544-1649

Dr. William R. Cotton  
Department of Atmospheric Science  
Colorado State University  
Ft. Collins, CO 80523 (303) 491-8593

Dr. Robert Curran  
Code EE  
NASA Headquarters  
600 Independence Avenue, SW  
Washington, DC 20546 (202) 453-1680

George Diak  
University of Wisconsin  
SSEC  
1225 W. Dayton Street  
Madison, WI 53706 (608) 263-5862

Mr. John Distefano  
MIT-Lincoln Laboratory  
P.O. Box 73  
Building V-108  
Lexington, MA 02173-0073 (617) 863-5500 ext. 3452

Dr. James Dodge  
NASA/Headquarters  
Mail Code EE-8, OSSA  
600 Independence Av.  
Washington, DC 20546 (202) 453-1680

Dr. G. Dave Emmitt  
Simpson Weather Associates  
809 E. Jefferson Street  
Charlottesville, VI 22902 (804) 979-3570

Dr. Oscar Essenwanger  
U.S. Army Missile Command  
Attn: AMSMI-RD-RE-AP  
Redstone Arsenal, AL 35898-5248 (205) 876-4872

Dr. James Evans (617) 863-5500 ext. 7475  
MIT-Lincoln Laboratory  
P.O. Box 73  
Building V-108  
Lexington, MA 02173-0073

Dr. George Fichtl, Chief (205) 544-1633  
Fluid Dynamics Branch  
Mail Code ED-42  
NASA/Marshall Space Flight Center  
Huntsville, AL 35812

Dr. Nat Fisher (205) 461-7074  
MIT/LL Radar Facility  
P.O. Box 6041  
Huntsville, AL 35806

Dr. Gregory S. Forbes (814) 863-2458  
Department of Meteorology  
Pennsylvania State University  
621 Walker Blvd.  
University Park, PN 16802

Dr. Henry Fuelberg (904) 644-6466  
Department of Meteorology  
Florida State University  
Tallahassee, FL 32306

Dr. T. Theodore Fujita (312) 962-8112  
The University of Chicago  
Department of the Geophysical Sciences  
5734 Ellis Avenue  
Chicago, IL 60637

Dr. Joseph H. Golden (301) 427-7722  
W/OTS22  
National Weather Service  
8060 13th Street, Rm. 715  
Silver Spring, MD 20910

Mr. Michael Goodman (205) 895-6257  
K. E. Johnson Environmental and Energy Center  
University of Alabama in Huntsville  
Huntsville, AL 35899

Mr. Steve Goodman (205) 544-1683  
Mail Code ED-43  
USRA/Marshall Space Flight Center  
Huntsville, AL 35812

Dr. Claude Green, Chief  
Atmospheric Effects Branch  
Mail Code ED-44  
NASA/Marshall Space Flight Center  
Huntsville, AL 35812 (205) 544-1658

Mr. Joe Haynes  
NOAA/NWS  
Meteorological Observatory  
500 Weather Station Rd.  
Old Hickory, TN 37138 (615) 758-5270

Dr. Gerald Heymsfield  
Mail Code 612  
NASA/Goddard Space Flight Center  
Greenbelt, MD 20771 (301) 344-6369

Dr. Ron Holle  
NOAA ERL WRP  
R/E 22  
325 Broadway St.  
Boulder, CO 80303 (303) 497-3000

Dr. Robert A. Houze  
Dept. of Atmospheric Sciences  
University of Washington  
Seattle, WA 98195 (206) 543-4250

Dr. Michael D. Hudlow  
National Weather Service  
W/OH3, Room 530  
8060 13th Street  
Silver Spring, MD 20910 (301) 427-7940

Dr. Umran S. Inan  
Dept. of Electrical Engineering  
STAR Laboratory  
321 Durand St.  
Stanford University  
Stanford, CA 94305 (415) 723-4994

Mr. Gary Jedlovec  
Cooperative Institute for  
Meteorological Satellite Studies  
1225 W. Dayton Street  
Madison, WI 53706 (608) 262-0544

Mr. Don Johnson  
FAA APM-310  
800 Independence Ave. S.W.  
Washington, DC 20591 (202) 426-8573

Dr. Michael Kalb (205) 544-1684  
Mail Code ED-43  
USRA/Marshall Space Flight Center  
Huntsville, AL 35812

Dr. Michael Kaplan (804) 865-7800  
MESO  
Langley Executive Center  
28 Research Drive  
Hampton, VI 23666

Dr. Kevin Knupp (205) 895-6257  
K. E. Johnson Environmental and Energy Center  
The University of Alabama in Huntsville  
Huntsville, AL 35899

Lt. Col E. Kolczynski (305) 494-5915  
ESMC/WER  
Patrick AFB, FL 32925

Dr. Carl Kreitzburg (215) 895-2708  
Dept. of Physics and Atmospheric Science  
Drexel University  
32nd and Chestnut Street  
Philadelphia, PA 19104

Dr. Phil Krider (602) 621-6836  
Institute of Atmospheric Physics  
University of Arizona  
Tucson, AZ 85721

Mr. Rich Lay (609) 484-5325  
FAA Technical Center, ACT-150  
Atlantic City Airport, NJ 08405

Dr. Robert Maddox (303) 497-3000  
NOAA/ERL  
WRP, R/E22  
325 Broadway St.  
Boulder, CO 80303

Dr. Tom Marshall (601) 232-5325  
Department of Physics and Astronomy  
University of Mississippi  
University, MS 38677

Dr. George McDonough, Director (205) 544-1412  
Systems Dynamics Laboratory  
Mail Code ED-01  
NASA/Marshall Space Flight Center  
Huntsville, AL 35812

Dr. Wayne McGovern  
Mesoscale Technique Branch  
Techniques Dev. Lab  
SDO/NWS/NOAA  
8060 13th Street  
Silver Spring, MD 20910 (301) 427-7773

Dr. Richard McNider  
K. E. Johnson Environmental and Energy Center  
The University of Alabama in Huntsville  
Huntsville, AL 35899 (205) 895-6257

Dr. S. Harvey Melfi  
Mail Code 600  
NASA/Goddard Space Flight Center  
Greenbelt, MD 20771 (301) 344-6171

Dr. Paul Menzel  
NOAA/NESDIS  
University of Wisconsin  
1225 W. Dayton Street  
Madison, WI 53706 (608) 364-5325

Mr. Paul Meyer  
Mail Code Ed-43  
NASA/Marshall Space Flight Center  
Huntsville, AL 35812 (205) 544-1654

Ms. Cindy Mueller  
NCAR/FOF  
P.O. Box 3000  
Boulder, CO 80307 (303) 497-8805

Mr. Al Paradis  
MIT-Lincoln Laboratory  
P.O. Box 73  
Lexington, MA 02173-0073 (617) 863-5500 ext. 3547

Dr. Don Perkey  
Dept. of Physics and Atmospheric Science  
Drexel University  
32nd and Chestnut Street  
Philadelphia, PA 19104 (215) 895-2708

Dr. Roger A. Pielke  
Department of Atmospheric Science  
Colorado State University  
Ft. Collins, CO 80523 (303) 491-8293

Mr. Mike Poellot  
P.O. Box 8216  
University Station  
Grard Fork, ND 58202 (701) 777-3180

Dr. James Purdom (303) 221-1344  
NOAA/NESDIS  
Colorado State University  
Dept. of Atmospheric Sciences  
Ft. Collins, CO 80523

Dr. Harry Orville (605) 394-2291  
Institute of Atmospheric Sciences  
South Dakota School of Mines and Technology  
Rapid City, SD 57701-3995

Dr. Peter Ray (904) 644-1894  
Department of Meteorology  
Florida State University  
Tallahassee, FL 32306

Mr. Ron Reap (301) 427-7772  
Mesoscale Technique Branch  
Techniques Dev. Lab  
8060 13th Street  
Silver Spring, MD 20910

Dr. Ron Rinehart (617) 863-5500 ext. 3299  
MIT-Lincoln Laboratory  
P.O. Box 73  
Building V-108  
Lexington, MA 02173-0073

Dr. Al Rodi (307) 766-4945  
University of Wyoming  
P.O. Box 3038  
Laramie, WY 82071

Dr. F. P. Robertson (205) 544-1655  
Mail Code ED-43  
NASA/Marshall Space Flight Center  
Huntsville, AL 35812

Dr. Dave Rust (405) 360-3620  
National Severe Storms Laboratory  
1313 Halley Circle  
Norman, OK 73609

Mr. Robert Saffle (301) 427-7772  
NOAA/TDL W/OSD 23  
8060 13th St.  
Silver Spring, MD 20910

Dr. Robert Schiffer (202) 453-1680  
NASA Headquarters  
Code EE  
600 Independence Avenue  
Washington, DC 20546

Dr. Tom Seliga (814) 865-4542  
College of Engineering  
The Pennsylvania State University  
101 Hammond Building  
University Park, PA 16802

Dr. Robert Serafin (303) 497-8830  
NCAR/FOF  
P.O. Box 3000  
Boulder, CO 80307

Dr. Joanne Simpson (301) 344-5105  
Mail Code 675  
NASA/Goddard Space Flight Center  
Greenbelt, MD 20771

Dr. Peter Sinclair (303) 491-8679  
Dept. of Atmospheric Science  
Colorado State University  
Fort Collins, CO 80523

Dr. Eric Smith (904) 644-6205  
Department of Meteorology  
Florida State University  
Tallahassee, FL 32306

Dr. Paul L. Smith (605) 394-2291  
Institute of Atmospheric Sciences  
South Dakota School of Mines and Technology  
Rapid City, South Dakota 57701-3995

Dr. Robert Smith, Deputy Chief (205) 544-1628  
Atmospheric Sciences Division  
Mail Code ED-41  
NASA/Marshall Space Flight Center  
Huntsville, AL 35812

Dr. William Smith, Chief (608) 263-4085  
Director, CIMSS  
University of Wisconsin  
1225 W. Dayton Street  
Madison, WI 53705

Dr. Roy Spencer (205) 544-1686  
Mail Code ED-43  
USRA/Marshall Space Flight Center  
Huntsville, AL 35812

Dr. James Spinhirne (301) 344-9099  
Mail Code 615  
NASA/Goddard Space Flight Center  
Greenbelt, MD 20771

Dr. Ramesh C. Srivastava (312) 962-8125  
Department of the Geophysical Sciences  
The University of Chicago  
5734 S. Ellis Avenue  
Chicago, IL 60637

Dr. Ron C. Taylor (202) 357-7624  
Meteorology Program (ATM)  
NSF  
1800 G Street, NW  
Washington, D.C. 20550

Dr. John Theon (202) 453-1680  
NASA Headquarters (EE-8)  
600 Independence Avenue, SW  
Washington, D.C. 20546

Mr. Don Turnbull (202) 472-7047  
FAA, APM-310  
800 Independence, Avenue, SW  
Washington, D.C. 20591

Dr. Louis Uccelini (301) 344-5786  
NASA Code 612  
NASA/Goddard Space Flight Center  
Greenbelt, MD 20771

Mr. Otha H. Vaughan (205) 544-1648  
Mail Code ED-43  
NASA/Marshall Space Flight Center  
Huntsville, Alabama 35812

Dr. William W. Vaughan, Chief (205) 544-1626  
Atmospheric Sciences Division  
Mail Code ED-41  
NASA/Marshall Space Flight Center  
Huntsville, AL 35812

Mr. John L. Vogel (217) 333-4261  
Climate Information Unit  
Illinois Dept. of E N R  
2204 Griffith Drive  
Champaign, IL 61820

Dr. Tom Vonder Haar (303) 491-8566  
Department of Atmospheric Sciences  
Colorado State University  
Fort Collins, CO 80523

Dr. Fred Vukovich (919) 541-5813  
Research Triangle Institute  
P.O. Box 12194  
Research Triangle Park, NC 27709

Dr. Roger Wakimoto  
Department of Atmospheric Science  
7127 Math Sciences Building  
UCLA  
Los Angeles, CA 90024 (213) 825-1751

Mr. Don Warren  
Data Services Branch (615) 632-8155  
Tennessee Valley Authority  
250 Evans Building  
Knoxville, TN 37902

Mr. Mark Weber  
MIT/Lincoln Laboratory (617) 863-5500 ext. 3294  
P.O. Box 73  
Lexington, MA 02173-0073

Dr. Thomas Wilheit  
Mail Code 675 (301) 344-5105  
NASA/Goddard Space Flight Center  
Greenbelt, MD 20771

Mr. Steve Williams  
K.E. Johnson Environmental and Energy Center (205) 895-6257  
University of Alabama in Huntsville  
Huntsville, AL 35899

Dr. Greg Wilson, Chief  
Atmospheric Physics Branch (205) 544-1616  
Mail Code ED-43  
NASA/Marshall Space Flight Center  
Huntsville, AL 35812

Dr. Jim Wilson  
NCAR/FOF (303) 497-8818  
P.O. Box 3000  
Boulder, CO 80307

Ms. Marilyn Wolfson  
MIT-Lincoln Laboratory (617) 863-5500  
P.O. Box 73  
Building V-108  
Lexington, MA 02173-0073

Mr. J. T. Young  
University of Wisconsin (608) 262-6314  
SSEC  
1225 W. Dayton Street  
Madison, WI 53706

Mr. Jim Young  
US Army Missile Command (205) 876-2449  
Attn: AMSMI-RD-TE-F (ASL Met Team)  
Redstone Arsenal, AL 35898-5250

Dr. Ed Zipser  
NCAR  
P.O. Box 3000  
Boulder, CO 80307

(303) 497-1000

## **Appendix B**

### **Acronyms**

## ACRONYMS

- ADAS - Automated Data Acquisition System  
AFOS - Automation of Field Operations and Services  
AHN - Athens, GA  
AMMS - Advanced Microwave Moisture Sounder  
AMPR - Advanced Microwave Precipitation Radiometer  
ARC - Ames Research Center  
ASD - Atmospheric Science Division  
ATC - Air Traffic Control  
AVHRR - Advanced Very High Resolution  
BNA - Nashville, TN  
CAPE - Convective Available Potential Energy  
CCD - Charge Couple Device  
CCOPE - Cooperative Convective Precipitation Experiment  
CIMSS - Cooperative Institute for Meteorological Satellite Studies  
CKL - Centerville, AL  
CLS - Cloud Lidar System  
COHMEX - Cooperative Huntsville Meteorological Experiment  
CSIS - Central Storm Information System  
CSU - Colorado State University  
DMP - Data Management Plan  
DMSP - Defense Meteorological Satellite Program  
DS - Dwell Soundings  
D/VIP - Digital Video Integrator and Processor  
EADS - Engineering Analysis & Data System  
EOS - Earth Observing System  
ER-2 - High Altitude Aircraft

FAA - Federal Aviation Administration  
FACE - Florida Area Cumulus Experiment  
FLOWS - FAA - Lincoln Laboratory Operational Weather Study  
FSU - Florida State University  
GALE - Genesis of Atlantic Lows Experiment  
GARP - Global Atmospheric Research Program  
GATE/MONEX - Global Atlantic Tropical Experiment/Monsoon Experiment  
GMD - Ground Meteorological Detector  
GMT - Greenwich Mean Time  
GOES - Geostationary Operational Environmental Satellite  
GOES - Next - The next GOES  
GSFC - Goddard Space Flight Center  
HIRS - High resolution Infrared Radiometer Sounder  
HIS - High-resolution Interferometer Spectrometer  
HP - Hewlett Packard  
HTS - Huntington, WV  
IBM - International Business Machines  
ICRAD - Interactive Color Radar Display  
IDE - Isolation Distributions Equipment  
IOP - Intense Observing Period  
IR - Infrared  
JAN - Jackson, MS  
KSC - Kennedy Space Center  
LAMPS - Limited Area Mesoscale Predicting System  
LEO - Low-Earth Orbit  
LI - Lifted Index  
LIP - Lightning Instrumentation Package

LIT - Little Rock, AR

LLP - Lightning, Location and Protection

LRP - Lightning Research Package

MAMS - Multi-spectral Atmospheric Mapping Sensor

MASS - Mesoscale Atmospheric Simulation System

MCIDAS - Main Computer Interactive Data Analysis System

MCR - Multi-channel Cloud Radiometer

MCS - Mesoscale Convective System

MDR - Manually Digitized Radar

MIST - Microburst and Service Thunderstorm

MLIDS - Modular Lightning Information and Display System

MPR - Microwave Precipitation Radiometer

MRI - Meteorology Research Incorporated

MSFC - Marshall Space Flight Center

MSI - Multi-Spectral Images

MSU - Microwave Sounding Unit

MTS - Microwave Temperature Sounder

NAMS - NASA Mesonet System

NASA - National Aeronautics and Space Administration

NASA/ARC - NASA/Ames Research Center

NCAR - National Center for Atmospheric Research

NCDC - National Climatic Data Center

NEXRAD - Next Generation Weather Radar

NMC - National Meteorological Center

NOAA - National Oceanic and Atmospheric Administration

NSF - National Science Foundation

NWS - National Weather Service

PAM - Portable Automated Meteorological (Observing System)  
PBL - Planetary Boundary Layer  
PDL - Processor Data Loads  
PI - Principal Investigator  
PMS FSSP - Particle Measurement System - Forward Scattering Spectrometer Probe  
PSU - Pennsylvania State University  
PVA - Positive Vorticity Advection  
RADAP - Radar Data Processor  
RAMS - Regional Atmospheric Modeling System  
SDSM & T - South Dakota School of Mining and Technology  
SESAME - Severe Storm and Mesoscale Experiment  
SFC - Surface  
SLO - Salem-Leckrone, IL  
SMMR - Scanning Multichannel Microwave Radiometer  
SPACE - Satellite Precipitation And Cloud Experiment  
SRRS - Service Record Retention System  
SSEC - Space Science and Engineering Center  
SSM - Sub-Synoptic Model  
SSM/I - Special Sensor Microwave Imager  
STORM - Stormscale Operational and Research Meteorology  
TASS - Terminal Area Simulation System  
TDR - Terminal Doppler Radar  
TOVS - Tiros Operational Vertical Sounder  
TVA - Tennessee Valley Authority  
UAH - University of Alabama at Huntsville  
UC - University of Chicago  
UCLA - University of California at Los Angeles

USGS - United States Geological Survey

USRA - Universities Space Research Association

UW - University of Wisconsin

VAS - VISSR Atmospheric Sounder

VHF - Very High Frequency

VISSR - Visible and Infrared Spin Scan Radiometer

WSI - Weather Service Incorporated

WSR - Weather Service Radar

**Field Program Observations under SPACE-COHMEX.**

83

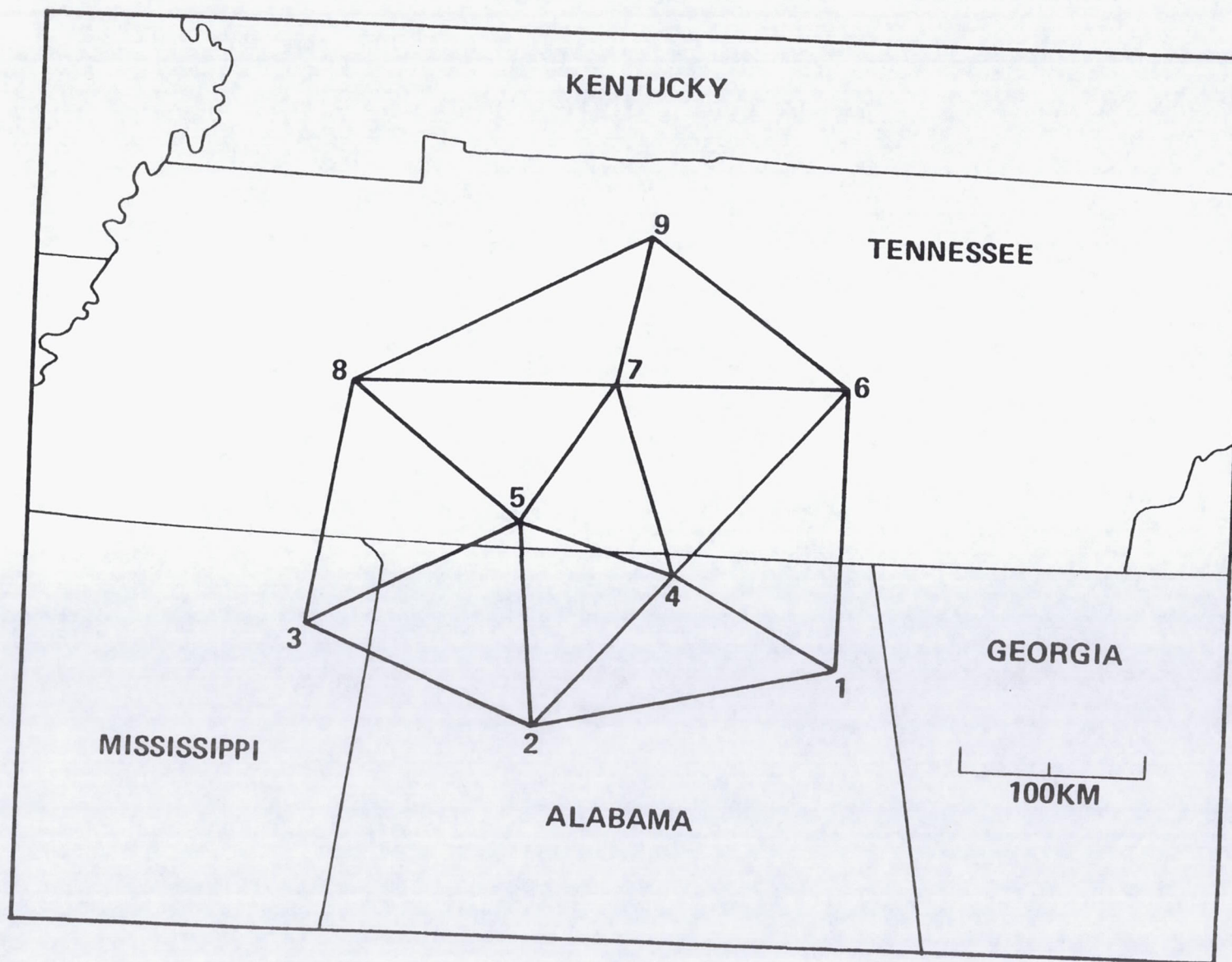


Fig. 5.3.2. The SPACE meso-beta scale rawinsonde sounding network.

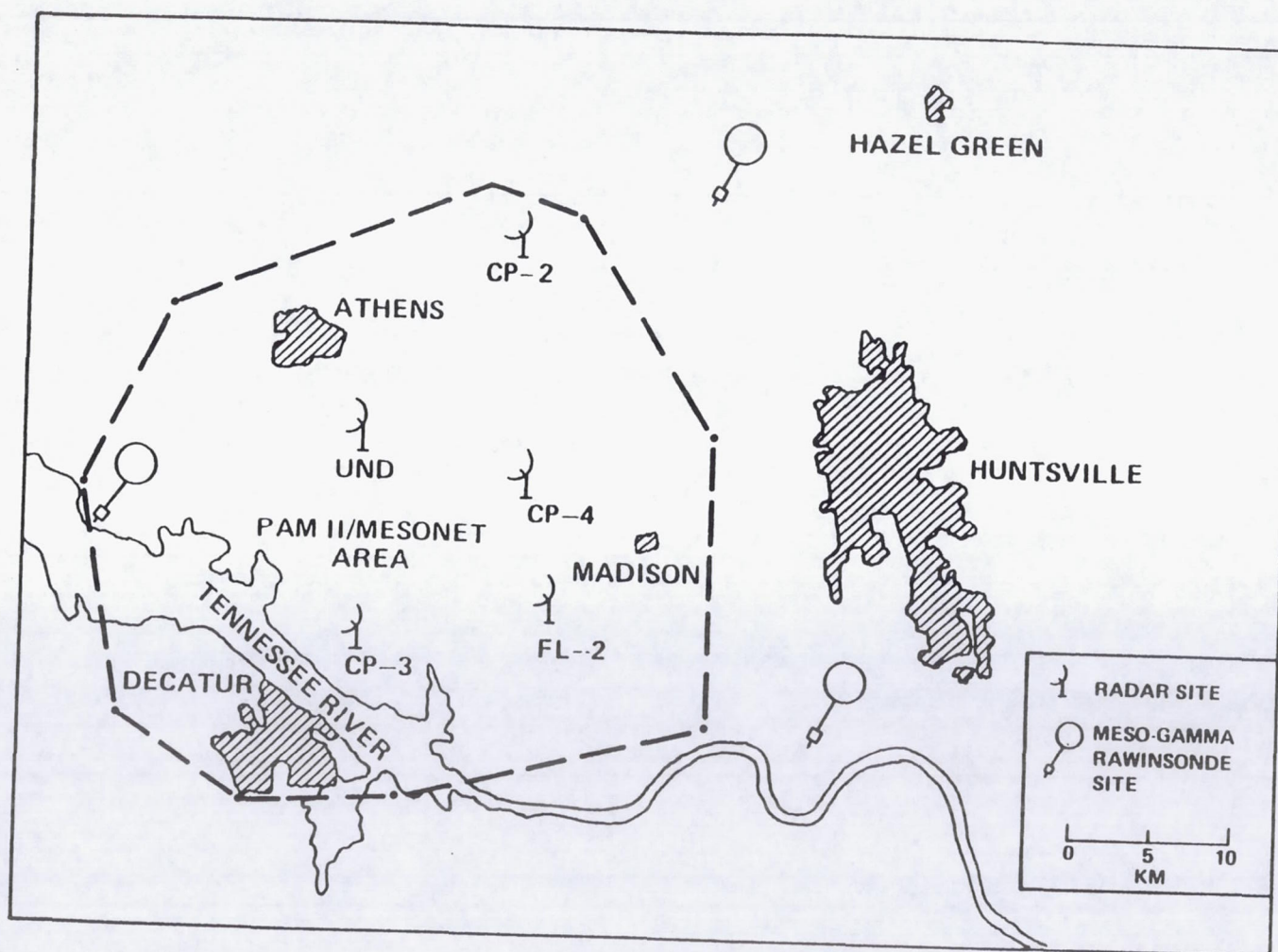


Fig. 5.3.3. The SPACE meso-gamma scale rawinsonde sounding network.

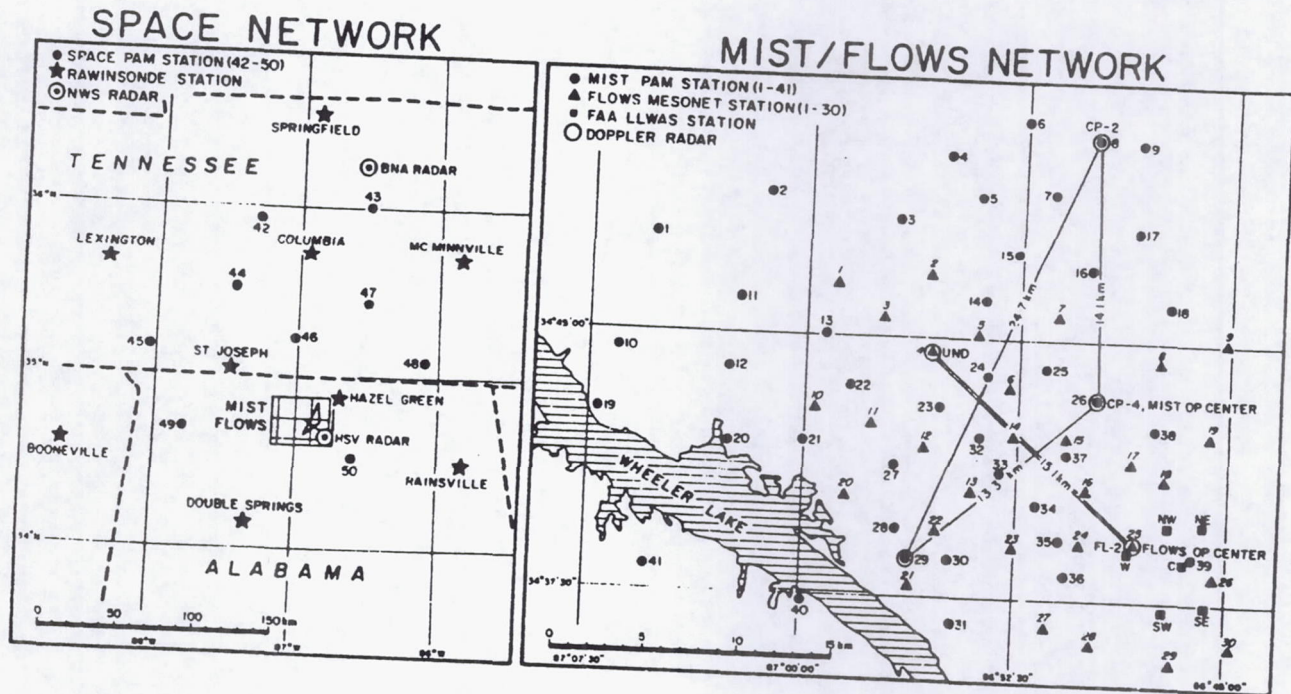


Fig. 5.4.2. (left) Locations of SPACE network surface stations.  
(right) Locations of MIST and FLOWS surface stations.

**Mesoscale Numerical Modeling of Boundary  
Layer Initiation of Convection.**

Tenth Conference on Weather  
Forecasting and Analysis  
American Meteorological  
Society, Tampa, Florida  
June, 1984.

DATA ANALYSIS AND MODEL SIMULATION  
OF THE INITIATION OF CONVECTION ON  
APRIL 24, 1982

Richard T. McNider

University of Alabama in Huntsville  
Huntsville, AL 35899

Gary J. Jedlovec Gregory S. Wilson

Marshall Space Flight Center  
Huntsville, Alabama

## 1.0 INTRODUCTION

Mesoscale boundary layer forcings have long been considered as a mechanism for inducing convective storm development either directly by producing sea breeze or topographic convergence zones [Pielke (1974), Kuo and Orville (1973)] or in a more subtle manner by destabilizing the atmosphere by differential advection of heat and moisture through creation of low level jets [Means (1954)]. While recent works; e.g., Uccellini and Johnson (1979) and Djuric and Damiani (1980) have significantly advanced understanding of the role of upper level dynamics to the development of low level jets and upper level divergence conducive to the formation of convective systems, thermal boundary layer forcing mechanisms appear to remain equal or dominant partners in the initiation and maintenance of many convective systems [Wong (1982), Uccellini et al. (1983), Carlson et al. (1983), Sun and Ogura (1979)]. Many times the role of mesoscale boundary layer forcing versus synoptic scale forcing is often obscured because both mechanisms appear to be operating simultaneously. This is not too surprising since synoptic conditions where upper level dynamics are important are also conducive to differential thermal forcing from either cloud shadowing or topography.

In the present study a combined modeling and data analysis is used to examine the initiation of a hail-producing mesoscale convective system which developed over the Texas panhandle near Amarillo, Texas, on April 24, 1982 and propagated east into Oklahoma. This case is of note because the development took place during the NASA AVE-VAS IV Experiment while a dense upper air mesoscale network was collecting data at three-hour intervals. In order to unravel the causes of convection, the situation was examined from both a synoptic point of view using MCDAS analyses and imagery as well as from a boundary layer forcing perspective using a numerical boundary layer model and subsynoptic analyses of the special network data.

## 2.0 SYNOPTIC ANALYSIS

The general synoptic situation for the study period is similar to the 9-10 May 1979, case discussed by Ogura et al. (1982). A 500 mb low trough at 12Z 24 April situated over the Colorado-New Mexico border moved across the study area (see Figure 1) so that by 12Z 25 April the closed center was located east of Amarillo. Surface and upper level winds near Amarillo during the period gradually shifted from a south or southwesterly direction to a more westerly direction.

On the morning of the 24th the skies near Amarillo were clear while 200 km to the east a large shield of stratus, associated with overrunning of a stationary front along the northern Gulf of Mexico, covered much of east Texas. Figure 2 shows a visible satellite picture at 1800Z showing the large shield of clouds over east Texas and the beginnings of the convective line in the Texas panhandle which is the focus of study here. By 1800Z, the line of stratus had retreated slightly to the east of its 12Z position.

The clear area in the Texas panhandle west of the stratus deck underwent intense surface heating while to the east dense cloud cover kept surface warming to a minimum. This heating is illustrated by Figure 3, which gives a time sequence of Amarillo soundings for three special observing times and shows the development of a nearly adiabatic layer up to near 350 mb. The evolution of such a deep near adiabatic profile is due not only to the surface heating but to cooling between 500 mb and 300 mb. This combination of strong surface heating and cold advection aloft effectively removed any barrier to developing convection.

The source of moisture for the convection is somewhat open to question. From a synoptic point of view upper level moistening (see Figure 3) was

due to flow from the cloudy region on the Colorado-New Mexico border. Near the surface, however, the development of a shallow slightly southeasterly flow during day (which will be discussed later) could have been drawing moisture from the east. Thus the synoptic setting is similar to the dryline condition discussed by Sun and Ogura (1979) in that moisture was available to the east of the stratus line or dryline.

Upper level synoptic dynamic forcing of convection is not strongly evident; however, a weak jet streak (see Figure 1) does propagate around the trough in northern Mexico well to the south of the study area. Such jet streak propagation and subsequent mass adjustment could have provided some forcing [Uccellini and Johnson (1979)], but, strongest lifting would seem to have occurred near the jet maximum not in the region near Amarillo.

### 3.0 MESOSCALE DATA ANALYSIS

As mentioned in the introduction the initiation of the convective line took place during the AVE-VAS IV data collection period so that special rawinsonde information was available. Unfortunately, the actual initiation of the convection line took place to the east of the special dense mesoscale rawinsonde network. Special three-hourly rawinsonde data, however, were available from regular stations in the area, and the dense mesoscale network was useful in describing the pre-convective mesoscale environment.

Figure 4. shows cross-sections of the wind and thermal structure in the study area on the early morning of the 24th (1400Z) from the special rawinsonde network. As can be seen, the isentropes show very little baroclinicity especially in the area between Amarillo and Crowell where the convection was later initiated. The winds over the western part of the domain were primarily southwesterly near the surface becoming more westerly with height. There is also little indication of convergence between Amarillo and Crowell.

This early morning structure can be compared to the quite different thermal and wind structure which developed later (2300Z) and given in Figure 5. The most striking feature is the pronounced baroclinic zone which has developed, apparently from the large variation in surface heating due to cloud shadowing. The structure is similar to the thermal structure in a sea breeze zone or the inland sea breeze structure described by Ogura et al. (1982). It is difficult to infer the actual horizontal thermal gradient due to station spacing and the analysis given here simply distributed the gradient evenly between stations.

The wind field is also quite different than the early morning structure with a southeasterly flow having developed near the surface to the east of Amarillo. This produces an area of surface convergence between Amarillo and Crowell which is accentuated by the fact that winds at Amarillo became more westerly due to the propagation of the synoptic scale trough. The development of this easterly component to the flow is evidently a dynamic response to the boundary layer thermal structure with a relative surface high forming to the east and a relative surface low to the west.

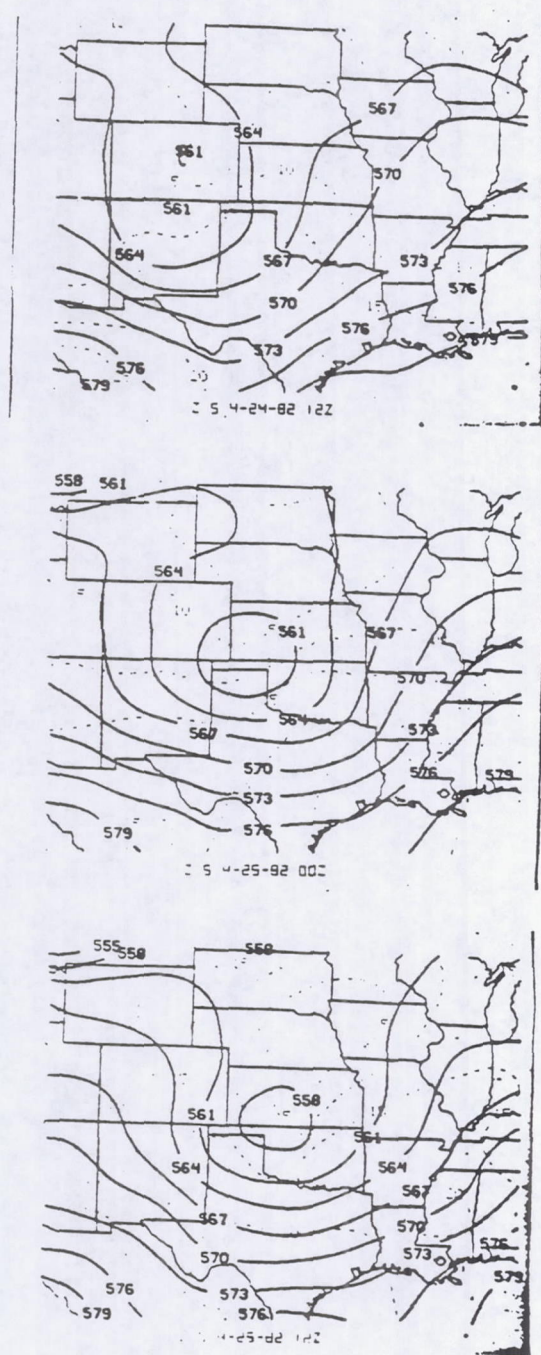


Figure 1. Time sequence of 500 mb analyses during the study period. Convection was initiated at approximately 1800Z, 24 April. Height contours are in decameters (solid) and isotachs are in meters/sec (dashed).



Figure 2. Visible satellite image at 1800Z, 24 April, showing the extensive cloud shield over east Texas and the beginnings of the convective line in the Texas panhandle.

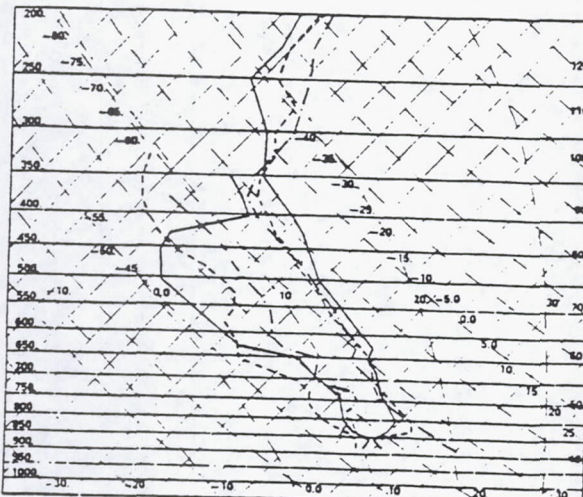


Figure 3. Time sequence of special three-hourly soundings at Amarillo. 1100Z (solid); 1400Z (dashed); 1700Z (dot-dashed). Note the extreme heating at the surface and cooling aloft.

Not only does the boundary layer thermal structure apparently produce the convergence zone but the remaining westerly flow aloft is such that strong advective warming is apparently occurring aloft. The result of this warm air from the west overrunning the cool pool of air to the east serves to strongly stabilize the atmosphere. This can be seen by the packing of the isentropes over Henrietta due perhaps to mesoscale subsidence.

The result of the developing southeasterly flow producing convergence is depicted in Figure 6. As can be seen the surface convergence is quite strong to the east of Amarillo and it is this surface convergence which evidently initiated the convective line. In the next section a modeling analysis is undertaken to examine the development of the thermal structure and the response of the wind field to the evolving thermal structure.

#### 4.0 MODEL ANALYSIS

##### 4.1 Mesoscale Forcing Mechanisms

The above analysis showed that a developing easterly component during the day of the 24th led to surface convergence east of Amarillo which could have been the triggering mechanism for the convective line which formed at approximately 1800Z. The analysis also indicated that the easterly component was a dynamic response to the evolving thermal structure. The synoptic situation and location of the easterly flow suggests that at least two mesoscale forcing mechanisms could have been operating to produce the thermal structure and the flow field:

- (1) Cloud Shading - Reduction in surface insolation by the stratus deck in east Texas coupled with clear skies in west Texas would lead to a surface east-west thermal gradient. This thermal gradient with concomitant differential boundary layer growth could produce a direct thermal circulation with easterly flow at the surface and westerly flow aloft. Such a direct circulation has been described as an inland sea breeze effect by Sun and Ogura (1979).
- (2) Topography - As can be seen the gently sloping topography upward from east to west would be conducive to a thermally driven upslope motion. Conceptually such an upslope flow with sharp changes of topographic slope east of Amarillo is also consistent with the surface observations.

A modeling analysis was undertaken to evaluate the relative role of these two forcing mechanisms in producing the thermal and wind structure described earlier.

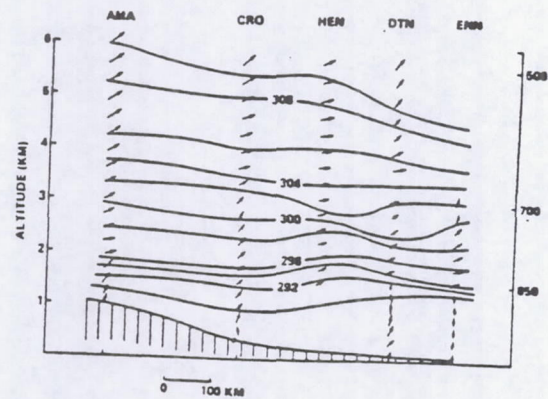


Figure 4. Cross-section analysis of potential temperature and horizontal winds running from Amarillo along the Oklahoma-Texas border utilizing special network stations operating during AVE-VAS IV. Time is 1100Z. Contour interval is 2K.

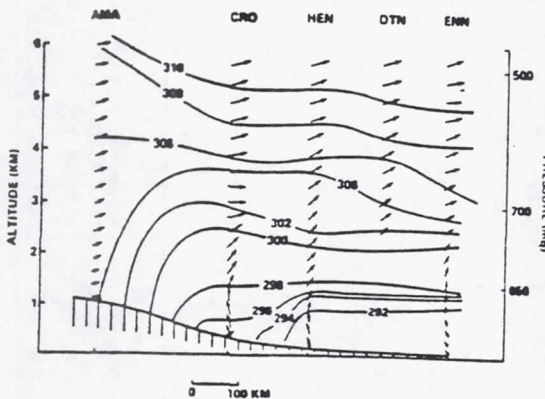


Figure 5. Same as 4. Time is 2300Z.

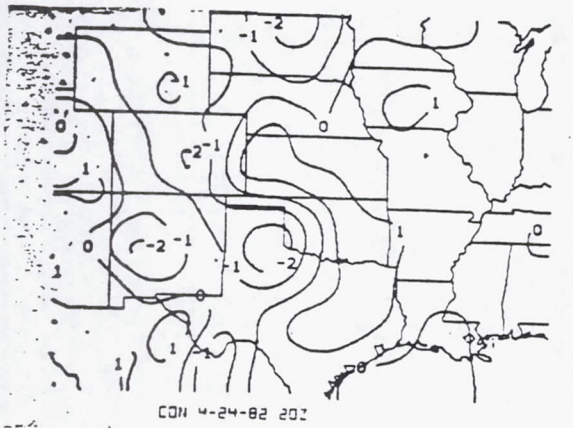


Figure 6. Surface divergence at 2000Z, 24 April. Contour interval is  $1 \times 10^{-5}$  per second.

#### 4.2 Model Description

The model used in this investigation is a two-dimensional version of the Colorado State University Hydrostatic Mesoscale Model. This basic model was initially described by Pielke (1974) while numerous papers in the literature (e.g., McNider and Pielke (1981), Mahrer and Pielke (1977), etc.) have since presented additional improvements and applications for the basic model. In terms of producing physically realistic flow fields the meteorological model has several significant strong points. These points are summarized below and the referenced paper should be consulted for details.

The first of the significant features in the model is the detailed treatment of the surface layer and the planetary boundary layer. The use of a prognostic equation suggested by Deardorff (1974) for formation and growth of the convective planetary boundary layer (PBL) in the model allows for an efficient parameterization scheme for vertical turbulent mixing within the convective PBL [Pielke and Mahrer (1975)]. The scheme

uses a cubic polynomial, suggested by O'Brien (1970) to define a profile for the vertical diffusion coefficients dependent upon values of the diffusion coefficients at the top of the surface layer and at the height of the PBL. Thus, given the surface characteristics, Deardorff's prognostic equation for the height of the convective PBL allows for the coupling or closure of the parameterization scheme for the vertical turbulent mixing processes.

In the surface layer use of detailed profile functions coupled with a surface heat budget equation allows a detailed and dynamic mechanism for surface forcing and decay processes in the model [Pielke and Mahrer (1975) and Mahrer and Pielke (1977)]. Vertical diffusivity profiles in the surface layer parameterization are based upon similarity theory using the non-dimensional profiles suggested by Businger (1973) and discussed for the present model application by Pielke and Mahrer (1975).

In the stable nocturnal boundary layer a local exchange coefficient scheme proposed by Blackadar (1979) and based on a local gradient Richardson number is utilized. The rationale for using a different scheme for the convective and stable boundary layers is based on the differences in scale of the turbulence. In the convective boundary layer, recent research, e.g., Kaimal et al. (1976), has shown the dominant turbulent scales in the convective boundary are on order of the PBL height which is much greater than the model grid spacing. Thus, local conditions (i.e., at a grid point) do not determine the turbulent exchange rates. In the nocturnal boundary layer the dominant scale of the turbulence is less than the vertical model grid spacing thus, local conditions should determine the mixing processes.

In summary the parameterization schemes in the surface and boundary layers allow for a time and spatial variation of vertical diffusion coefficients which are directly coupled to the dynamic and thermodynamic processes in the full model. McNider and Pielke (1981) indicated the combined local and non-local scheme simulated the mean structure of the diurnal evolving boundary layer as well as higher order turbulence models.

A second significant feature in the model is the inclusion of short-wave and long-wave radiation [Mahrer and Pielke (1977)]. Short-wave radiation is handled through a fixed empirical transmission function for oxygen, ozone and carbon dioxide, while for water vapor, a variable absorption of solar radiation is used which depends on the specific humidity. Radiative heating at the surface is dependent upon solar angle and angle of incidence so that the effect of topographic slope is included. Long-wave radiation is included in the model atmosphere through calculation of total radiative heating or cooling due to net radiative fluxes in each model layer. Long-wave emitters included are the ground, water vapor and carbon dioxide.

A third important feature in the model is the use of a surface energy budget equation to determine land surface temperatures [Mahrer and Pielke (1977)]. The budget equation includes incoming solar short-wave radiation, long-wave radiation,

latent, sensible and soil heat fluxes along with outgoing long-wave radiation. A final physical feature in the model, which deserves mention, is the use of a terrain following coordinate system which allows inclusion of topography in a general manner [Mahrer and Pielke (1975)].

#### 4.3 Model Cases

Three basic model cases were used to examine the forcing mechanisms described above:

- 1) A model case utilizing topography alone.
- 2) A model case employing cloud shading alone.
- 3) A model case using both cloud shading and topography.

All cases used a horizontal grid resolution of 25 km and a 25 mb vertical resolution. All used a uniform surface roughness of .04 meters. The model cases were initialized with the 1400Z, 24 April, Amarillo sounding. Isentropes were initialized to be terrain following which is fairly consistent with the thermal structure given in Figure 4. Model integration was carried out to 0000Z, 25 April. In order to isolate boundary layer effects geostrophic winds were kept at their 1400Z value.

##### 4.3a Case 1: Topography

Topography was digitized along an east-west line running from just west of the New Mexico border to near the Oklahoma-Arkansas line. Driven by the strong insolation to the surface energy budget, a convective boundary layer grew rapidly over the whole region. However, in this case as well as subsequent cases, the depth of the convective boundary layer appeared to be underestimated, evidently due to the neglect of synoptic cold air advection aloft. In response to the differential heating along a geopotential surface due to the topography a more southerly component began to develop in the model atmosphere. The model thermal structure as well as the flow field is given in Figure 7. The baroclinic field as well as the convergence field (Figure 8.) is quite modest compared to the observations in Figure 5. Thus forcing due to topography alone does not appear to explain the strong convergence and thermal structure observed.

##### 4.3b Case 2: Cloud Shading

The effect of cloud shading was parameterized in the model by varying the albedo in the surface energy budget from .2 in the cloud free area to .8 in the totally overcast area in east Texas. These values were based upon empirical values for insolation as a function of cloud cover by Williams (1979). A region 150 Km wide with the albedo varying between .2 and .8 was used for the transition region between clear skies and the totally overcast area. The albedo specification was held constant during the period of integration. This parameterization neglects upper level radiative effects of clouds and the dynamic and time evolution of the cloud field due to the developing thermal and flow structure.

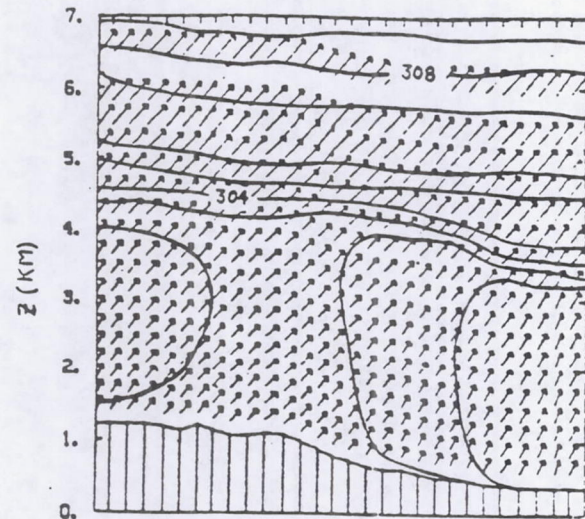


Figure 7. Model cross-section for Case 1 with topography only. Contour interval is 1°K. Time is 2000Z.

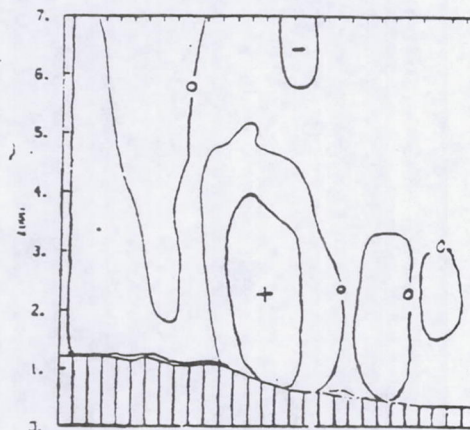


Figure 8. Model convergence for Case 1 at 2000Z. Contour interval is  $1 \times 10^{-5}$  per second. Dashed lines indicate divergence.

Figure 9. shows the thermal and flow structure for the cloud shading case. As can be seen a sharp thermal gradient develops due to the variation in surface forcing. The flow field responds to this thermal gradient with a slight easterly component at the surface. The convergence due to this developing easterly component is quite strong as indicated in Figure 10. In general the pattern is more representative of the observations than Case 1.

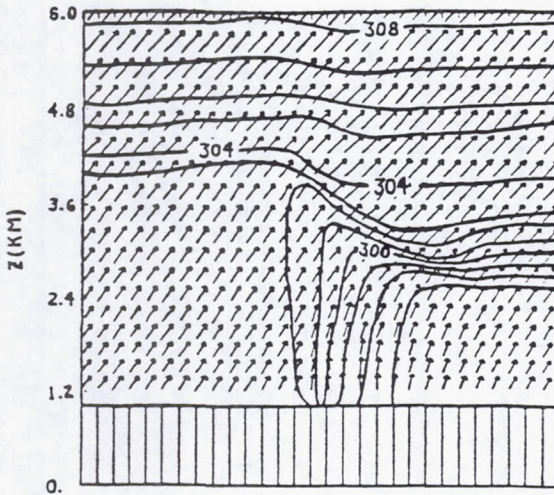


Figure 9. Model cross-section for Case 2 with cloud shading only. Contour interval is 1°K. Time is 2000Z.

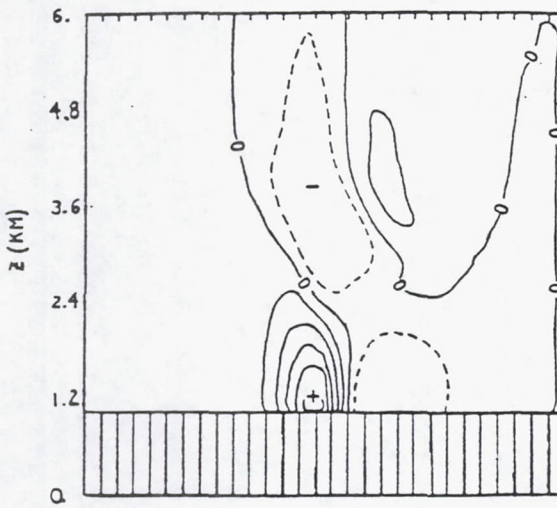


Figure 10. Model convergence for Case 2 at 2000Z. Contour interval is  $1 \times 10^{-5}$  per second.

#### 4.3c Case 3: Cloud Shading and Topography

Since both topography and cloud shading could be operating simultaneously to force convergence, the combined case was examined. Figure 11. shows the flow field and thermal structure which evolved in the combined case. The specification of the cloud distribution at 1400Z places it near the region of largest slope in the topography, thus the physical mechanisms tend to reinforce each other. Figure 12. shows the strong convergence field arising from this combined case. The thermal and flow structure appear to agree well qualitatively with the observations in Figure 5.

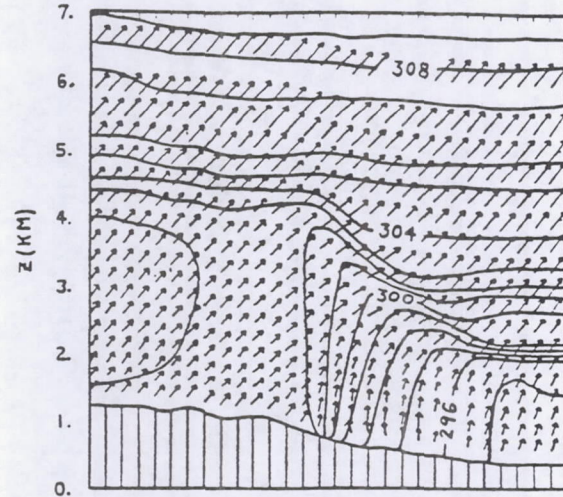


Figure 11. Model cross-section for Case 3 for combined cloud shading and topography.

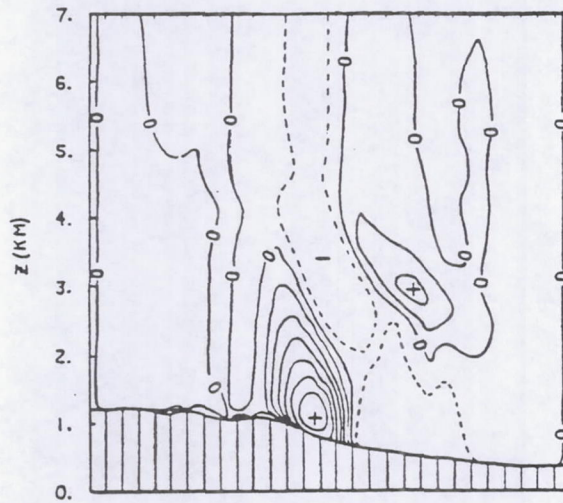


Figure 12. Model convergence for Case 3 at 2000Z.

It should be noted also that the easterly component which develops at the surface can tap moisture to the east, thus supplying a source of moisture for the convection. This is in agreement with the description given by Sun and Ogura (1979) for the source of moisture in their case study of convection along a dryline.

#### 5.0 CONCLUSIONS

This combined data and modeling analysis shows that both synoptic and mesoscale processes separately and in concert help to force the con-

vection. From the synoptic view the destabilization of the atmosphere aloft due to cold advection is important in removing any cap to deep convective development. The upper level moistening due to flow from the northwest also helps to increase the convective instability of the atmosphere. The mesoscale convergence due to cloud shading appears dominant over that of topography; however, the convergence due to topography, especially its sustained effect, cannot be ignored. The developing mesoscale circulation also appears to tap a surface supply of moisture feeding the convection.

The modeling study conducted here was quite simple. A more complete study is required including both synoptic variations in the thermal and flow field as well as time dependent incorporation of the cloud field. We have also completely neglected the role of latent heat feedback [Fritch and Maddox (1981)] in accentuating the thermal circulation.

#### 6.0 ACKNOWLEDGEMENTS

This research was sponsored by the Marshall Space Flight Center, Huntsville, Alabama, through the Universities Space Research Association. The authors wish to acknowledge G. D. Emmitt for his role in initiating this research.

#### 7.0 REFERENCES

1. Blackadar, A. K., 1979: High resolution models of planetary boundary layer. Advances in Environmental and Scientific Engineering, Vol. I, Gordon and Breach.
2. Businger, J. A., 1973: Turbulent transfer in the atmospheric surface layer. Workshop on Micrometeorology, Amer. Meteor. Soc., Boston, MA.
3. Carlson, T. N., S. G. Benjamin and G. S. Forbes, 1983. Elevated mixed layers in the regional severe storm environment: conceptual model and case studies, Mon. Wea. Rev., 1453-1473.
4. Deardorff, J. W., 1974: Three-dimensional numerical study of turbulence in an entraining mixed layer. Bound. Layer Met. 7, 199-226.
5. Djuric, Dusan and M. S. Damiani, 1980: On the formation of a low level jet over Texas, Mon. Wea. Rev., 108, 1854-1865.
6. Kaimal, J. C., J. C. Wyngaard, D. A. Haugen, O. R. Cote, Y. Izumi, S. J. Caugney, and C. J. readings, 1976: Turbulence structure in the convective boundary layer. J. Atmos. Sci., 33, 2152-2168.
7. Kuo, J. and H. D. Orville, 1973: A radar climatology of summertime convective clouds in the Black Hills. J. Appl. Meteor., 12, 359-368.
8. Mahrer, Y. and R. A. Pielke, 1977: The effects of topography on the sea and land breezes in a two-dimensional numerical model. Mon. Wea. Rev., 105, 1151-1162.
9. McNider, R. T. and R. A. Pielke, 1981: Diurnal boundary layer development over sloping terrain. J. Atmos. Sci., 38, 2198-2212.
10. Means, L. L., 1954: A study of the mean southerly wind maximum in low levels associated with a period of summer precipitation in the mid-west. Bull. Amer. Meteor. Soc., 35, 166-170.
11. O'Brien, J. J., 1970: A note on the vertical structure of the eddy exchange coefficient in the planetary boundary layer. J. Atmos. Sci., 31, 1213-1215.
12. Ogura, Y., H. Juang, K. Zhang and S. Soong, 1982: Possible triggering mechanisms for severe storms in SESAME-AVE IV (9-10 May 1979). Bull. Amer. Meteor. Soc., 63, 503-515.
13. Pielke, R. A., 1974: A three-dimensional numerical model of the sea breezes over South Florida. Mon. Wea. Rev., 102, 115-139.
14. Pielke, R. A. and Y. Mahrer, 1975: Representation of the heated planetary boundary layer in mesoscale models with coarse vertical resolution. J. Atmos. Sci., 32, 2288-2308.
15. Sun, W. Y. and Y. Ogura, 1979: Boundary layer forcing as a possible trigger to squall line formation. J. Atmos. Sci., 36, 235-254.
16. Uccellini, L. W. and D. R. Johnson, 1979: The coupling of upper and lower tropospheric jet streaks and implications for the development of severe convective storms. Mon. Wea. Review., 107, 682-703.
17. Uccellini, L. W. and R. A. Petersen, P. Kocin, M. Kaplan, J. Zack and V. Wong, 1983: Mesoscale simulations of the President's Day Cyclone: impact of sensible and latent heating on pre-cyclogenetic environment. Proceedings of Sixth Conference on Numerical Weather Prediction, Omaha, NE, 6-9 June 1983.
18. Williams, B. B., 1979: Forecasting available solar energy. UAH Tech Note 79-01, University of Alabama in Huntsville.
19. Wong, V., 1982: On the effect of PBL parameterizations in mesoscale numerical weather prediction models. Pro. of the NATO Advanced Study Institute on Mesoscale Meteorology, Gascogne, France.

## Simulation of Mesoscale Convective Response

Richard T. McNider

K.E. Johnson Environmental and Energy Center  
University of Alabama in Huntsville  
Huntsville, Alabama 35899

Fred J. Kopp

Institute of Atmospheric Sciences  
South Dakota School of Mines  
Rapid City, South Dakota

Michael W. Kalb

Universities Space Research Associates  
Atmospheric Sciences Division  
Marshall Space Flight Center  
Huntsville, Alabama

Gregory S. Wilson

Atmospheric Sciences Division  
NASA Marshall Space Flight Center  
Huntsville, Alabama

### 1. INTRODUCTION

Scale interaction is a fundamental problem in numerical weather prediction. While it is well known that large scale processes can produce atmospheric responses on smaller scales, numerical models are usually limited in their ability to resolve both scales due to domain and grid size restrictions imposed by available computers. Also, the physical processes which have to be explicitly resolved or level of parameterization for the processes in the numerical model are quite different for the various scales. Thus, computer restrictions again limit the amount of physics which can be incorporated over the whole domain. This has led to a hierarchy of numerical models of various scales ranging from global models to synoptic models to cloud models.

While there has been a large amount of effort devoted to initializing or transferring scale information from global models to synoptic models and downscale to regional or mesoscale models, there has not been as much work in transferring mesoscale information to cloud scale models. Chen and Orville (1980) in a pioneering study showed that incorporation of mesoscale convergence substantially altered the convective response in a cloud model and indicated that some knowledge of mesoscale convergence is needed to effectively forecast convection.

The purpose of this investigation is to transfer thermodynamic and dynamic information downscale from a two-dimensional mesoscale model to a two-dimensional cloud model and examine the differential convective response in the cloud

model to the mesoscale structure. This departs from Chen and Orville (1980) in that in their sensitivity study they simply imposed a hypothetical mesoscale convergence. They also did not include concomitant mesoscale thermodynamic structure with the mesoscale convergence. The work reported below is closest to that of Cotton *et al.* (1976) which examined the cumulus scale response to mesoscale circulations over South Florida by initializing a cloud model using a sounding from a mesoscale model. In that study, however, only a one-dimensional cloud model was used so that the only mesoscale information which could be transferred to the cloud model were perturbations in the vertical thermodynamic structure due to the mesoscale environment. In the present study, because a two-dimensional cloud model is used, the vertical structure of the mesoscale convergence and mesoscale shear, as well as mesoscale thermodynamic structure can be incorporated into the cloud model and their effects examined.

In this study a mesoscale model is applied to the Texas Panhandle on April 24, 1982 during which a moderately strong convective line formed to the east of Amarillo, Texas. A previous report of this case (McNider *et al.*, 1984) showed that mesoscale boundary forcing was a major factor in setting up thermodynamic and dynamic structure which appeared conducive to the initiation of convection. It was not determined in that study whether this mesoscale structure would actually lead to strong preferred areas of convection. To address this question a cloud model is initialized at various points within the mesoscale model domain and the differential

response of the cloud model examined.

## 2. MODEL DESCRIPTIONS

### 2.1 Mesoscale Model

The mesoscale model used in the present investigation is a two-dimensional version of the Colorado State University Hydrostatic Mesoscale Model. This basic model was initially described by Pielke (1974) while additional papers in the literature have since described improvements or changes in the basic model. The reader should refer to McNider and Pielke (1981), Mahrer and Pielke (1977) and McCumber and Pielke (1981) for a recent description of the model. Primary features of the model are listed below.

- ° The model employs a high resolution planetary boundary layer formulation. For the convective boundary layer a profile form for exchange coefficients is specified based on the height of the PBL (determined from a prognostic equation suggested by Deardorff (1974)) and the magnitude of the surface heat flux. When the surface heat is stable a local exchange coefficient scheme proposed by Blackadar (1979) based on a local gradient Richardson Number is used.
- ° Short-wave and long-wave radiation is incorporated as forcing in the model.
- ° The model is forced at the surface by a surface energy budget. The budget equation includes incoming short-wave and long-wave radiation, latent, sensible and soil heat fluxes along with out-going long-wave radiation.
- ° A terrain following coordinate system is utilized to allow inclusion of topography in a general manner.
- ° An absorbing layer is utilized near the top boundary to reduce wave reflection from the model top.

Figure 1. depicts the mesoscale model domain size and grid resolution used in the present study. The domain and grid structure for the cloud model is shown for comparison.

### 2.2 Cloud Model

The cloud model used in the present study is a two-dimensional model developed by investigators in the Institute of Atmospheric Sciences at the South Dakota School of Mines. The model is a two-dimensional, slab-symmetric model, i.e. no variations are allowed in the second horizontal dimension. The reader should refer to Orville and Kopp (1977) for a description of the physics and microphysics used in the model. Some of the important features (which are more completely summarized in Chen and Orville (1980)) are:

- ° The model equations are the Navier-Stokes equations in the form of a vorticity equation, the first law of thermodynamics in the form of a

prognostic equation for potential temperature, and the equation of state for an ideal gas.

- ° The model employs first order closure for subgrid scale processes with the eddy exchange coefficient dependent upon grid scale vorticity, deformation and stability through a gradient Richardson Number.
- ° Water processes are divided into five classes: water vapor, cloud water, rain-water, cloud ice and hail.
- ° Microphysical processes assume a Marshall and Palmer (1948) distribution for rain drop size distribution for hail after Smith et al (1975).
- ° Accretion is simulated.

A description of the initialization of cloud model in terms of an initial stream function is given in section 4. The second author on this paper was primarily responsible for the cloud model experiments and modifications to the cloud model necessary for the present investigation.

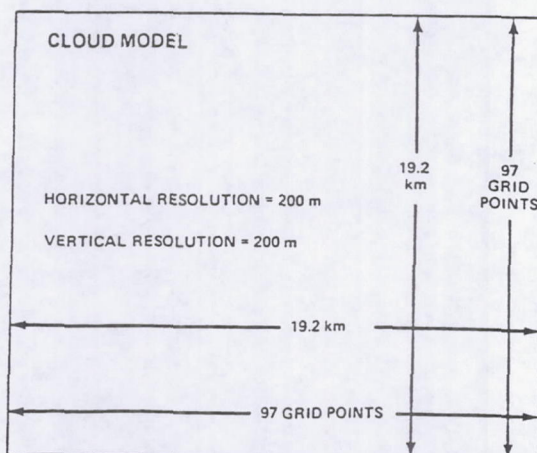
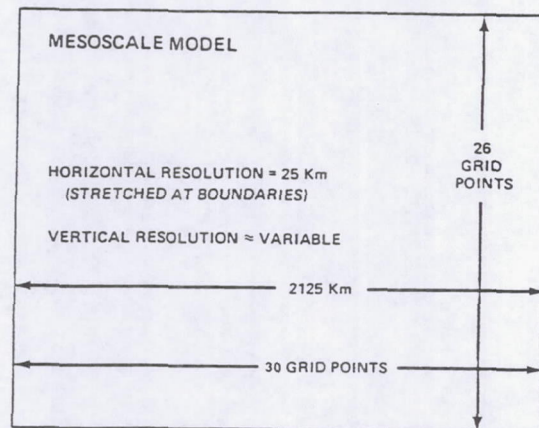


Fig. 1. Schematic of mesoscale model and cloud domain, grid size and grid number.

### 3. APRIL 24, 1982 CASE STUDY

As noted in the introduction, McNider et al. (1984) reported on a data and model analysis of the mesoscale environment preceding the formation of the convective line in the Texas Panhandle on April 24, 1982. Because this day was a data collection period under the AVE-VAS field program, special 3-hour rawinsondes were available in a dense mesoscale network. Figure 2. using this special data shows a sharp mesoscale baroclinic zone which developed between Amarillo (AMA) and Henrietta, Texas (HEN) by 2300 GMT. The dynamic response to this thermal gradient was a low level easterly boundary layer flow which opposed the westerly synoptic flow. This can be seen by the wind vectors based on the rawinsonde data.

In the companion mesoscale modeling study in McNider et al. (1984) it was demonstrated that dense cloud shading over east Texas and strong surface heating over west Texas, accentuated somewhat by the sloping topography, produced the sharp thermal gradient. Figure 3. shows the mesoscale model prediction of the thermal structure and flow field which can be compared to the observations in Figure 2. As can be seen, there is a large variation in the thermodynamic structure across the domain with a deep warm boundary layer over the west and a shallow cool boundary layer to the east. This variation in temperature and boundary layer depth produces an inland sea breeze like circulation (Sun and Ogura, 1979) with surface easterly flow and accentuated westerly flow aloft above the boundary layer. Mesoscale subsidence as part of this circulation produces a packing of isentropes aloft over and to the east of the baroclinic zone, giving a sharp capping inversion near the top of the boundary layer.

The surface easterly flow which develops due to the thermal gradient opposes the synoptic westerly flow producing a sharp convergence zone. Figure 4. shows the convergence field from the mesoscale model and indicates the large but shallow zone of convergence near the western boundary of the baroclinic zone. In the following sections the thermodynamic and convergence structure depicted in Figures 3. and 4. will be used to initialize the cloud model.

### 4. INITIALIZATION OF THE CLOUD MODEL

The mesoscale model predicted convergence zone in Figure 4. is on the order of 125 km wide whereas the initial convective line which formed was less than 20 km wide. Thus, the response and organization of the convection occurred on a scale well below the resolution of the mesoscale model. In order to examine the differential convective response due to the mesoscale structure, the cloud model was initialized at various points in the model domain. The grid numbers at the bottom of Figure 4. show the grid points for which the cloud model was run. As seen in Figure 1., the cloud model domain is 20 km which places it completely within the 25 km grid of the mesoscale model.

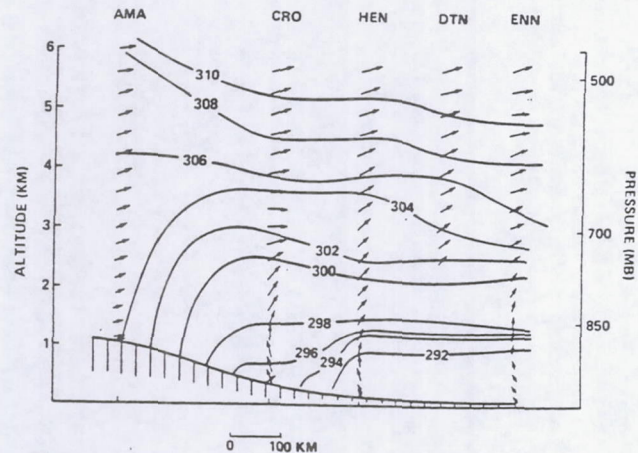


Fig. 2. Cross-section analysis of potential temperature and horizontal winds from Amarillo-Texas border. Data are from special network stations operating under AVE-VAS IV. Time 2300z. Contour interval 2°K.

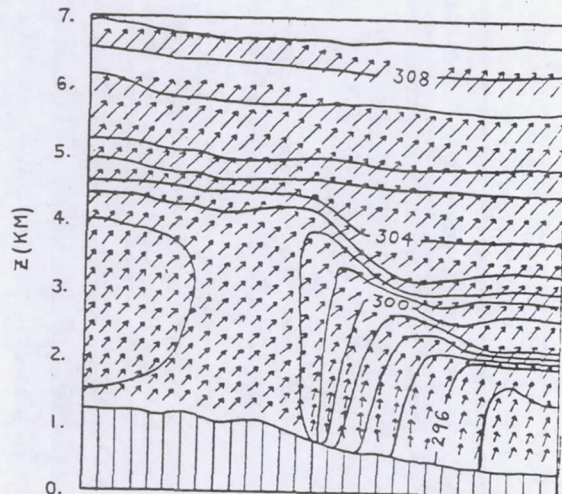


Fig. 3. Mesoscale model produced cross-section of potential temperature and horizontal winds. Time is 2000z. Contour interval is 1°K. Thermal structure from this time was used in the cloud model initiation.

#### 4.1 Thermodynamic Structure

To initialize the cloud model from the mesoscale model, data from the mesoscale model was converted into a standard sounding format. Grid level information for pressure, temperature, and humidity were linearly interpolated to 25 mb standard levels up to a height of 9 km. Above this height, data from the actual sounding at Amarillo was used. This data file for the particular grid point of interest was then read into

the cloud model as the initial sounding and interpolated to the 200 meter grid levels. The thermodynamic conditions were assumed uniform within the horizontal domain of the cloud model, i.e. there were no horizontal gradients imposed in temperature and humidity.

#### 4.2 Dynamic Structure

Part of the dynamic information from the mesoscale model was transferred to the cloud model using the convergence initialization procedure described by Chen and Orville, (1980). In this procedure the wind field employed in the model is assumed to be separable into cloud scale and mesoscale components. The mesoscale component is assumed to be constant with time which, as will be discussed later, is not strictly valid for the current simulation.

The mesoscale component can also be thought of as being decomposed into two components - one component being a mesoscale model grid cell average,  $\bar{u}$ , defined by

$$\bar{u}_{i,k} = (\hat{u}_{i,k} + \hat{u}_{i+1,k})/2$$

where  $i$  and  $k$  are horizontal and vertical grid points in the mesoscale model and  $\hat{u}$  is the easterly wind component in the mesoscale model. The second component,  $\hat{u}'$ , is the variation within the mesoscale model grid cell.

The cloud model flow field was initiated using the grid cell convergence values from the model depicted in Figure 4. Thus, the cloud model is initialized using the divergent component of the velocity field from the mesoscale model. The convergence is only contributed by the grid cell perturbation, thus the convergence is defined by

$$\frac{\partial \hat{u}}{\partial x} = \frac{\partial \hat{u}'}{\partial x}$$

This point is made because use of convergence as the initial mesoscale dynamic field in the cloud model only incorporates that part of the mesoscale field which varies across the grid cell. Thus mean shear,  $\partial \hat{u}/\partial z$ , in the mesoscale field is neglected since only  $\partial \hat{u}'/\partial z$  is incorporated through the convergence initialization. The mean mesoscale shear  $\partial \hat{u}/\partial z$  must be added separately which will be discussed later.

The convergence profile from the mesoscale model was input to the cloud model from which the  $u$  and  $w$  fields were computed and a stream function constructed. Figures 5. and 6. show the initial  $u$  field and streamfunction in the cloud model due to the mesoscale convergence profile taken from grid point 14 in the mesoscale model. A compensation region above 7 km reduces the integrated convergence to zero at 10 km. As can be seen, the convergence initialization creates a circulation similar to that of the mesoscale model with relative low level easterly flow near the surface and westerly winds aloft with maximum vertical velocities near mid-depth of the planetary boundary layer (i.e. 2 km).

In addition to the convergence and thermodynamic initialization a thermal perturbation of  $.5^{\circ}\text{C}$  was employed to trigger convection in the

cloud model. The perturbation is used primarily to ensure that convection is initiated near the center of the cloud model domain. A random perturbation whose scale is determined by boundary similarity theory Kaimal et al. (1976) might be a more physically appealing initialization.

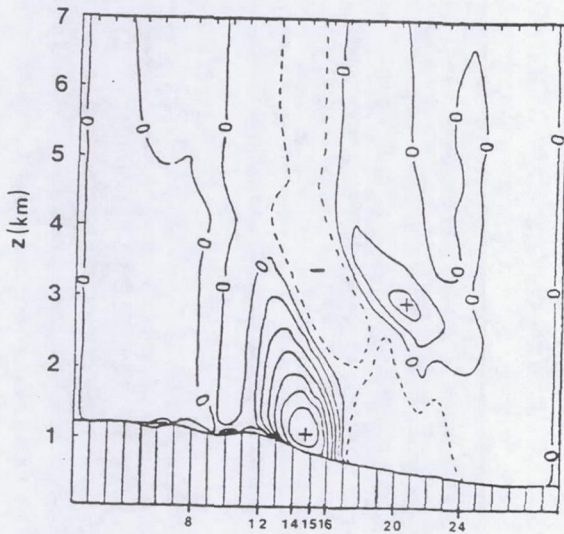


Fig. 4. Mesoscale model produced convergence for 2000z corresponding to the dynamic field in Figure 3. The convergence profile used in the cloud model was based on this data.

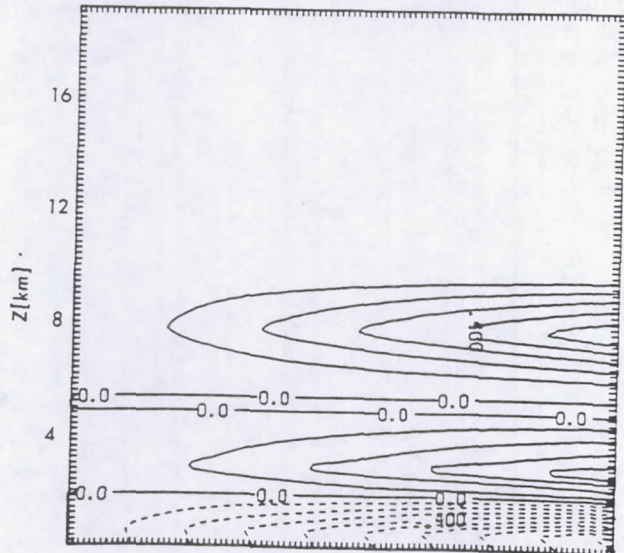


Fig. 5. Contours of the east-west mesoscale perturbation velocity,  $u$ , used as the initial field in the cloud model. Field corresponds to grid point 14 in the mesoscale model at 2000z. Contour interval is  $.1 \text{ m/s}$ . Dashed contours indicate easterly flow.

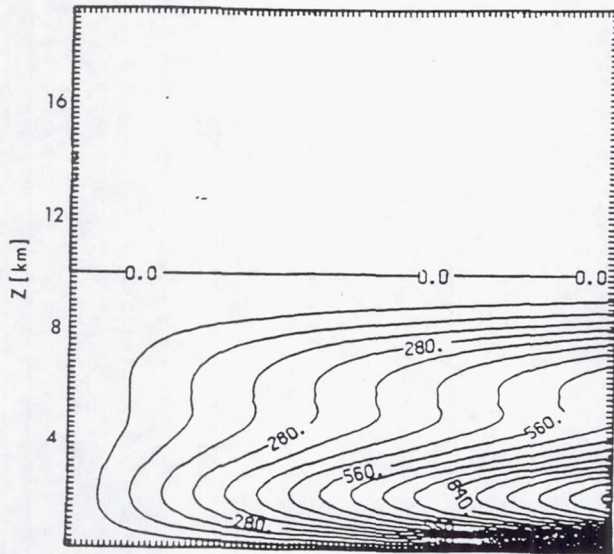


Fig. 6. Contours of the stream function used as the initial circulation in the cloud model based upon the convergence values at grid point 14 in the mesoscale model at 2000z.

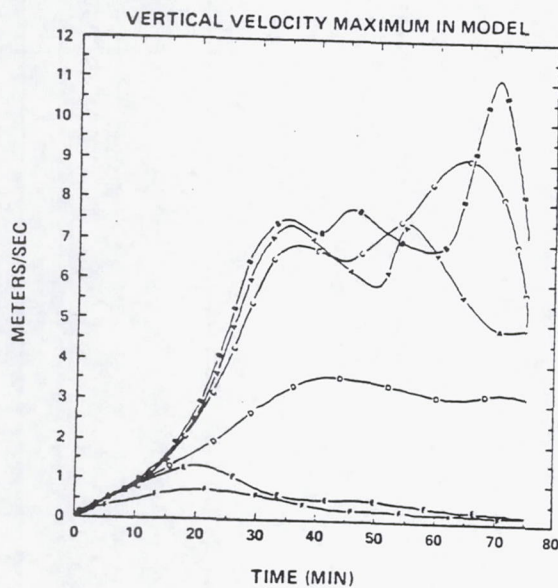


Fig. 7. Time series plot of maximum vertical velocity at any cloud model grid during the period of integration of the cloud model. A- mesoscale model grid point 8, B- grid point 12, C- grid point 14, D- grid point 15, E- grid point 16, F- grid point 20.

##### 5. DIFFERENTIAL CONVECTIVE RESPONSE

As outlined in the introduction the main purpose of the investigation is to determine whether the mesoscale dynamic and thermodynamic environment leads to preferred areas for the initiation and maintenance of cumulus scale convection. Using procedures above, the cloud model was run for grid points 8, 12, 14, 15, 16, 20, and 24

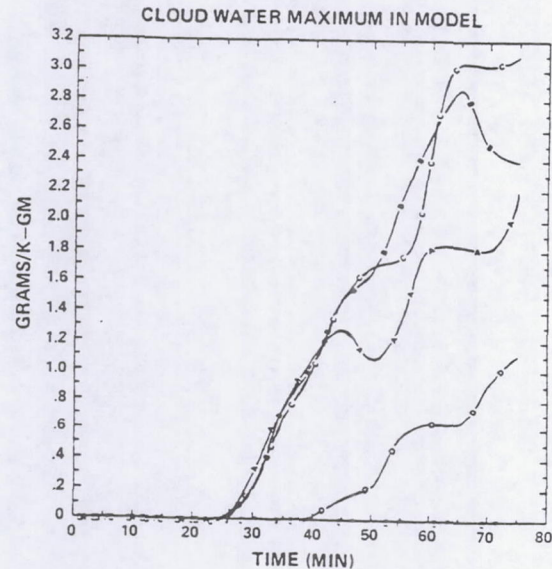


Fig. 8. Time series plot maximum of cloud water content at any cloud model grid during the period of integration of the cloud model. A- mesoscale model grid point 8, B- 12, C- 14, D- 15, E- 16, F- 20.

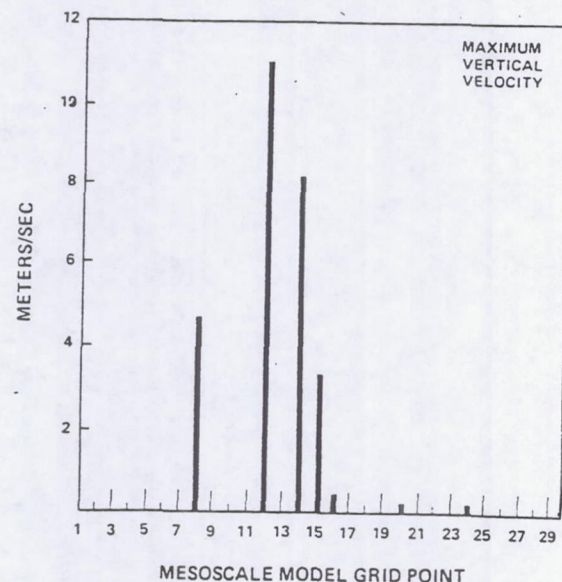


Fig. 9. Cross-section through the mesoscale model domain depicting maximum cloud model vertical velocity as a function of position at cloud model time of 70 minutes.

as depicted in Figure 4. for a 2000 GMT start which was approximately the time the actual convection line was initiated. Figure 7. gives a measure of the differential convective response across the mesoscale domain by depicting a time plot of the maximum vertical velocity at any grid point in the cloud model during the period of integration. Likewise Figure 8. gives the maximum cloud water at any cloud model grid point. As can be seen while some oscillation exists in

time there is a consistent variation in the strength of the vertical velocity and cloud water at the different grid points.

In order to give a better physical perspective on the differential response, Figures 9. and 10. show the maximum vertical velocity and cloud water on the same horizontal scale as Figures 3. and 4. Note that the maximum convective response occurs in the region of mesoscale convergence. This is consistent with the sensitivity studies of Chen and Orville (1980) which indicated that convergence plays two roles in enhancing the convective response: first, destabilizing the atmosphere through a general lifting and, second, the convergence (perhaps due to the destabilization) shifts the eddy response to larger scale, longer lived eddies.

In the present case, however, it is not only the convergence, but, also the large mesoscale variation in the thermodynamic stability across the region which affects the response. Over the western region intense heating produced a deep nearly adiabatic boundary layer while over the east, mesoscale subsidence and divergence aloft has produced a strong capping inversion. Closer examination of Figures 9. and 10. show that the maximum convective response is off-set from the area of maximum surface convergence toward the area where the boundary layer is deeper. This serves two purposes in producing stronger convective response. First, the thermodynamic profile is less stable, so that less energy is required to sustain the convection and, second, the deeper boundary layer allows the vertically integrated convergence to be larger.

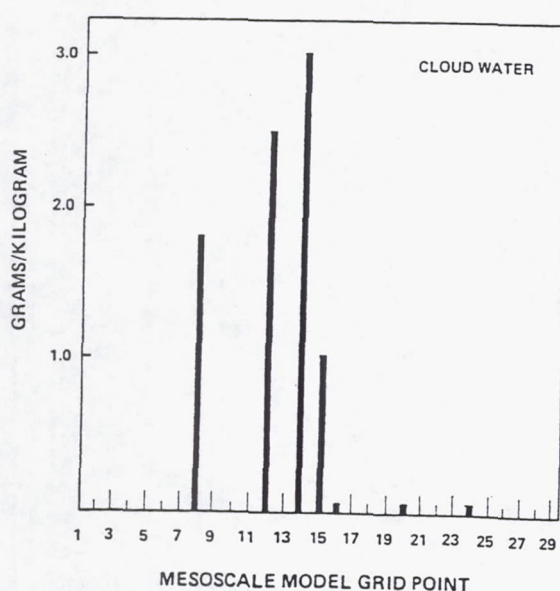


Fig. 10. Cross-section through the mesoscale model domain depicting maximum cloud water content as a function of position at cloud model time of 70 minutes.

## 6. CONCLUSIONS

This study addresses the suggestion of Chen and Orville (1980) that mesoscale information be included in a cloud model initialization. It also goes a step further by including both the mesoscale dynamic structure and the concomitant thermodynamic structure.

The one-way transfer of information from a mesoscale model to a cloud model indicates that the mesoscale environment can alter dramatically convective response. It also demonstrates the importance of including both mesoscale thermodynamic and dynamic information in the initialization of a cloud model.

Three major caveats must be applied to the above study. First the mesoscale environment which was kept constant during the period of integration of the cloud model in fact continued to change, thus, the initial sounding was not completely valid through the period. Second, the developing convection undoubtably altered the mesoscale environment to some extent. This was completely neglected in the dry mesoscale model since a convective parameterization was not used. Realistic evaluation of both these time-dependent feed backs between scales would require either nesting or a combination mesoscale and cloud model integrated over the whole domain. Such investigations will have to await further model development and increased computer capacity. Third the mean mesoscale shear  $\partial u / \partial z$  was not included in the present investigation. Preliminary work including the mesoscale shear will be reported at the conference. Finally, synoptic variations were not included in the mesoscale model integration. McNider *et al.*, (1984) previously showed that the synoptic environment was not completely quiescent. While synoptic dynamic forcing did not appear strong, substantial cooling occurred between 500 mb and 300 mb. This cooling aloft coupled with surface heating produced a nearly adiabatic profile from the surface to 350 mb. The convection in the cloud model in the present study was quite modest and this destabilization aloft which was not included would have increased the strength of the convection based upon sensitivity studies using the actual sounding as opposed to the mesoscale model sounding.

## 7. REFERENCES

Blackadar, A.K., 1979: High resolution models of the planetary boundary layer. Advances in Environmental and Scientific Engineering. Vol. I, Gordon and Breach.

Chen, C.H. and H.D. Orville, 1980: Effects of mesoscale convergence on cloud convection. J. Appl. Meteor. 19, 256-274.

Cotton, W.R., R.A. Pielke and P.T. Gannon, 1976: Numerical experiments on the influence of the mesoscale circulation on the cumulus scale. *J. Atmos. Sci.*, 33, 252-261.

Deardorff, J., 1974: Three-dimensional numerical study of the height and mean structure of a heated planetary boundary layer. Boundary-Layer Meteor., 7, 81-106.

Kaimal, J., J.C. Wyngaard, D.A. Haugen, O.R. Cote, Y. Izumi, S.J. Caughey and C.J. Readings, 1976: Turbulence structure in the convective boundary layer. J. Atmos. Sci., 33, 2152-2168.

Mahrer, Y. and R.A. Pielke, 1977: The effects of topography on land and sea breezes in a two-dimensional mesoscale model. Mon. Wea. Rev., 105, 1152-1162.

Marshall, J.S. and W.M. Palmer, 1948: The distribution of rain drops with size. J. Meteor., 5, 165-166.

McCumber, M.C. and R.A. Pielke, 1981: Simulation of the effects of surface fluxes of heat and moisture in a mesoscale numerical model. I. Soil layer. J. Geophys. Res., 86, 9929-9938.

McNider, R.T., G.J. Jedlovec, and G.S. Wilson, 1984: Data analysis and model simulation of convection on April 24, 1982. Proceedings of Tenth Conference on Weather Analysis and Forecasting, Clearwater, Florida, AMS.

McNider, R.T. and R.A. Pielke, 1981: Diurnal boundary layer development over sloping terrain. J. Atmos. Sci., 38, 2198-2212.

Orville, H.D. and F.J. Kopp, 1977: Numerical simulation of the life-cycle of a hailstorm. J. Atmos. Sci., 34, 1596-1618.

Pielke, R.A., 1974: A three-dimensional numerical model of the sea breezes over South Florida. Mon. Wea. Rev., 102, 115-139.

Smith, P.L., Jr., C.G. Myers, and H.D. Orville, 1975: Radar reflectivity factors in calculations in numerical cloud models using bulk parameterizations of precipitation. J. Appl. Meteor., 14, 1156-1165.

Sun, W.Y. and Y. Ogura, 1979: Boundary layer forcing as a possible trigger to squall line formation. J. Atmos. Sci., 36, 235-254.

# A PARAMETERIZATION OF RADIATION HEATING AT THE SURFACE IN A NUMERICAL CLOUD MODEL

Fred J. Kopp, Harold D. Orville, James A. Jung,<sup>1</sup> and Richard T. McNider<sup>2</sup>

Institute of Atmospheric Sciences  
South Dakota School of Mines and Technology  
501 East St. Joseph Street  
Rapid City, South Dakota 57701-3995

## 1. INTRODUCTION

A two-dimensional, time-dependent model has been used in a predictive mode during two recent field projects. Initially, the model was tested for its predictive capabilities during the COHMEC project in 1986. During this project, radiative heat flux into the surface layer of the model was parameterized and incorporated. A morning sounding from the Huntsville Redstone Arsenal was used to initialize the model. The simulated heat flux at the surface would heat out the inversion and generate convective clouds. In a second project, the North Dakota Thunderstorm Project in 1989, the model was used in a predictive mode with the output being utilized for briefing purposes.

In the following, we will develop the parameterized radiation heat flux that was incorporated in the model and describe the results from the two experimental attempts at using the model in the predictive mode.

## 2. CLOUD MODEL

The model is a two-dimensional, time-dependent finite difference grid with 200 m grid spacing. The domain is a 20-km horizontal by 20-km vertical region. Partial differential equations predict air flow, water vapor, cloud water, ice, rain, hail, snow, heat, and other miscellaneous variables. The model is described at greater length in Orville and Kopp (1977) as well as other papers. The critical changes that have been made in this particular model involved changes in the boundary layer heat flux.

The surface energy equation has been modified to change control of surface temperature as used in our past models where the surface temperature was prescribed as a time-dependent change. We now prescribe a constant flux of heat into the surface layer of the model which is also balanced by an eddy transport of heat out of the surface layer.

The energy equation in the model is embodied in the following equation at the surface:

$$\frac{\partial \phi}{\partial t} = -V \cdot \nabla \phi + \frac{2K}{H\theta} \frac{\partial \theta}{\partial z} + \frac{2}{H} K \frac{L}{C_p T_{oo}} \frac{\partial Q}{\partial z} - \frac{2D}{\rho_0 C_p H\theta} \quad (1)$$

where the first term on the right is the advection, followed by the vertical diffusion of heat and vapor, and last the radiation heat source.

In the above,  $\phi$  is defined initially as:

$$\phi = \frac{\theta}{\theta} + \frac{Lr}{C_p T_{oo}} \quad (2)$$

where  $\theta$  is the potential temperature,  $\theta$  is the deviation of potential temperature from the base state, and  $r$  is the mixing ratio.  $L$  is the latent heat of vaporization,  $C_p$  is heat capacity of air, and  $T_{oo}$  is temperature.  $K$  is the eddy diffusion coefficient,  $V$  is velocity,  $\rho_0$  is density, and  $H$  is the grid spacing.

The variable  $D$  in (1) is the energy flux into the surface layer of height  $H/2$ . The energy flux used is about  $300 \text{ J m}^{-2} \text{ s}^{-1}$  at the surface. This is a fraction of the short wave solar energy reaching the surface.

In the event that clouds form overhead, the heating rate is reduced to one-half of the original heating rate. This is a very highly parameterized simulation of the radiative flux of the surface. No attempt has been made to simulate long wave radiation interactions at the surface, nor has any attempt been made to simulate the time-dependent short wave variation that occurs as the sun rises, reaches its zenith, and sets.

## 3. RESULTS

During the COHMEC project, the model was run on some but not all of the days. As seen in Fig. 1,

<sup>1</sup>Present Affiliation: James A. Jung, North Dakota Atmospheric Resource Board, P.O. Box 1833, Bismarck, ND 38502.

<sup>2</sup>Present Affiliation: Richard T. McNider, Dept. of Mathematics and Statistics, University of Alabama in Huntsville, Huntsville, AL 35899.

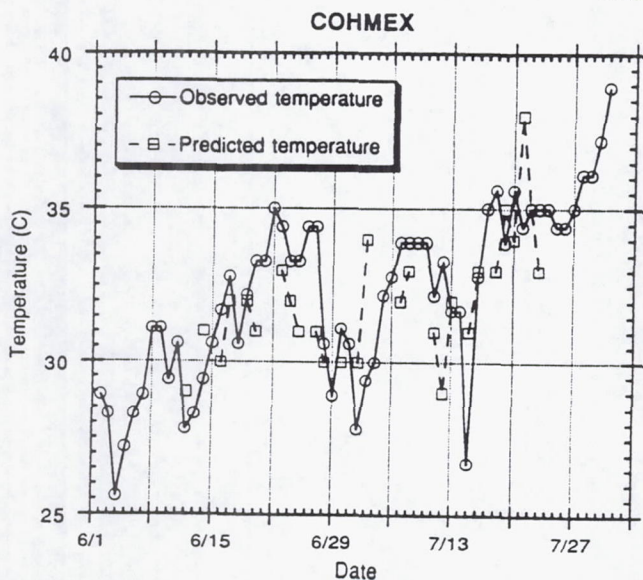


Fig. 1: Observed high temperature for each day of the COHMEX project and the corresponding model predicted temperature.

the model was run on approximately 25 of the 60 days shown in the figure. The model tends to underpredict as well as overpredict temperature. For this particular project, the correlation coefficient for the data shown in the scatter diagram, Fig. 2, was 0.5. The use of the model during this project was largely experimental, with little use made of the model results for the weather briefings. The briefings were held early in the morning before the cloud model could be run. Facilities for displaying model results were limited in any case due to a major failure of part of the McIDAS hardware at the Marshall Space Flight Center.

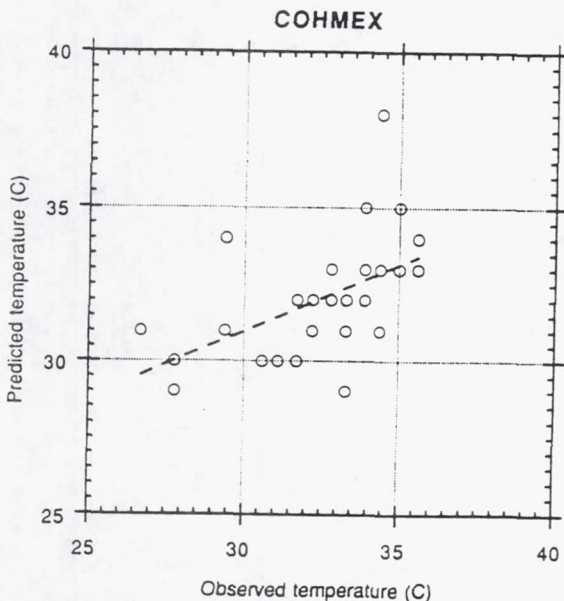


Fig. 2: Scatter plot of COHMEX model predicted vs. observed temperature. The dashed line is a regression line fitted to data. The correlation coefficient is 0.5.

During the North Dakota Thunderstorm Project, the model was used in a predictive mode and the results were intended to be used during the briefings which were held in the late morning. The 12 Z soundings were available at 8:00 local time and were run on the NCAR computer system. Results were generally available by 9:00-10:00 local time with the graphics being downloaded to a microcomputer and printed at the project site.

Figure 3 shows the observed high temperature as well as the predicted temperature for each day during the project. There are three missing data points for predicted temperature as those were declared down days and the model was not run. This figure shows a much closer correlation between the observed temperature and the model predicted temperature. Figure 4 is a scatter diagram of the data and the regression line has a correlation coefficient of > .85. The largest deviation shown in Fig. 3 is approximately 8°C with most of the differences being on the order of 2-3 degrees Celsius.

During the project, a subjective log was kept indicating whether the model had done a good job of predicting cloud development during the day or not. This was generally indicated by making a "+" for a good simulation, a "0" for a fair simulation, and a "-" for a poor simulation. For the 35 days simulated, eight minuses and six zeros were recorded. Figure 5 has this information recorded on it as a +1, 0, or -1. One might expect the big temperature errors made by the model to result in a poor simulation. However, note that 2 July is considered to be a fair day. On the other hand, 8 July, which is a fairly close correlation between predicted and observed temperature, was a minus day, indicating a poor simulation of the cloud growth and, in fact, the model overpredicted the cloud growth on that day. We estimate that the model scored about 75%, for predicting cloud growth, missing about 25% of the time. In some cases, the model did not predict enough cloud growth, but the dominant model result

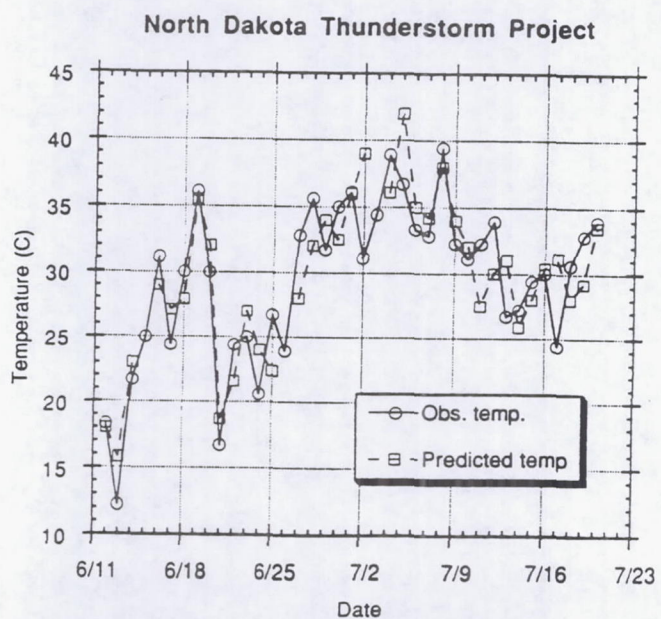


Fig. 3: As in Fig. 1, but for the North Dakota Thunderstorm Project.

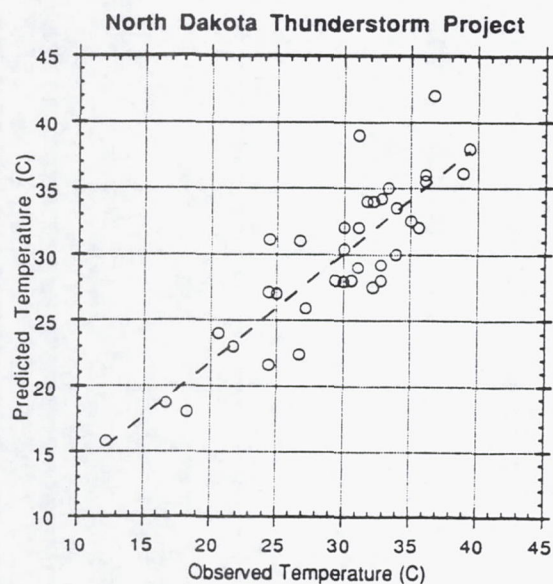


Fig. 4: Scatter plot for the North Dakota Thunderstorm Project of model predicted vs. observed high temperature. The dashed line is a regression line. Correlation of the data is 0.85.

was to predict more cloud growth than actually occurred on the days that the model missed.

Figure 6 shows the precipitable water and the surface mixing ratio from the 12 Z soundings for the project period. The interesting thing to note is that there are substantial changes in both the precipitable water and surface layer mixing ratio. These changes are fairly well correlated with each other. The first few days of the project are characterized by high pressure moving in which led to a drying out of the atmosphere. Subsequent variations are generally related to frontal passages with the accompanying air mass changes. When these changes occur during the day, the initial conditions used from the 12 Z sounding for the model are probably changing rapidly.

#### 4. DISCUSSION

While the model was successful on approximately 75% of the days in predicting the cloud characteristics, the obvious question comes as to why does it fail on the other 25% of the days. During the project, the model was run more than once, frequently with convergence or divergence imposed to get a model response from various synoptic scale effects that were expected to be taking place. In spite of this, we still had failures on 25% of the days and, consequently, the first thought is that the model may be overheating and becoming more convective than the natural convection. An analysis of Fig. 3 related with the failures does not suggest that this is a real problem. In particular, the 2 July difference between the predicted and observed temperature was not a model failure day. Most of the questionable days have only a few degrees difference between the observed and predicted temperature, and there is no difference for the model being either warmer or colder than the observed temperature. There seems to be a general mix of both occurrences. Consequently, a better radiation scheme simulation

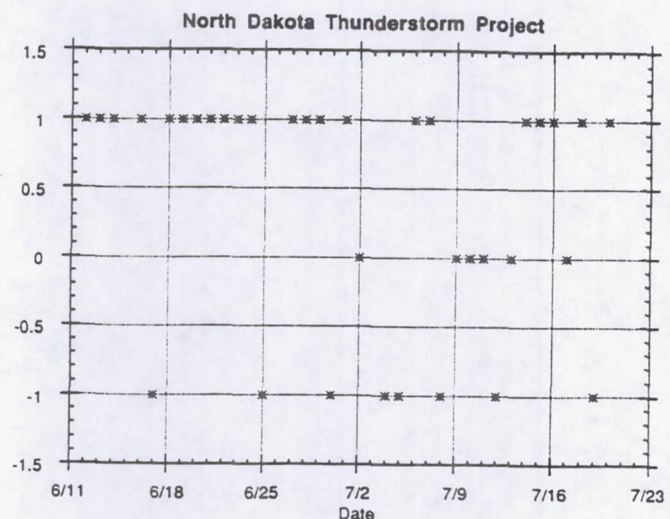


Fig. 5: Plot of day vs. model prediction of cloud characteristics. A "1" indicated good results, "0" is fair, and "-1" is poor.

at the surface would probably not improve the results.

Analysis of Fig. 6 shows that many of the model failures take place on a day when there is high precipitable water and surface moisture but which is followed the next day by a very steep decline in these variables. This suggests that, on some occasions, the atmosphere is probably drying out in the morning hours prior to the time significant convective activity can occur. Consequently, the model is being run with too much surface moisture, perhaps resulting in an over-prediction of the convective activity for the day. On the days when the model underpredicted the activity (10 July and 13 July), there was a relative minimum in the precipitable water and surface moisture which was followed the next day by substantially increased precipitable water and

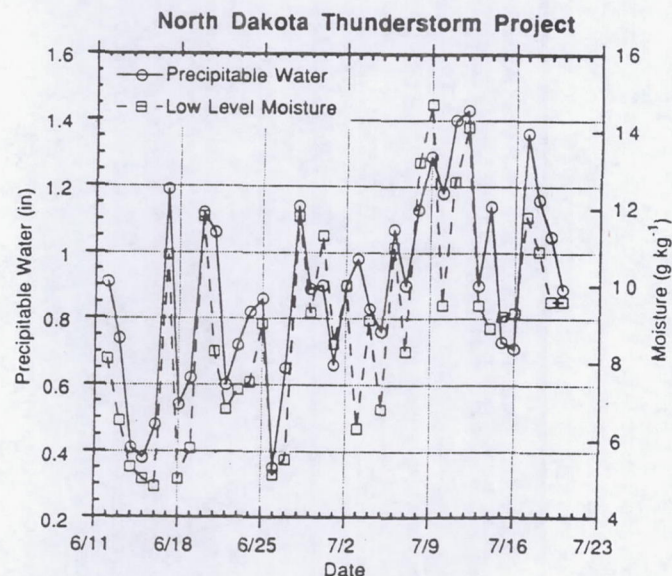


Fig. 6: Plot of precipitable water and low level moisture vs. the day of the project.

surface moisture, at least on the 10th. It may well have been during the day on the 10th that there was substantial advection of surface moisture into the region resulting in greater convective activity which was not picked up by the model as a result of the dryness in the 12 Z sounding.

## 5. CONCLUSIONS

The two-dimensional model was quite successful in simulating the convection on the basis of using the 12 Z sounding during the North Dakota project. It was able to do this in a predictive sense prior to the convection taking place. Results in a graphic form were available for a weather briefing in the late morning hours. While the model guidance was not used to any great extent by the project directors, there were times when they might have made better decisions if they had paid more attention to the model results. In particular, on one day the model forecast cloud

tops to be at approximately the -2°C to -5°C level which would have been an ideal opportunity for a particular seeding experiment which was not conducted. This was nearly the only opportunity to have done so during the project.

Acknowledgments. This paper was written under sponsorship of the National Science Foundation under Grant No. ATM-8901355 and the National Aeronautics and Space Administration under Grant No. NAG-8-632. NOAA funding is also acknowledged under Contract No. ARB-IAS-89-2 with the North Dakota Atmospheric Resource Board. Thanks are also extended to Mrs. Joie Robinson for her work in preparing the manuscript.

## REFERENCES

- Orville, H. D., and F. J. Kopp, 1977: Numerical simulation of the life history of a hail-storm. *J. Atmos. Sci.*, 34, 1596-1618.  
[Reply: *J. Atmos. Sci.*, 35, 1554-1555]

## Specification of the Scale and Magnitude of Thermals Used to Initiate Convection in Cloud Models

RICHARD T. MCNIDER

*Department of Mathematics and Statistics, University of Alabama in Huntsville, Huntsville, Alabama*

FRED J. KOPP

*Institute of Atmospheric Sciences, South Dakota School of Mines, Rapid City, South Dakota*

8 December 1988 and 5 June 1989

### ABSTRACT

Boundary layer similarity techniques are employed to specify the scale and intensity of a thermal perturbation used to initialize a cloud in a numerical cloud model. Techniques are outlined to specify the needed similarity variables from external information. Finally, the cloud model response using the similarity scaled thermal is analyzed employing variations in the similarity variables giving an indication of the importance of the correct specification of the initiating thermal.

### 1. Introduction

Many cloud models impose a temperature perturbation in order to initiate moist convection (e.g., Orville and Kopp 1977; Klemp and Wilhelmson 1978; and Miller and Pearce 1974). This perturbation is variously meant to represent either characteristic inhomogeneities arising in a convective boundary layer, variations in surface thermal properties or the influence of pre-existing cumuli. In practice, however, the choice for both the magnitude and scale for this perturbation has in most instances been ad hoc with little physical guidance being used. Unfortunately, the selection of the magnitude and scale of the perturbation can condition the subsequent convective response in that too large a perturbation can initiate moist convection which might not naturally occur. Conversely, too small a perturbation will not produce a natural response. Tripoli and Cotton (1980) provide a short discussion of the weaknesses in thermal specification and offered an alternative specification of a saturated bubble based on radar information.

If the role of the cloud model is restricted to understanding mature cloud dynamics or cloud microphysics (such as in some of the studies mentioned above), then an ad hoc perturbation is generally sufficient. However, as cloud models have become sophisticated, some model studies are beginning to examine the initiation of convection as a forecast problem. For such an investigation the magnitude of the thermal perturbation is critical.

One alternative to specifying a perturbation is to provide a surface heat flux to the cloud model and carry out a large eddy simulation (LES) so that thermal and velocity perturbations of the proper scale naturally develop. Recently Balaji and Clark (1988) using an LES approach indicated that subsequent deep convection is in fact conditioned by the initial convection. The LES procedure, however, is computationally expensive in that the cloud model may have to run for several hours prior to the period of moist convective interest in order to develop the proper spectral response. Also, with the LES method, there is no assurance that the clouds of interest will form near the center of the domain, away from the effects of lateral boundaries.

In the present study it is proposed that the scale and intensity of the perturbation used to initialize a cloud model be determined using boundary layer similarity. While other scales may be operating to alter the convective potential (mesoscale or synoptic-scale lifting), the magnitude of the vertical velocities on the meso-scale and synoptic scale is generally one to two orders of magnitude less than the magnitude of boundary-layer scale eddies. Over the last decade there have also been great strides in developing similarity expressions for turbulent statistics in the convective boundary layer (e.g., Kaimal et al. 1976; Caughey 1981) which makes this specification possible.

In the following, similarity expressions are utilized to specify a characteristic scale and intensity of a thermal perturbation used in a two-dimensional cloud model. The length scale is selected based on the peak wavelength in the temperature fluctuation spectrum, while the magnitude of the perturbation is based upon the upper tail of the distribution of thermal boundary layer fluctuations. Two methods are also proposed for

*Corresponding author address:* Dr. Richard T. McNider, Atmospheric Science and Remote Sensing Laboratory, University of Alabama at Huntsville, Huntsville, AL 35899.

choosing the realistic magnitudes of the characteristic similarity variables which determine the scale and intensity of the perturbation. Finally, the comparative response of the cloud model to the specified perturbation versus the response to the heated spinup of a large eddy approach is given. Additional examples are given of the differential cloud model response to mesoscale variations in boundary layer attributes.

The specification of the scale and intensity of the thermal based on boundary layer similarity provides some of the scale selection demonstrated to be important in the work of Balaji and Clark (1988). It should also be noted that the scale and intensity of the thermal based on planetary boundary attributes taken from a specific sounding also provides implicit incorporation of effects such as inhomogeneities in surface properties and/or the presence of a preexisting field of cumuli.

## 2. Perturbation parameterization

In the following, the thermal perturbation is specified only in two dimensions (the horizontal dimension,  $x$ , and vertical dimension,  $z$ ) but can easily be extended to three dimensions assuming horizontal symmetry in the second horizontal dimension. The functional form of the thermal perturbation,  $\theta'$ , from a base state is assumed to be Gaussian and given by

$$\theta'(x, z) = A\sigma_\theta(z) \exp\left[-\left(\frac{x - x_c}{0.5\lambda_m}\right)^2\right] \quad (1)$$

where  $x_c$  is the center of the model domain,  $\sigma_\theta(z)$  is the standard deviation of thermal fluctuations in the boundary layer and  $\lambda_m$  is a characteristic length scale of the thermal fluctuations. The parameter  $A$  determines the part of the  $\sigma_\theta$  distribution selected. For example, for  $A = 2$ , a thermal perturbation is chosen which would be two standard deviations above the mean of the distribution so that for a normal distribution, the magnitude of the fluctuation would be in the top 2% of all fluctuations.

In a cloud model, it is normally desired that the perturbation be specified in the center of the model domain to avoid boundary effects. Thus (1) gives a thermal perturbation centered in the domain whose size and intensity is dependent upon two physical parameters,  $\sigma_\theta$  and  $\lambda_m$  which will now be specified from boundary layer similarity.

The horizontal length scale,  $\lambda_m$ , is taken to be the wavelength having the maximum spectral density in the temperature fluctuation spectrum. In a convective boundary layer this scales with the boundary layer height,  $z_i$ , (Kaimal et al. 1976), and most of the convective boundary layer can be approximated by

$$\lambda_m = 1.5z_i. \quad (2)$$

From boundary layer similarity, the standard deviation of thermal fluctuations,  $\sigma_\theta$ , scales with both the con-

vective velocity scale,  $w_*$ , and  $z_i$  and is given by Caughey (1981) as

$$\sigma_\theta^2(z) = 1.8\left(\frac{z}{z_i}\right)^{-2/3} T_*^2 \quad (3)$$

where

$$T_* = \overline{w'\theta'_s}/w_* \quad (4)$$

and

$$w_* = \left(\frac{z_i g}{\theta} \overline{w'\theta'_s}\right)^{1/3}. \quad (5)$$

The quantity,  $\overline{w'\theta'_s}$  is related to the surface heat flux and  $g$  is gravity. Note that  $\overline{w'\theta'_s}$  is related to the surface heat flux,  $H_0$ , by  $H_0 = \rho c_p \overline{w'\theta'_s}$ , where  $\rho$  is the air density and  $c_p$  is the specific heat capacity. Combining (4) and (5) into (3) yields

$$\sigma_\theta(z) = 1.34z^{-1/3}(\overline{w'\theta'_s})^{2/3}\left(\frac{\theta}{g}\right)^{1/3}. \quad (6)$$

In order to utilize (1)–(5) two external physical parameters,  $z_i$  and  $\overline{w'\theta'_s}$  have to be specified. The planetary boundary layer height can generally be estimated from the sounding used to initialize the cloud model as the height of the nearly adiabatic layer; i.e., the height to which  $d\theta/dz \approx 0$ . The surface flux, however, is not normally directly available from routine observations. A boundary layer model with a surface energy budget can provide estimates of the surface heat flux as a function of external information such as surface roughness, latitude, day of the year etc. (see McCumber and Pielke 1981). This is the method employed in the examples used in this paper.

An alternative, which is gaining acceptance in the air pollution community, is an estimate based on routine observations such as cloud cover, wind speed and auxillary information such as sun angle and surface roughness. Van Ulden and Holtslag (1983) provide methodologies for these estimates. Perhaps easier to utilize are a set of nomograms developed by F. B. Smith in Pasquill and Smith (1983). The nomograms give surface heat flux, friction velocity and Monin-Obukov length from data on surface roughness, wind speed and vertical variation in potential temperature which can be obtained from the sounding.

As an example of the dependence of  $\sigma_\theta$  on heat flux, Table 1 gives  $\sigma_\theta$  for various values of the surface heat flux. For this table,  $z$  was taken to be 100 meters. Thus, for  $A = 3$  the maximum magnitude of the perturbation in (1) would range upward to 1.3 degrees. At a height of 10 meters the maximum fluctuation would be over 3 degrees.

## 3. Examples of perturbation parameterization

A cloud model developed by investigators at the Institute of Atmospheric Sciences at the South Dakota

TABLE 1. Characteristic values of  $\sigma_\theta$  as a function of heat flux from Eq. (6). The height,  $z$ , was taken to be 100 meters and  $\theta = 300$  K.

Surface heat flux $H_Q$ ( $\text{W m}^{-2}$ )	Small		Moderate			Relatively large		
	60.0	120.0	180.0	240.0	300.0	360.0	420.0	480.0
$\sigma_\theta$	0.12	0.19	0.25	0.30	0.35	0.40	0.44	0.48

School of Mines is used to demonstrate the application of the similarity scaled perturbations. The model is a two-dimensional, slab-symmetric model; i.e., no variations are allowed in the second horizontal dimension. The reader should refer to Orville and Kopp (1977) or Chen and Orville (1980) for a description of the cloud model.

In the following demonstrations the planetary boundary layer height,  $z_i$ , and surface heat flux,  $\rho c_p w' \theta'_s$  are taken from a mesoscale boundary-layer model with a surface energy budget. See Pielke and Mahrer (1975) or McNider and Pielke (1981) for a description of the mesoscale model. Figure 1 shows an example of the mesoscale variation of the heat flux and  $z_i$  from a two-dimensional mesoscale simulation over west Texas in which cloud cover to the east suppressed surface heating and boundary layer development (see Fig. 2 for a satellite image and schematic of the model domain). Figure 3 shows the model-simulated temperature field indicating a deep mixed layer to the west and a shallow more stable environment to the east. Figure 4 shows corresponding variations in  $\lambda_m$  and  $\sigma_\theta$  from (2) and (3). As can be seen, substantial variation in the intensity and scale of a perturbation exists.

To demonstrate the application of the scaled perturbation versus a LES heated spinup simulation, the cloud model is integrated for two cases. Both cases use the 1700 UTC sounding taken from the mesoscale model at the approximate location of Amarillo, Texas. In the first case, the cloud model is initialized using the similarity scaled perturbation applicable at Amarillo, i.e., with a heat flux of approximately  $420 \text{ W m}^{-2}$  and a boundary layer height of 3300 meters. For comparison, a second case was run in which the cloud model was not initialized with a perturbation, but, the model was heated at the surface using the surface heat flux applicable at Amarillo ( $420 \text{ W m}^{-2}$ ). Figure 5 shows the cloud moist convective response for both cases in terms of maximum vertical velocity over the period of integration. For the case without perturbation, the model atmosphere remains horizontally homogeneous and individual convective elements cannot appear. After 30 minutes, however, the case with no imposed perturbation shows a stronger response to the heating. The transition occurs as roundoff error gradually produces a computational homogeneity. Unnaturally, however, the air next to the ground has become very unstable and when computational inhomogene-

ties finally develop they tap this overly strong source of buoyant energy to produce a very strong thermal and associated vertical motion at 36 min. This thermal is also inconsistent with the planetary boundary layer depth which is an attribute of the sounding. This experiment is perhaps somewhat artificial in that LES modelers normally impose some perturbations near the surface. For example, Balaji and Clark (1988) impose a random white noise at the surface in their LES simulations. It does, however, show that heated spinup must be treated carefully.

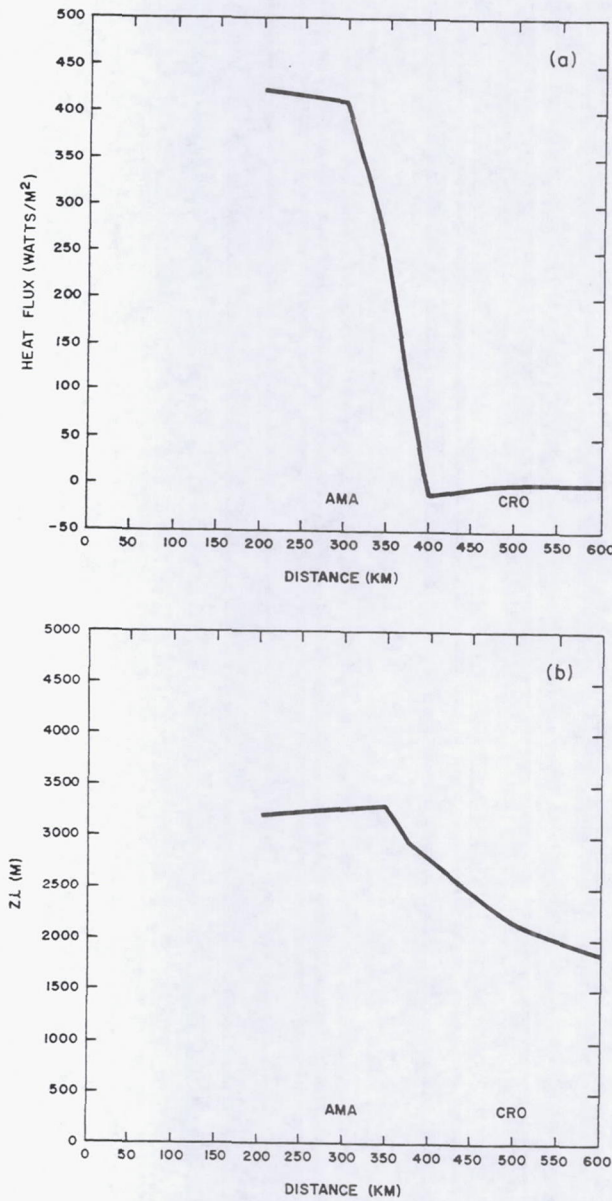


FIG. 1. Variation in (a) heat flux across the model domain and (b) planetary boundary layer height across the model domain. Height is in meters and horizontal distance is in kilometers. AMA stands for Amarillo and CRO stands for Crowell, Texas.

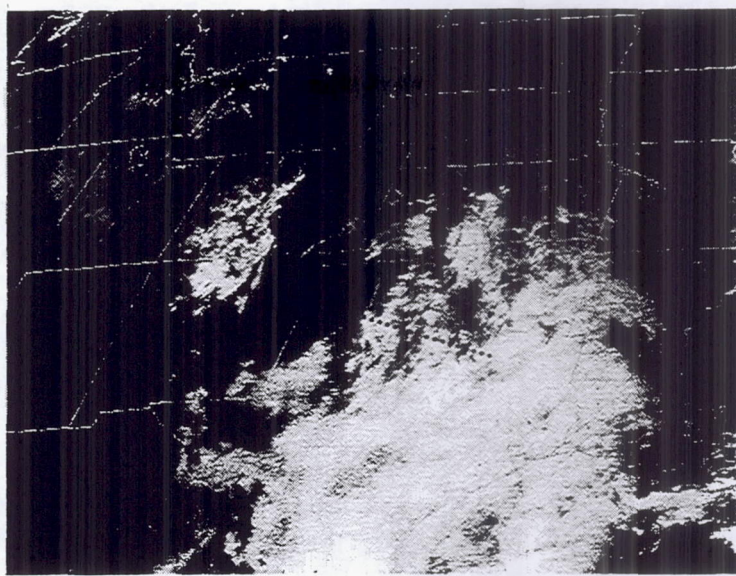


FIG. 2. Satellite view of the region over which the mesoscale model simulation was carried out. Large variations in the surface heat flux occurred across the domain between the clear and cloudy areas. The dashed line shows the two-dimensional cross section employed by the mesoscale model.

The response of the cloud model to the imposed scaled-thermal seems more reasonable. This is based on the fact that as heating continues, the subsequent velocity response of the model at longer integration

times is more in line with the initial response to the imposed perturbation than to the overly large initial response to the homogeneous heating. This is as it should be, since the specified perturbation is supposed to be compatible with the planetary boundary layer depth and heat flux imposed. The initial response is, in fact, slightly larger which may be due to the choice

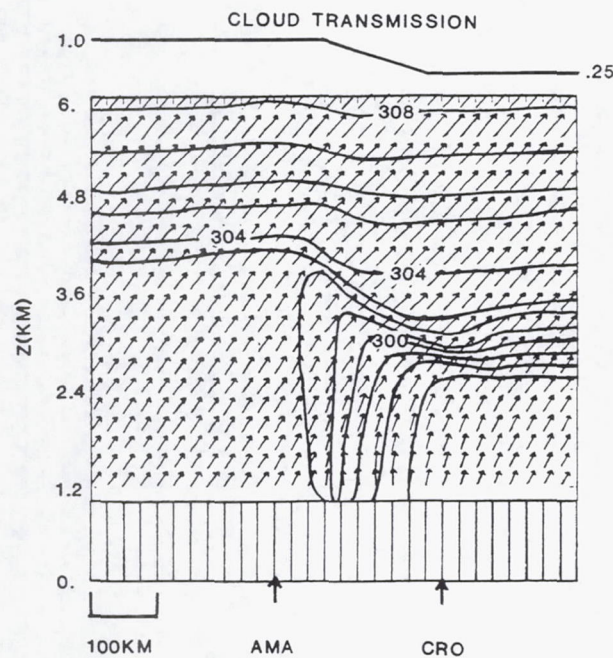


FIG. 3. Potential temperature field and wind field output of a mesoscale model simulation for 24 April 1982 used as input information for the cloud simulations in this study.

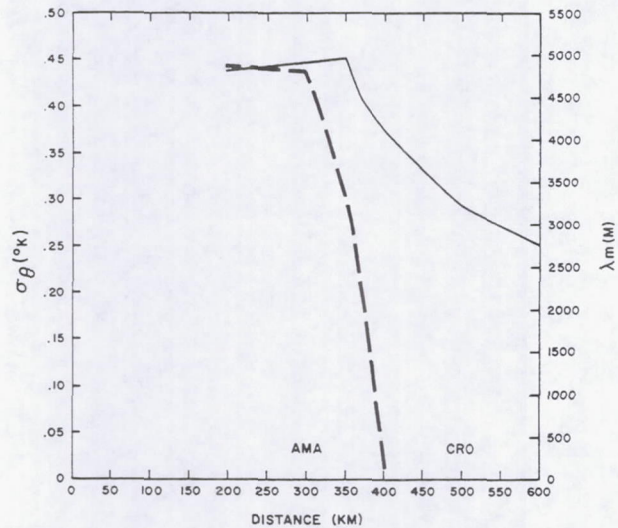


FIG. 4. Variations in the scale and magnitude of thermal perturbations due to varying  $H_0$  and  $z_i$  across the model domain. Variations in  $\lambda_m$  are solid; variations in  $\sigma_\theta$  are dashed. Variations in  $\sigma_\theta$  were calculated at a height of 100 m.

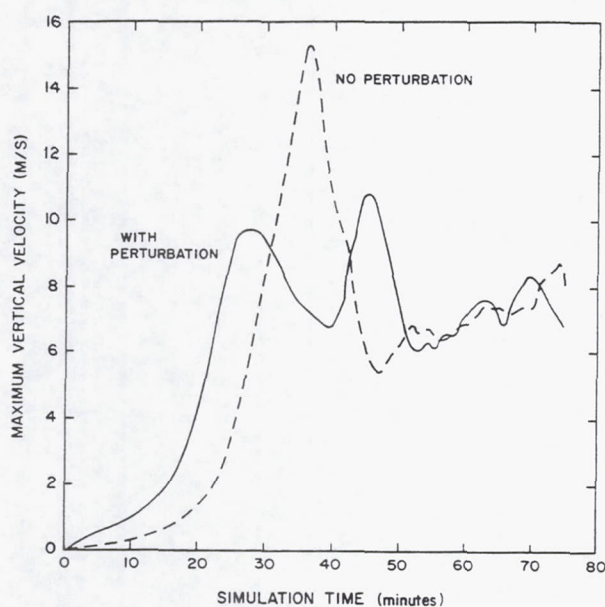


FIG. 5. Maximum vertical velocity predicted by the cloud model at any grid in the domain over the period of integration. The dashed line is for the case with no perturbation and the solid line is for the case using the similarity scaled perturbation discussed in the text.

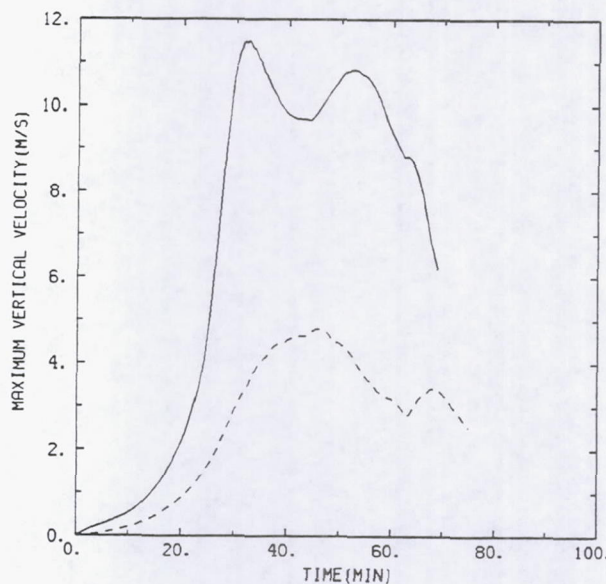


FIG. 6. Cloud model response to variations in perturbation scale and intensity. The sounding used was applicable to Amarillo. The solid line shows the response when the thermal used was based on conditions at AMA while the dashed line shows the response to a thermal based on conditions at CRO.

of  $A = 3$  in the simulation, which corresponds to a perturbation with a magnitude in the top 0.1% of all thermals.

The second example of the similarity scaled thermal examines the comparative cloud model response to variations in the scale and intensity of the thermal across the mesoscale region described in Figs. 1–4. In the first comparative case the cloud model was initialized using the sounding near Amarillo. Using this sounding the model was run first using the heat flux and boundary layer height applicable at the same location, i.e.,  $H_0 = 420 \text{ W m}^{-2}$  and  $z_i = 3300 \text{ meters}$ . Using the same sounding, the cloud model was then rerun using the heat flux and boundary layer height applicable at Crowell, i.e.,  $H_0 = 12 \text{ W m}^{-2}$  and  $z_i = 2200 \text{ meters}$ . Using  $A = 3$  in (1) yields a maximum amplitude of the perturbation of nearly 3 degrees near the surface for the first run and approximately 0.3 degrees for the second run. As would be expected the cloud model response given in Fig. 6 is quite different in the two runs. Assuming that the first run is the true response, it demonstrates that using too small a perturbation would underestimate the natural convective response.

In the second comparative case the cloud model was initialized using the sounding applicable at Crowell, which is a more stable sounding than the Amarillo sounding. The model was then run using the heat flux and boundary layer height applicable for the Crowell location, i.e.  $H_0 = 12 \text{ watts}$  and  $z_i = 2200 \text{ meters}$ . As above, using the same sounding, the model was rerun

using the heat flux and boundary layer height applicable at Amarillo, i.e.  $H_0 = 420 \text{ watts}$  and  $z_i = 3300 \text{ meters}$ . The results are shown in Fig. 7. Again assuming the first run is the true response, it demonstrates that pick-

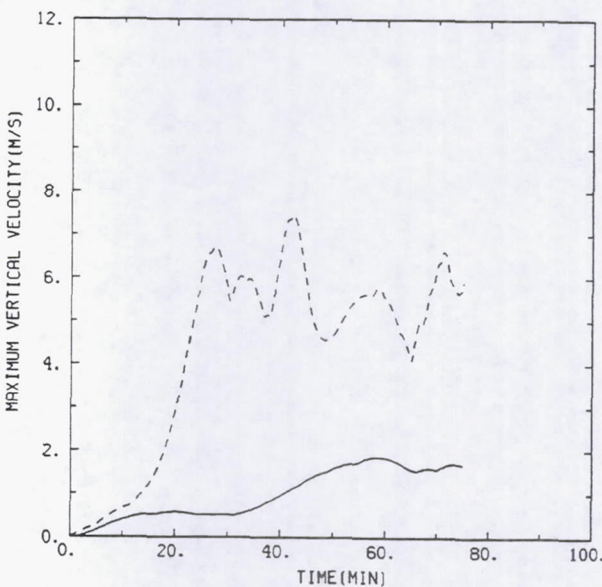


FIG. 7. As in Fig. 6 except sounding used was applicable to Crowell. The solid line shows the response when the thermal used was based on conditions at CRO while the dashed line shows the response to a thermal based on conditions at AMA.

ing a perturbation too large may cause an overestimate to the convective response.

#### 4. Conclusions

A simple methodology is given for specifying a thermal perturbation in a cloud model consistent with dry planetary boundary attributes. While other scales may be applicable for some studies such as cumulus dominated boundary layers, it is felt if boundary layer thermals are assumed to be the triggering mechanism that this methodology at least gives an objective method for choosing the magnitude and scale of a thermal perturbation. Even where cumulus dominated layers exist, if the sounding is applicable to this situation and the boundary layer depth is chosen from this sounding, then part of the proper scaling for the thermal is included. The technique described here has advantages over a LES initialization in that it is computationally more efficient and ensures that the dominant moist convection will initially occur in the center of the domain. It should be noted, however, that the LES method, where computer resources permit, provides a more realistic selection of the proper spectral response.

*Acknowledgments.* The authors would like to thank F. R. Robertson, M. Kalb and G. Wilson for their comments and suggestions. This study was sponsored by the National Aeronautics and Space Administration Contract NAS8-36479. The second author was a University Space Research Associate Visiting Scientist at Marshall Space Flight Center during this study, supported under NASA Contract NAS8-35830.

#### REFERENCES

- Balaji, V., and T. L. Clark, 1988: Scale selection in locally forced convective fields and the initiation of deep cumulus. *J. Atmos. Sci.*, **45**, 3188-3211.
- Caughey, S. J., 1981: Observed characteristics of the atmospheric boundary layer. F. T. M. Nieuwstadt and H. van Dopp, Eds. *Atmospheric Turbulence and Air Pollution Modelling*. D. Reidel, 358 pp.
- Chen, C. H., and H. D. Orville, 1980: Effects of mesoscale convergence on cloud convection. *J. Appl. Meteor.*, **19**, 256-274.
- Kaimal, J. C., J. C. Wyngaard, D. A. Haugen, O. R. Cote, U. Izumi, S. J. Caughey and C. J. Readings, 1976: Turbulence structure in the convective boundary layer. *J. Atmos. Sci.*, **33**, 2152-2169.
- Klemp, J. B., and R. B. Wilhelmson, 1978: The simulation of three-dimensional convective storm dynamics. *J. Atmos. Sci.*, **35**, 1070-1096.
- McCumber, M. C., and R. A. Pielke, 1981: Simulation of the effects of surface fluxes of heat and moisture in a mesoscale numerical model. I: Soil layer. *J. Geophys. Res.*, **86**: 9929-9938.
- McNider, R. T., and R. A. Pielke, 1981: Diurnal boundary layer development over sloping terrain. *J. Atmos. Sci.*, **38**, 2198-2212.
- Miller, M. J., and R. P. Pearce, 1974: A three-dimensional primitive equation model of cumulonimbus convection. *Quart. J. Roy. Meteor. Soc.*, **100**, 133-154.
- Orville, H. D., and F. J. Kopp, 1977: Numerical simulation of the life history of hailstorms and hail cells. *J. Atmos. Sci.*, **34**, 1596-1618.
- Pasquill, F., and F. B. Smith, 1983: *Atmospheric Diffusion*, 3rd ed.. Wiley and Sons. 437 pp.
- Pielke, R. A., and J. Mahrer, 1975: Representation of the heated planetary boundary layer in mesoscale models with coarse vertical resolution. *J. Atmos. Sci.*, **32**, 2288-2308.
- Tripoli, G. J., and W. R. Cotton, 1980: A numerical investigation of several factors contributing to the observed variable intensity of deep convection over South Florida. *J. Appl. Meteor.*, **19**, 1037-1063.
- Van Ulden, A. P., and A. A. M. Holtslag, 1985: Estimation of atmospheric boundary layer parameters for diffusion applications. *J. Climate Appl. Meteor.*, **24**, 1196-1207.

**Collection, archival and distribution of SPACE-COHMEX data sets.**

## SPACE / COHMEX DATA INVENTORY DOCUMENT

by

Steven F. Williams<sup>1</sup>  
University of Alabama in Huntsville  
Huntsville, AL 35899

H. Michael Goodman<sup>1</sup>  
University of Alabama in Huntsville  
Huntsville, AL 35899

Kevin R. Knupp<sup>1</sup>  
University of Alabama in Huntsville  
Huntsville, AL 35899

James E. Arnold<sup>2</sup>  
NASA Marshall Space Flight Center  
Huntsville, AL 35812

### 1.0 INTRODUCTION

The Satellite Precipitation And Cloud Experiment (SPACE) sponsored by the National Aeronautics and Space Administration (NASA) / Marshall Space Flight Center (MSFC) was conducted during June and July 1986. This field program ran concurrently with the Microburst and Severe Thunderstorm (MIST) program, sponsored by the National Science Foundation (NSF), and the FAA-Lincoln Laboratory Operational Weather Study (FLOWS), sponsored by the Federal Aviation Administration (FAA). All three experiments formed a comprehensive and unique data base for the study of remote sensing and convection under the acronym COHMEX (COoperative Huntsville Meteorological EXperiment). Please refer to the SPACE Experiment Design document (Arnold, et al., 1986) for further details and facilities in the SPACE portion of the experiment.

This document supersedes the Preliminary Data Document (NASA/MSFC, 1986) published October 1986, and contains additional information concerning data sets and daily atmospheric conditions throughout the project. Some data sets described in this document are currently being archived and quality assured, and may not be available for distribution at the time of this printing. Although this is the final data document, erratas or addendums may be issued at a later date.

Section 2.0 contains a brief overview of the field program facilities and activities. A description of the types of data collected with sample data products where applicable are provided. The intent is to acquaint the scientist with formats of data products to assist in research activities. This overview is sub-divided into six major data categories; 1) sounding systems, 2) radars, 3) high altitude aircraft based remote sensors, 4) aircraft, 5) satellite, and 6) surface systems.

<sup>1</sup>Senior Research Associate, Atmospheric Science and Remote Sensing Laboratory, Johnson Research Center

<sup>2</sup>Chief, Remote Sensing Branch (ED43), Earth Science and Applications Division

The largest section (3.0) presents daily meteorological conditions and summaries of data collected during the experiment. A synoptic overview of the field program is included. Daily summaries provide the following information: 1) synoptic, cloud/precipitation overviews; 2) 1200 GMT National surface and 500 mb maps; 3) aircraft/remote sensor, rawinsonde, radar, and satellite operations; 4) hourly data collection activities; 5) a visible or infrared satellite image; 6) a rawinsonde sounding (skew-T diagram); 7) a 24-h lightning density summary; and 8) a 24-h precipitation map. These summaries provide an insight to the scientist in selecting research days and data requirements.

Appendix A displays the flight tracks of the two high altitude, remote sensing aircraft (the NASA ER-2, and the NASA U2-C). Please note that some of the flights did not occur over the SPACE region. There were a number of ER-2 and U2-C flights off the Virginia coast. These flights were supported by the SPANDAR radar installation at Wallops Island, VA (Table A-1). In addition, there was one ER-2 flight along the east coast of Florida and a U2-C lightning investigation flight centered over Kentucky. Appendix B supplies a complete list of acronyms (LOA) used in this document. Appendix C contains a list of investigators and major participants who took part in COHMEC. *This list is not intended to be a complete list of COHMEC participants, but rather individuals that could provide information and insight on respective data sets.* The appendix provides address and telephone numbers to obtain data information, and request data sets.

Any comments or questions concerning the data should be directed to the SPACE data manager. All data requests must be submitted in writing to:

SPACE Data Manager  
NASA/MSFC Mail Code ED-43  
Earth Science and Applications Division  
Marshall Space Flight Center, Alabama 35812

Telephone: (205) 544-1650  
(FTS) 824-1650

#### References

Arnold, J.E., Wilson, G.S., Williams, S.F., and McNider, R.T., 1986: *Satellite Precipitation and Cloud Experiment. Experiment Design Document.* Johnson Research Center, University of Alabama in Huntsville, Alabama. 150 pp.

*Satellite Precipitation and Cloud Experiment: Preliminary Data Inventory Document.* NASA Marshall Space Flight Center, Alabama. October 1986.

## 2.0 OVERVIEW OF FIELD PROGRAM COMPONENTS AND ACTIVITIES

### 2.1 SOUNDING SYSTEMS

#### 2.1.1 Rawinsonde

Conventional upper air soundings were taken from a combination of three rawinsonde networks as shown in Fig. 2.1-1. The stations and locations are described in Table 2.1-1. Over 1,100 soundings were taken during the field program, and Fig. 2.1-2 shows the distribution of these soundings by station and date.

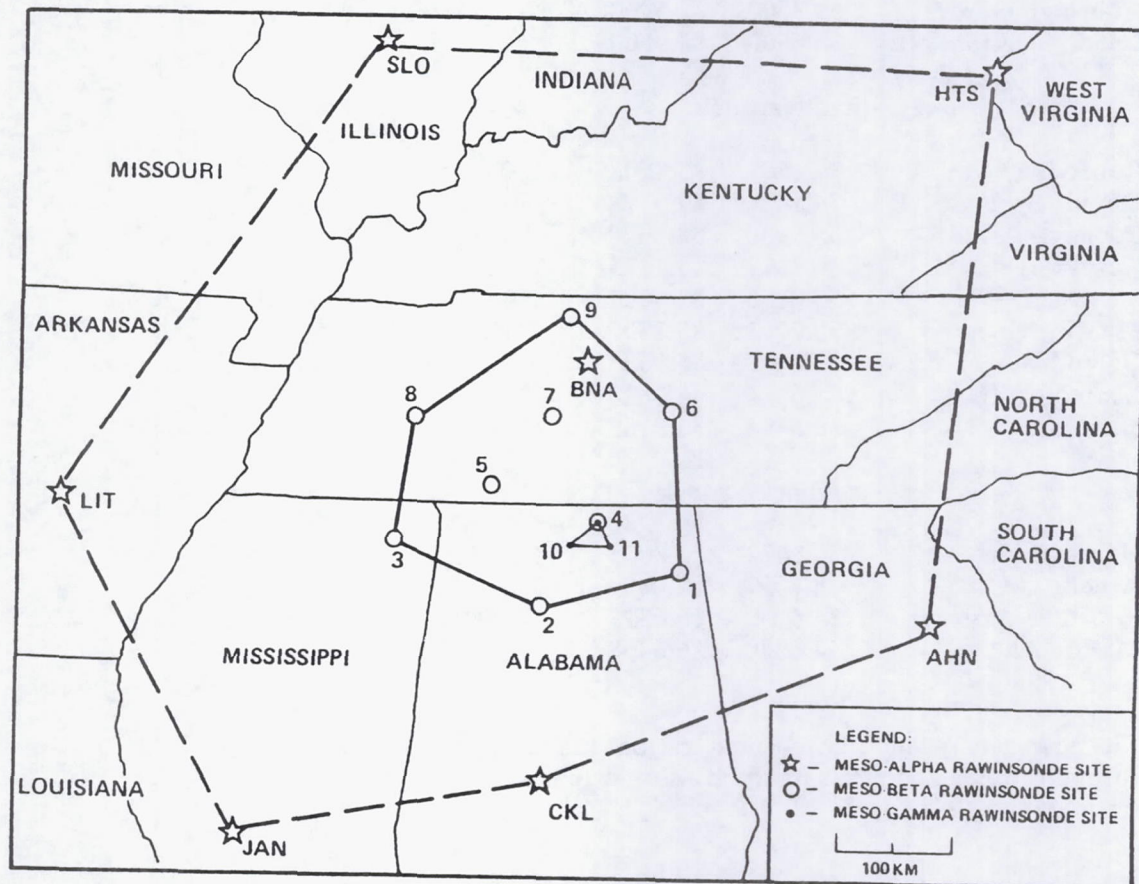


Figure 2.1-1 COHMEX rawinsonde network.

The U.S. Army (Redstone Arsenal, AL) released a sounding each morning (1200 GMT) for forecasting purposes. An early afternoon release (1800 GMT) established a climatological data base and provided local support for COHMEX operations. Additional releases occurred when meteorological conditions warranted, or to augment the Meso-gamma network. The daily 1800 GMT sounding, when available, is presented in Section 3.2.

**Table 2.1-1 SPACE Rawinsonde Network**

Site No.	Site Name	Latitude	Longitude	Elevation ft (m)
----------	-----------	----------	-----------	---------------------

**Meso-alpha Network**

72229	Centerville, AL	32.0000	87.2300	459 (140)
72235	Jackson, MS	32.3300	90.0800	328 (100)
72311	Athens, GA	33.9400	83.3200	807 (246)
72327	Nashville, TN	36.2500	86.5700	590 (180)
72340	Little Rock, AR	34.7400	92.2400	260 (079)
72425	Huntington, WV	38.3600	82.5400	807 (246)
72433	Salem-Leckrone, IL	38.6600	88.9800	574 (175)

**Meso-beta Network**

1	Rainsville, AL	34.4567	85.8608	1230 (375)
2	Double Springs, AL	34.1436	87.3378	750 (229)
3	Booneville, MS	34.5936	88.6478	385 (117)
4	Hazel Green, AL	34.8672	86.7075	815 (248)
5	St. Joseph, TN	35.0258	87.4803	810 (247)
6	McMinnville, TN	35.7033	85.8392	1040 (317)
7	Columbia, TN	35.7153	86.9633	722 (220)
8	Lexington, TN	35.6514	88.3828	505 (154)
9	Springfield, TN	36.5444	86.9183	710 (216)

**Meso-gamma Network**

4	Hazel Green, AL	34.8672	86.7075	815 (248)
10	Athens, AL	34.7097	87.0894	655 (200)
11	Redstone Arsenal, AL	34.6100	86.6317	570 (174)
12	MSFC, AL*	34.6250	86.6458	596 (182)

\* The Marshall Space Flight Center station was used for special releases and as a substitute Meso-gamma network station.

### COHMET Rawinsonde Soundings

June 1986

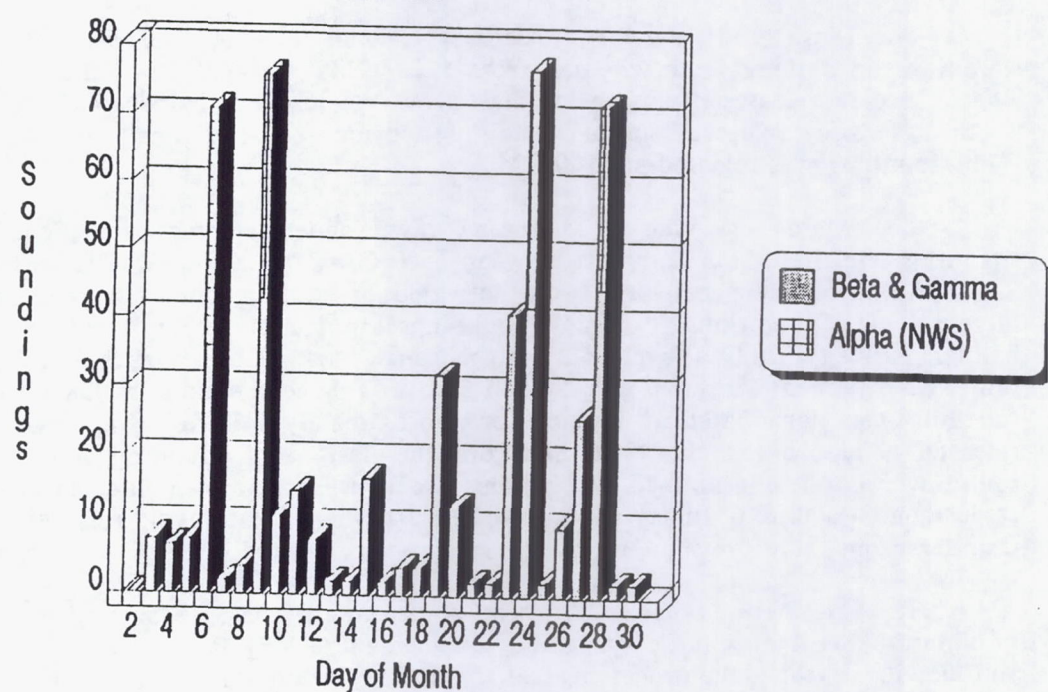


Fig. 2.1-2a Daily frequency of SPACE rawinsonde soundings for June, 1986.

### COHMET Rawinsonde Soundings

July 1986

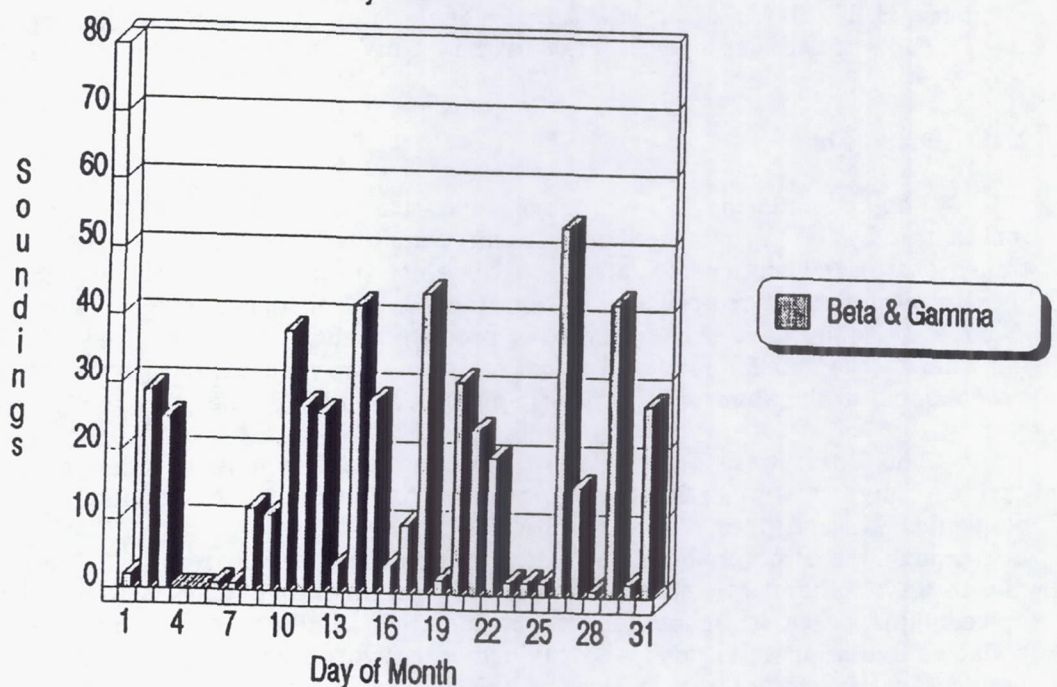


Fig 2.1-2b. Daily frequency of SPACE rawinsonde soundings for July, 1986. Note: There were no Alpha soundings taken during July 1986.

The Meso-alpha network (existing National Weather Service NWS stations) released soundings on a three hour schedule from 1200 GMT to 0600 GMT during four days in June. These special releases followed normal NWS rawinsonde launch and tracking procedures. Soundings were released approximately 1 h prior to designated sounding times (i.e. a 1200 GMT sounding was released at 1100 GMT).

The Meso-beta and Meso-gamma rawinsonde networks were configured to release soundings in three hour intervals between 1500 GMT and 0300 GMT on a full operational day. Sub-portions of these networks were activated or special soundings released depending upon meteorological conditions. Complete soundings are comprised of data from the surface up to balloon burst, typically a level of 25 mb. Normal tracking time for these soundings was 90-100 min with an ascent rate of  $5 \text{ m s}^{-1}$  ( $1000 \text{ ft min}^{-1}$ ). Special soundings taken on a 1.5 h frequency schedule were terminated at 100 mb, or approximately 1 h following release. Soundings were released at approximately 45 min before the designated sounding times (i.e. a 1500 GMT sounding was released at 1415 GMT). This procedure was implemented to center flight duration at designated sounding times. A concerted effort was made to avoid releasing a radiosonde into a thunderstorm, therefore some release times may vary around the designated sounding times.

The raw thermodynamic and wind angle data are being processed in the same manner as previous NASA Atmospheric Variability Experiment (AVE) data. A description of the procedures and details of the data processing can be found in Fuelberg (1974). The sounding data are available in both contact and interpolated 25-mb format. Final Data sets are archived in ASCII fixed block and record length files.

#### References

Fuelberg, H.E., 1974: *Reduction and Error Analysis of the AVE II Pilot Experiment Data*. Center for Applied Geosciences Texas A & M University, College Station, Texas. 131 pp.

#### 2.1.2 Raman Lidar

Raman scattering is weak molecular scattering whose wavelength is shifted from the incident radiation by a fixed amount associated with rotational and/or vibrational-rotational transitions of the scattering molecule. The shift from the laser wavelength is characteristic of specific atmospheric molecules. In the atmosphere, nitrogen, oxygen, water vapor, and carbon dioxide molecules have been observed to produce Raman scattering. Melfi (1972) has shown that the ratio of the Raman-scattered signal for the water vapor shifted to the signal from nitrogen is proportional to the atmospheric specific humidity (units of  $\text{g kg}^{-1}$ ).

The lidar consists of a laser (wavelength 355 nm) and a telescope (diameter 1.5 m) optically aligned with each other. The telescope and laser are mounted in an environmentally controlled van and peer vertically through a hatch in the van's roof. The laser pulse propagates up through the atmosphere and is scattered by molecules and aerosols. Most of the scattering is due to Rayleigh and Mie scattering. However, a small amount is scattered at the shifted Raman wavelengths. The telescope collects the radiation that is scattered back toward the lidar. The collected radiation is filtered and divided into two channels. The first channel has a narrow bandpass filter centered on the Raman shifted wavelength due to water (406 nm) and the second channel has a filter centered on the Raman shifted wavelength due to nitrogen (387 nm). The signal from each channels provide measure of the atmospheric scattering which can be analyzed to provide a measurement of specific humidity vs. altitude. A more complete description of the Raman lidar is given in Melfi and Whiteman (1985).

Figure 2.1-3 displays a black and white rendition of lidar derived specific humidity over the Athens, Alabama site (34.7608 N, 86.9786 W), as a function of both time and altitude during the morning of 22 July 1986. The moisture sounding shows the temporal history of the mixing ratio between 0800 - 1000 GMT (0300 and 0500 CDT). The moisture features apparent in this image are:

1. The high moisture associated with the previous days planetary boundary layer. This feature is well mixed and stratified, and extends up to 1.8 km.
2. There is a gradual moistening of the free troposphere in the altitude range between 1.8 km and 4.0 km as the specific humidity changes from  $2 \text{ g kg}^{-1}$  (at 3:04 am) to  $9 \text{ g kg}^{-1}$  (5:00 am). It appears that there were two times when moisture increased in this altitude range rather abruptly, first at 3:15 am and again at about 4:00 am.
3. The dry/moist feature at an altitude between 4 and 5 km. The moist feature generally subsides over the two hour period, but begins to rise toward the end of the period.
4. The small scale variation in moisture in the free troposphere. This is seen as a stippled appearance of the moisture above 1.8 km.

### RAMAN LIDAR MEASUREMENTS OF SPECIFIC HUMIDITY ATHENS, AL JULY 22, 1986

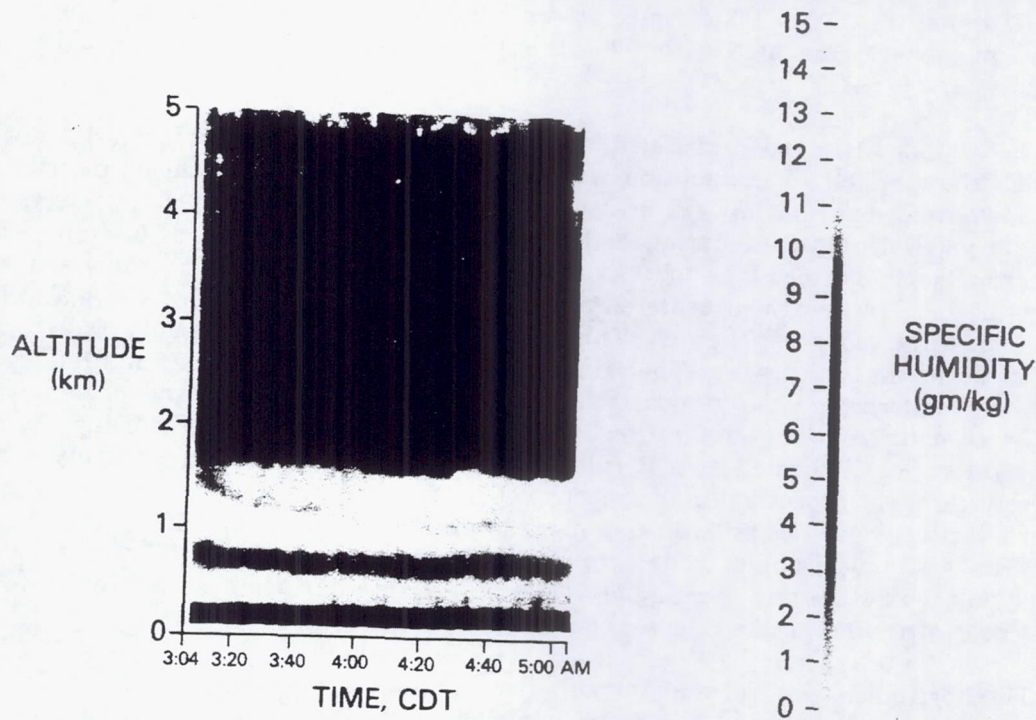


Fig. 2.1-3. Raman lidar depiction of derived specific humidity over Athens, AL on 22 July 1986

## References

Melfi, S. H., 1972: Remote Measurements of the Atmosphere Using Raman Scattering, *Appl. Opt.* 11, 1605-1610

Melfi, S. H., and D. Whiteman, 1985: Observation of Lower-Atmospheric Moisture Structure and its Evolution Using a Raman-Lidar, *Bull. Amer. Meteor. Soc.* 66, 1288-1292

### 2.1.3 Ultra High Frequency (UHF) Radar Wind Profiler

A Ultra High Frequency (UHF) Doppler radar wind profiler was co-located with the Raman lidar 5 km south of Athens, Alabama, and about 35 km west of Huntsville (34.7608 N, 86.9786 W). The Doppler radar wind profiler transmitted energy at 405.25 MHz from antenna, separated by 90° in azimuth, at 15° oblique angles from zenith. One of the off zenith beams was oriented 53° (NE) along the radial to the CP-2 radar, while the other was oriented at 323° (NW) from azimuth. The Doppler shifted, backscattered energy is received by each antenna, and the radial velocities are measured along each beam. The horizontal wind components are then computed from the radial velocities (assuming the vertical velocity is zero). The vertical component of the wind is measured directly with a beam directed toward zenith (Augustine and Zipser, 1987). Since there was an abundance of Doppler radars in the near vicinity, the primary focus of the UHF wind profiler was to collect vertical velocity data. However, horizontal wind data was collected throughout the experiment. A characteristic of the UHF wind profiler is its sensitivity to precipitation. This sensitivity was used to determine the size of the hydrometeors since the terminal velocity of a hydrometeor is related to the square root of its diameter. The size estimates can then be compared with the size estimates deduced from the CP-2 Doppler radar (Forbes and Carrol, 1987).

The 405.25 MHz radar operated at a reduced power and therefore, did not normally collect data above 7 km. The attention was focused in the lowest 2.5 km of the storms, where inflow, downdraft, and outflow features were present. Figure 2.1-4 is a time section of wind profiler air vertical velocities during and surrounding the passage of a gust front across the profiler from north-northeast to south-southwest on 31 July 1986. The thunderstorms which produced the outflow remained centered at least 15-20 km from the profiler, and only a brief shower reached the ground at the site. This shower, and other rain shafts aloft, fell from the anvil of a storm to the north and west. The rain shafts were sufficiently isolated, and fell on a slant, so that they only intercepted the vertical beam occasionally. This caused the pockets seen in the figure. Most velocities were output directly from the routine spectrum processing algorithm. Air velocities at locations indicated by a R (rain contamination) or a T (turbulence) were determined subjectively through inspection of the spectra. Upward vertical velocities as large as  $6 \text{ m s}^{-1}$  and downward vertical velocities as large as  $7 \text{ m s}^{-1}$  were noted in the immediate vicinity of the gust front. The scanning Doppler radars revealed the passage of a fine line across the profiler accompanying the gust front, traveling at  $41 \text{ km h}^{-1}$ . Using this value, an approximate horizontal scale has been attributed to the time section.

The horizontal wind for another gust front passage is depicted in Fig. 2.1-5. The figure shows contours of the measured horizontal wind velocities for a gust frontal passage on 25 July 1986. The frontal passage can clearly be seen at 2215 GMT.

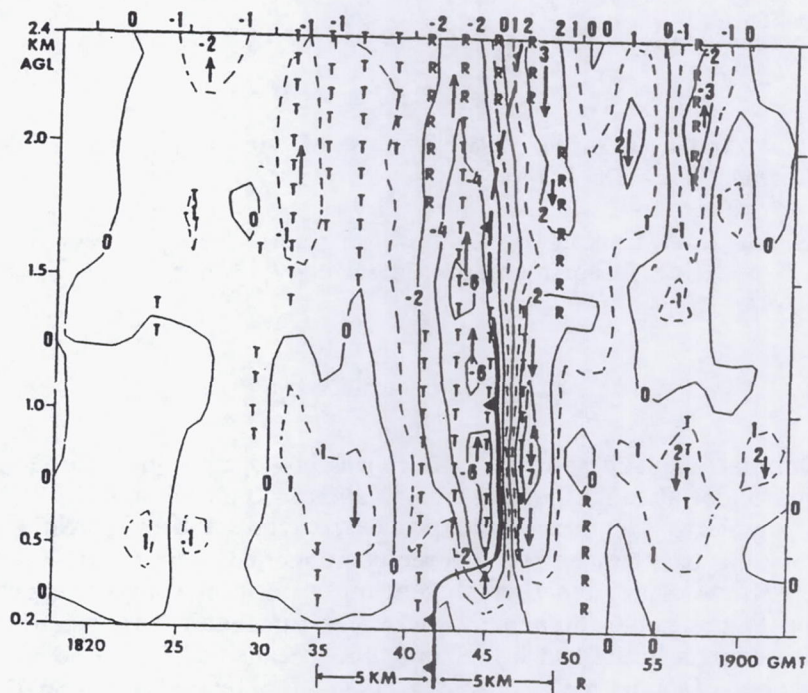


Fig. 2.1-4. Time section of UHF wind profiler-derived air vertical velocity  $\text{m s}^{-1}$  accompanying and surrounding the passage of a gust front on 31 July 1986. Velocities are output directly from the routine profiler algorithms, except where rain (R) and turbulence (T) yielded erroneous results. In these cases, velocities have been inserted based upon interpretation of the multi-peaked spectrum. Time passage of gust front wind shift, and approximate time-space conversion scale are indicated.

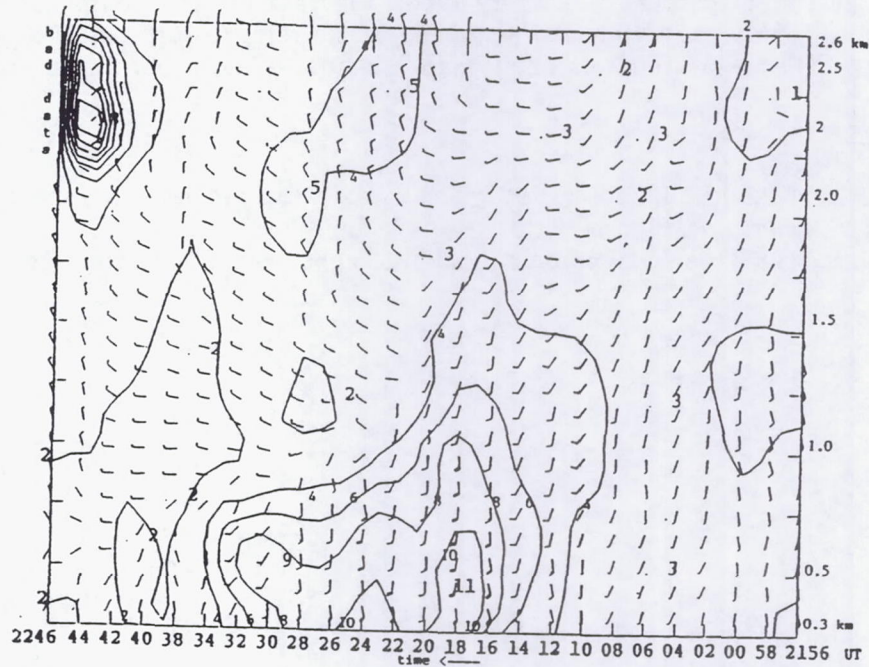


Fig. 2.1-5. Time section of the UHF Doppler wind profiler measured horizontal wind vectors for a gust frontal passage on 25 July 1986.

## References

- Augustine, J. A. and E. J. Zipser, 1987: The use of wind profilers in a mesoscale experiment.  
*Bull. Amer. Soc.*, 68, 4-17
- Forbes, G. S. and L. A. Carroll, III, 1987: *Initial results from the Penn State wind profiler in MIST/SPACE*, Department of Meteorology, Pennsylvania State University, University Park, PA

### 2.1.4 Sodar

A Doppler acoustic sounder (sodar) was co-located with the Doppler UHF wind profiler and the Raman lidar at the Athens, Alabama site (34.7608 N, 86.9786 W).. The sodar operates on the same principle as the UHF wind profiler, except it uses acoustic pulses. The sodar used during the SPACE experiment was a three component system (north-south component, east-west component, vertical component) which sent out a pulse of sound energy at 1600 Hz. The pulse is backscattered to the same antenna by thermal or mechanical turbulence. The effective vertical range of the sodar is limited to less than 1 km, because of the rapid attenuation of sound waves in the atmosphere (Augustine and Zipser, 1987). The sodar operated for most of the period except during precipitation events at the site. As soon as the rainfall subsided the sodar was restored to an operational status.

A gust front is an ideal meteorological phenomena to be measured by a sodar. A gust front is characterized by strong vertical wind shear and a large vertical thermal gradient. The vertical wind shear and thermal gradient provide favorable conditions for acoustic scattering. Figure 2.1-6 is a contoured plot of vertical velocities at the Athens, Alabama sodar site at the time of a gust front passage on 25 July 1986. Figure 2.1-7 is a contoured plot of the horizontal wind vectors for the same time as Fig. 2.1-6. Please refer to Fig. 2.1-5 for a comparison of sodar and wind profiler measured horizontal wind velocities (please note the different z-axis scales).

## References

- Augustine, J. A. and E. J. Zipser, 1987: The use of wind profilers in a mesoscale experiment.  
*Bull. Amer. Soc.*, 68, 4-17
- Forbes, G. S., 1987: (personal communication), Pennsylvania State University, University Park, PA.

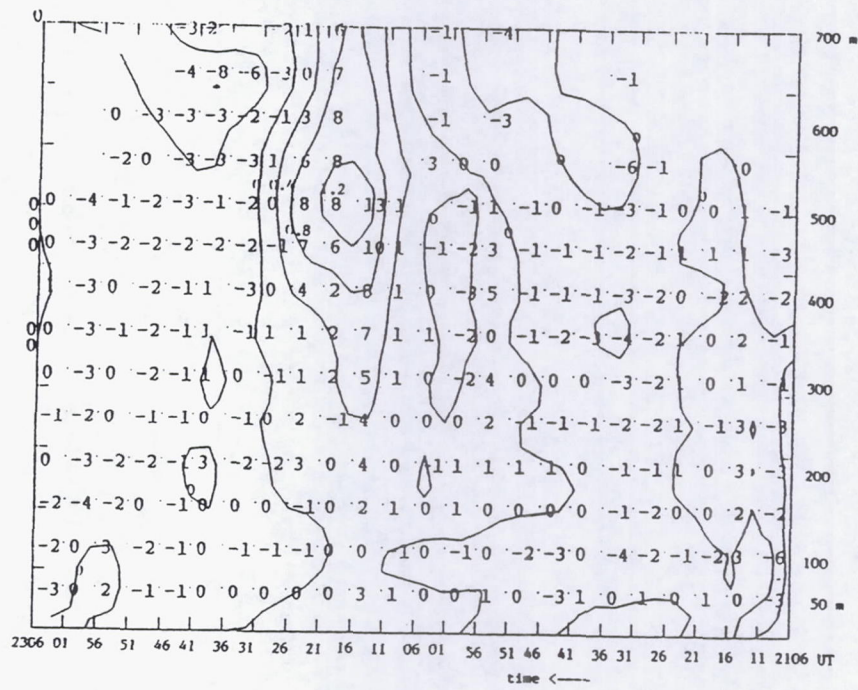


Fig. 2.1-6. Time section of the sodar measured vertical velocities for a gust frontal passage on 25 July 1986.

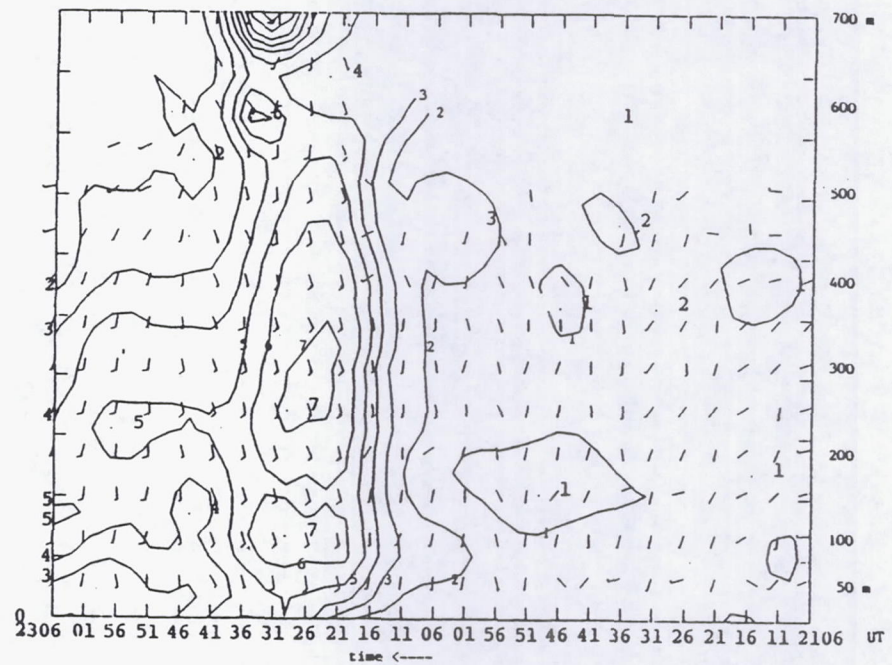


Fig. 2.1-7. Time section of the sodar measured horizontal velocities for a gust frontal passage on 25 July 1986.

**Page intentionally left blank**

## 2.2 RADARS

Radars available during COHMEC consisted of five research Doppler radars in addition to a RADar DAta Processor (RADAP) device installed on the Nashville (BNA) WSR-57 radar. Radar locations are shown in Fig. 2.2-1 and listed in Table 2.2-1. General radar characteristics are given in Table 2.2-2. The National Center for Atmospheric Research (NCAR) radars (CP-2, CP-3 and CP-4) were generally under the control of MIST Principal Investigators whenever convective activity was close to or within the MIST network. The two Doppler radars associated with the FLOWS program (FL-2 and UND) typically worked as a pair independent from the NCAR radars. When thunderstorms were either within or very close to the MIST/FLOWS network, FL-2 often sampled to a maximum range of 50 km.

Radar surveillance coverage was provided on large scales under low resolution ( $2^{\circ}$  elevation and azimuth steps, 1 n mi range steps, and 10 min time increments) by the BNA RADAP whenever it was operational. These scans started at an elevation of  $0.5^{\circ}$  and were incremented upwards to 2, 4, 6, . . . ,  $22^{\circ}$  if echoes were present at higher elevations, and if NWS personnel allowed the cycle to continue automatically. In general, multiple elevation volume scans were acquired systematically during episodes of deep convection. RADAP data were unavailable for two extended time periods in June (June 5 to June 12, and June 15 to 25, and other isolated days - see Section 3.2, Daily Summaries for details) due to hardware problems. An Interactive Color RADar Display (ICRAD) was ingesting BNA RADAP data at MSFC throughout the field program. The ICRAD data consisted of  $3 \times 5$  nm resolution images of cloud top height, vertical integrated liquid water content, rainfall estimation, and reflectivity.

Additional low-elevation radar surveillance scan coverage was provided by CP-4 at a low elevation scan whenever the MIST radars were operational. These surveillance scans were generally acquired every 6 min at  $0.5^{\circ}$  elevation at ranges out to 115 km. See Fig. 2.2-1 for coverage area relative to the SPACE mesonet. Sampling resolution was typically  $\sim 1^{\circ}$  in azimuth and 200 m in range. Surveillance scans were taken less frequently and systematically by the other Doppler radars. UND often implemented NEXRAD full volume scans at multiple elevations. At times when thunderstorms were located beyond 150 km range, CP-2 was used for long-range surveillance scans out to 300 km (0.5 Pulse Repetition Frequency).

Multiple Doppler radar data were acquired only within the stippled rectangle shown in Fig. 2.2-1. As stated earlier, the three MIST/NCAR radars worked independently from the two FLOWS radars due to operational constraints. Quite often, however, common storm volumes were scanned in a non-coordinated fashion. During coordinated multiple Doppler operations, the three NCAR radars attempted to scan the full depth of thunderstorms over a horizontal area of  $\sim 200 \text{ km}^2$  at  $\sim 2.5$  min cycle times. Because of geometrical constraints (baseline effects), it was commonly impossible to cover the entire life cycle of convective cells under ideal multiple Doppler coverage. However, it appears that a great deal of multiple Doppler data were acquired under good temporal and spatial resolution.

When not conducting multiple Doppler scans, the NCAR radars (CP-2 and CP-4 in particular) typically conducted full volume scans on echoes that were within range. Such scans consisted of Plan Position Indicator (PPI), Range Height Indicator (RHI) and Velocity Azimuth Display (VAD) modes. When aircraft operations were taking place, high spatial and temporal resolution radar scans were implemented to provide support whenever possible. In some cases when thunderstorms were located over the MIST network, but aircraft were elsewhere, radar support was much less frequent, but this was generally not a problem.

Clear air returns were usually very good from the surface upwards to 4-5 km above ground level. Quite often, and particularly under easterly flow conditions, an elevated layer of enhanced reflectivity (apparently from insect backscattering) existed near the 3-4 km level. CP-2 was able to detect clear-air echoes out to 100 km or more, and CP-4 out to 60 km or greater. Such return was valuable in detection of fine-scale wind profiles and perturbations in flow within the clear air around thunderstorms.

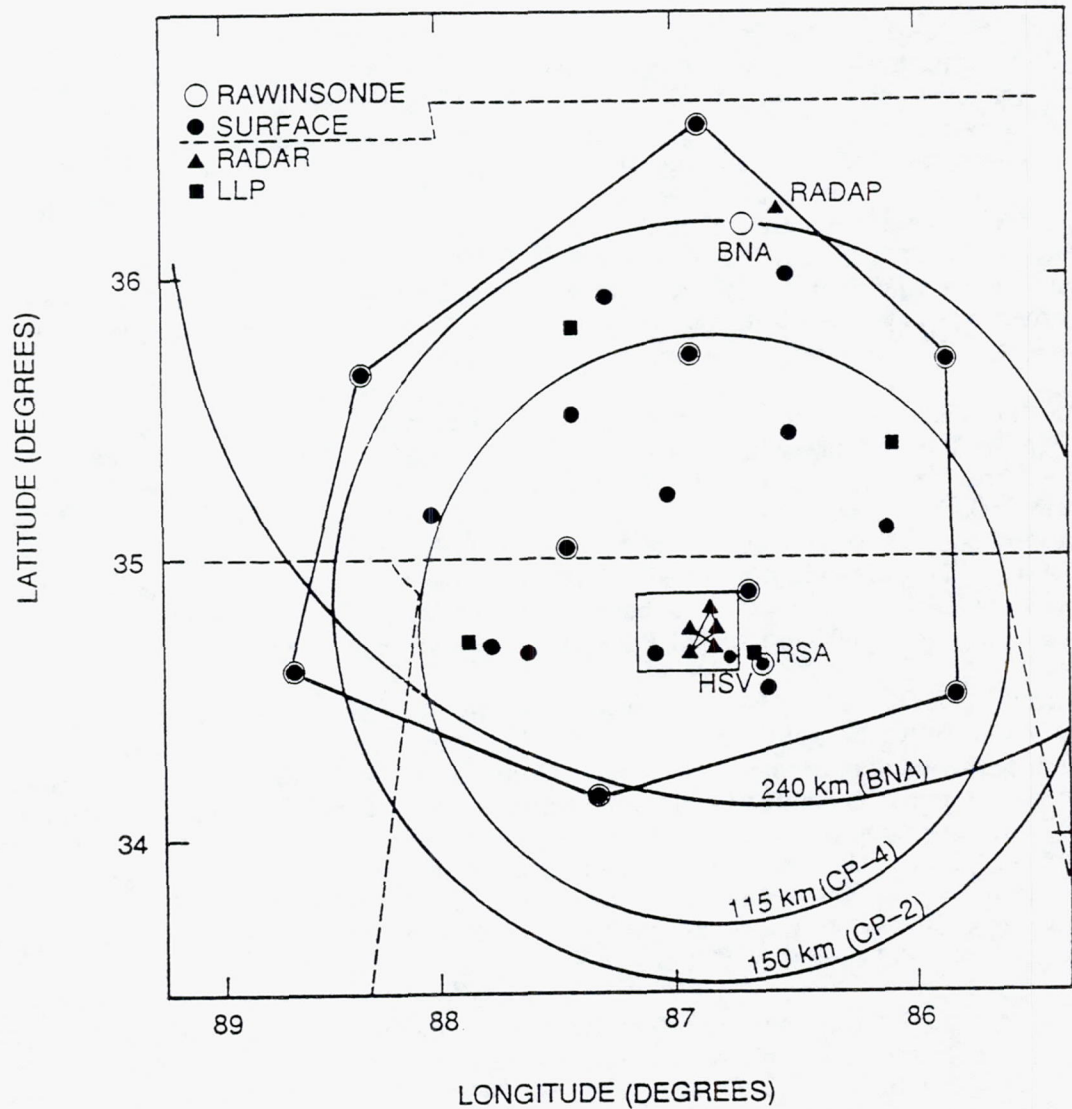


Fig. 2.2-1. Locations of COHME radar, rawinsonde, surface, and lightning detection sites. Shaded region represents the MIST/FLOWS mesonet area. Circles represent typical maximum ranges for the designated radars.

Table 2.2-1 COHDEX Radar Network

WBAN No.	Site Name	Latitude (deg N)	Longitude (deg W)	Elevation Above MSL ft (m)
93862	CP-2	34.8486	86.8325	866 (264)
	CP-3	34.6433	86.9381	604 (184)
	CP-4	34.7217	86.8286	672 (205)
	FL-2	34.6535	86.8053	636 (194)
	UND	34.7425	86.9268	663 (202)
	Tupelo, MS	38.3600	82.5400	325 (099)
13897	Nashville, TN	36.2500	86.5700	590 (180)

Table 2.2-2. General parameters of the COHDEX radars.

Radar	Wavelength (cm)	Peak Power (kw)	System Noise Power (dBz)	Beamwidth (deg)	Maximum Range (km)	Measured Parameters
CP-2	10.7/3.2	1200/200	-104/-107	0.93/0.94	156	ZH, ZX, VR, SW, ZDR, LDR, NCP
CP-4	5.5	400	-106	1.11	115	ZH, VR, NCP
CP-3	5.5	400	-104	1.02	?	ZH, VR
FL-2	10.6	1100	-108	0.96	48-200	ZH, VR, SW
UND	5.4	250	-98	0.99	56-226	ZH, VR, SW
RADAP	10.0	410		2.2	240	ZH

Available parameters:

ZH	- Reflectivity factor at horizontal polarization
ZX	- X-band reflectivity factor (CP-2 only)
VR	- Radial velocity
SW	- Width of the Doppler Spectrum (standard deviation)
ZDR	- Differential reflectivity factor (S-band)
LDR	- Linear depolarization ratio (X-band)
NCP	- Normalized coherent power

**Page intentionally left blank**

## 2.3 AIRCRAFT BASED REMOTE SENSORS

### 2.3.1 Advanced Microwave Moisture Sounder (AMMS)

The Advanced Microwave Moisture Sounder (AMMS) flew on the ER-2 high altitude aircraft. The AMMS instrument senses microwave radiation in the 92 GHz and 183 GHz frequencies. The image in Fig. 2.3-1 displays the five channels available from the AMMS instrument. The image is a completely processed AMMS photograph, including the effects of calibration smoothing and filtering. The brightness temperatures were converted linearly to a gray scale having 256 levels from black to white. The intensity scale at the top of each picture shows the relationship between temperature and gray scale.

The image is divided into two 22.5 min sections with time increasing from top to bottom. Tick marks are positioned at 1 min intervals. The temperature resolution scale was expanded using a tri-folded gray scale. Each gray scale revolution represents a fifty degree temperature range (130 K to 180 K, 180 K to 230 K, and 230 K to 280 K). The 92A channel is the unfolded 92 GHz channel with an 80 K temperature range. The 92A channel is used as a reference image, since it shows ground features more clearly than the 92 GHz tri-folded swath. The other three channels are all centered around the 183 GHz frequency. The  $183^{\pm}2$  GHz channel is the summation absorption of the 181 GHz and 185 GHz frequencies. Likewise, the  $183^{\pm}5$  GHz and the  $183^{\pm}9$  GHz channels are summations of the 178 GHz and 188 GHz, and the 174 GHz and 192 GHz absorptions, respectively. The  $183^{\pm}2$  GHz channel is more sensitive to upper atmospheric moisture than the  $183^{\pm}5$  GHz channel. Therefore, the  $183^{\pm}5$  GHz channel "sees" moisture at lower levels and is more sensitive to surface features than the  $183^{\pm}2$  GHz channel. A similar comparison can be made for the  $183^{\pm}5$  GHz and  $183^{\pm}9$  GHz channels.

No geometric corrections are applied to the data. The width of the pixels as projected to the ground at the swath border ( $45^{\circ}$  view angle) is twice that at the center of the swath (nadir viewing). The total swath width at the ground is twice the aircraft altitude. The scans are from right to left of the aircraft track. The orientation of the images is as if the observer looked down while facing the rear of the aircraft.

### References

- Krupp, B. M., D. P. Kaiser, I. Hakkarinen, 1986: *Observations with the Advanced Microwave Moisture Sounder (AMMS) during the 1986 Genesis of Atlantic Lows Experiment (GALE)*, Science Applications Research, Lanham, MD.

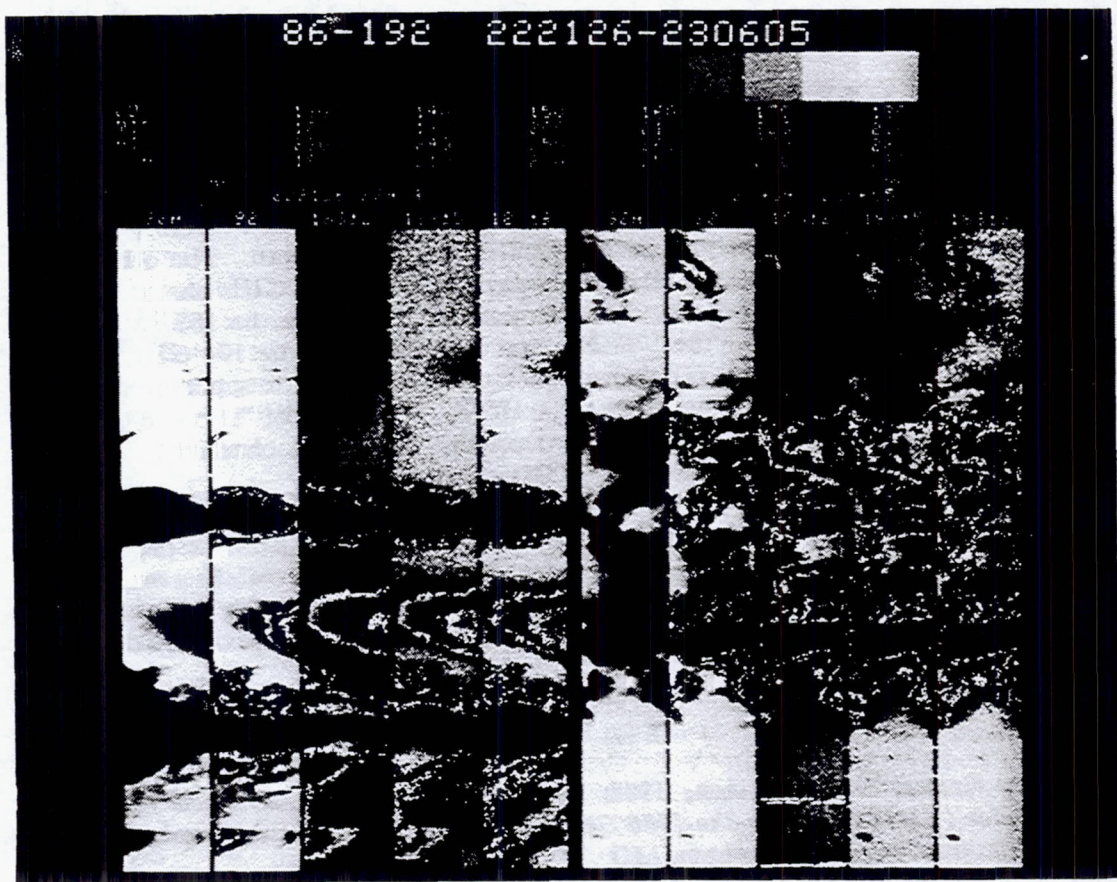


Fig. 2.3-1. A five channel AMMS image (calibrated and filtered) for a flight on the ER-2 on 11 July 1986. The image is divided into two 22.5 min sections with time progressing from top to bottom.

### 2.3.2 Microwave Precipitation Radiometer (MPR)

The Microwave Precipitation Radiometer (MPR) is an airborne dual polarized radiometer operating at 37 and 18 GHz. The MPR was mounted in a wing pod of the NASA ER-2 high altitude aircraft. The MPR was used to determine the extent to which the scattering produced by precipitation (especially ice) can be used to retrieve rain rates over land and ocean.

Preliminary data analysis has shown scattering from thunderstorms, at 37 GHz, causes brightness temperatures ( $T_B$ ) to fall below 200 K (compared with a background  $T_B$  of about 270 K). On occasion  $T_B$  have approached 100 K. The 18 GHz storm signatures also showed strong  $T_B$  depressions (to below 200 K).

Figure 2.3-2 shows an example of the 37 and 18 GHz signatures over ocean, wet ground and storms. Note the difference between the 37 and 18 GHz channels allows discrimination between the wet surfaces (emissive) such as the ocean, and the precipitation (volume scatters). This is because the emissivity of the wet surfaces increases with frequency, while that of the precipitation decreases with frequency.

#### References

Spencer, R. W., T. T. Wilheit, R. E. Hood, A. T. C. Chang, 1987: Precipitation detection with ER-2 flights of the Microwave Precipitation Radiometer (MPR), *Proceedings of the Second Airborne Science Workshop*, February 3-6, 1987, Miami, FL.

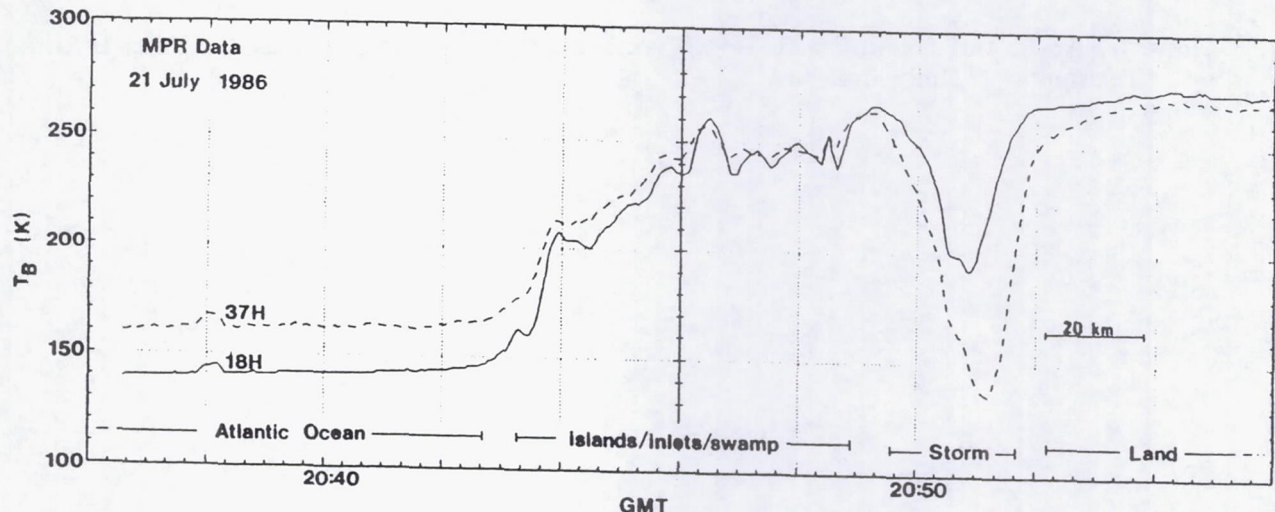


Fig. 2.3-2. MPR data collected 21 July 1986 as the ER-2 made a south to north pass over the Georgia-South Carolina coastline to intercept a storm just inland of the Atlantic Ocean. National Weather Service radars reported a storm height of 12 km with reflectivities exceeding 50 dBZ for this storm. Note the ability of two frequencies to discriminate between the ocean surface (as well as wet land and other water bodies) and the storm. Because a preliminary calibration was used here, brightness temperature depressions could be in error by 10%.

### 2.3.3 Millimeter-Wave Temperature Sounder (MTS)

The Massachusetts Institute of Technology Millimeter-Wave Temperature Sounder (MTS) is a scanning millimeter-wave spectrometer using eight channels of decreasing opacity (118-75 GHz) oxygen resonance. The MTS flew aboard the NASA ER-2 high altitude aircraft. It performed a cross-track scan approximately every 6 sec, with 14 spots of 7.5° beamwidth per scan. The field of view is  $\pm 45^\circ$  from nadir and the atmosphere is uniformly sampled at the mid-altitude height of  $\sim 10$  km for  $200 \text{ m s}^{-1}$  airspeed.

The MTS also supports a single channel nadir-viewing fixed-beam radiometer sensing atmospheric emissions in the microwave oxygen absorption complex at 53.7 GHz. The MTS is configured with a wide angle color Charge Couple Device (CCD) video camera and Video Cassette Recorder (VCR) with time-date overlay, providing nadir-viewing optical imagery.

Figure 2.3-3 shows typical brightness temperature structure observed by the MTS during a flight of the NASA ER-2 over the SPACE area. The strip map images reveal strong convective cells, characterized by reductions in radiometric brightness which sometimes exceed 80 K (saturated dark regions). These large negative perturbations in brightness temperature are produced by strong scattering of the cosmic radio background by convected ice near the cloud tops. The perturbations are of less magnitude in the more opaque channels. The most opaque channel (far-right) responds only to the most convective and ice laden cells.

The MTS radiometric data sets are approximately 42 min in length. The strip map images are 14 pixels across track and 384 pixels ( $\sim 500$  km) along the flight track.

### References

- Gasiewski, A. J., and Staelin, D. H. 1987: (personal communication), Massachusetts Institute of Technology, Cambridge, MA.

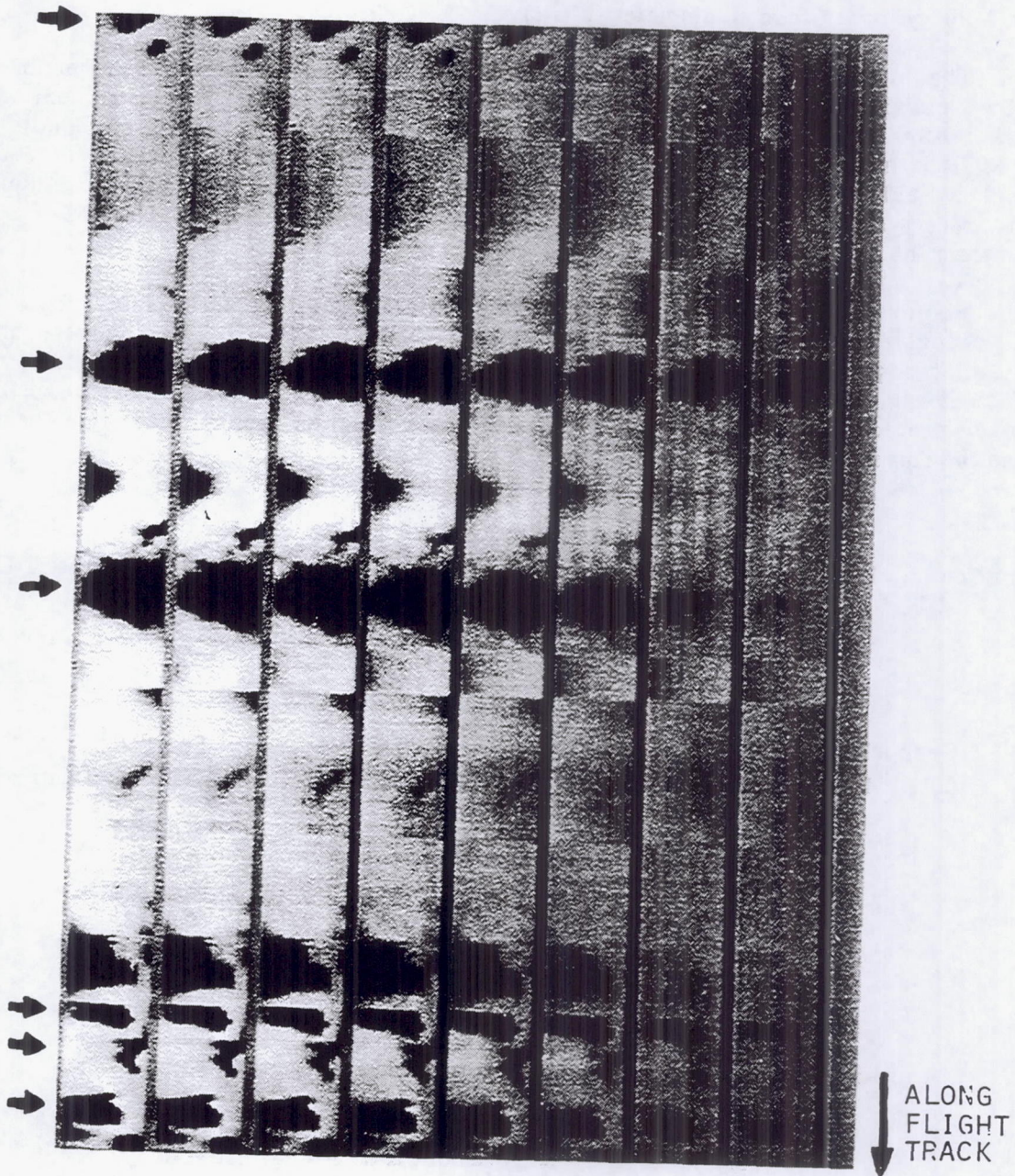


Fig. 2.3-3. An eight channel MTS brightness temperature image from a flight of the NASA ER-2 over the SPACE region. Time progresses from top to bottom along a 42 min (~500 km) flight track. Dark spots (saturated regions) are area in which the radiometric brightness exceeded 80 K.

### 2.3.4 Multispectral Cloud Radiometer (MCR)

The Multispectral Cloud Radiometer (MCR) is a high resolution radiometer with six narrow bandwidth near-infrared channels and one infrared channel. The instrument was flown on the NASA ER-2 high altitude aircraft and was used for remote sensing of cloud properties. The MCR is mounted downward-facing from the aircraft and actively scans at 3.47 times per second, a field  $\pm 45^\circ$  of nadir. All channels are sampled simultaneously with 336 samples across each active scan. The instrument field of view is 7 milliradians. Tables 2.3-1 and 2.3-2 summarize the characteristics and primary functions of each channel.

Figure 2.3-4 is a sample of MCR data from a ER-2 flight on 02 July 1986. All seven MCR channels are shown for the time period 194014 - 194240 GMT. The data were taken along the leading edge of a developing line of thunderstorms. Flight direction was from top to bottom in each image, corresponding to a total distance of about 30 km. Note the clear distinction in channel 5 of ice phase (darker area) and water phase (brighter area). Note from the channel 7 image the corresponding colder cloud top of the ice cloud.

#### References

Spinhirne, J., 1987: (personal communication), NASA/Goddard Space Flight Center, Greenbelt, MD.

Table 2.3-1 Summary of MCR Channels

<u>Channel Number</u>	<u>Central Wave Number (cm<sup>-1</sup>)</u>	<u>Central Wavelength (um)</u>	<u>Spectral<sup>1</sup> Resolution (um)</u>
1	13271.0	0.75355	0.00093
2	13147.0	0.76063	0.00116
3	13098.0	0.76345	0.00108
4	7340.0	0.3623	0.0088
5	6079.0	1.6451	0.054
6	4630.0	2.1599	0.0894
7	844.0	11.843	1.073

<sup>1</sup> full width at half maximum

Table 2.3-2 Primary functions of MCR channels

<u>Channel No.</u>	<u>Primary Function</u>
1	Visible reflectance, A-band altimetry
2	O <sub>2</sub> A-band altimetry, volume scattering coefficient
3	O <sub>2</sub> A-band altimetry, volume scattering coefficient
4	Water vapor
5	Cloud phase, particle size
6	Cloud phase, particle size
7	Brightness temperature

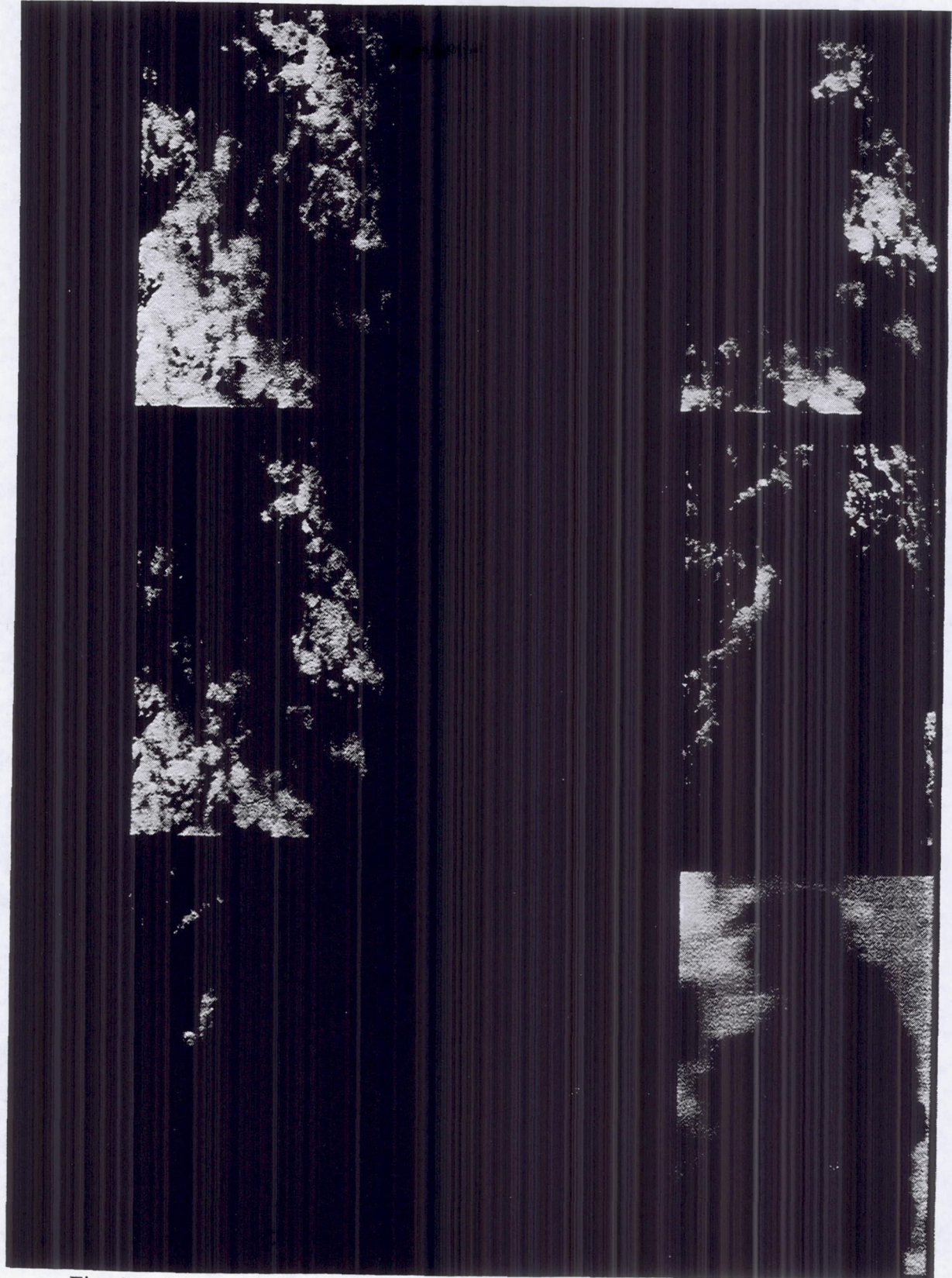


Fig. 2.3-4. A seven channel MCR image from a NASA ER-2 flight on 2 July 1986. Time progresses from top to bottom.

### 2.3.5 Cloud and Aerosol Lidar System (CALS)

The Cloud and Aerosol Lidar System (CALS) was flown onboard the NASA ER-2 during the period 17 June to 04 July 1986. The CALS instrument is a nadir viewing lidar system which can obtain the absolute height to cloud and land boundaries. The CALS can determine the structure within cloud tops and the amount of aerosol scattering. The CALS is co-located in a ER-2 superpod with the MCR and is aligned with the MCR nadir pixel.

Figure 2.3-5 is an example of the processed lidar data for 17 June 1986. The image shows the detection of thin cirrus at the tropopause and boundary layer altitude as indicated by the aerosol structure.

#### References

Spinhirne, J., 1987: (personal communication), NASA/Goddard Space Flight Center, Greenbelt, MD.

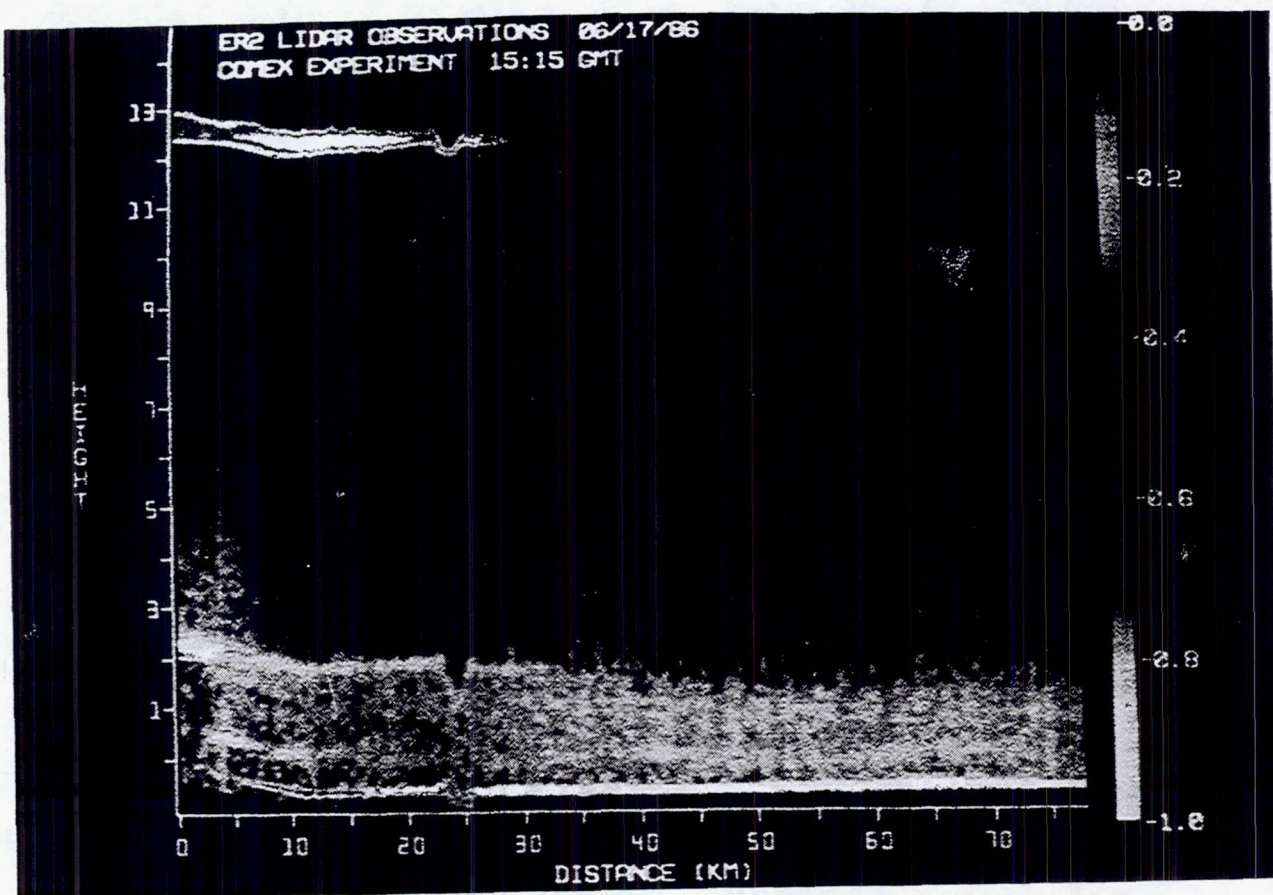


Fig. 2.3-5. CALS image for 17 June 1986. This image shows a thin cirrus layer at the tropopause (12 - 13 km) and the height of the boundary layer as indicated by the aerosol structure.

### **2.3.6 Lightning Research Package (LRP) and Lightning Instrument Package (LIP)**

Observations of the optical and electrical characteristics of cloud top lightning were obtained during SPACE using an integrated complement of sensors flown over active thunderstorms from the NASA high altitude U-2C aircraft. The Lightning Research Package (LRP) sensor complement included two optical pulse detectors, two spectrometers, three imaging sensors, a fast/slow electric field change meter, two electric field mills, and conductivity probes (see Table 2.3-3). Most of the data from these sensors were recorded on an instrumentation tape recorder. The Optical Array Sensor (OAS) and spectrometer data were also digitized on an event by event basis and recorded as a fast Pulse Code Modulation (PCM) bit stream. In addition, data from the electric field mills and conductivity probes were continuously multiplexed and recorded in a slow PCM format. Aircraft locations were obtained throughout the experiment from both an on-board Inertial Navigation System (INS) and a ground based tracking system. Therefore, aircraft lightning measurements can readily be correlated with other ground based and aircraft data sets.

Figure 2.3-6 is an example of the simultaneous optical pulse (Optical Pulse Sensor OPS and Wide Angle Detector WAD) and fast/slow electric field change (Fast Antenna FA and Slow Antenna SA) data for an intracloud discharge event. This observation was obtained on a July 14, 1986. Figure 2.3-7 shows on an expanded time scale the OPS and FA signals for two pulses in this same event.

A Charged Coupled Device (CCD) television camera was installed in the U-2C to collect real time television images of the cloud top structure and lightning discharges. This video data and IRIG-B time were recorded on a video cassette recorder. The camera had a 8 mm lens (FOV of 60°) and selectable interference filter (777.4 or 868.3 nm) for flight and looked through a window in the bottom hatch of the U-2C. The filter used on the television camera is identical to those on the OPD and OAS. The sensor on the television camera is a CCD silicon array (488 lines x 380 pixels). The frame integration time was 33 ms, the frame rate was 30 frames per second, and the synchronization was 2:1 standard interlace.

Two 70 mm Vinten cameras were installed to obtain high quality pictures of the thundercloud tops and associated lightning. Various filters were used to optimize photography based on the selected film for the particular flight period. Based upon the aircraft speed and the 9 s time interval, 92.8 percent overlap occurs on the photos which provides stereo imagery photography. However, for the COHMEX flight program the normal field of view of the cameras were obscured by the installation of two conductivity probes which were installed just prior to the flight program.

A small instrument package, the Lightning Instrument Package (LIP), was installed and flown in the nose section of the NASA ER-2 aircraft. Table 2.3-4 lists the sensors included in this package.

#### References

- Blakeslee, R., 1987: (personal communication), NASA/Marshall Space Flight Center, Huntsville, AL.
- Vaughan, O. H. Jr., 1984: *NASA Thunderstorm Overflight Program - Atmospheric Electricity Research: An overview Report on the Optical Lightning Detection Experiment for Spring and Summer 1983*, NASA Technical Memorandum 86468, November 1984.

Table 2.3-3 Lightning Research Package: NASA U-2C

<u>Sensor</u>	<u>Measurement</u>
Optical Pulse Sensor (OPS)	Optical pulse detection, flash/pulse statistics
Wide Angle Detector (WAD)	Optical pulse detection, flash/pulse statistics
Optical Array Sensor (OAS)	Low resolution image 50x50 photodiode array
CCD-TV	Video image
Vinten Camera	High Resolution photographic image
Broad Band Spectrometer	Lightning spectra (300 nm)
High Resolution Spectrometer	Lightning spectra (30 nm)
Electric Field Change Antenna	Fast/slow electric field changes
Electric Field Mill	Vertical component of electric field
Conductivity Probe	Electric field changes
	Air conductivity

Table 2.3-4 Lightning Instrument Package: NASA ER-2

<u>Sensor</u>	<u>Measurement</u>
Dual Optical Pulse Sensor (OPS)	Optical pulse detection at two different wavelengths, flash/pulse statistics
CCD-TV	Video image
Electric Field Change Antenna	Fast/slow electric field changes

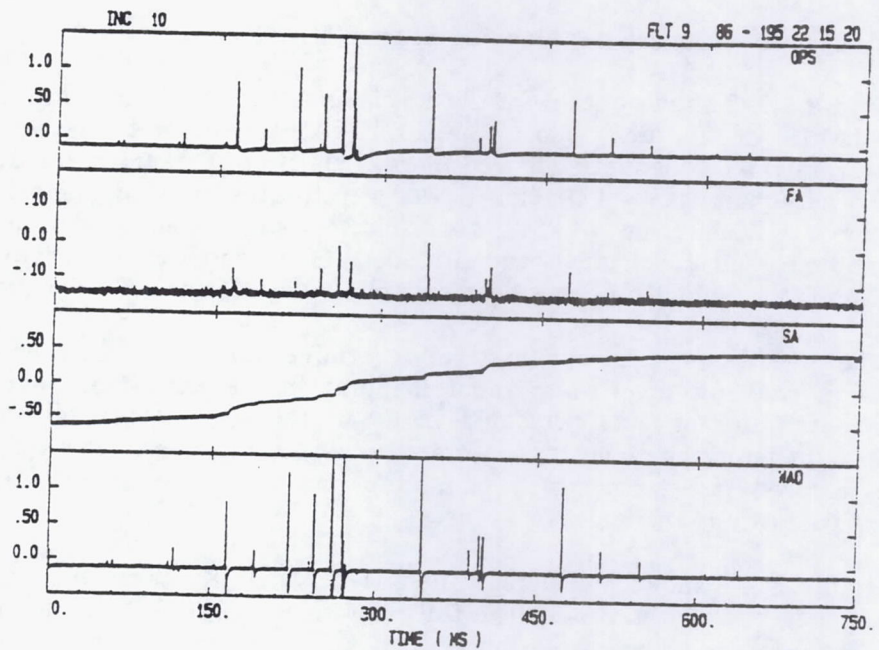


Fig. 2.3-6. Simultaneous optical pulse (OPS and WAD) and fast/slow antenna electric field change data for an intracloud discharge event on 14 July 1986 at 221520 GMT.

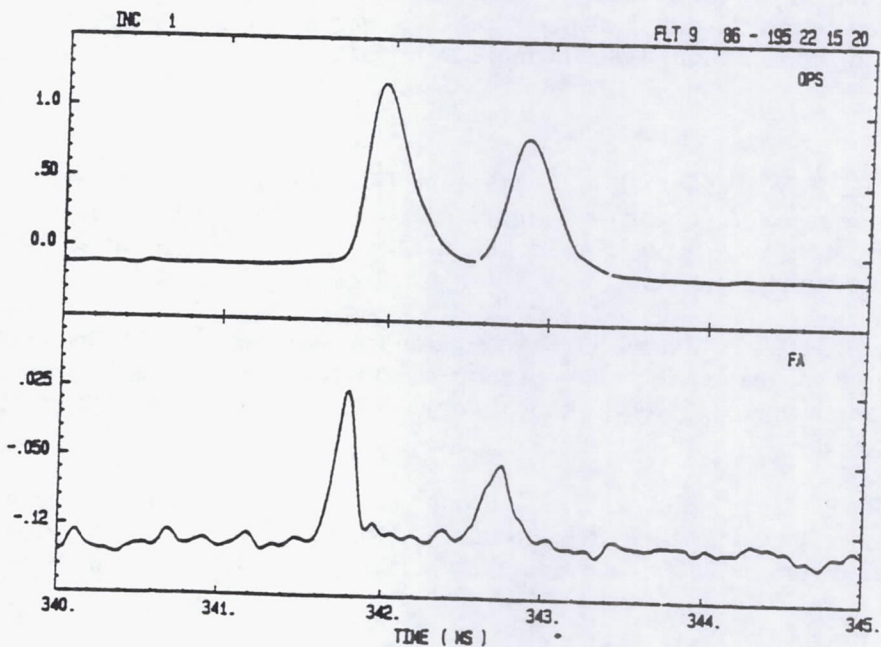


Fig. 2.3-7. Same as Fig. 2.3-6 but on an expanded time scale.

### 2.3.7 Multispectral Atmospheric Mapping Sensor (MAMS)

Figure 2.3-8 shows data from the 12 channels of the Multispectral Atmospheric Mapping Sensor (MAMS) on 26 June 1986. The displayed data presents reflected solar energy in the visible/near-infrared (channels 1-8) and thermal emission from the earth, atmosphere, and clouds in the infrared (channels 9 - 12). Half power wavelengths for each channel are given below each image strip. Data from MAMS are collected simultaneously through the same optical configuration for all 12 channels and provides 100 m nadir resolution over a swath width of 36km. Data from each channel has been subsampled by a factor of 8 for display purposes.

The MAMS is primarily used to determine surface thermal heat fluxes, land scene classification, and low-level water vapor mapping in the cloud-free environment. During the twenty-one minutes of data presented in the figure, a decaying thunderstorm was sampled. Reflected light from the cloud tops saturate the sensor in some of the visible channels, however valuable infrared measurements of cloud top thermal structure and surrounding atmospheric moisture variability is available.

Figure 2.3-9 shows higher resolution MAMS data for selected channels for the region in the rectangular box of Fig. 2.3-8. The full resolution data are subsampled by a factor of 2 in this display. This figure covers a portion of Huntsville, Alabama and the Tennessee River valley. Reflectivity differences between clouds, vegetation, and water can be observed in the visible channel. The water vapor channel measures energy emitted by mid-tropospheric water vapor and shows mesoscale variability throughout the scene. The driest mid-tropospheric air lies to the south (bottom) of the Tennessee River valley. The right hand side of the image presents channels 10 and 11 which both measure energy emitted from the earth's surface and clouds at 11 micrometers. Channel 10 was set such that it measured cold temperatures and 11 warm temperatures. Therefore a large combined dynamic temperature range can be achieved with sufficient sensitivity for qualitative work. In the cold channel varying cloud top temperatures can be observed while the warm channel indicates varying surface temperature (see Jedlovec et al., 1986a,b and Menzel et al., 1986 for more information).

### References

- Jedlovec, G. J., W. P. Menzel, R. J. Atkinson, G. S. Wilson, and J. Arvesen, 1986: *The Multispectral Atmospheric Mapping Sensor (MAMS): Instrument description, calibration, and data quality*. NASA Technical Memorandum 86565, Marshall Space Flight Center, Huntsville, AL, 37pp.
- Jedlovec, G. J., W. P. Menzel, G. S. Wilson, and R. Atkinson, 1986: Detection of mountain induced mesoscale wave structures with high resolution moisture imagery. *Second Conference on Satellite Meteorology / Remote Sensing and Applications*, AMS, Boston, 365-369.
- Menzel, W. P., G. J. Jedlovec, G. S. Wilson, 1986: Verification of small scale features in VAS imagery using high resolution MAMS imagery. *Second Conference on Satellite Meteorology / Remote Sensing and Applications*, AMS, Boston, 108-113.

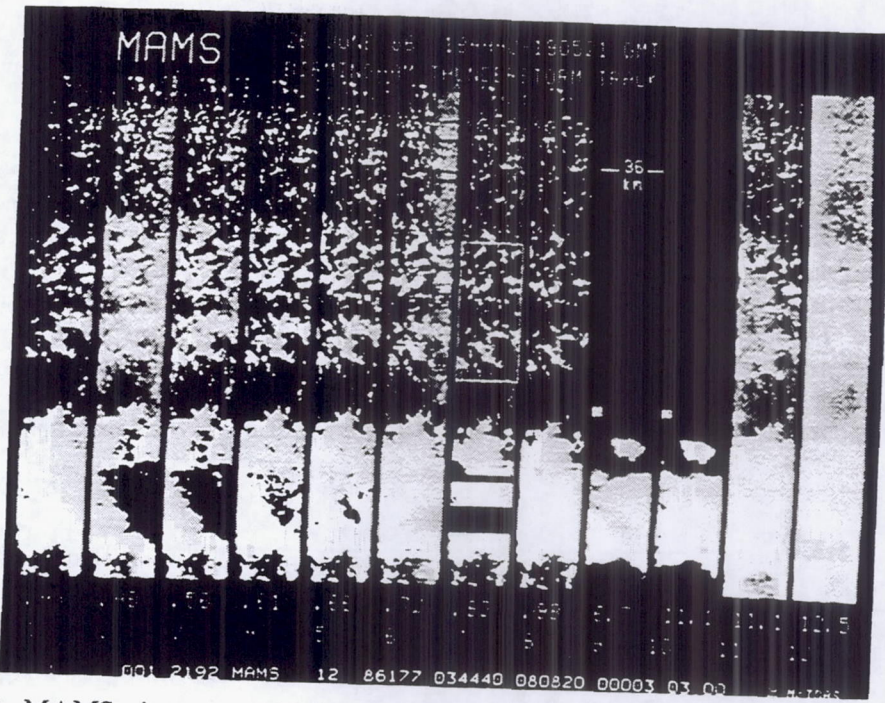


Fig. 2.3-8. MAMS image on 26 June 1986 over the SPACE region. Channels 1-8 presents reflected solar energy in the visible/near infrared wavelengths. Channels 9-12 presents thermal emission from the earth, atmosphere and clouds in the near infrared wavelengths.

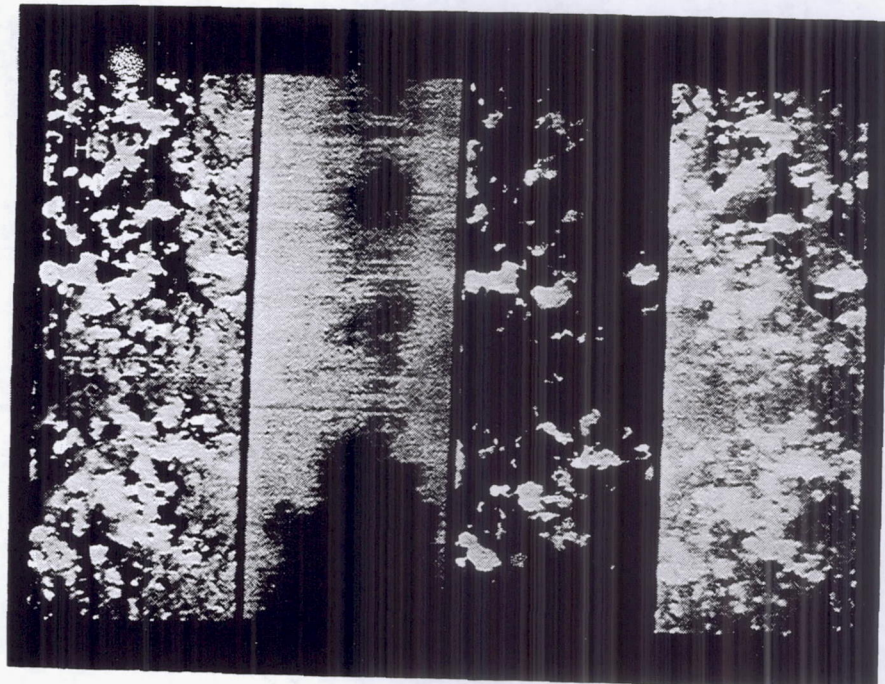


Fig. 2.3-9. Same as Fig. 2.3-8 except only channels 7, 9, 10, and 11 at a higher resolution.

### 2.3.8 High-resolution Interferometer Sounder (HIS)

Figure 2.3-10 presents data from the High-resolution Interferometer Sounder (HIS) for 15 June 1986 at 1910 GMT. The data have been processed to present a spectral distribution of emitted energy from the earth and atmosphere. Energy units have been converted to brightness temperatures for display. The HIS obtains radiance measurements in three bands; band 1 from 600 to  $1100\text{ cm}^{-1}$  (16.7 to 9.1 micrometers), band 2 from 1100 to  $1800\text{ cm}^{-1}$  (9.1 to 5.6 micrometers), and band 3 from 2000 to  $2600\text{ cm}^{-1}$  (5.6 to 3.7 micrometers). These high spectral resolution measurements are observed every six seconds and are used to infer surface and atmospheric temperature structure, and the distribution of various gaseous and cloud constituents.

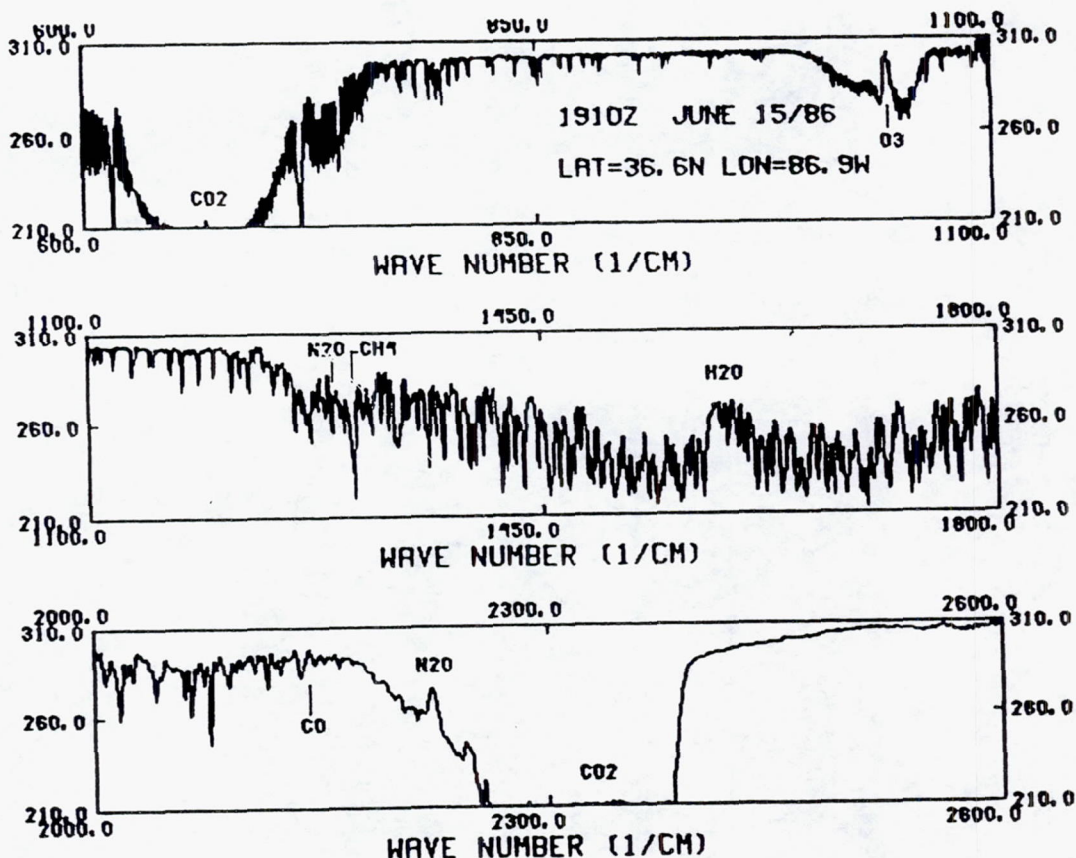


Fig. 2.3-10. HIS data for 15 June 1986 at 1910 GMT. (Top) Band 1: 600 to  $1100\text{ cm}^{-1}$ , (Middle) Band 2:  $1100$  to  $1800\text{ cm}^{-1}$ , (Bottom) Band 3:  $2000$  to  $2600\text{ cm}^{-1}$

### References

Smith, W. L., 1987: (personal communication), Cooperative Institute for Meteorological Studies, Space Science and Engineering Center, University of Wisconsin, Madison, WI.

## 2.4 AIRCRAFT

### 2.4.1 South Dakota School of Mines and Technology T-28

The South Dakota School of Mines and Technology (SDSM&T) T-28 aircraft flew 14 research flights in which it made 74 mid-level storm penetrations over the SPACE region. The T-28 flights were directed from the CP-2 radar station. Radar reflectivity structure, Doppler and differential reflectivity data were used to select the storms and storm penetration tracks. The aircraft was equipped with instruments which collected kinematic, hydrometeor, and electrical field measurements. A complete description of the basic instrumentation is described in Johnson and Smith (1980). A Particle Measuring Systems (PMS) 2D-P probe and two electric field mills were installed for the experiment.

The static pressure and temperature values are each measured by two separate instruments. A Rosemount 1301-A-4-B is the primary static pressure sensing instrument. It is backed up with a Ball EX-210-B pressure sensor. The temperature measurements are made with a Rosemount and a NCAR reverse-flow sensors. The NCAR reverse-flow sensor is the preferred instrument for in-cloud measurements. A low-level tower fly-by was made on 24 July 1986 at the Redstone Arsenal. Preliminary results suggest that the T-28 pressure and temperature probes were working satisfactorily. The pressure measurements differed <0.5 mb, while the temperature measurements were within 0.5°C.

The hydrometeor measurements by the T-28 fall into four particle size categories. The sensors are listed below:

1. Cloud droplets up to 30 micrometers in diameter with a J-W cloud liquid water concentration sensor and up to 45 micrometers with the PMS Forward Scattering Spectrometer Probe (FSSP).
2. Intermediate size particles from 30 to greater than 1000 micrometers with a PMS 2D-P optical array spectrometer.
3. Raindrops, graupel, and snowflakes from 1 mm to 5 mm with a continuous hydrometeor sampler.
4. Hailstones from 4 mm to 5 cm with a hail spectrometer.

Figure 2.4-1 shows the values of cloud liquid water concentration and hailstone concentration along with strong updraft and turbulence during a cloud penetration on 14 July 1986. The coincidence of these local maxima are indicative of particle growth during the penetration.

The electric field measurements were made on seven SPACE flights from 9 - 24 July 1986. The two electric field mills were mounted in a vertically opposed orientation, with one on the canopy and the other on the lower bay door. Electric field strengths up to  $-100 \text{ KV m}^{-1}$  were measured on four of the flights.

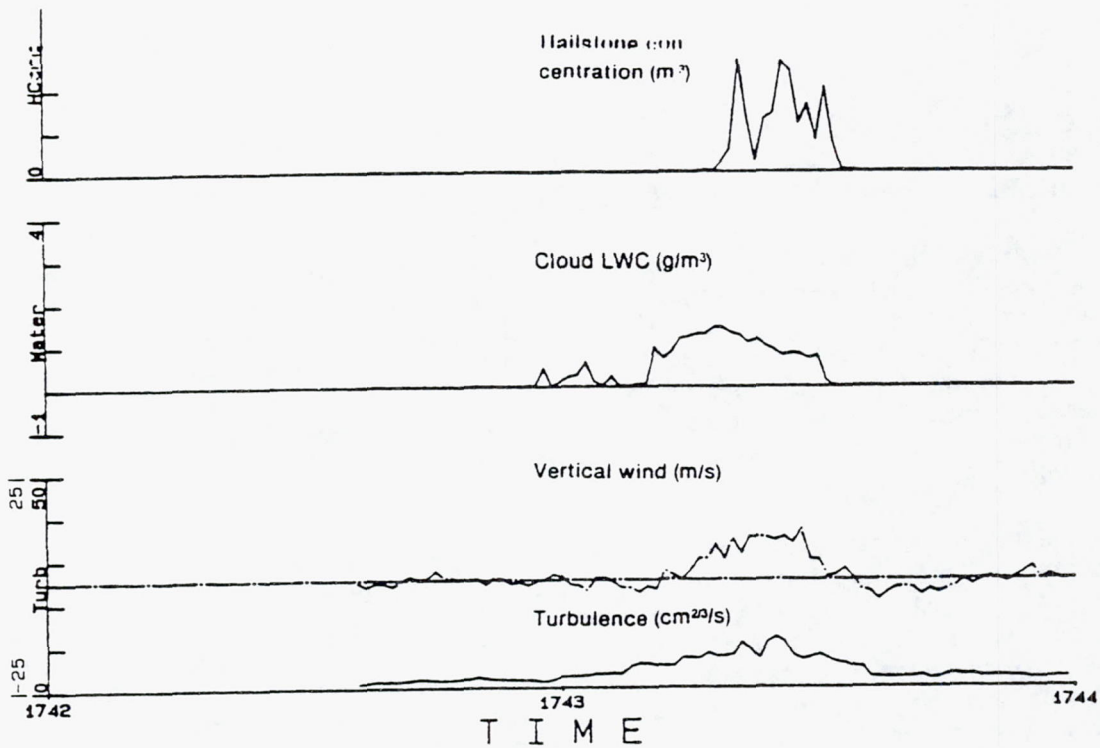


Fig. 2.4-1. Time plot of selected data from the sixth T-28 penetration on 14 July 1986. Hailstone concentrations are from the hail spectrometer and cloud Liquid Water Concentrations (LWC) from the FSSP. The time scale can be converted to an approximate distance scale using the nominal T-28 flight speed of  $0.1 \text{ km s}^{-1}$ .

#### References

- Johnson, G. N., and P. L. Smith, Jr., 1980: Meteorological instrumentation system on the T-28 thunderstorm research aircraft. *Bull. Amer. Meteor. Soc.*, 61, 972-979.
- Musil, D. J. and P. L. Smith, Jr., 1986: *T-28 Data Acquisition During COHMEC 1986*, Institute of Atmospheric Sciences, South Dakota School of Mines and Technology, Report SDSMT/IAS/R-86/08.

### 2.4.2 University of North Dakota Cessna Citation

The University of North Dakota (UND) Cessna Citation carried PMS probes (FSSP, 2D-C, 1D-P) for measuring cloud and precipitation size spectra. An Inertial Navigation System/Gust Probe system was employed for wind and turbulence measurements. A Johnson-Williams hot-wire cloud liquid water sensor, an NCAR type reverse flow temperature sensor, a dewpoint hygrometer (cooled-mirror design), pressure transducers for measuring static and pitot pressures were also used during the flights. Side looking 16 mm time lapse cameras recorded the events during flight maneuvers. All measurements were digitally recorded by the Citation data system and displayed in real time aboard the aircraft. Data processing followed relatively standard procedures for the basic meteorological parameters and data from the PMS probes. Figure 2.4-2 is a representation of the PMS 2D-P hydrometeor particle data for a flight on 3 June 1986.

#### References

Poellot, Michael 1987: (personal communication), University of North Dakota, Grand Forks, ND.

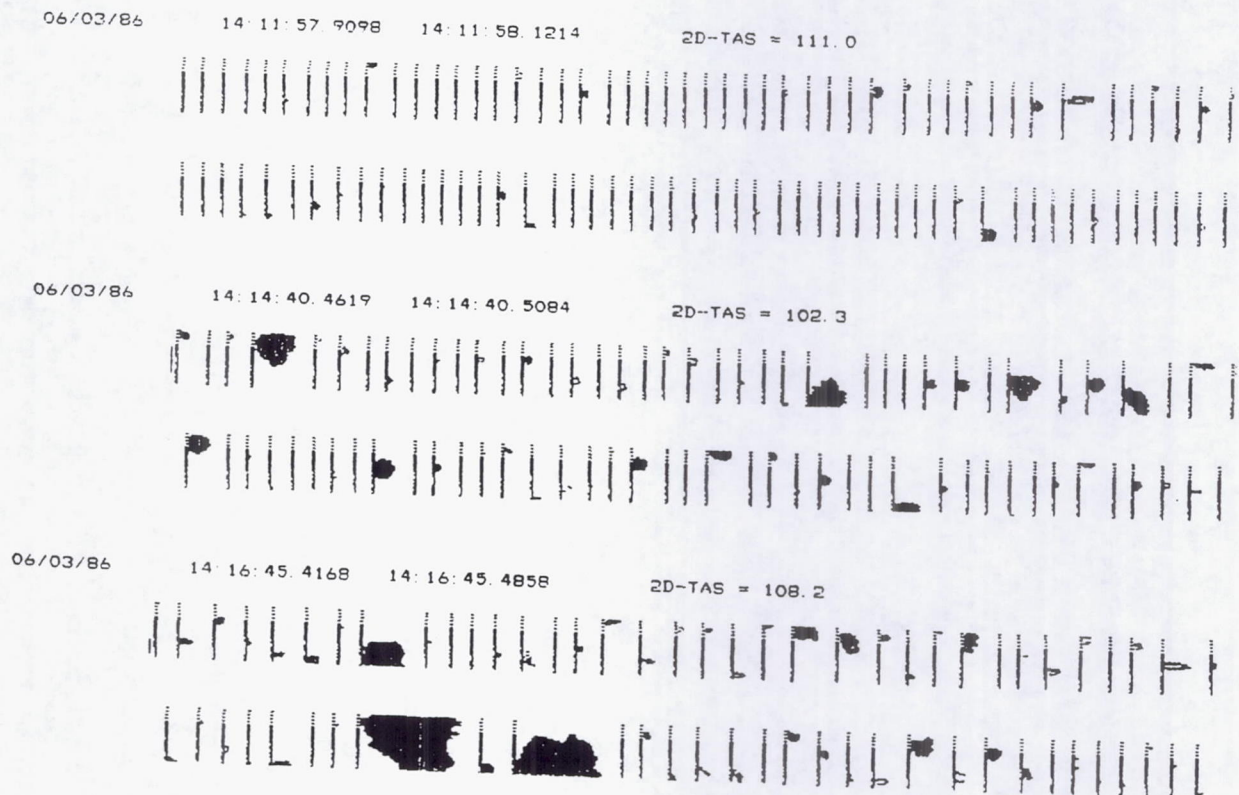


Fig. 2.4-2. PMS 2D-P hydrometeor particle data for a flight on 3 June 1986.

### **2.4.3 National Oceanic and Atmospheric Administration P-3**

The National Oceanic and Atmospheric Administration (NOAA) P-3 aircraft carried a full complement of meteorological, cloud physics, radar and photographic instruments during the COHMEC experiment. Meteorological state variables measured include free air temperature, dewpoint temperature, static and dynamic pressure, and horizontal and vertical wind components. Surface radiation was recorded with a Office of Aircraft Operations (OAO) modified PRT-5 sensor. The cloud physics package records cloud droplet and hydrometeor spectra, liquid water content, and icing rate.

The P-3 is outfitted with a C-band PPI lower fuselage, 360° scan (horizontal) fan beam radar, and a Doppler X-band RHI tail, 360° scan (vertical) radar. Cloud structure is recorded with a 70 mm Hasselblad camera mounted in the belly of the fuselage and 16 mm time lapse cameras mounted on the nose and sides of the fuselage.

Figure 2.4-3 is a plot of an aircraft flight track with accompanying measured wind velocities. Figure 2.4-4 is a temperature and dewpoint time series graph during the same flight. These plots were produced on board the aircraft in real time.

#### References

*NOAA/OAO MIST Operations Plan*, 1986: NOAA Office of Aircraft Operations, Miami, FL

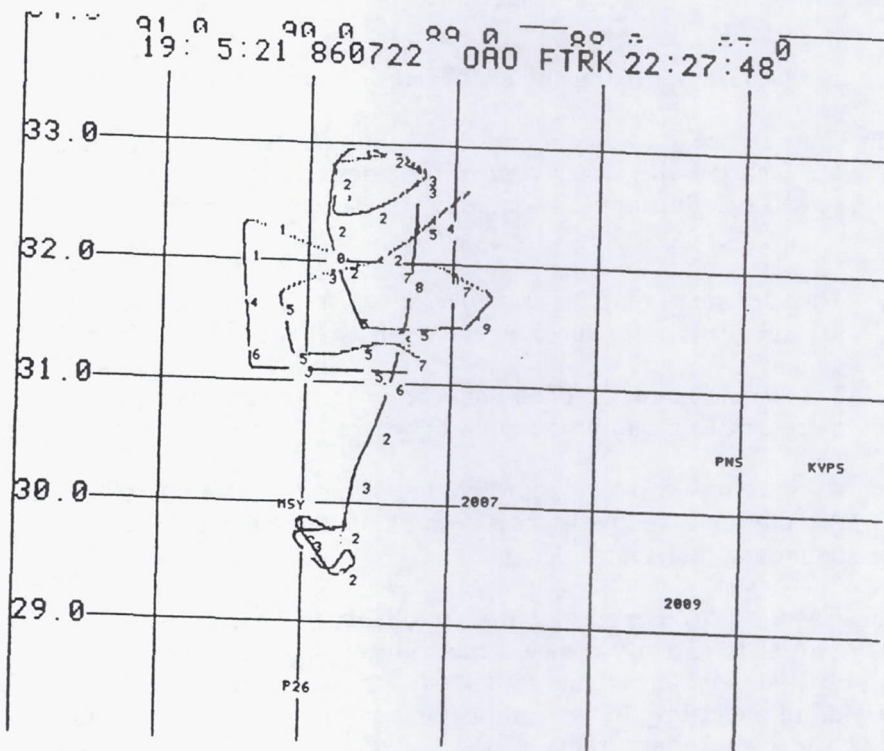


Fig. 2.4-3. Flight track of the P-3 on 22 July 1986 over southern Mississippi and Alabama, and the Gulf of Mexico. Numbers along the flight track are wind velocities ( $\text{m s}^{-1}$ ).

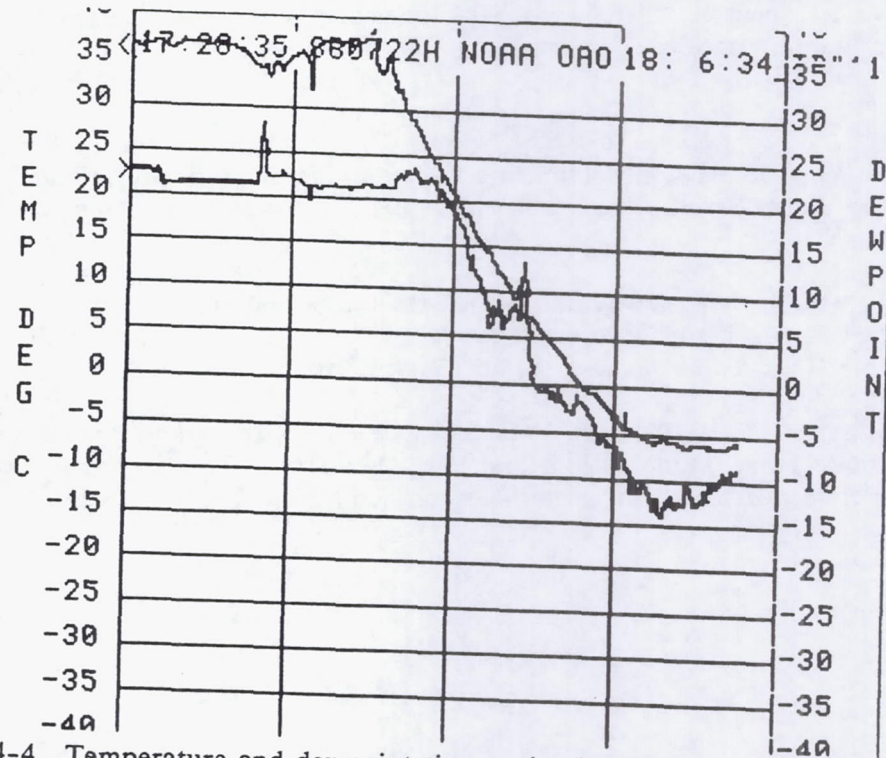


Fig. 2.4-4. Temperature and dewpoint time series for the same flight on as in Fig. 2-4-3.

#### 2.4.4 National Oceanic and Atmospheric Administration Cessna T207

The importance of the merger and intersection of thunderstorm produced outflow boundaries (arc clouds) with other convective lines and boundaries in triggering deep convection has been discussed by Purdom (1979a, 1979b). He concluded that:

1. Thunderstorm outflow boundaries can maintain their identity as arc clouds for several hours after the convective array that produced them has dissipated.
2. The development of deep convection is favored in regions where the arc cloud merges with a cumulus region or where it intersects another boundary.
3. As the convective regime evolves through the course of the day, and much of the cumulus field dissipates, most of the new thunderstorms develop at the boundary intersection points.

The Cessna T207 penetrated the arc clouds in clear air and below the cumulus congestus cloud base in order to directly measure the convective scale interactions. The NOAA Cessna T207 has been outfitted with instrumentation for the direct measurement of the three-dimensional velocity field, temperature, dewpoint, pressure, atmospheric gases and particulates. The gust velocity ( $u'$ ,  $v'$ ,  $w'$ ,  $w$ ) measurement system has been designed to be independent of the aircraft sensitivity to atmospheric motions and/or pilot induced motions. An on-board doppler wind system provides accurate measurements of ground speed and aircraft drift angle. Combining these data with the aircraft heading and true airspeed, provide mean (averaged every 5 sec) horizontal wind components ( $u$ ,  $v$ ). The dewpoint and total temperature are continuously recorded at a sampling rate of 0.04 sec.

#### References

- Purdom, J. F. W., 1979a: The developments and evolution of deep convection. *Preprints 11th Conference on Severe Local Storms*, Kansas City, MO, Amer. Meteor. Soc., Boston, MA 143-150.
- Purdom, J. F. W., 1979b: A new role for high resolution satellite imagery in convective cloud weather modification projects. *Preprints 7th Conference on Inadvertent and Planned Weather Modification*, Amer. Meteor. Soc., Boston, MA, 100.
- Sinclair, P. C., and J. F. W. Purdom, 1983: Shuttle recovery requirements and the development of arc lines from thunderstorm outflows. *Preprints 9th Conference on Aerospace and Aeronautical Meteorology*, Amer. Meteor. Soc., Boston, MA 287-292.

## 2.5 SATELLITE SYSTEMS

There was one geostationary (GOES Central) and four polar orbiting (DMSP-F6, DMSP-F7, NOAA-9, Nimbus-7) satellites which collected data over the SPACE region.

### 2.5.1 GOES Central

The Geostationary Operational Environmental Satellite (GOES) Central satellite provided visible and infrared imagery on the hour and half past the hour. However, at 0530, 1130, 1730, and 2330 GMT the infrared images were replaced with a 6.7 micrometer water vapor image. On some days the GOES satellite was placed in the Rapid Interval Scan Operations Plan (RISOP) mode. While in RISOP, visible and infrared images of the continental United States were taken, in five minute intervals, between 14 and 29 and between 44 and 59 minutes past the hour.

In addition to the visible and infrared images, VISSR Atmospheric Sounder (VAS) images were collected on many days throughout the experiment. VAS images occur at 15 and 45 minutes past the hour. Three VAS wavelengths, the 6.7 micrometer mid-level water vapor (channel 10), the 11.2 micrometer atmospheric window (channel 8) and 12.7 micrometer low-level water vapor (channel 7) images were archived at MSFC. The precipitable water and lifted index VAS products derived from the VAS soundings are stored at the University of Wisconsin-Madison (UW-M) Space Science and Engineering Center (SSEC).

The 2 km resolution GOES visible and infrared images (center point 35° N and 87° W) were archived at MSFC. Some of the 1 km visible images, and 4 km visible and infrared images were archived at MSFC, but a complete set of imagery at these resolutions must be obtained from the University of Wisconsin-Madison SSEC. Please note: The GOES satellite bar graphs on the daily data inventory sheets (section 3.2) only indicate the visible, infrared, RISOP and VAS images presently archived at MSFC. Additional images will be added to the archive at a later date.

Video tape (VHS) movies comprised of visible and infrared images were generated for the daily COHMEX weather briefings. These movies contain loops of the visible and infrared images at various loop speeds. The tapes are stored at MSFC and are available for distribution.

### 2.5.2 Defense Meteorological Satellite Program (DMSP)

The data from the Defense Meteorological Satellite Program (DMSP) polar orbiting satellites (F6 and F7) were not stored on magnetic media. The DMSP images are stored in photographic form at the National Snow & Ice Center at the University of Colorado.

Tables 2.5-1 and 2.5-2 list the revolution numbers and times of all satellite orbits, F6 and F7 respectively, which view the SPACE region.

Table 2.5-1 Revolution numbers and times for DMSP F6

VEHID F6

REV	DATE	Z TIME									
177030	5-19-86	5/48	177108	5-19-86	17/13	177170	5-20-86	5/27	177180	5-20-86	7/ 8
177248	5-20-86	16/51	177258	5-20-86	18/33	177320	5-21-86	6/47	177398	5-21-86	18/11
177468	5-22-86	6/26	177538	5-22-86	17/50	177600	5-23-86	6/ 4	177678	5-23-86	17/28
177740	5-24-86	5/43	177750	5-24-86	7/24	177818	5-24-86	17/ 7	177890	5-25-86	7/ 3
177958	5-25-86	16/46	177968	5-25-86	18/27	178030	5-26-86	6/41	178108	5-26-86	18/ 6
178170	5-27-86	6/20	178248	5-27-86	17/44	178310	5-28-86	5/59	178388	5-28-86	17/23
178450	5-29-86	5/37	178460	5-29-86	7/19	178528	5-29-86	17/ 2	178538	5-29-86	18/43
178600	5-30-86	6/57	178668	5-30-86	16/40	178678	5-30-86	18/21	178740	5-31-86	6/36
178818	5-31-86	18/ 0	178880	6- 1-86	6/15	178958	6- 1-86	17/39	179020	6- 2-86	5/53
179098	6- 2-86	17/17	179160	6- 3-86	5/32	179170	6- 3-86	7/13	179238	6- 3-86	16/56
179248	6- 3-86	18/37	179310	6- 4-86	6/52	179388	6- 4-86	18/16	179450	6- 5-86	6/30
179528	6- 5-86	17/55	179590	6- 6-86	6/ 9	179668	6- 6-86	17/33	179730	6- 7-86	5/48
179740	6- 7-86	7/29	179808	6- 7-86	17/12	179870	6- 8-86	5/26	179880	6- 8-86	7/ 8
179948	6- 8-86	16/50	179958	6- 8-86	18/32	180020	6- 9-86	6/45	180098	6- 9-86	18/19
180160	6-10-86	6/25	180238	6-10-86	17/49	180300	6-11-86	6/ 3	180378	6-11-86	17/28
180440	6-12-86	5/42	180450	6-12-86	7/23	180518	6-12-86	17/ 6	180528	6-12-86	18/48
180598	6-13-86	7/ 2	180658	6-13-86	16/45	180668	6-13-86	18/26	180738	6-14-86	6/41
180808	6-14-86	18/ 5	180870	6-15-86	6/19	180948	6-15-86	17/44	181010	6-16-86	5/58
181088	6-16-86	17/22	181150	6-17-86	5/37	181160	6-17-86	7/18	181228	6-17-86	17/ 1
181238	6-17-86	18/42	181300	6-18-86	6/57	181368	6-18-86	16/39	181378	6-18-86	18/21
181440	6-19-86	6/35	181518	6-19-86	17/59	181580	6-20-86	6/14	181658	6-20-86	17/38
181720	6-21-86	5/52	181730	6-21-86	7/34	181798	6-21-86	17/17	181860	6-22-86	5/31
181870	6-22-86	7/12	181938	6-22-86	16/55	181948	6-22-86	18/37	182010	6-23-86	6/51
182088	6-23-86	18/15	182150	6-24-86	6/30	182228	6-24-86	17/54	182298	6-25-86	6/ 8
182368	6-25-86	17/32	182430	6-26-86	5/47	182440	6-26-86	7/28	182508	6-26-86	17/11
182580	6-27-86	7/ 7	182648	6-27-86	16/50	182658	6-27-86	18/31	182720	6-28-86	6/45
182798	6-28-86	18/10	182860	6-29-86	6/24	182938	6-29-86	17/48	183000	6-30-86	6/ 3
183078	6-30-86	17/27	183140	7- 1-86	5/41	183150	7- 1-86	7/23	183218	7- 1-86	17/ 6
183228	7- 1-86	18/47	183290	7- 2-86	7/ 1	183358	7- 2-86	16/44	183368	7- 2-86	18/25
183430	7- 3-86	6/40	183508	7- 3-86	18/ 4	183570	7- 4-86	6/19	183648	7- 4-86	17/43
183710	7- 5-86	5/57	183788	7- 5-86	17/21	183850	7- 6-86	5/36	183860	7- 6-86	7/17
183928	7- 6-86	17/ 0	183938	7- 6-86	18/41	184000	7- 7-86	6/56	184078	7- 7-86	18/20
184140	7- 8-86	6/34	184218	7- 8-86	17/59	184280	7- 9-86	6/13	184358	7- 9-86	17/37
184420	7-10-86	5/52	184430	7-10-86	7/33	184498	7-10-86	17/16	184560	7-11-86	5/30
184570	7-11-86	7/12	184638	7-11-86	16/54	184648	7-11-86	18/36	184710	7-12-86	6/50
184788	7-12-86	18/14	184850	7-13-86	6/29	184928	7-13-86	17/53	184990	7-14-86	6/ 7
185068	7-14-86	17/32	185130	7-15-86	5/46	185140	7-15-86	7/27	185208	7-15-86	17/10
185218	7-15-86	18/52	185280	7-16-86	7/ 6	185348	7-16-86	16/49	185358	7-16-86	18/30
185420	7-17-86	6/45	185498	7-17-86	18/ 9	185560	7-18-86	6/23	185638	7-18-86	17/48
185700	7-19-86	6/ 2	185778	7-19-86	17/26	185840	7-20-86	5/41	185850	7-20-86	7/22
185918	7-20-86	17/ 5	185928	7-20-86	18/46	185990	7-21-86	7/ 1	186058	7-21-86	16/43
186068	7-21-86	18/25	186130	7-22-86	6/39	186208	7-22-86	18/ 3	186270	7-23-86	6/18
186348	7-23-86	17/42	186410	7-24-86	5/56	186420	7-24-86	7/38	186498	7-24-86	17/21
186550	7-25-86	5/35	186560	7-25-86	7/16	186628	7-25-86	16/59	186638	7-25-86	18/41
186700	7-26-86	6/55	186778	7-26-86	18/19	186848	7-27-86	6/34	186918	7-27-86	17/58
186980	7-28-86	6/12	187058	7-28-86	17/36	187120	7-29-86	5/51	187130	7-29-86	7/32
187198	7-29-86	17/15	187270	7-30-86	7/11	187338	7-30-86	16/54	187348	7-30-86	18/35
187410	7-31-86	6/49	187488	7-31-86	18/14						

Table 2.5-2 Revolution numbers and times for DMSP F7

VEHID F7															
REV	DATE	Z TIME	REV	DATE	Z TIME	REV	DATE	Z TIME	REV	DATE	Z TIME	REV	DATE	Z TIME	REV
129050	5-14-86	9/ 7	129060	5-14-86	10/48	129120	5-14-86	20/31	129130	5-14-86	22/13				
129200	5-15-86	10/28	129260	5-15-86	20/11	129270	5-15-86	21/52	129340	5-16-86	10/ 7				
129410	5-16-86	21/32	129480	5-17-86	9/47	129550	5-17-86	21/11	129620	5-18-86	9/26				
129630	5-18-86	11/ 8	129690	5-18-86	20/51	129760	5-19-86	9/ 6	129770	5-19-86	10/47				
129830	5-19-86	20/31	129840	5-19-86	22/12	129910	5-20-86	10/27	129980	5-20-86	21/51				
130050	5-21-86	10/ 6	130120	5-21-86	21/31	130190	5-22-86	9/46	130260	5-22-86	21/11				
130330	5-23-86	9/26	130340	5-23-86	11/ 7	130400	5-23-86	20/50	130470	5-24-86	9/ 5				
130480	5-24-86	10/47	130540	5-24-86	20/30	130550	5-24-86	22/11	130620	5-25-86	10/26				
130690	5-25-86	21/51	130750	5-26-86	10/ 6	130830	5-26-86	21/30	130900	5-27-86	9/45				
130970	5-27-86	21/10	131040	5-28-86	9/25	131050	5-28-86	11/ 6	131110	5-28-86	20/49				
131180	5-29-86	9/ 4	131190	5-29-86	10/46	131250	5-29-86	20/29	131260	5-29-86	22/10				
131330	5-30-86	10/25	131400	5-30-86	21/50	131470	5-31-86	10/ 5	131540	5-31-86	21/30				
131610	6- 1-86	9/45	131680	6- 1-86	21/ 9	131750	6- 2-86	9/24	131760	6- 2-86	11/ 5				
131820	6- 2-86	20/49	131890	6- 3-86	9/ 4	131900	6- 3-86	10/45	131960	6- 3-86	20/28				
131970	6- 3-86	22/10	132040	6- 4-86	10/25	132110	6- 4-86	21/49	132180	6- 5-86	10/ 4				
132250	6- 5-86	21/29	132320	6- 6-86	9/44	132390	6- 6-86	21/ 8	132460	6- 7-86	9/23				
132470	6- 7-86	11/ 5	132530	6- 7-86	20/48	132600	6- 8-86	9/ 3	132610	6- 8-86	10/44				
132670	6- 8-86	20/28	132680	6- 8-86	22/ 9	132750	6- 9-86	10/24	132820	6- 9-86	21/49				
132890	6-10-86	10/ 3	132950	6-10-86	21/28	133030	6-11-86	9/43	133100	6-11-86	21/ 8				
133170	6-12-86	9/23	133180	6-12-86	11/ 4	133240	6-12-86	20/47	133310	6-13-86	9/ 2				
133320	6-13-86	10/44	133380	6-13-86	20/27	133390	6-13-86	22/ 8	133460	6-14-86	10/23				
133530	6-14-86	21/48	133600	6-15-86	10/ 3	133670	6-15-86	21/27	133740	6-16-86	9/42				
133810	6-16-86	21/ 7	133880	6-17-86	9/22	133890	6-17-86	11/ 3	133950	6-17-86	20/47				
134020	6-18-86	9/ 1	134030	6-18-86	10/43	134090	6-18-86	20/26	134100	6-18-86	22/ 8				
134170	6-19-86	10/22	134240	6-19-86	21/47	134310	6-20-86	10/ 2	134380	6-20-86	21/27				
134450	6-21-86	9/42	134520	6-21-86	21/ 6	134590	6-22-86	9/21	134600	6-22-86	11/ 3				
134660	6-22-86	20/46	134730	6-23-86	9/ 1	134740	6-23-86	10/42	134800	6-23-86	20/25				
134810	6-23-86	22/ ?	134880	6-24-86	10/22	134950	6-24-86	21/46	135020	6-25-86	10/ 1				
135090	6-25-86	21/26	135160	6-26-86	9/41	135230	6-26-86	21/ 6	135300	6-27-86	9/20				
135310	6-27-86	11/ 2	135370	6-27-86	20/45	135440	6-28-86	9/ 0	135450	6-28-86	10/41				
135510	6-28-86	20/25	135520	6-28-86	22/ 6	135590	6-29-86	10/21	135660	6-29-86	21/46				
135730	6-30-86	10/ 1	135800	6-30-86	21/25	135870	7- 1-86	9/40	135940	7- 1-86	21/ 5				
136010	7- 2-86	9/20	136020	7- 2-86	11/ 1	136080	7- 2-86	20/44	136150	7- 3-86	8/59				
136160	7- 3-86	10/41	136220	7- 3-86	20/24	136230	7- 3-86	22/ 5	136300	7- 4-86	10/20				
136370	7- 4-86	21/45	136440	7- 5-86	10/ 0	136510	7- 5-86	21/24	136580	7- 6-86	9/39				
136650	7- 6-86	21/ 4	136720	7- 7-86	9/19	136730	7- 7-86	11/ 0	136790	7- 7-86	20/44				
136860	7- 8-86	8/59	136870	7- 8-86	10/40	136930	7- 8-86	20/23	136940	7- 8-86	22/ 5				
137010	7- 9-86	10/20	137080	7- 9-86	21/44	137150	7-10-86	9/59	137220	7-10-86	21/24				
137290	7-11-86	9/39	137360	7-11-86	21/ 3	137430	7-12-86	9/18	137440	7-12-86	11/ 0				
137500	7-12-86	20/43	137580	7-13-86	10/39	137640	7-13-86	20/22	137650	7-13-86	22/ 4				
137720	7-14-86	10/19	137790	7-14-86	21/13	137860	7-15-86	9/58	137930	7-15-86	21/23				
138000	7-16-86	9/38	138070	7-16-86	21/ 3	138140	7-17-86	9/18	138150	7-17-86	10/59				
138210	7-17-86	20/42	138290	7-18-86	10/38	138350	7-18-86	20/22	138360	7-18-86	22/ 3				
138430	7-19-86	10/18	138500	7-19-86	21/43	138570	7-20-86	9/58	138640	7-20-86	21/22				
138710	7-21-86	9/37	138780	7-21-86	21/ 2	138850	7-22-86	9/17	138860	7-22-86	10/58				
138920	7-22-86	20/41	139000	7-23-86	10/38	139060	7-23-86	20/21	139070	7-23-86	22/ 2				
139140	7-24-86	10/17	139210	7-24-86	21/12	139280	7-25-86	9/57	139350	7-25-86	21/22				
139420	7-26-86	9/36	139490	7-26-86	21/ 1	139560	7-27-86	9/16	139570	7-27-86	10/57				
139630	7-27-86	20/41	139710	7-28-86	10/37	139770	7-28-86	20/20	139780	7-28-86	22/ 2				
139850	7-29-86	10/17	139920	7-29-86	21/11	139990	7-30-86	9/56	140060	7-30-86	21/21				
140130	7-31-86	9/36	140200	7-31-86	21/ 0										

### 2.5.3 Nimbus 7

The Nimbus 7 satellite has a 955 km sun-synchronous polar orbit with an equator crossing at noon (ascending) and midnight (descending) local time. The satellite carries a variety of instruments many of which are no longer operational. Two instruments which functioned during SPACE and have applicability to the SPACE experiment are the Solar Backscatter UltraViolet/Total Ozone Mapping Spectrometer (SBUV/TOMS) and the Scanning Multichannel Microwave Radiometer (SMMR). The SBUV/TOMS operated full time daily, while the SMMR was turned on every other day. The times listed in the daily data inventory sheets indicate the orbital times when the satellite passed closest to the SPACE region.

#### References

Chen, H. S., 1985: *Space Remote Sensing Systems An Introduction*, Academic Press, 257pp.

### 2.5.4 NOAA-9

The NOAA-9 satellite operates in a near-polar circular sun-synchronous orbit with a nominal altitude of about 870 km and an inclination angle near 98°. The satellite crosses the equator at 3:00 p.m. local time in the ascending orbit. The primary sensor on the NOAA-9 is the Advanced Very High Resolution Radiometer (AVHRR). The AVHRR is a cross-track scanning system with five spectral channels in the visible, near-infrared, and infrared spectra. The spectral band widths are listed in Table 2.5-3. The instantaneous field of view (IFOV) of each sensor is approximately 1.4 milliradians thereby producing a resolution of 1.1 km at nominal altitude.

Table 2.5-3 AVHRR Spectral Band Widths

<u>Channel #</u>	<u>Band Width (micrometers)</u>
1	0.58 - 0.68
2	0.72 - 1.10
3	3.55 - 3.93
4	10.30 - 11.30
5	11.50 - 12.50

The TIROS Operational Vertical Sounder (TOVS) is also carried aboard the NOAA-9 satellite. The TOVS units consists of four sensors: the High Resolution Infrared Radiation Sounder/2 (HIRS/2), the Microwave Sounding Unit (MSU), the Stratospheric Sounding Unit (SSU), and the Solar Backscatter UltraViolet Radiometer/2 (SBUV/2).

The HIRS/2 measures the incident radiation in the infrared region of the spectrum including both the longwave (15 micrometers) and shortwave (4.3 micrometers). The MSU is a passive scanning microwave spectrometer. The MSU has four channels in the 5.5 micrometer oxygen region. The four channels are centered on 50.3, 53.74, 54.96 and 57.95 GHz respectively, with a 200 MHz bandwidth. The SSU is a step-scanned far-infrared spectrometer in the 15 micrometer carbon dioxide absorption band region. The instrument measures radiation emitted from carbon dioxide at the top of the Earth's atmosphere. Finally the SBUV/2 determines the total ozone and its vertical concentration distribution above the ozone maximum by measuring the scattered solar radiance. The SBUV/2 uses 12 narrow wavelength bands in the 250 to 340 nm range.

References

- Chen, H. S., 1985: *Space Remote Sensing Systems An Introduction*, Academic Press, 257pp.
- Kidwell, K. B., 1986: *NOAA Polar Orbiter Data Users Guide*, NOAA/NESDIS/NCDC Satellite Data Services Division, Washington, D.C.

**Page intentionally left blank**

## 2.6 SURFACE SYSTEMS

Surface networks utilized for the field program included various automated mesonet systems, the western TVA raingage network, the NASA Lightning Location and Protection (LLP) lightning detection network, the National Severe Storm Laboratory (NSSL) mobile laboratory, and various private and agency cooperative meteorological observer networks. These measurements consisted of both existing and special deployed stations. A unique aspect of COHMEC provided the highest density of automated mesonet stations assembled for a field program.

### 2.6.1 Automated Mesonet Systems

The automated surface observation systems (89 stations) were operational on a 24-h a day basis. They included the NCAR second generation Portable Automated Mesonet (PAM II) network (Pike et al., 1983), the FAA Automated Mesonet System (FAMS) (Wolfson, M.M., 1987), and the NASA Mesonet System (NAMS). Figure 2.6-1 shows the distributions of these stations in relation to the radars. The PAM II and FAMS networks provided 1-min average data of wind velocity, temperature, dewpoint, pressure, and precipitation (nine PAM II stations also recorded direct solar insolation). The NAMS network provided 5-h averages of wind velocity, peak wind gust, temperature, dewpoint, precipitation, and direct, diffuse, and reflected solar insolation. All data are archived in Common Mesonet Format (CMF) developed by NCAR (NCAR 1985) for uniformity of mesonet data. Details of data format and file structure are available from NCAR.

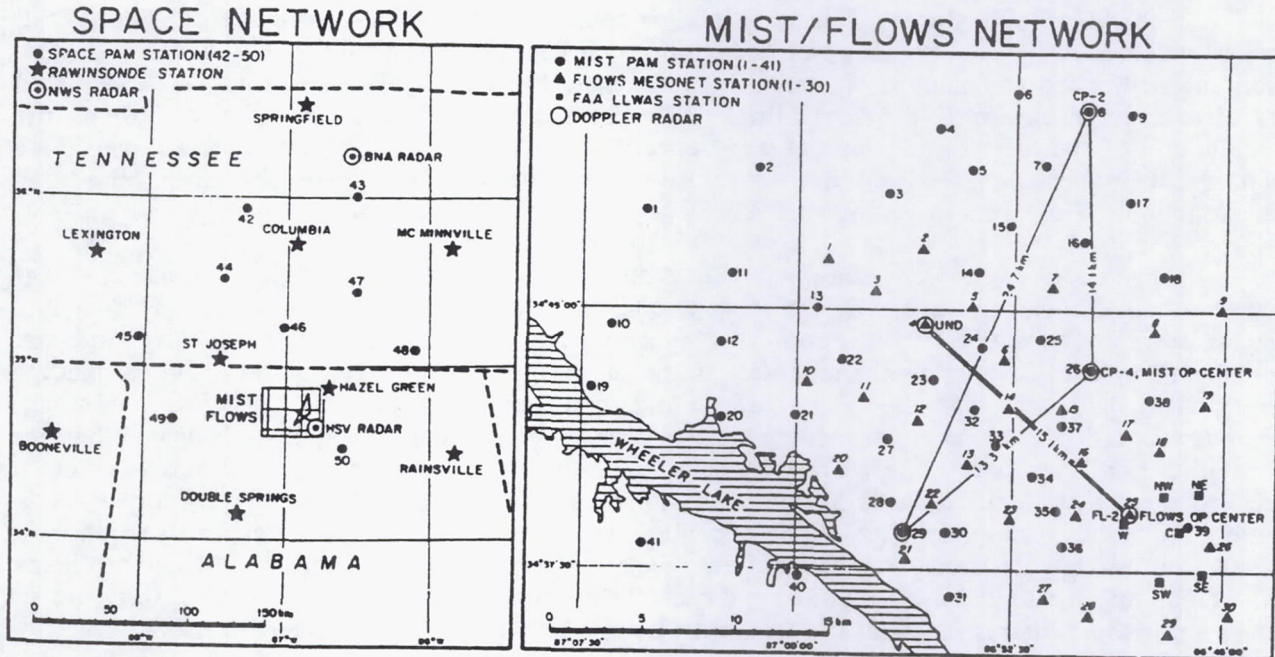


Fig. 2.6-1 (Left) Locations of the SPACE network surface stations. (Right) Locations of the MIST and Flows surface stations.

## References

- Pike, J. M., Brock, F. V., and S. R. Semmer, 1983: Integrated Sensors for PAM II. *Proceedings of the Fifth Symposium on Meteorological Observations and Instrumentation*, Toronto, Ont., Canada. April 11-15, 1983.
- Wolfson, M.M., 1987: The FLOWS Automatic Weather Station Network. *Proceedings of the Sixth Symposium on Meteorological Observations and Instrumentation*, New Orleans, Louisiana. January 12-16, 1987.
- Common Mesonet Format Documentation*, National Center for Atmospheric Research, Boulder, Colorado. December 1985.

### 2.6.2 Tennessee Valley Authority Automated Raingage Network

Seventy-two existing Tennessee Valley Authority (TVA) automatic raingage stations collected precipitation data during the field program. Of these 72 gages, 62 were the standard TVA telephone linked Automated Data Acquisition System (ADAS) gage 6-h measurements, and 10 were Very High Frequency (VHF) radio gage 2-h measurements. Figure 2.6-2 shows the TVA automatic raingage network distribution in relation to the NAMS network. Daily 24-h plots of TVA ADAS raingage rainfall amounts are presented in Section 3.2.

The ADAS gages are weighing raingages connected to a telephone modem. The ADAS gages were dialed by a TVA computer at 6-h intervals beginning at 0500 GMT (0000 CDT). The computer recorded the amount of water in the bucket. The 6-h rainfall amounts were calculated as difference in consecutive 6-h readings. The 24-h rainfall amounts are the greater of the summation of the 6-h readings or the difference 0500 GMT reading for consecutive days. Some data recording problems existed due to faulty circuit boards, noisy telephone lines, and gage malfunctions. However, in general the ADAS gages operated satisfactorily.

The ADAS gages were equipped with a modified data recording circuit board. The gage operated simultaneously as a ADAS 6-h gage and as a TVA 5-min raingage. The TVA 5-min gages powered up every five minutes, read the raingage, and powered down. The reading was compared to the previous 5-min reading. If the new reading exceeded the previous reading by at least 0.75 mm, then the gage reading and time stamp was stored in the TVA 5-min gage memory board (the memory was dumped at a later time). The gage could only remember the previous 5-min reading. Therefore, consecutive 5-min rainfall amounts of 0.50 mm were never recorded as rainfall, since the 0.75 mm threshold was never exceeded. Consequently, the TVA 5-min gages grossly underestimated light rainfall. The TVA 5-min recording gages suffered from faulty circuit boards, noisy telephone lines, gage malfunctions, and other recording problems. Over half of this data were lost due to the above problems. Despite the lost data, this data set does show some interesting rainfall rates and amounts associated with thunderstorm passages.

### 2.6.3 Lightning Detection Network

The NASA 4-station Lightning Location and Protection (LLP) lightning detection network recorded both positive and negative cloud to ground lightning flashes over portions of an eight state area. The system ran continuously during the field program, and the data were archived at MSFC. Calibration factors have been applied to the data to correct any antenna offset errors. However, these corrections were not applied to the twenty-four hour plots of lightning density as presented in Section 3.2.

The lightning detection and location system at MSFC uses four radio direction finding systems linked to a central computer to determine the location, time, number of component return strokes, polarity, and signal intensity of lightning discharges to ground. The basic system is manufactured by Lightning, Location, and Protection, Incorporated. In post analysis, estimates of the peak return stroke current, semi-major and semi-minor axis of the error ellipse, equivalent circular error radius, and area of the error ellipse are computed. The locations of the four direction finders are shown in Table 2.6-1 below.

Table 2.6-1. Location of LLP direction finders

<u>Direction Finder</u>	<u>Latitude</u>	<u>Longitude</u>
1	34.64916	86.66917
2	35.39916	86.07694
3	35.83750	87.44386
4	34.71667	87.88167

Figure 2.6-3 shows the average diurnal variation of lightning activity during the months of June and July, 1986. The large peak between 1600 and 1700 GMT lags solar noon by 3-5 hours. This diurnal lightning peak has been observed by others in Florida (e.g., Maier, et al, 1984), and in the Western U. S. (e.g., Reap, 1986). The semidiurnal lightning peak in the morning at 0700 local coincides with the time of maximum convergence associated with the S pressure wave (Wallace, 1975; Brier and Simpson, 1969). This morning peak occurs on more than 30 of the 60 days in the field program. In addition, when convection is already present in the early morning hours, we also observe an increase in lightning rates (storm intensification) at 0700 local time.

Figure 2.6-4a and b depict the cloud-to-ground lightning discharge recorded by the LLP network during June and July 1986. The figures include both positive and total discharges (positive and negative).

#### References

- Brier, G. W., and J. Simpson, 1969. Tropical cloudiness and rainfall related to pressure and tidal variations, *Q. J. Roy. Meteor. Soc.*, 95, 120-147.
- Maier, L. M., E. P. Krider, and M. W. Maier, 1984. Average diurnal variation of summer lightning over the Florida Peninsula, *Mon. Wea. Rev.*, 112, 1134-1140.
- Reap, R. M., 1986. Evaluation of cloud-to-ground lightning data from the Western United States for the 1983-84 Summer Seasons, *J. Clim. Appl. Meteor.*, 25, 785-799.
- Wallace, J. M., 1975. Diurnal variations in precipitation and thunderstorm frequency over the conterminous United States, *Mon. Wea. Rev.*, 103, 406-419.

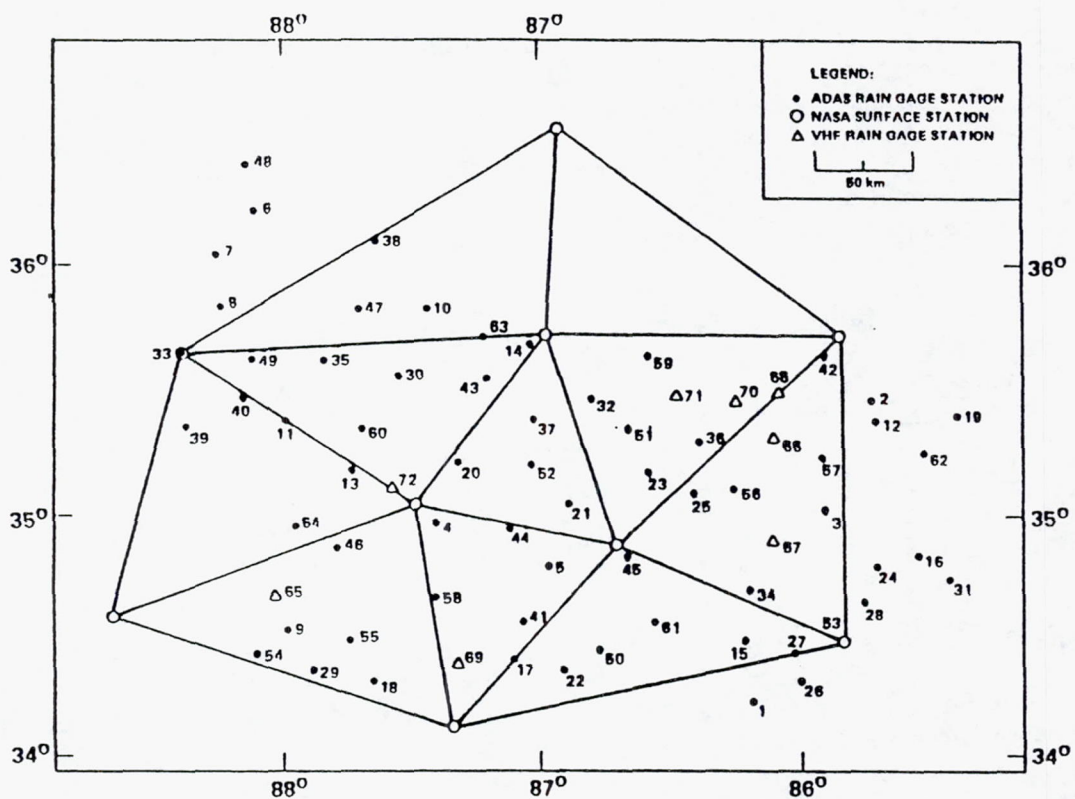


Fig. 2.6-2. TVA automatic raingage network and the NAMS network.

### *DIURNAL LIGHTNING ACTIVITY SPACE EXPERIMENT*

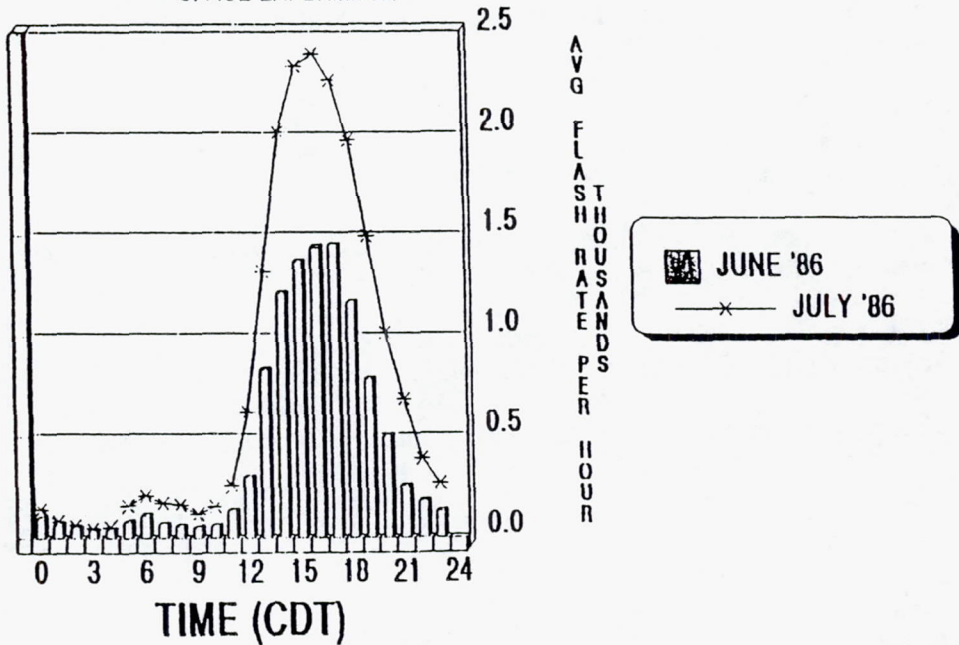


Fig. 2.6-3. Average diurnal variation of lightning over the SPACE network during

**Lightning Discharges to Ground**  
June 1986 (12Z–12Z)

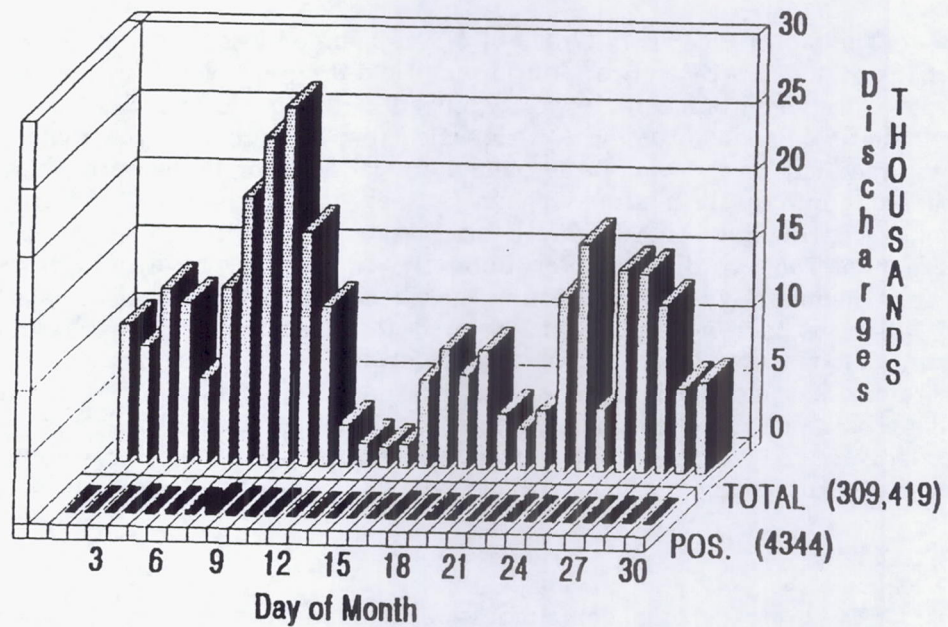


Fig. 2.6-4a. Cloud-to-ground lightning discharge recorded by the LLP network during June 1986.

**Lightning Discharges to Ground**  
July 1986 (12Z–12Z)

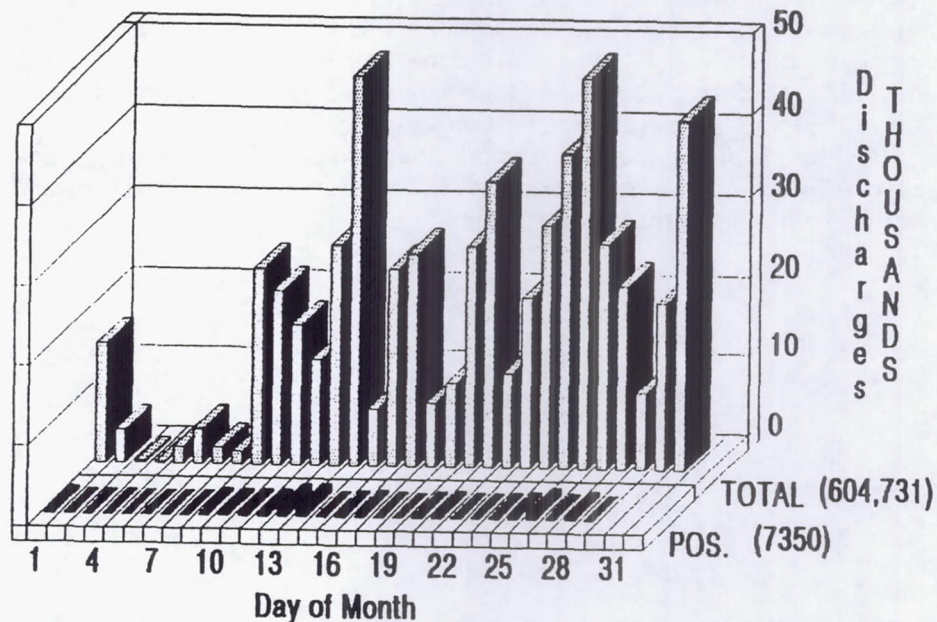


Fig. 2.6-4b. Cloud-to-ground lightning discharge recorded by the LLP network during July 1986.

#### **2.6.4 Mobile Laboratory**

The Storm Electricity Group of NSSL operated a mobile van laboratory (Rust, 1986) over portions of the SPACE network during the field program, which made quantitative measurements in the storm environment. It was equipped with an electric field mill sensor to record the electrostatic component of the electric field from lightning and the higher frequency components of the radiated wave form, an 8-channel optical detector to measure return stroke velocity from cloud-to-ground return stroke channels, and two television video recording systems: one television providing high contrast black and white, the other in color with an external microphone for recording thunder. Both television systems have audio tracks recording comments of crew members with encoded time on their images. The mobile laboratory also carried an IRIG-B time code generator synchronized to international time-broadcast station WWV and a Loran-C navigation receiver and data recording to provide location. In addition, the mobile laboratory was modified for SPACE with a receiver and recorders for the telemetry from the balloon borne electric field meter, the incorporation of a deployable Maxwell current sensor, and the University of Arizona wide band, transient optical detector for comparison with remote sensor measurements.

#### References

Rust, W.D., 1986: (personal communication), National Severe Storm Laboratory, Norman, Oklahoma.

#### **2.6.5 Other Surface Systems**

Data from other existing surface measurement stations in the SPACE network and surrounding area are included in the data base. The NWS Cooperative Observer network recorded 24-h totals of rainfall and temperature data. Some of these stations recorded 1-h precipitation amounts. TVA operated a network of private observers and hydro-station facilities that recorded 24-h rainfall totals. The Department of Energy, Army Corps of Engineers, and the U.S. Geological Survey all maintained various meteorological recording stations in the area. Certain Agricultural Extension offices recorded standard meteorological measurements as well as soil moisture and acid deposition observations.

### 3.0 METEOROLOGICAL CONDITIONS AND DATA INVENTORY

#### 3.1 Synoptic Overview of the Field Program

The most prominent weather/climate feature during the June-July intense SPACE operational period was the drought that affected much of the Southeast (see Bergman et. al., 1986). During the June to July period, the drought was most significant over eastern Tennessee, the Carolinas, and northern Georgia. The portions of the SPACE mesonet over northern Alabama and south-central Tennessee received significantly more rainfall, although below normal conditions were experienced over most of this region. Despite the general drought conditions, a variety of synoptic weather and precipitating cloud systems were observed over the SPACE mesonet in June and July.

Some details on the general weather conditions observed at the Huntsville (HSV) Weather Service Office (WSO) during June and July are given in Fig. 3.1-1. Additional information derived from daily soundings (usually 1800 GMT) taken mainly from Redstone Arsenal (~20 km east-southeast of the HSV WSO) are given in Fig. 3.1-2 through Fig. 3.1-5. As depicted in these figures, several different synoptic regimes were experienced during the experimental program. The most unstable and moist periods, as indicated by low lifted index values and high precipitable water (Figs. 3.1-2a and b, and Figs. 3.1-3a and b, respectively) included 2-11 June, 24-29 June and much of July. The most stable and dry periods occurred during 12-16 June, 18-22 June, 3-5 July and 29-30 July. Stable periods were in general associated with development of upper-level ridges over or near the SPACE mesonet, and also with post cold frontal air masses. A total of seven cold frontal passages during the two-month period were observed on 2-3 June, 12 June, 17 June, 24 June, 2 July, 20 July and 29 July. The most significant cold frontal passages in terms of cooling and drying occurred on 12 June, 17 June and 2 July. Warm core anticyclone episodes over or near the SPACE mesonet were observed during the following time periods: 3-4 June, 13-15 June, 18-23 June, 26 June, 5-10 July, 16-20 July and 22-26 July.

Precipitable water values derived from Redstone Arsenal sounding were often greater than 40 mm. Average values during July were greater and more persistent than those of June, in accordance with climatology. It also appears that precipitable water values from the Nashville sounding site located 150 km to the north were lower by at least 10% on the average. Air mass stability characteristics displayed distinct trends during June, but were more consistent during July. Typical values of lifted index on active thunderstorm days were about -5, with a minimum of -9.5. A vertically integrated stability index, such as Convective Available Potential Energy (CAPE) displayed more daily variability (Fig 3.1-4a and b). Typical CAPE values on thunderstorm days were around  $2000 \text{ J kg}^{-1}$ . This value includes parcel sensible temperature excess only and does not consider virtual effects of water loading, which are large in moist environments. Bulk Richardson number calculations (Weisman and Klemp, 1984), obtained from the formula:

$$RI = CAPE / (0.5 U^2),$$

also varied substantially (Fig. 3.1-5a and b) from day to day. These values were seldom less than 100, and often greater than 500. The wind shear ( $U$ ) is the difference between the environmental wind speeds at low levels (500 m) and the density weighted average wind from the surface to 6 km. Figures 3.1-6a and b depict the wind shear for June and July 1986.

Vertical shear of the horizontal wind was most often weak, as shown in Fig. 3.1-7a and b. Wind shear was objectively determined, following Weisman and Klemp (1984), by computing the difference between the average wind vector within the lowest 500 m and the density-weighted wind vector over the lowest 6 km. This difference is defined herein as the shear vector magnitude  $U$ . Periods that experienced moderate wind shear (defined as a shear vector magnitude greater than  $5 \text{ m s}^{-1}$ ) include 4 June, 9 June, 11-12 June, 17 June, 24 June, 1 July, 11-15 July and 28-31 July. It is noteworthy that these time periods encompass many of the intense thunderstorm days.

A brief description of thunderstorm/precipitation events is provided in Table 3.1-1. Specific details are given in the Daily Summaries in Section 3.2. Days that experienced widespread thunderstorm activity over the SPACE mesonet include 6 June, 11 June, 24 June, 28 June, 11 July, 13 July, 14 July, and 31 July. On many other days thunderstorms were intense, but areal coverage was scattered. In general, stratiform precipitation was most prevalent over the southern SPACE mesonet from 3 June to 11 June, and from 13 July to 15 July. Lack of stratiform precipitation close to the Doppler radars during other time periods was somewhat surprising.

The following section describes in detail daily weather events and experimental operations.

#### References

- Bergman, K.H., C.F. Ropelewski, and M.S. Halpert, 1986: The record Southeast drought of 1986. *Weatherwise*, 39, 262-266.
- Weisman, M.L. and J.B. Klemp, 1984: The structure and classification of numerically-simulated convective storms in directionally varying environments. *Mon. Wea. Rev.*, 112, 2479-2499.

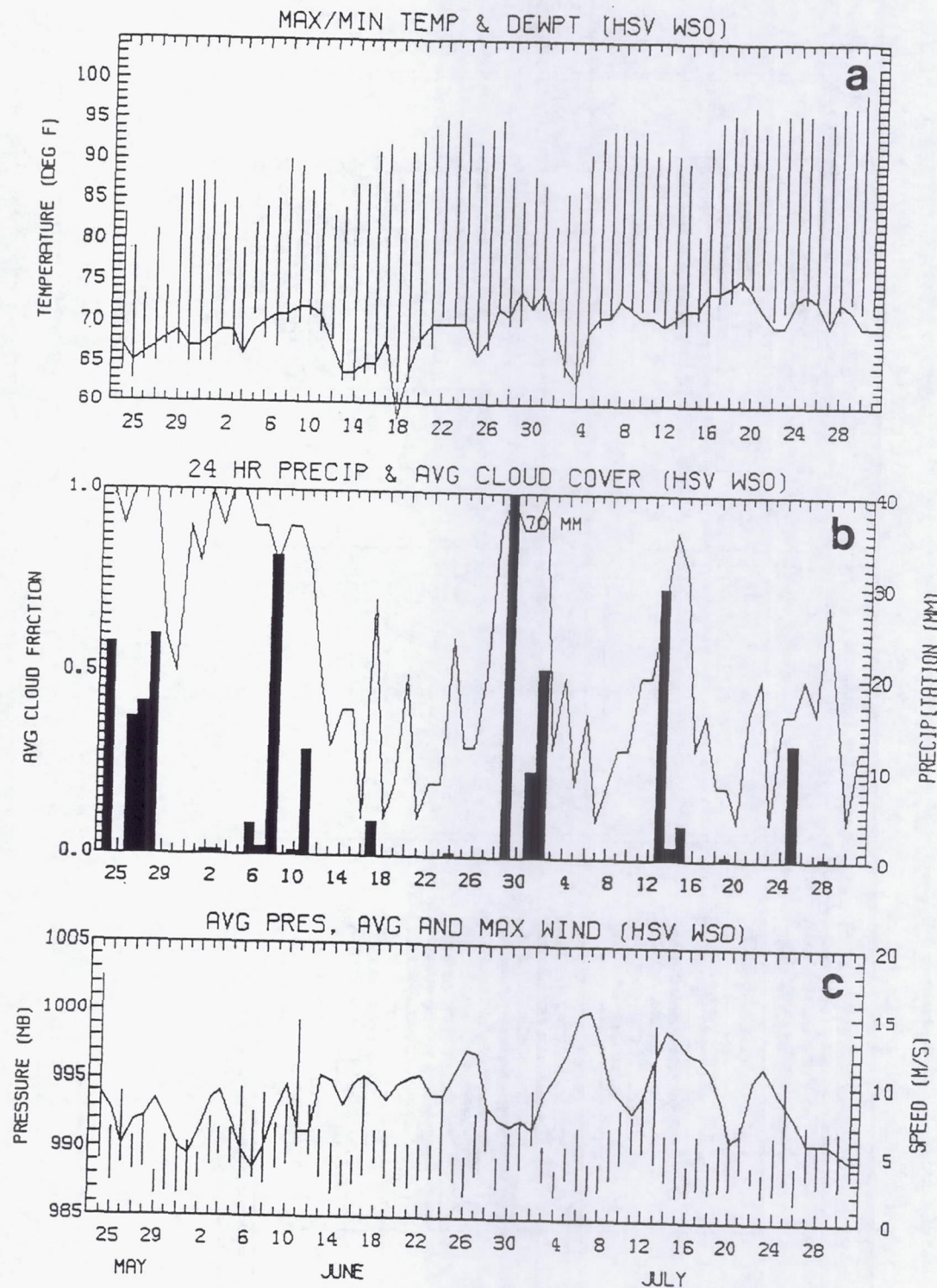


Fig. 3.1-1. General weather conditions at the Huntsville (HSV) Weather Service Office during June and July 1986. (Top) Maximum/minimum temperatures and average dewpoint. (Middle) Average cloud cover and 24-h precipitation (histogram). (Bottom) Average pressure with the average and maximum wind speed.

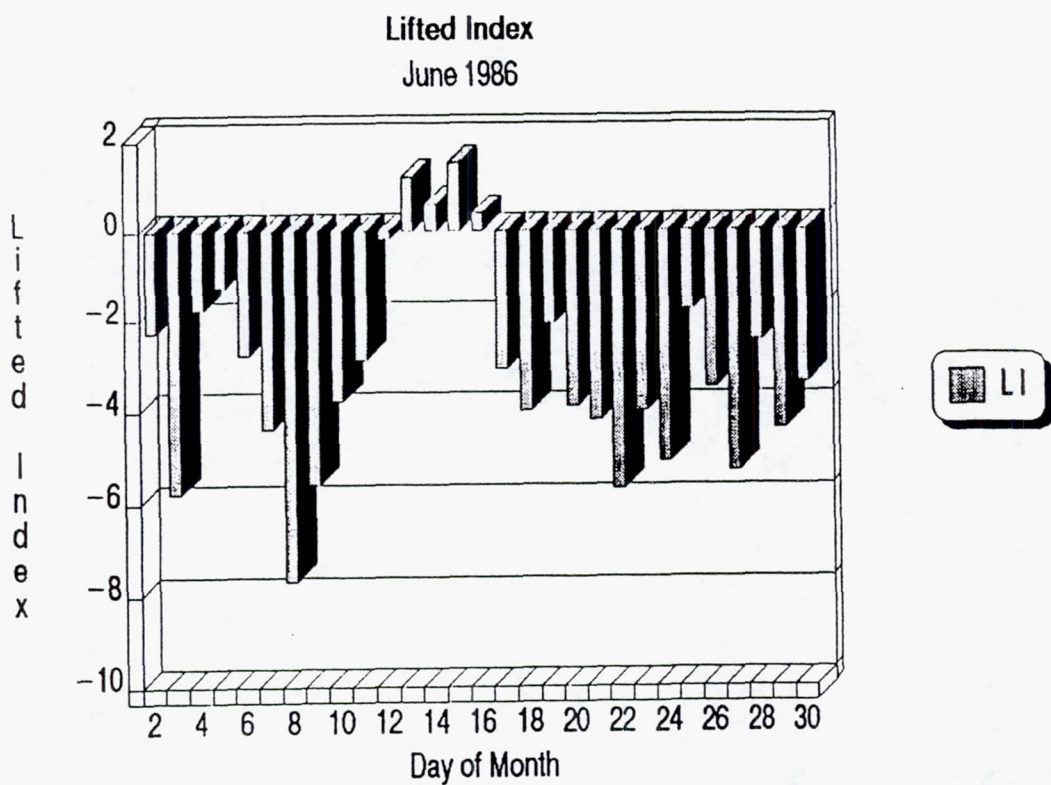


Fig. 3.1-2a. Lifted Index ( $^{\circ}\text{C}$ ) from daily rawinsonde soundings during June 1986.

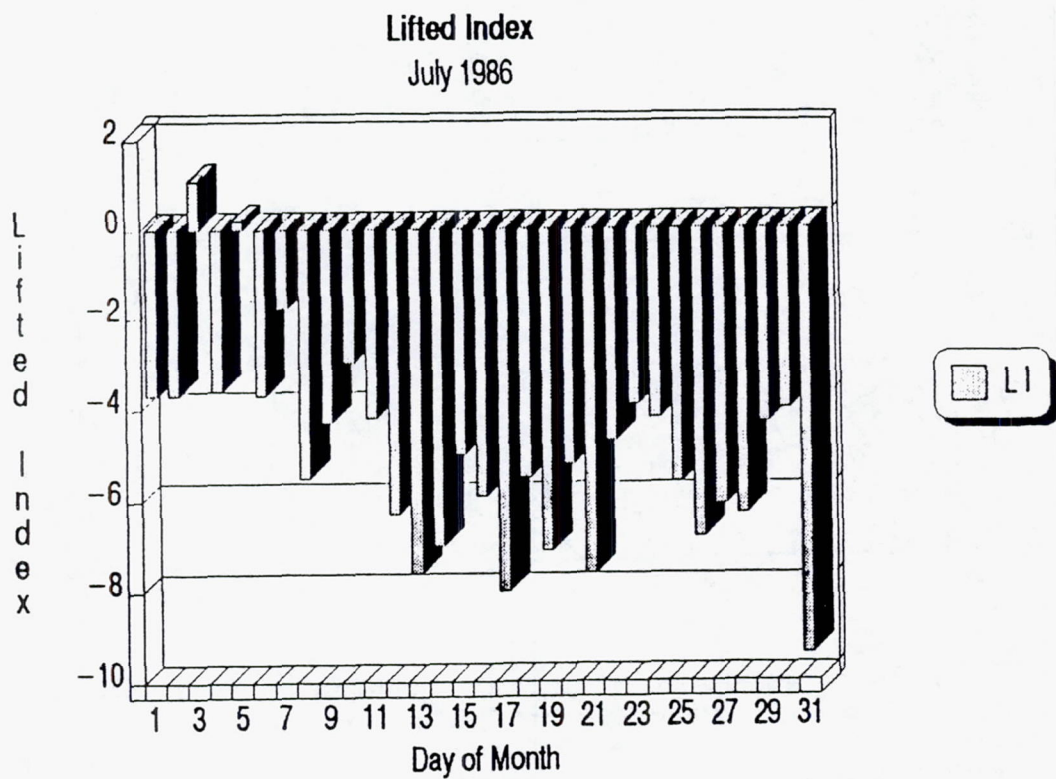


Fig. 3.1-2b. Lifted Index ( $^{\circ}\text{C}$ ) from daily rawinsonde soundings during July 1986.

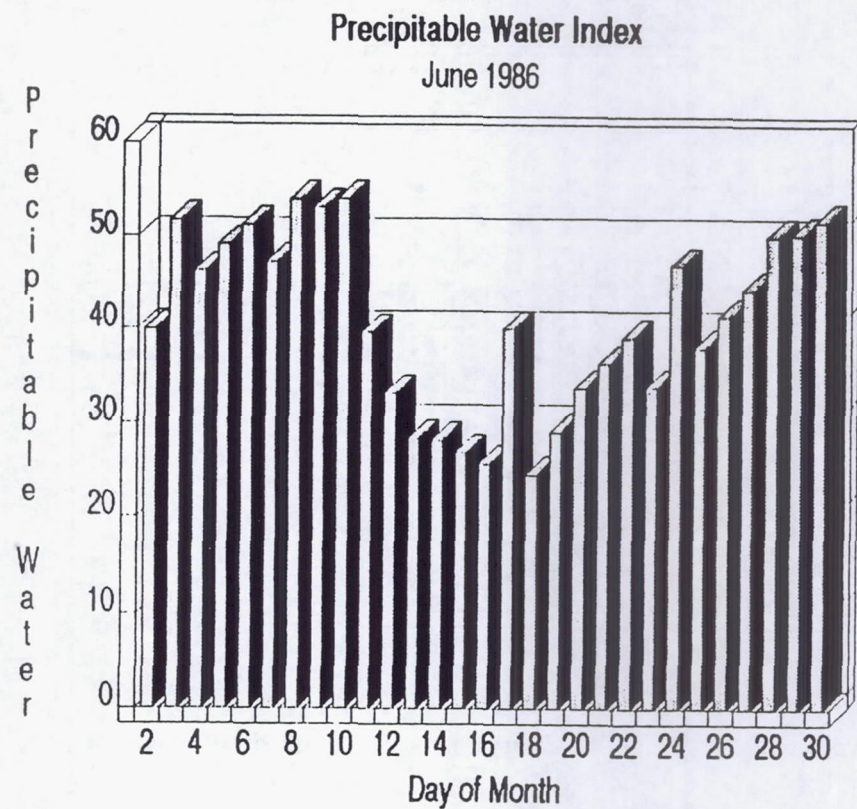


Fig. 3.1-3a. Precipitable Water (mm) from daily rawinsonde soundings during June 1986

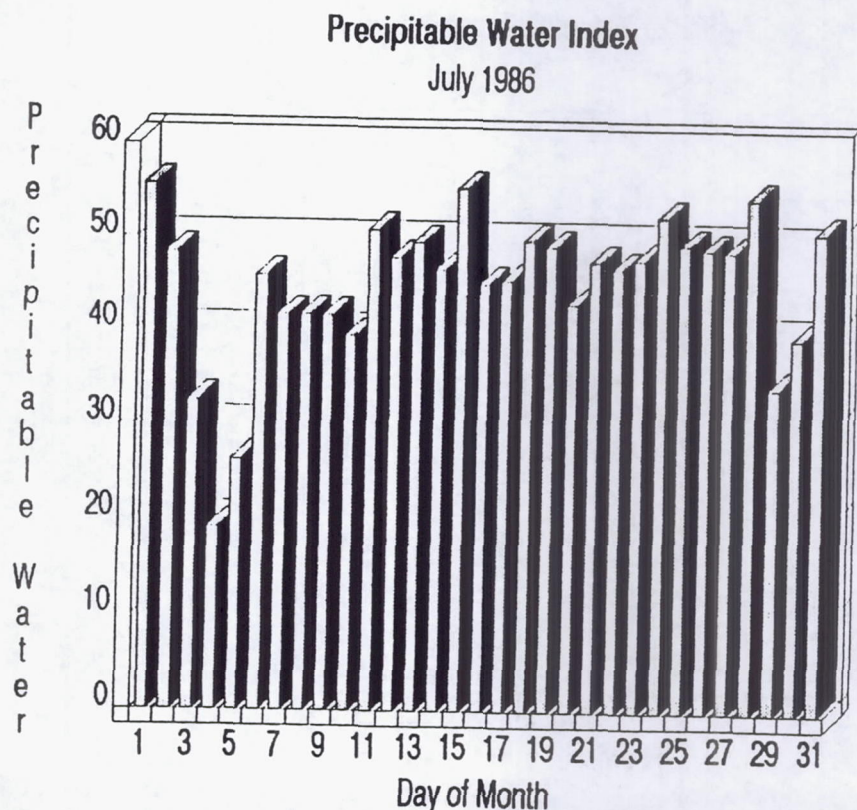


Fig. 3.1-3b. Precipitable Water (mm) from daily rawinsonde soundings during July 1986.

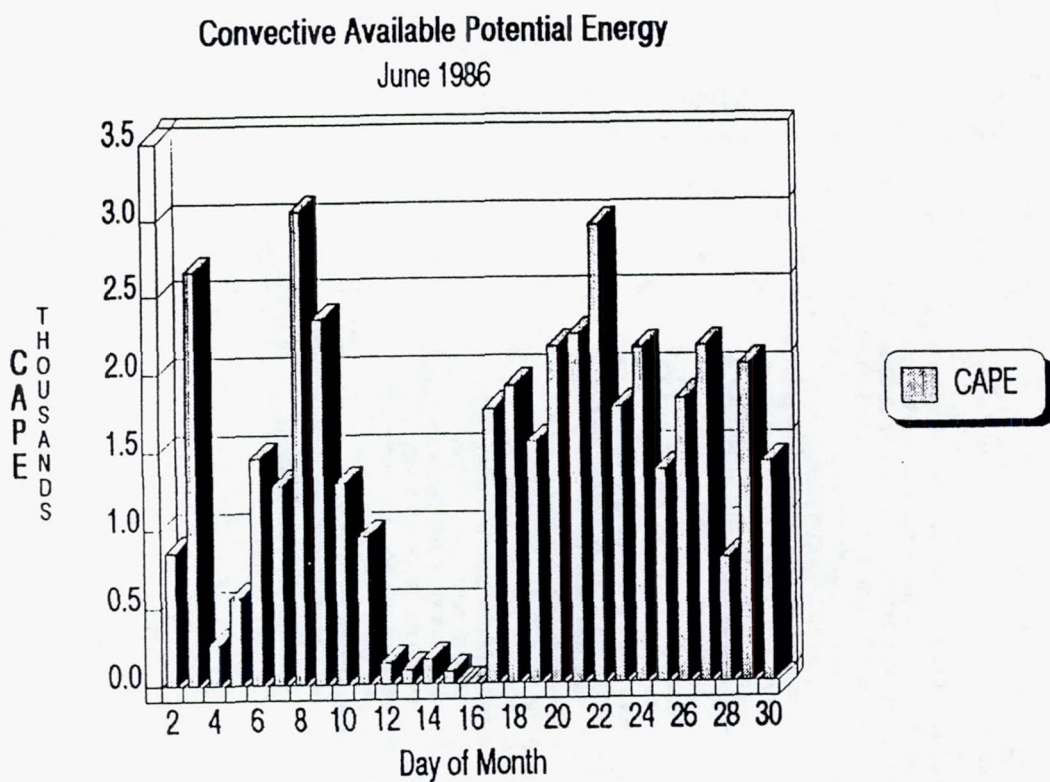


Fig. 3.1-4a. Convective Available Potential Energy ( $\text{J kg}^{-1}$ ) from daily rawinsonde soundings during June 1986.

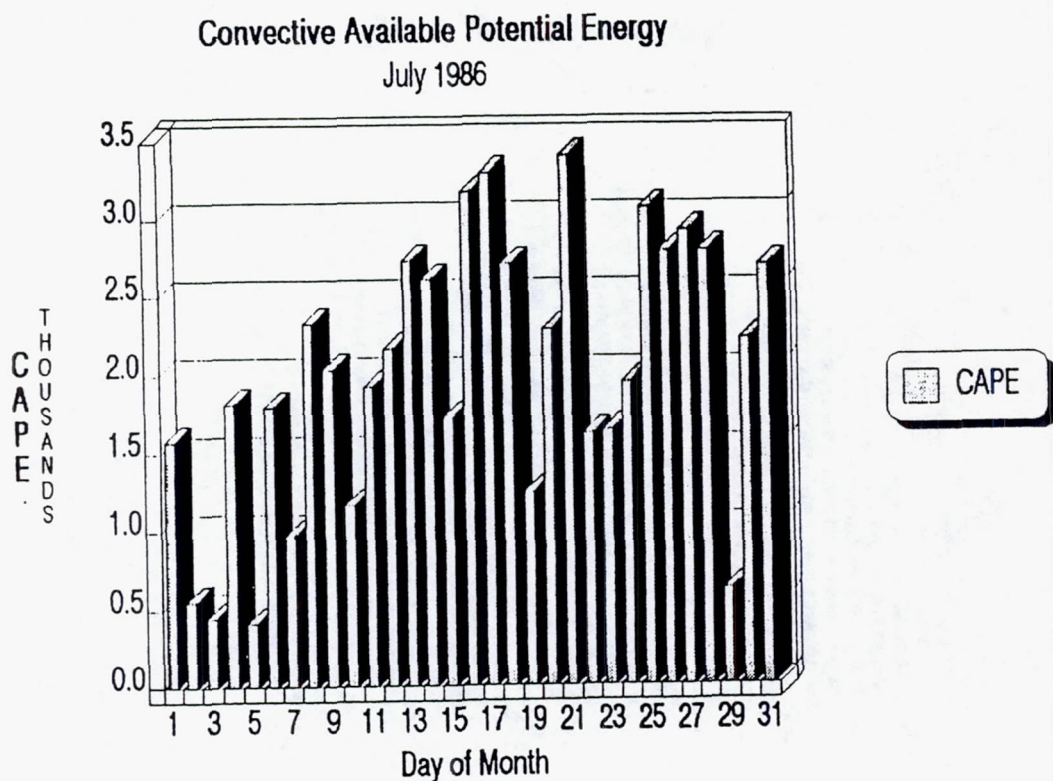


Fig. 3.1-4b. Convective Available Potential Energy ( $\text{J kg}^{-1}$ ) from daily rawinsonde soundings during July 1986.

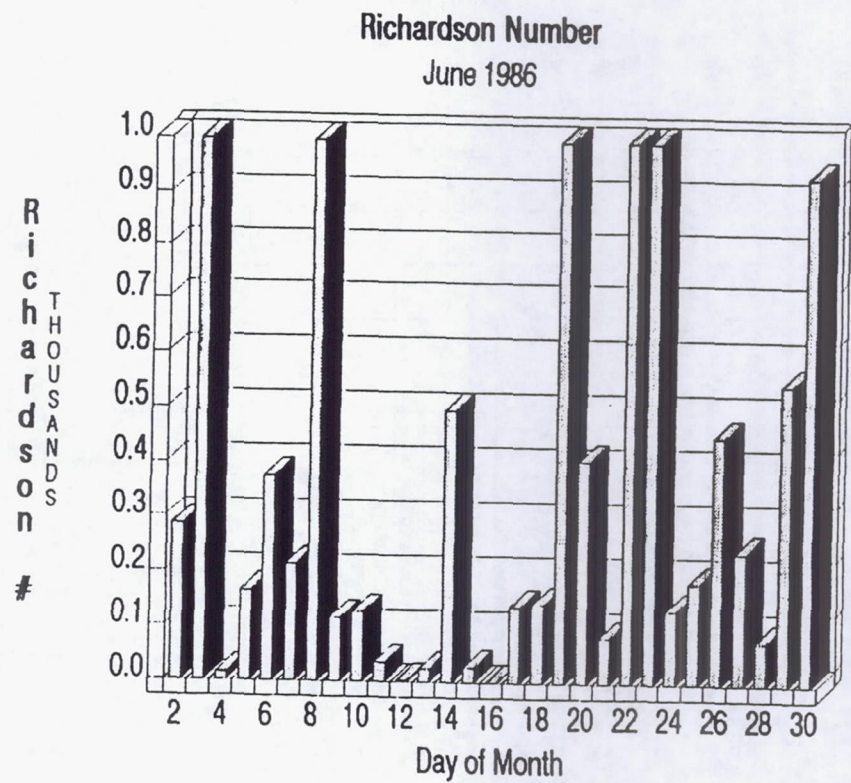


Fig. 3.1-5a. Richardson Number from daily rawinsonde soundings during June 1986

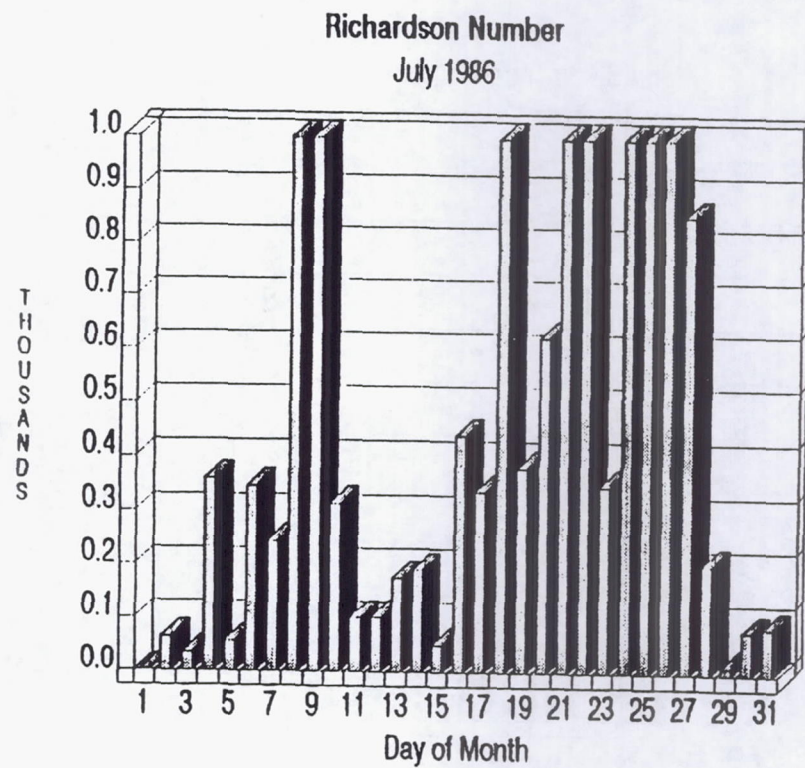


Fig. 3.1-5b. Richardson Number from daily rawinsonde soundings during July 1986.

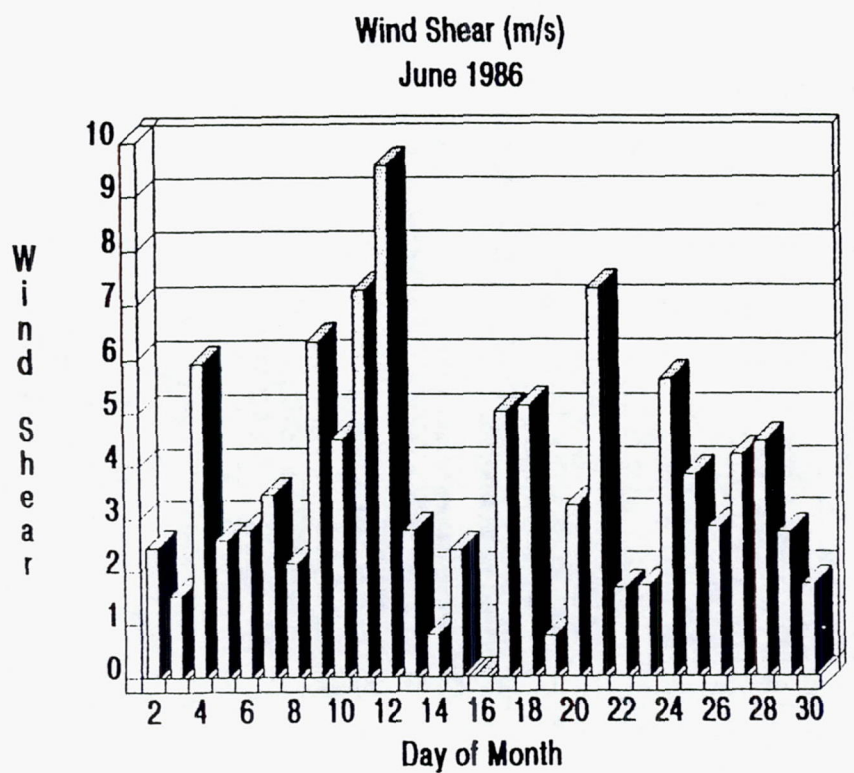


Fig. 3.1-6a. Wind shear from daily rawinsonde soundings during June 1986.

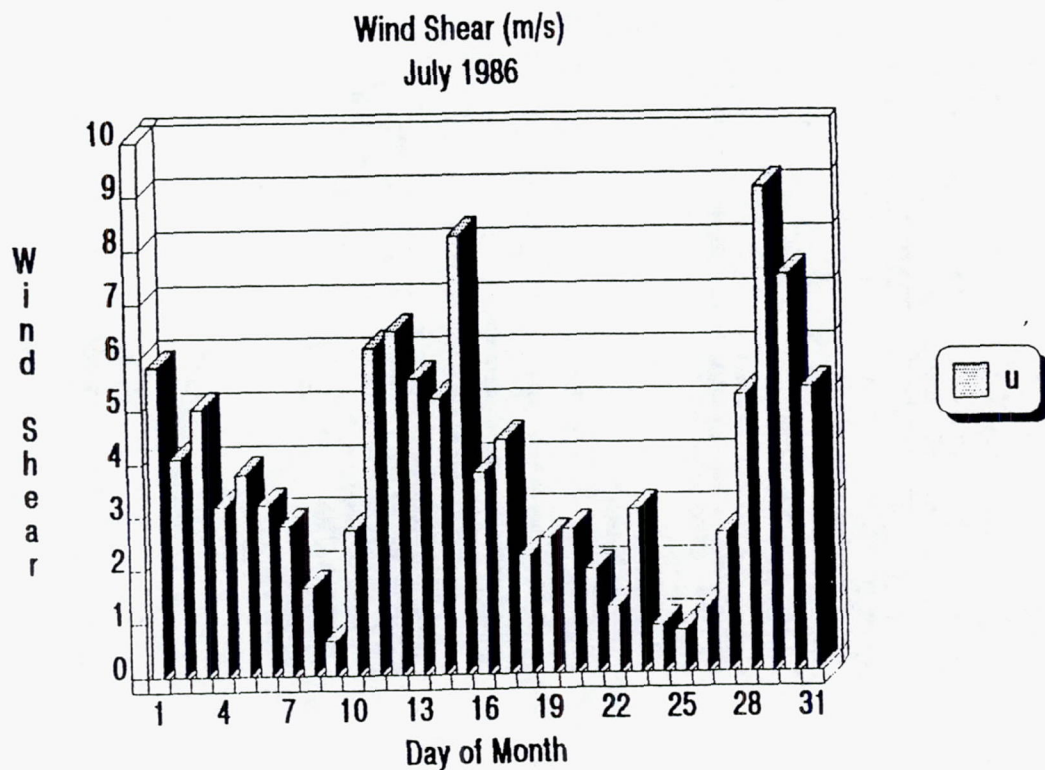


Fig. 3.1-6b. Wind Shear from daily rawinsonde soundings during July 1986.

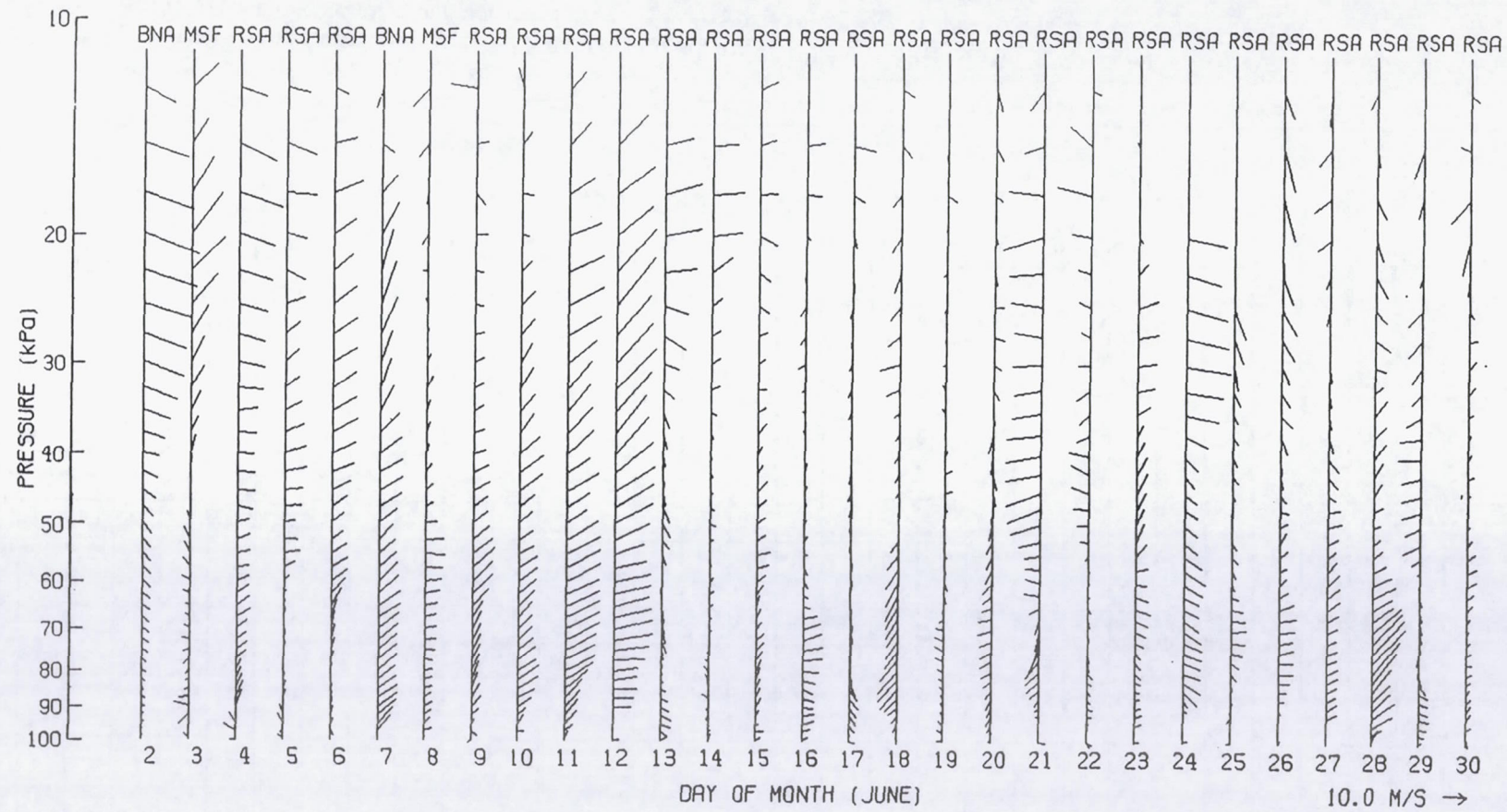


Fig. 3.1-7a. Daily vertical profiles of wind during June, 1986. Most measurements are taken from the 1800 GMT Redstone Arsenal, AL (RSA) sounding. When RSA soundings were not available, 1200 GMT Nashville, TN (BNA) soundings, or soundings released from NASA/MSFC, AL (MSF) close to 1800 GMT were used. **Please note:** The wind directions on the figure are vectors and not wind barbs. Therefore, these vectors depict the direction to which the wind is heading.

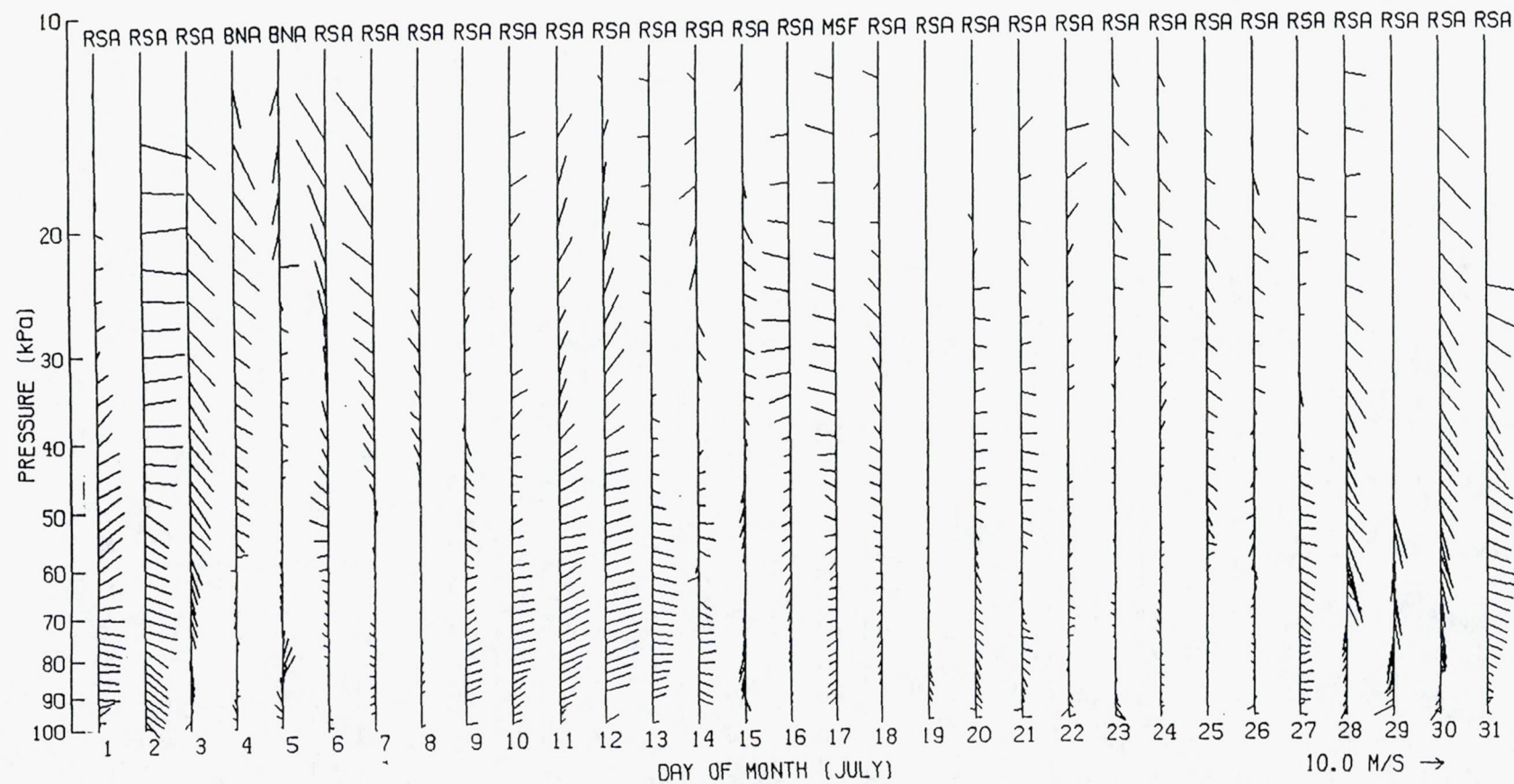


Fig. 3.1-7b. Same as Fig. 3.1-7a except during July, 1986. Please note: The wind directions on the figure are vectors and not wind bars. Therefore, these vectors depict the direction to which the wind is heading.

Table 3.1-1. Abbreviated daily weather and precipitation events for June.

DAY	BRIEF WEATHER DESCRIPTION
June 2	Scattered TRW, locally heavy rainfall over both SPACE and MIST/FLOWS mesonets.
June 3	Scattered TRW over the SPACE net, a few intense cells, some stratiform precipitation.
June 4	Early morning showers, quiet afternoon, evening MCS moved into and dissipated over the western SPACE mesonet.
June 5	Moderately weak convective line and stratiform precipitation over the western and central SPACE mesonet.
June 6	MCS over the western and central SPACE mesonet, scattered TRW elsewhere.
June 7	Scattered RW and TRW, many moderately intense over the northern SPACE mesonet.
June 8	Active TRW, locally-heavy rainfall, vigorous outflow, stratiform precipitation.
June 9	Weak RW during the morning, clearing by mid-afternoon.
June 10	Convective/stratiform line over the central SPACE and MIST/FLOWS networks.
June 11	Active day with early MCS over the western SPACE net, and late squall line over the central SPACE mesonet. Passage of SWT over the SPACE mesonet.
June 12	Cold frontal passage by 1200 GMT, stable post-frontal conditions thereafter.
June 13	Suppressed day, no TRW or RW.
June 14	Suppressed day, no TRW or RW.
June 15	Suppressed day, no TRW or RW.
June 16	Very weak isolated RW over the SPACE mesonet.
June 17	Cold frontal passage, scattered intense TRW along front, strong outflow and heavy rain over the MIST/FLOWS mesonet.
June 18	Stable post-frontal day, no TRW or RW.
June 19	Isolated weak TRW/RW over NE corner of the SPACE mesonet.
June 20	Widely-scattered and weak RW/TRW.
June 21	Isolated intense multicell TRW 50 km east of the MIST/FLOWS mesonet over hills, rest of SPACE mesonet remained inactive.
June 22	Weak isolated RW over W and SW SPACE mesonet.
June 23	Persistent and intense multicell TRW over the E central SPACE net, scattered TRW over N SPACE net, evening MCS over N SPACE net.
June 24	Surface trough plus cold front over the SPACE net; widespread intense TRW from MIST net to S SPACE net (MCS).
June 25	Stable post-frontal day, no TRW or RW.
June 26	Isolated TRW and RW SW of MIST/FLOWS mesonet late afternoon to early evening.
June 27	Scattered weak to moderate RW and TRW over SE SPACE mesonet.
June 28	Hurricane Bonnie remnants (clouds and SWT), widespread precipitation, region of intense TRW over central SPACE net late afternoon to early evening.
June 29	Early morning convective line that produced heavy rain over MIST/FLOWS net, scattered afternoon TRW over SPACE mesonet, some intense.
June 30	Weak RW around the MIST/FLOWS net, stronger TRW over N SPACE net.

Abbreviations: TRW - thunderstorm, RW - shower, MCS - mesoscale convective system (defined as a cluster of merged TRW/RW), SWT - short-wave trough

Table 3.1-1 (continued). Abbreviated daily weather and precipitation events for July.

DAY	BRIEF WEATHER DESCRIPTION
July 1	Widely-scattered, intense TRW and RW, decreasing in intensity during the afternoon.
July 2	Cold frontal and SWT passage, prefrontal precipitation band with embedded TRW/RW.
July 3	Stable post-frontal conditions, air mass cooler and much drier.
July 4	Stable conditions, developing upper-level ridge over the SPACE mesonet.
July 5	Building upper-level ridge over N Carolina, moisture return over SW SPACE net, weak isolated RW.
July 6	Upper-level ridge over N Carolina, increasing low-level moisture, scattered intense TRW over SPACE mesonet and just east of MIST/FLOWS mesonet.
July 7	Numerous weak RW over SPACE mesonet, only one TRW.
July 8	Isolated RW/TRW over SPACE net, intense TRW system 60 km SW of MIST/FLOWS net.
July 9	Small MCS over central and southern SPACE mesonet.
July 10	Scattered weak RW during afternoon over SPACE mesonet, late TRW development over NW MIST/FLOWS net.
July 11	Wide variation of numerous but scattered RW and TRW over and around the MIST/FLOWS net, some weak and some intense. Late MCS over the SE SPACE mesonet.
July 12	Isolated RW during afternoon, dissipating MCS with deep outflow over the SPACE and MIST net early evening.
July 13	Development of a MCS over central and southern SPACE net and MIST net, intense TRW, vigorous outflow, heavy rain and large area of stratiform precipitation.
July 14	MCS development over SPACE network, but limited stratiform precipitation; intense TRW with heavy rain and strong outflow.
July 15	Small MCS over SPACE net from morning to early afternoon, clearing over the SPACE mesonet thereafter. Afternoon TRW line over N SPACE net.
July 16	Scattered TRW over SPACE and MIST/FLOWS net, moderate in intensity.
July 17	Intense TRW over central SPACE net, late MCS over SE border of SPACE net.
July 18	Scattered TRW over NW and S borders of SPACE net.
July 19	Intense TRW just NE of MIST net, strong outflow.
July 20	Isolated intense TRW just E of MIST/FLOWS net, TRW line over N central SPACE net.
July 21	TRW along S border of SPACE mesonet, clear elsewhere.
July 22	TRW along S and SE border of SPACE mesonet, clear elsewhere.
July 23	Clear, dry day over the SPACE net, some TRW along the SE border of the SPACE net.
July 24	Intense TRW over SE SPACE net, just SE and E of the MIST net.
July 25	Intense TRW over MIST/FLOWS and central SPACE mesonets, well-defined outflows.
July 26	Small MCS development over the central SPACE net, late evening large MCS moved into the SPACE net from the NW.
July 27	Mostly clear and suppressed.
July 28	Late development of very intense TRW over the E SPACE mesonet, just E of the MIST/FLOWS mesonet, electrically active.
July 29	Isolated weak TRW over the central SPACE net during the afternoon.
July 30	Hot, dry day.
July 31	Active MCS day over the SPACE net (3 MCS's), intense TRW with large hail, strong outflow and much lightning.

Abbreviations: TRW - thunderstorm, RW - rain shower, MCS - mesoscale convective system  
(defined as a cluster of merged TRW/RW), SWT - short-wave trough

### 3.2 Daily summaries

Data collected during the COHMEC period (June 2 - July 31) are summarized in Tables 3.2-1 and 3.2-2 for June and July 1986, respectively. These tables provide a general reference of data collection by day of the month to assist the researcher in determining case study days. A more detailed data collection summary is included in the daily summaries that follow.

This section contains a detailed description of each day's conditions and data collection during the field program (June 2 - July 31). The six page format for each day is consistent to allow easy comparison between days. Text includes a daily synoptic and cloud/precipitation overview, with a summary of aircraft, rawinsonde, radar, and satellite operations. Room for researcher's notes and comments have been provided. Figure (a) presents the national 1200 GMT surface, 500 mb, minimum/maximum temperatures, and 24-h precipitation maps (Daily Weather map Series).

The hourly collection of COHMEC data are presented in Table (a). Bar graphs indicate data collection times from 1000 GMT to 1200 GMT (following day) for Sounding Systems, Radars, Remote Sensors, Aircraft, Satellite, and Surface Systems individual platforms. Cross hatching in the RADAP row indicates times when only ICRAD data was available. The times listed for remote sensors are the takeoff and landing times of the high altitude aircraft at the Wallops Flight Facility (WFF). The flight time from WFF to the SPACE network was approximately 1.5 h. The aircraft could remain over the network for a maximum of 3.5 h before returning to WFF. A few of the high altitude flights were not flown over the SPACE network. These are designated as "NS" in the table. See Appendix A for a detailed plot of the flight tracks and times of each mission. Times indicated for the aircraft are also takeoff and landing times from their respective airports. The GOES satellite data listed in the table represent only the data presently archived at MSFC. Additional images will be added to the data base at a later time. The approximate overpass times of the polar orbiting satellites are designated by triangles in the table. These images are not archived at MSFC.

A daily satellite image is presented in Fig. (b). Most of these images are visible 2 km resolution, taken during the afternoon (i.e. 1800 GMT - 2300 GMT) when convective activity is at a peak. Four km resolution infrared images were used when maximum convective activity occurred at night.

A daily rawinsonde sounding (skew-T diagram) is presented in Fig. (c). Most of these soundings were taken at Redstone Arsenal or MSFC at approximately 1800 GMT. Soundings from the NWS Nashville, TN, station (1200 GMT) were used when any local soundings were not available. Calculations of Precipitable Water (PW), Lifted Index (LI), Convective Available Potential Energy (CAPE), and the Richardson number (RI) are included below each figure. Please note: The wind directions on the skew-T diagram are vectors and not wind barbs. Therefore, these vectors depict the direction to which the wind is heading.

Figure (d) depicts a 24-h composite (1200 GMT to 1159 GMT) of lightning ground strike density for the SPACE network. Each gray scale represents a higher level of lightning density as indicated in the figure's legend. The data used in these plots have not been corrected for measured site errors. Totals of rainfall for approximately the same 24-h time (1100 GMT to 1100 GMT) period (Fig. (e)) are presented using the TVA ADAS raingage network data.

TABLE 3.2-1 COHMEX Daily Data Collection Summary for June 1986

	1	2	3	4	5	6	7	8	9	10	11	12	13	14	15	16	17	18	19	20	21	22	23	24	25	26	27	28	29	30
Redstone																														
NASA MSFC																														
Athens																														
Hazel Green																														
Springfield																														
Lexington																														
Columbia																														
McMinnville																														
St. Joseph																														
Booneville																														
Double Springs																														
Rainsville																														
NWS Alpha																														
UHF Profiler																														
SODAR																														
LIDAR																														
BNA RADAP																														
CP-2																														
CP-3																														
CP-4																														
FL-2																														
UND																														
BNA Kavouras																														
TUP Kavouras																														
MAMS																														
HIS																														
MPR																														
MTS																														
MCR																														
AMMS																														
CALS																														
LIP																														
LRP																														
T-28																														
Cessna 207																														
Citation																														
P-3																														
GOES VIS/IR																														
GOES VAS																														
GOES RISOP																														
NOAA 9																														
DMSP																														
NIMBUS 7																														

TABLE 3.2-2 COHDEX Daily Data Collection Summary for July 1986

	1	2	3	4	5	6	7	8	9	10	11	12	13	14	15	16	17	18	19	20	21	22	23	24	25	26	27	28	29	30	31
Redstone																															
NASA MSFC																															
Athens																															
Hazel Green																															
Springfield																															
Lexington																															
Columbia																															
McMinnville																															
St. Joseph																															
Booneville																															
Double Springs																															
Ransville																															
NWS Alpha																															
UHF Profiler																															
SODAR																															
LIDAR																															
BNA RADAP																															
CP-2																															
CP-3																															
CP-4																															
FL-2																															
UND																															
BNA Kavouras																															
TUP Kavouras																															
MAMS																															
HIS																															
MPR																															
MTS																															
MCR																															
AMMS																															
CALS																															
LIP																															
LRP																															
T-28																															
Cessna 207																															
Citation																															
P-3																															
GOES VIS/IR																															
GOES VAS																															
GOES RISOP																															
NOAA 9																															
DMSP																															
NIMBUS 7																															

## SYNOPTIC AND PRECIPITATION OVERVIEW

2 June 1986

### Synoptic Conditions

A surface anticyclone of ~1026 mb intensity moved eastward over the Great Lakes region during the day. This high was associated with a relatively vigorous short wave trough and managed to push a weak cold front into the northern SPACE mesonet during the afternoon and evening. Over the larger synoptic scale, a broad ridge was located over the western U.S. Upper level flow of  $\sim 10 \text{ m s}^{-1}$  was generally westerly over the SPACE mesonet, and abundant moisture existed from the surface to middle levels. Over the SPACE region, typical surface temperature and dewpoint values were 29 and 20 °C, respectively, while surface flow was weak ( $\sim 2\text{-}3 \text{ m s}^{-1}$ ) and variable from a northerly direction.

### Cloud/Precipitation Overview

Middle level cloudiness persisted during the morning hours and limited afternoon maximum surface temperatures to 26-30 °C. Widely scattered thunderstorm activity formed over the mesonet by 1700 GMT, after which moderately intense thunderstorms were common within or near the MIST/FLOWS network until 2100 GMT. This area of thunderstorm activity appeared to attain maximum coverage and intensity around 1900 GMT. Although individual cells were short-lived, locally heavy rainfall was produced. Another area of stronger thunderstorms formed over northern Tennessee around 1800 GMT. This activity assumed a broken line configuration (oriented east to west), and reached maximum intensity from 2100 to 2300 GMT as the line advanced slowly southward. Reflectivity factor values in some cells near BNA exceeded 57 dBZ. By 0000 GMT, the general linear configuration was replaced by a small cluster of intense thunderstorms just southwest of BNA. Recorded rainfall was isolated, but peaked at 17.5 mm over the MIST/FLOWS network, and at 25 mm over the SPACE network.

### Notes:

2 June 1986



## **OPERATIONAL SUMMARY**

**2 June 1986**

### **Rawinsonde Operations**

Special rawinsondes were launched from NASA/MSFC at 1200, 2100, and 0000 GMT. The latter two soundings were released after local thunderstorm activity peaked, although some secondary development did occur over the western SPACE mesonet around 2300 GMT.

### **Radar Operations**

This was an initial MIST/FLOWS radar shakedown day. Therefore, only limited data were collected by CP-3 and CP-4 in the 2000-2200 GMT time slot. Dual and single Doppler data on several local cells were acquired. CP-2 was not yet operational (and would not be until 10 June), and FL-2 was down due to software modifications.

### **Satellite Operations**

Normal operations.

### **Aircraft Operations**

No operations.

### **Notes:**

Day: MONDAY

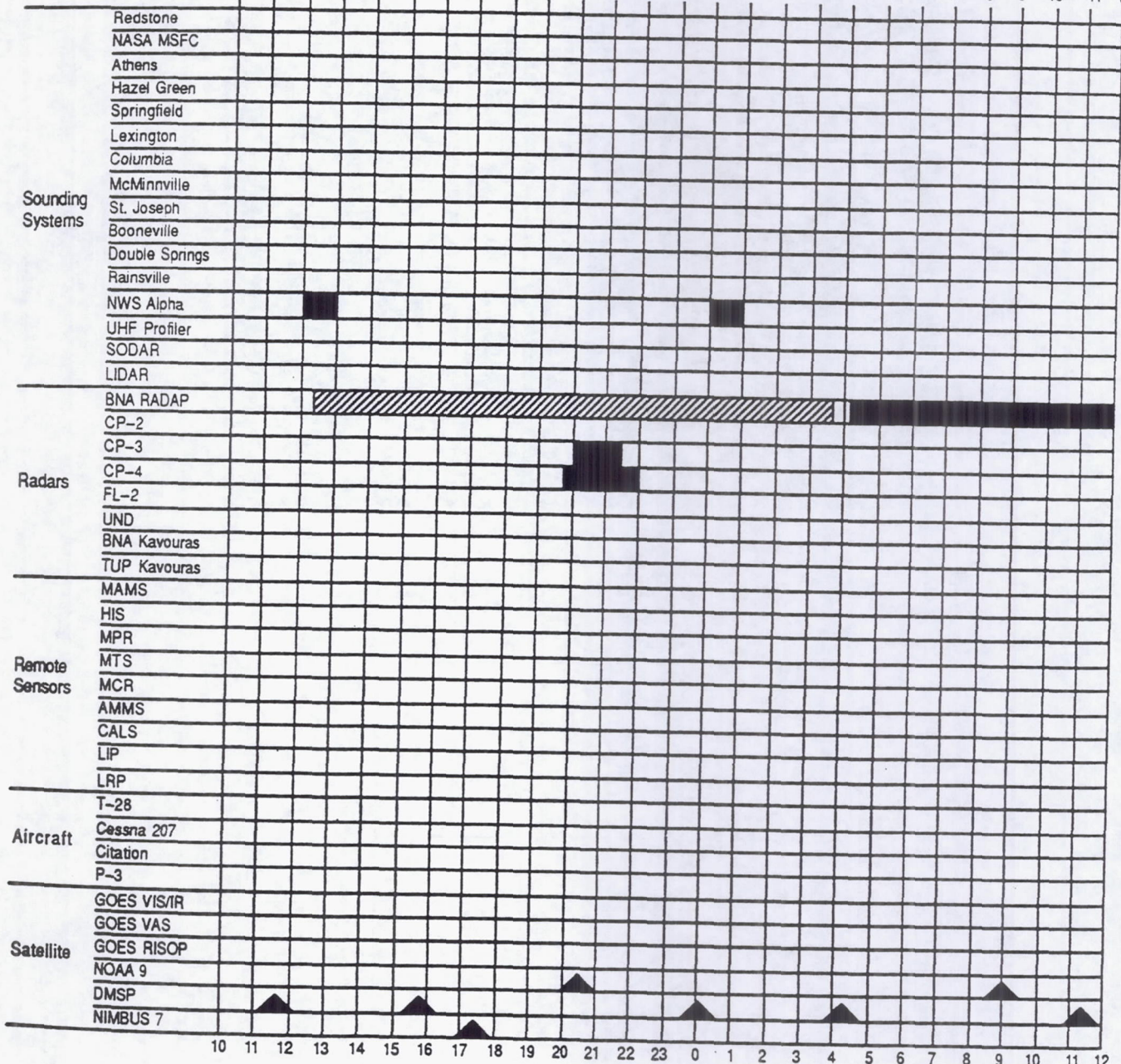
Date: 6/2/86

Julian Day: 153-154

## Hourly Collection of COHDEX Data

Time (GMT)

10 11 12 13 14 15 16 17 18 19 20 21 22 23 0 1 2 3 4 5 6 7 8 9 10 11 12



## Comments

Surface Systems	PAM	MISSING STATIONS 4, 8 & 9
	FAM	OPERATIONAL
	NAM	MISSING STATIONS 3, 4, 6, 7, 8 & 9
	TVA ADAS	MISSING STATIONS 15, 27, 45, 56 & 63
	LLP	OPERATIONAL
	Mobile Lab	NOT OPERATIONAL

2 June 1986

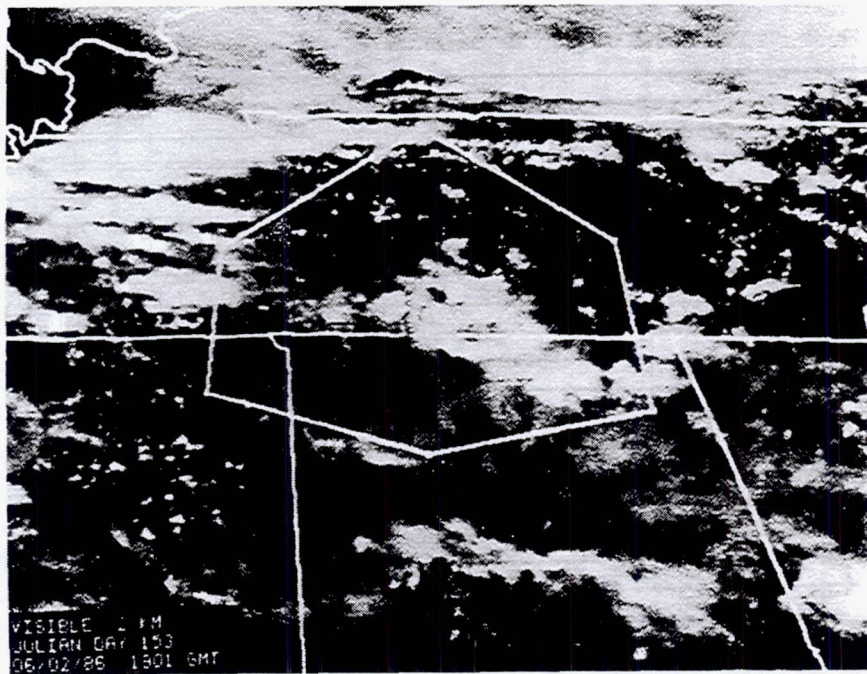


Fig. 3.2-1b. Visible 2 km GOES Central satellite image for 2 June 1986 1901 GMT

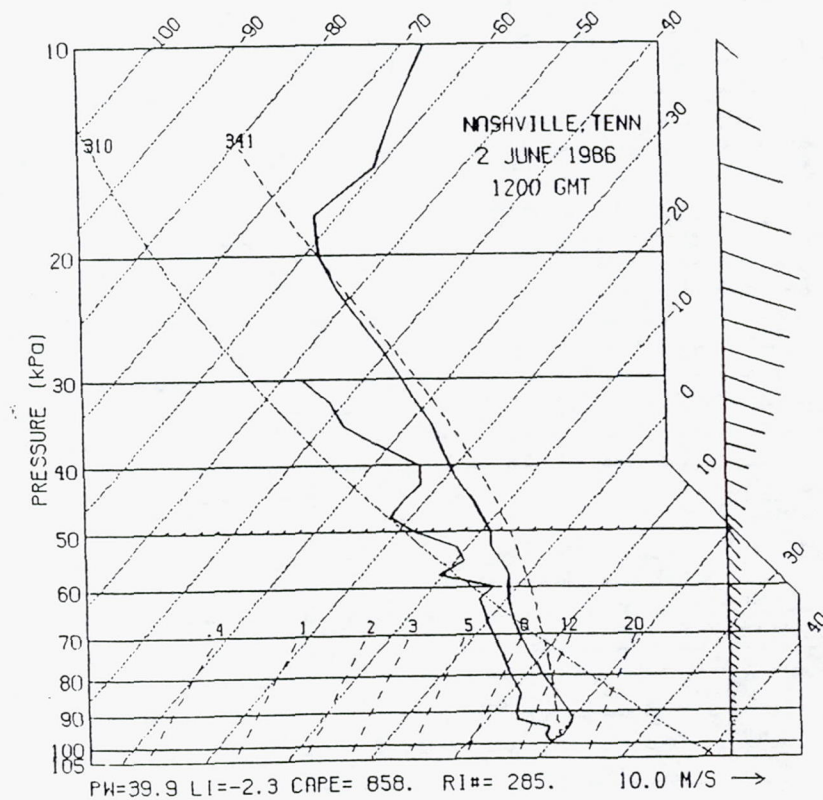


Fig. 3.2-1c. Nashville, TN, rawinsonde sounding for 2 June 1986 1200 GMT

2 June 1986

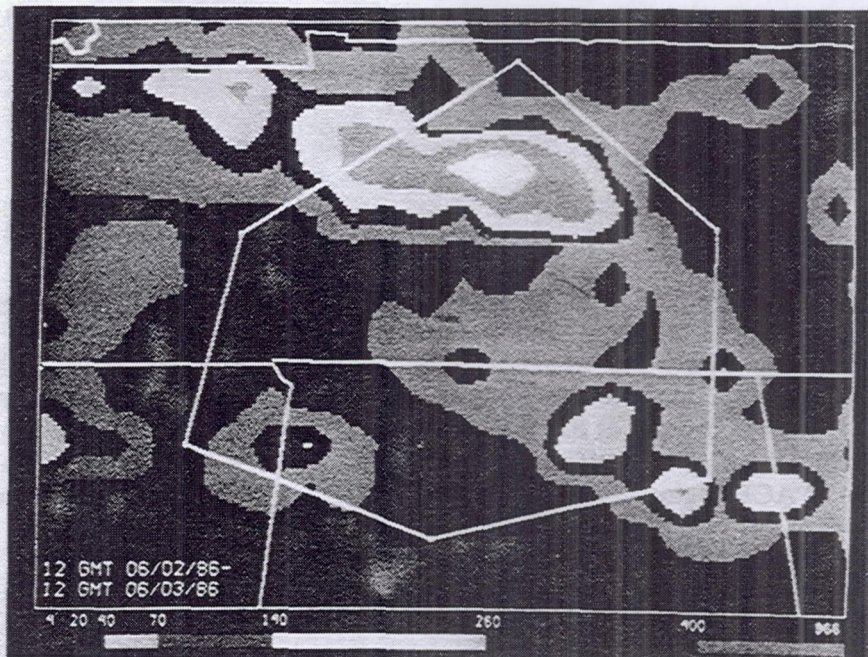


Fig. 3.2-1d. Twenty-four hour lightning strike density plot for 2-3 June 1986

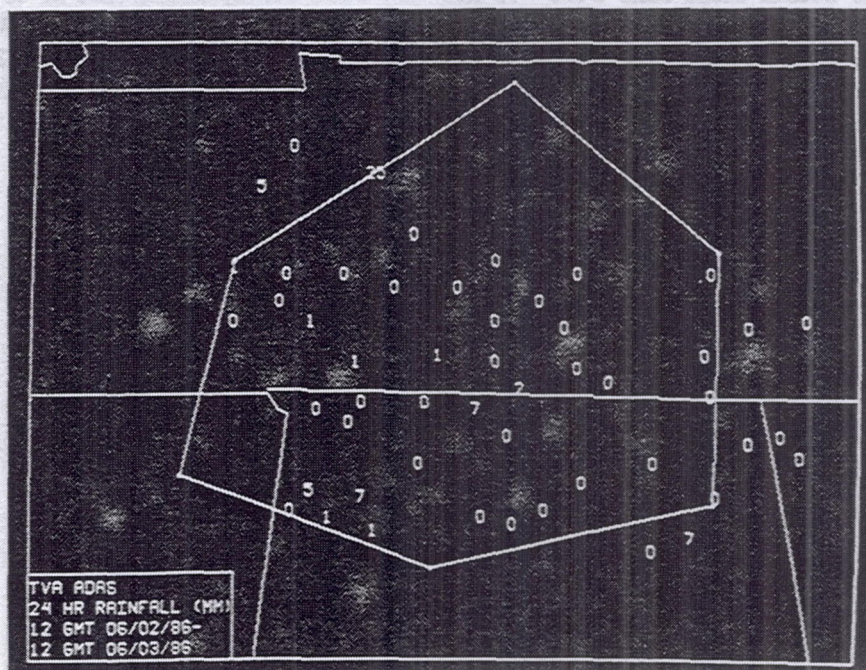


Fig. 3.2-1e. Twenty-four hour TVA ADAS rainfall totals (mm) for 2-3 June 1986

## **SYNOPTIC AND PRECIPITATION OVERVIEW**

**3 June 1986**

### **Synoptic Conditions**

The cold front that edged into the northern SPACE region yesterday moved through the southern portion of the mesonet and turned stationary during the day. A broad surface anticyclone moved eastward over the New England states during the day, and a ridge extended southwestward from the high center to over the SPACE network. A relatively moist south to southwesterly flow was present at 850 and 700 mb, with winds above remaining weak as an upper level high showed signs of intensifying over the Southeast. Afternoon temperature and dewpoint values over the SPACE region were 28 and 20 °C in the presence of light and variable flow.

### **Cloud/Precipitation Overview**

Precipitating deep convection began relatively early by 1700 GMT along a boundary associated with an early morning cloud cover over northern Mississippi. Initial activity was confined to the eastern half of the SPACE network, from the MIST/FLOWS network and to the northeast. Cells that formed near the MIST/FLOWS network appeared to be most intense initially, exhibiting strongly diverging tops and moderately strong low level outflow winds of  $\sim 15 \text{ m s}^{-1}$ . Outflows were commonly associated with individual precipitating cells and appeared to generate secondary convection. Several microbursts were logged by FL-2 personnel between 1721 and 1840 GMT near Athens, and also south to southwest of the MIST/FLOWS network. Maximum tops within these cells were  $\sim 13 \text{ km}$ . By 2000 GMT, a long line of cells extended from near HSV northeastward along the western foothills of the Appalachian Mountains to the Kentucky-Tennessee border. Much of this convection turned stratiform after 2100 GMT. Late afternoon convection was not prominent over the central and northern SPACE network. Rainfall reports were locally heavy, with two 25+ mm reports in the MIST/FLOWS network and two 30+ mm reports over the SPACE network.

### **Notes:**

3 June 1986

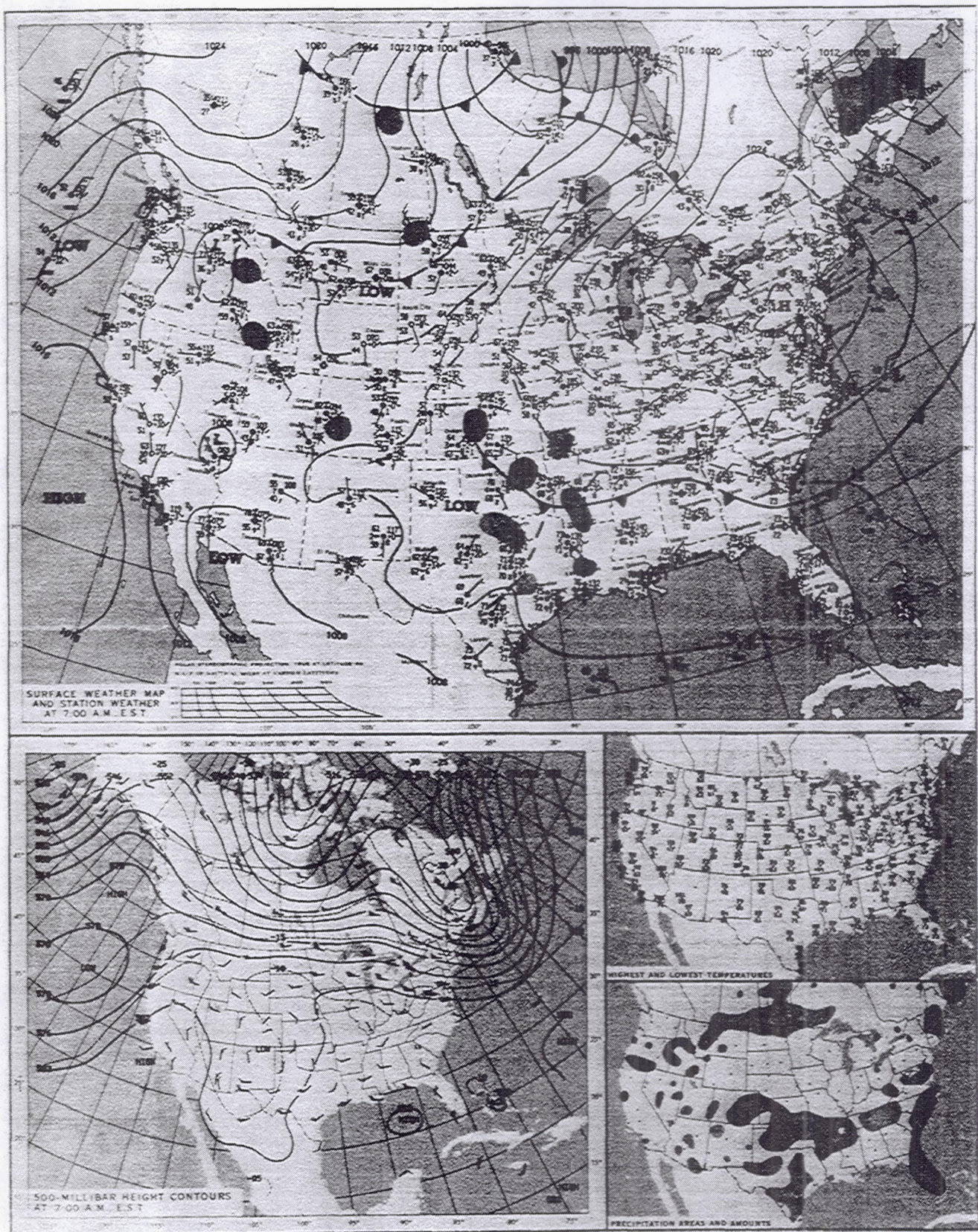


Fig. 3.2-2a. Synoptic weather conditions for 3 June 1986 1200 GMT